DOE/DP/40050-9
Distribution Category UC21

THE DEVELOPMENT OF FERROMAGNETIC SPINELS FOR OPTICAL ISOLATION AT 10.6 μm

Final Report

Kenneth J. Teegarden

The Institute of Optics
University of Rochester
Rochester, New York 14627

May 1980

Prepared For

THE U.S. DEPARTMENT OF ENERGY

UNDER CONTRACT NO. DE-AS02-76DP40050.A003

DISCLAIMER

NOTICE

ABSTRACT

Vacuum hot pressing was used to fabricate $CdCr_2S_4$, $CdCr_2Se_4$ and (1-x) $CdCr_2S_4 \cdot x\ CdCr_2Se_4$ discs with diameters of 1.25 cm from fine powders and small single crystals to relative densities as high as 99.6%. Optical attenuation coefficients of $\sim 1.0\ cm^{-1}$ at 10.6 m were obtained for $CdCr_2S_4$, and values of 12.1 cm^{-1} and 14.9 cm^{-1} for the selenide and sulfer-selenide mixture. Two-and three-phonon absorption bands were found to limit the transmission of $CdCr_2S_4$ at $\lambda > 10$ μm. Extrinsic absorption mechanisms caused the higher attenuation coefficients in $CdCr_2Se_4$ and the mixture. The main extrinsic mechanisms at long wavelengths were free carrier absorption (in $CdCr_2Se_4$) and an impurity absorption band at 16.3 μm due to Cr_2O_3. At short wavelengths the attenuation coefficient was dominated by scattering from pores and second phases. Free carrier absorption was found to be induced by free selenium present in the starting powders. Suppression of this absorption was achieved by optimizing the hot-pressing procedure in order to remove free selenium. The presence of pores was attributed to incomplete densification arising from the presence of second phases (CdSe and Cr_2Se_3) and the absence of plastic deformation as a densification mechanism. Laser damage thresholds of 250 $MWcm^{-2}$ and 100 $MWcm^{-2}$ were measured at 10.6 μm for $CdCr_2S_4$ and $CdCr_2Se_4$, respectively.

TABLE OF CONTENTS

LIST OF TABLES

LIST OF FIGURES

I. OBJECTIVES

The chalcogenide spinels are ferro or ferrimagnetic semiconductors which display large magneto-optical effects in modest applied fields and are transparent in the infrared from about 2 μm to 17 μm depending on the specific compound. The physical properties of the chalcogenide spinels have been reviewed by Jacobs (1).

The objective of this project was to develop these materials for use as Faraday isolators at 10.6 μm. At the beginning of the project the difficulties which had to be overcome were lack of knowledge about the intrinsic level of optical absorption to be expected, small crystal size, and lack of information about laser damage thresholds. We proposed to overcome the crystal size problem by hot-pressing powders rather than using single crystals, and minimizing optical absorption by the proper choice of pressing parameters. Laser damage studies were also to be conducted to evaluate the use of the materials in high power laser systems.

II. SUMMARY OF RESULTS

Initially, $CdCr_2S_4$ was emphasized in the work because earlier studies showed that hot-pressed samples of this compound could be produced with optical attenuation coefficients of about 1.0 cm^{-1}, and with magnetic properties substantially the same as those obtained in single crystals (1,2). One of the contributions of this project was to show that an intrinsic limit to the transmission of $CdCr_2S_4$ at 10.6 μm is imposed by multiphonon transitions associated with reststrahl vibrations. This work is described in section 5.2.1. of this report and in technical report 4056-3. This intrinsic limit corresponds to an attenuation coefficient of about .3 cm^{-1} at 10.6 μm. Hence state of the art hot-pressed $CdCr_2S_4$ is within a factor of three of the intrinsic limit. The transmission of an antireflection coated element of the proper thickness for a Faraday isolator at 10.6 μm would thus be 89%.

In addition to being limited in transparency by multiphonon transitions, $CdCr_2S_4$ has a Curie point of about 80°F, near to the boiling point of liquid nitrogen. This means that careful temperature control may be needed when $CdCr_2S_4$ is used as an isolator. On the other hand, the Curie temperature of $CdCr_2Se_4$ is 130°K. Hence cooling with liquid nitrogen is more effective than for the sulfide.

Also the longer wavelength reststrahl of the selenide should lead to a reduced multiphon absorption at 10.6 m. An extrapolation of the intrinsic absorption coefficient of $CdCr_2Se_4$ leads to a value of 0.6 cm^{-1} at 10.6 μm. For these reasons the focus of the project was shifted to $CdCr_2Se_4$, as a potentially better candidate for a Faraday isolator at 10.6 μm. However, hot-pressed samples of $CdCr_2Se_4$ were found to have attenuation coefficients much greater than the predicted intrinsic value, or the value found previously in single crystals. It was found that this extrinsic attenuation was due to scattering from pores, free carier absorption and absorption by impurities such as Cr_2O_3. An analysis of the absorption processes in hot-pressed $CdCr_2S_4$ and $CdCr_2Se_4$ is presented in section 5.2.

An extensive study of the densification of powders of $CdCr_2Se_4$ was undertaken in an effort to reduce the attenuation at 10.6 μm. This included photoacoustical and x-ray analysis of the composition of the starting powders as well as x-ray and infrared analysis of hot-pressed samples. The optical absorption coefficient of the hot-pressed samples was correlated with density and impurity content. It was found that incomplete densification of $CdCr_2Se_4$, and hence scattering, occurred because of residual second-phase particles of CdSe and Cr_2Se_3. Decomposition of $CdCr_2Se_4$ was found to occur during hot pressing. These results are described in detail in section 5.1.

The alloy $(1-x)CdCr_2S_4 \cdot xCdCr_2Se_4$ was also studied over the compositional range $0<x<1$. It was found that although the reststrahl edge shifted to longer wavelengths for increasing values of x, the extrinsic attenuation coefficient also increased continuously. The alloy was found to consist partially of a solid solution and partially of a physical mixture, thus scattering due to index mismatch and from pores because of incomplete densification undoubtedly contributed to the increase in attenuation coefficient.

The photoacoustic studies of powders of $CdCr_2Se_4$ and $CdCr_2S_4$ are particularly interesting because they represent some of the first spectroscopic data ever taken in the infrared using this technique. These studies are described in section VI.

Laser damage studies were conducted on hot-pressed $CdCr_2S_4$ and $CdCr_2Se_4$, using a pulsed Co_2 laser with a peak power of about 17 MW (0.7 Joules in a 40 nsec pulse). It was found that the threshold for damage at 10.6 μm was 250 $MWcm^{-2}$ for $CdCr_2S_4$ and 100 $MWcm^{-2}$ for $CdCr_2Se_4$.

III. BACKGROUND

3.1. Properties of $CdCr_2Se_4$ and $(1-x)CdCr_2S_4 \cdot x\ CdCr_2Se_4$

3.1.1 Crystal Structure and Crystal Growth

A. $CdCr_2Se_4$

$CdCr_2Se_4$ has a spinel structure with a space group Fd3m(1). The spinel structure is made up of eight face centered cubic arrangements of chalcogenide anions with 96 interstices, of which 64 are octahedral sites and 32 tetrahedral sites; of these only 24 are occupied by divalent and trivalent cations.

There are three basic types of spinel structures(3):

1. normal
2. inverse
3. random.

As will be seen later, the type of structure has a large effect on the electrical, optical and magnetic properties. In a normal spinel all of the divalent cations occupy the tetrahedral sites and all of the trivalent cations occupy the octahedral sites as shown in the general chemical formula

$$[A]^t[B_2]^o X_4^c$$

where t = tetrahedral, o = octahedral, and c = cubic close packed site. The inverse spinel has all of the divalent cations at the octahedral sites with one half

of the trivalent cations in the tetrahedral sites and one half in the octahedral sites as shown in the general chemical formula:

$$[B]^{t}[A\ B]^{o}X_4^{c}$$

The random spinel structure has a distribution of cations at the octahedral and tetrahedral sites as shown in the general chemical formula:

$$[A_{1/3}B_{2/3}]^{t}[A_{2/3}B_{4/3}]^{o}X_4^{c}$$

The type of structure is determined by the site preference energy of the cations(3, 4, 5). Table 3.1 lists octahedral and tetrahedral site preference energies of metal cations in oxide spinels. These same energies can also be used as an upper limit in chalcogenide spinels due to the larger anionic radius.

$CdCr_2Se_4$ has a normal spinel structure with all the Cd^{2+} ions at the tetrahedral sites and all the Cr^{3+} ions at the octahedral sites, Figure 3.1. A perfect spinel structure would have the structure parameter u equal to 0.375, but in most materials it deviates from 0.375. The deviation is an indication of a distortion of the cubic close packing induced by the cations, i.e. octahedrally

TABLE 3.1. OCTAHEDRAL SITE PREFERENCE ENERGY OF SOME TRANSITION METAL CATIONS IN THE SPINEL STRUCTURE (4).

ION	OCTAHEDRAL SITE PREFERENCE ENERGY* Kcal/g at.wt.
Zn^{2+}	-31.6
Cu^{2+}	- 0.1
Ni^{2+}	9.0
Co^{2+}	-10.5
Fe^{2+}	- 9.9
Fe^{3+}	-13.3
Mn^{2+}	-14.7
Mn^{3+}	3.1
Cr^{3+}	16.6
Cd^{2+}	-29.1
In^{3+}	-40.2
Ga^{3+}	-15.4

*Negative values indicate that the ion is unstable at the octahedral site.

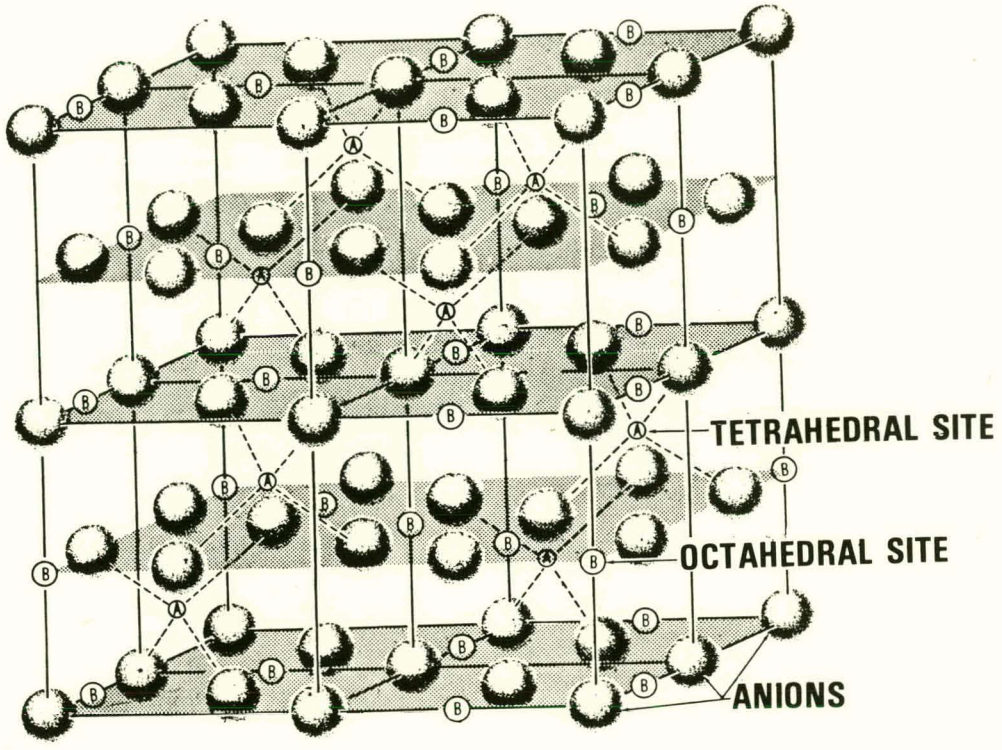

Figure 3.1. Idealized spinel structure showing anions in a cubic closest-packed array, cations A and B in tetrahedral and octahedral sites respectively (adopted from (7).

coordinated cations are displaced along the [111] direction (6). In $CdCr_2Se_4$ the u-parameter is slighlty larger than 0.375, u=0.390. The lattice parameter of materials with a spinel structure is determined mainly by the packing of the anions since the cations are much smaller than the anions and occupy the interstitial sites. The physical properties of $CdCr_2Se_4$ are listed in Table 3.2.

Single crystals of $CdCr_2Se_4$ have been grown by liquid transport(8, 9, 10) vapor-liquid transport(11), vapor transport(12), and flux growth(13). The largest single crystals grown to date have been 1-4mm on the side in a period of one week by the liquid transport method. Chemical vapor depositing (CVD) has also been attempted at RCA Laboratories, however only small single crystals were grown(14). The kinetics of growth are apparently very slow and a saturation point is reached. Powders up to 100μm on the side have also been grown by a solid state reaction of CdSe and Cr_2Se_3 and/or the individual elements in a selenium atmosphere. The phase diagram of the CdSe-Cr_2Se_3 pseudo binary system is shown in Figure 3.2(15).

According to Barraclough and Meyer(15) $CdCr_2Se_4$ forms by a peritectoid reaction where CdSe and Cr_2Se_3 solid phases react on cooling to form the spinel phase. It is unfortunate that the reaction is not a peritectic reaction since in this case there would exist a range of composition and $CdCr_2Se_4$ could be grown from the melt. Recently,

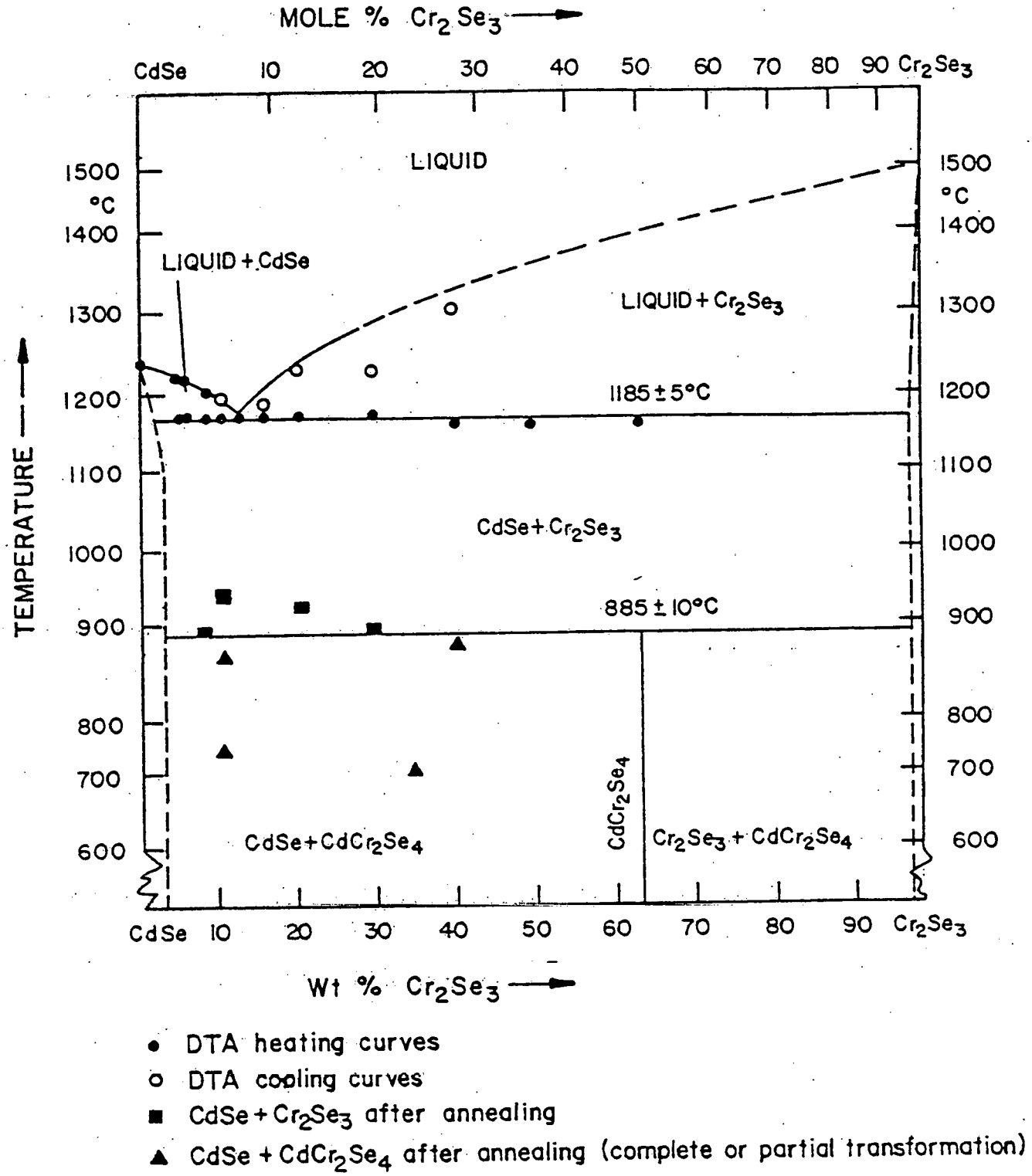

Figure 3.2. Equilibrium phase diagram of CdSe - Cr_2Se_3; (adopted from (15)).

TABLE 3.2. CRYSTALLOGRAPHIC AND ELECTRICAL PROPERTIES OF SINGLE CRYSTALS AND POLYCRYSTALLINE (HOT-PRESSED) $CdCr_2Se_4$

PROPERTY	SINGLE CRYSTALS	POLYCRYSTALLINE (HOT-PRESSED)
Lattice parameter Å	10.721 - 10.755 (75, 76, 94, 95)	10.737 (96)
Structure parameter u	0.390 (25)	
Density (gm/cm^3) calculated	5.681 - 5.739 (75, 88, 74, 95)	5.714 (96)
measured	5.55 (95)	5.693 (96)
Electrical resistivity (Ωcm) 297K	8×10^2	10^3 - 5×10^3 (96)
77K	10^4	10^6 - 10^7 (96)
Type of Electrical Conduction	n and p (94)	mixed n and p (2)

however, T. Kiyosawa and K. Masumoto(16) have found that $CdCr_2Se_4$ dissolves in a selenium melt and is in equilibrium with the selenium rich melt which has a CdSe content in excess of CdSe - Cr_2Se_3 at T ~ 900°C. The solubility, however, decreases rapidly as T decreases from 900° to 860°C. This, therefore, suggests that there is a possibility of obtaining single crystals of $CdCr_2Se_4$ as a primary solid from such a melt. This also suggests that single crystals by a liquid phase exitaxy (LPE) can be grown. Growth parameters, however, still remain to be determined.

The reaction mechanism of CdSe and Cr_2Se_3 at T < 885°C has not yet been investigated completely. However the reaction is thought to occur by a solid state reaction of the two phases by a diffusion of the cations across the phase boundary. Excess selenium, however, must always be present in order to prevent the eventual decomposition of the spinel phase eq. 3.1.

$$CdSe(s) + Cr_2Se_3(s) + xSe_2(g) \rightarrow CdCr_2Se_4(s) + xSe_2(g) \qquad 3.1$$

in the absence of selenium at T > 500°C in vacuum.

$$CdCr_2Se_4(s) \rightarrow Cd(g) + \tfrac{1}{2}Se_2(g) + Cr_2Se_3(s)$$

$$\rightarrow CdSe(s) + Cr_2Se_3(s) \qquad 3.2$$

where CdSe forms by the reaction of selenium and cadmium

gas at the cold end of the growth chamber.

A second method of growing fine powders is by the reaction of co-precipitated Cd and Cr hydroxides with excess selenium in a flowing hydrogen gas stream using an incremental temperature increase(17).

B. $(1-x)CdCr_2S_4$ x $CdCr_2Se_4$

$(1-x)CdCr_2S_4 \cdot x\ CdCr_2Se_4$(18) is a solid solution of $CdCr_2S_4$ and $CdCr_2Se_4$ with a lattice parameter that varies linearly with composition while the structure parameter u remains constant at 0.390 over the entire compositional range $0 \leq x \leq 1$. Table 3.3 presents a summary of the crystallographic and magnetic data. Single crystal growth of the quarternary compound has been achieved by flux growth from mixtures of the elements and binary compounds in 30%$CdCl_2$ at 800-850°C with 2°/hr. cooling rate(19).

3.1.2. Optical and Electrical Properties

In this section the optical and electrical properties of $CdCr_2Se_4$ are described. Also, compositional variations of the spinel structure are discussed in terms of the induced changes of the optical and electrical properties in order to tailor the desired optical and magneto-optical properties.

A. Intrinsic

At this point in time it is almost futile to discuss the intrinsic optical properties of $CdCr_2Se_4$ or $(1-x)CdCr_2S_4$ .x $CdCr_2Se_4$, since it has been impossible

TABLE 3.3. SUMMARY OF CRYSTALLOGRAPHIC AND MAGNETIC PROPERTIES OF $(1-x)CdCr_2S_4 \cdot x\ CdCr_2Se_4$ (Adopted from (18)).

Composition	Lattice Paramter, Å	u Parameter	Magnetic Moment (μ_B/molecule) at 4.2K	Curie Temperature, K
$CdCr_2S_4$	10.244	0.390	5.15	84.5
$CdCr_2S_3Se_1$	10.352	0.389	5.56	84.7
$CdCr_2Se_2$	10.479	0.389	5.76	93.1
$CdCr_2S_1Se_3$	10.610	0.390	5.73	110.0
$CdCr_2Se_4$	10.755	0.390	5.62	129.5

to grow intrinsic single crystals. To date, very little research has been carried out on the preparation of intrinsic single crystals and especially hot-pressed materials. Therefore, the study of intrinsic properties of all chromium chalcogenide spinels has been severely limited by the availability of pure large single crystals or hot-pressed materials.

Like all optical materials, the region of transparency is limited by electronic absorption at short wavelengths and infrared active phonons at long wavelengths (reststrahl and multiphonon absorption). In $CdCr_2Se_4$ the first absorption band occurs at ~1.3ev from the selenium valence band to the narrow d-conduction band derived from the Cr^{2+} levels (the host ions are in a Cr^{3+} state). This band has been found to red-shift upon cooling(20,21,22,23). The total decrease in the photon energy between the temperature at which the edge is at its highest energy and OK is about 0.2ev. The magnitude of the absorption in the red-shifting band varies quite strongly from one specimen to another. Photoconductivity is observed in the same band and it has been observed in p-type materials. Although there are publications in which photoconductivity in the same band is In^{3+} and Ga^{3+} doped $CdCr_2Se_4$, which are normally n-type, the red-shifting band is explained by a conduction d- band broadening and not a valence band

broadening in the ferromagnetic region. This also leads to a small increase in electron mobility, as observed in n-type $CdCr_2Se_4$, in the ferromagnetic region(25).

D.C. electrical resistivity measurements of single crystals and hot-pressed $CdCr_2Se_4$ show drastic differences depending upon whether the materials are "stoichiometric" or not. Selenium deficient single crystals are n-type and have been found to have an activation energy for electrical conduction of 0.23ev(26,27) between 300 K and 180 K with a resistivity maximum at ~150 K(28). "Stoichiometric" single crystals are p-type but have been found to have a monotonically increasing resistivity with a small variation of the resistivity near the Curie temperature. The change in resistivity near T_c for n-type $CdCr_2Se_4$ is attributed to a collective model where the conduction d-band broadens thus increasing the mobility and also reducing the donor ionization energy. In p-type $CdCr_2Se_4$ the small change in the resistivity behavior is attributed to a small exchange interaction between the valence band and the localized acceptor band.

At long wavelength the intrinsic transparent window is limited by transverse optical phonon absorption and multiphonon absorption. Transverse optical phonon or reststrahl absorption in materials with a spinel structure arise from the fundamental vibrations of BX_6 and AX_4 complexes with the BX_6 complex absorption occuring at shorter

wavelengths(29,30). Multiphonon absorption arise from the interaction of a photon with more than one phonon. Such higher order absorption bands arise from two possible mechanisms: (a) anharmonic coupling between phonons arising from third and higher order terms in the potential energy, and (b) second and higher order terms in the electric moment(31,32). In binary optical materials such as NaCl, KCl, CaF_2, ZnS, ZnSe, CdS etc. multiphonon absorption has been found to severely limit them at frequencies near 2 and 3 phonon absorption bands(33,34).

Two-phonon absorption has also been found to occur in ternary $CdCr_2S_4$ at $\lambda = 12.5\mu m$(35). This absorption band is thought to limit $CdCr_2S_4$ intrinsically at 10.6μm. $CdCr_2Se_4$ on the other hand has two-phonon absorption bands occuring at longer wavelengths starting at $2LO. = 585cm^{-1}$ (17.16μm) theoretical. This is in agreement with the structure seen in the single crystal spectra reported by Bongers and Zanmarchi(36) and A.G. Gurevich et alia(37), Figure 3.3. At shorter wavelength no structure is seen because of the still relatively high absorption coefficient. Table 3.4 lists the transverse and longitudinal optical phonon frequencies of $CdCr_2S_4$ and $CdCr_2Se_4$ where the values have been obtained from reflectivity measurements on hot-pressed samples(38).

Solid solutions of $(1-x)CdCr_2S_4 \cdot x\ CdCr_2Se_4$ are expected to give rise to optical phonon frequencies between those of the sulfide and those of the selenide.

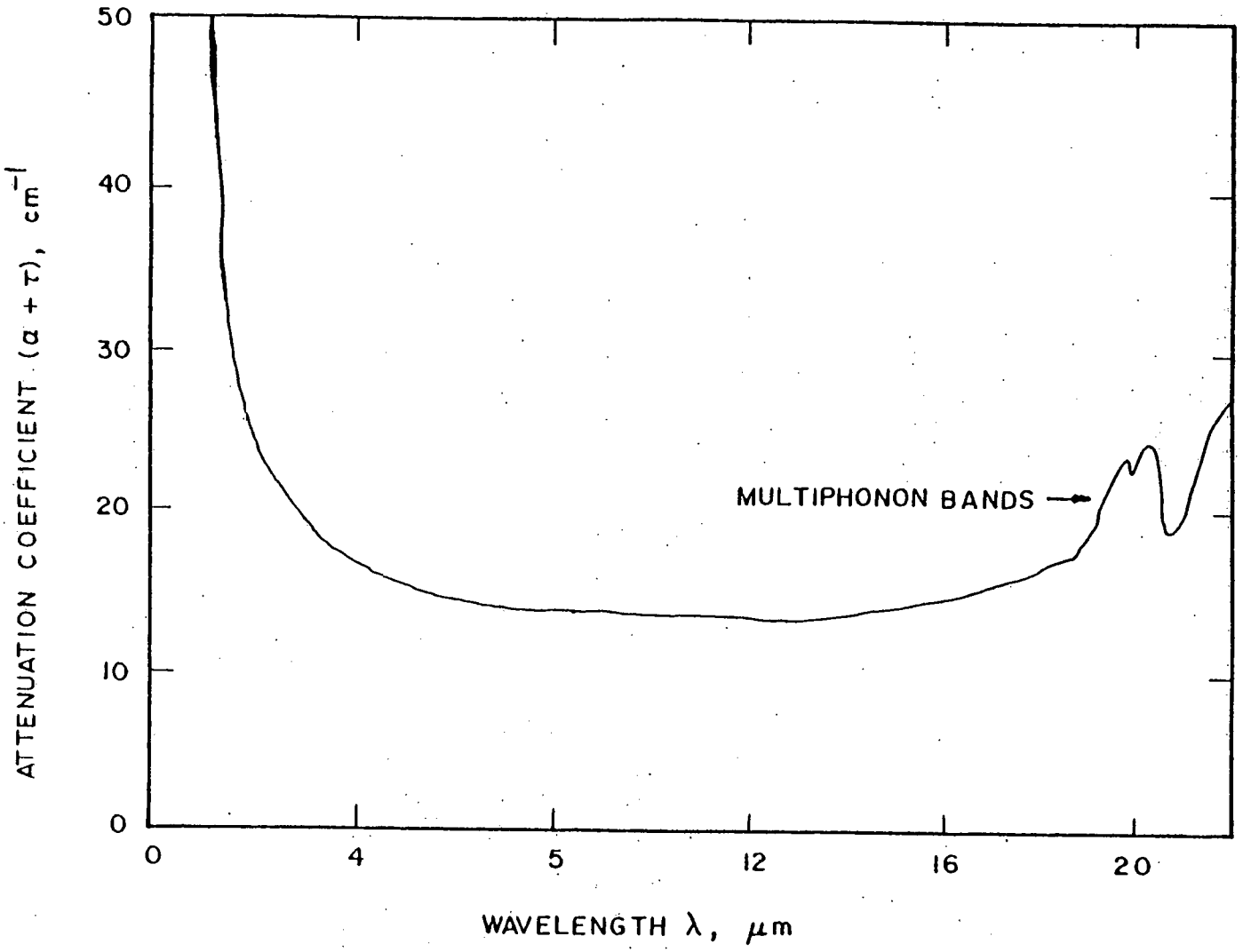

Figure 3.3. Absorption spectrum of $CdCr_2Se_4$ single crystal (adopted from (36).

TABLE 3.4. OPTICAL PHONON MODES OF $CdCr_2S_4$ and $CdCr_2Se_4$

MATERIAL	T.O. cm^{-1}	L.O. cm^{-1}
$CdCr_2S_4$	379.3 ± 0.3 (38)	392.5 ± 0.3 (38)
79K	326.6 ± 0.4	350.4 ± 0.4
300K	376.9 ± 0.2	389.9 ± 0.3
	321.6 ± 0.3 (38)	347.2 ± 0.3 (38)
	240, 235 (38, 30)	
	97, 95	
$CdCr_2Se_4$	291.6 ± 0.5	295.0 ± 0.5 (38)
79K	270.9 ± 0.3	286.2 ± 0.3
	189.0 (39)	
	78.7	
300K	288.1 ± 0.6	291.3 ± 0.4 (38)
	266.2 ± 0.2	281.3 ± 0.4
	188.0 (39, 30)	
	74.5, 74	

Therefore the major intrinsic sources of absorption away from the reststrahl and electronic absorption edge are multiphonon absorptions. These can be shifted and/or reduced by changing the sulfur and selenium concentration in the mixed system $(1-x)CdCr_2S_4 \cdot x\ CdCr_2Se_4$.

B. Extrinsic

Extrinsically, there can be many types of absorption and attenuating mechanisms. The attenuating mechanisms in hot-pressed materials can be divided into two types. The first is impurity absorption and the second is scattering.

1. Impurity Absorption

Impurity absorption can occur in several ways: (1) by doping $CdCr_2Se_4$ thus giving rise to donors or acceptors and/or free carrier absorption and (2) impurity reststrahl absorption.

Donor bands in $CdCr_2Se_4$ can be introduced by annealing in vacuum and thus introducing selenium and cadmium vacancies. Experiments show that selenium has a higher vapor pressure and a selenium deficient $CdCr_2Se_4$ is usually found to have an activation energy of 0.23ev . Donor bands can also be introduced by doping $CdCr_2Se_4$ with In^{3+} and Ga^{3+} at the tetrahedral sites. Absorption bands in In^{3+} and Ga^{3+} doped $CdCr_2Se_4$ have been observed at 0.57ev and 0.66ev respectively

both by electrical resistivity measurements and optical transmission measurements. In^{3+} doped selenium deficient hot-pressed $CdCr_2Se_4$ samples have shown activation energies of 0.23ev. Also, upon annealing in a selenium atmosphere in order to remove selenium vacancies responsible for the 0.23ev band, an activation energy of 0.57ev resulted from the In^{3+} (26).

P-type conduction has been observed in Ag^+ doped $CdCr_2Se_4$, but, no absorption bands were observed in the infrared(40). Excess selenium in hot-pressed $CdCr_2Se_4$ is also believed to cause p-type conduction and free-carrier absorption in the infrared. This is accomplished by an excess of shallow holes due to excess selenium at grain boundaries. Classically free-carrier absorption can be described by(41):

$$\alpha = \frac{e^3\lambda^2}{4\pi^2 c^3 \varepsilon_o n}\left[\frac{N}{\mu_n m_n^{*2}} + \frac{P}{\mu_p m_p^{*2}}\right] \qquad 3.2$$

where N is the free electron concentration in $\#/cm^3$, μ is the mobility, m_n^* & m_p^* are the effective electron and hole mass, μ_n and μ_p are the electron and hole mobilities, c is the velocity of light, ε_o is the permittivity of free space and n is the index of refraction. This type of absorption has been found in materials with shallow donors or acceptors such as Ge(42) where the λ^2 dependence is usually obeyed. In this description scattering is not taken into consideration.

Phonons in binary second phases such as CdSe, Cr_2Se_3, CdO, Cr_2O_3 strongly couple to electromagnetic radiation and if the optical phonon frequencies fall into the intrinsically transparent region of $CdCr_2Se_4$ absorption bands can be observed with an intensity proportional to second phase concentrations. Therefore, care must be taken in reducing second phase concentration, especially oxides.

2. Scattering

Scattering is thought to be the major attenuation mechanism in hot-pressed and/or sintered materials. Possible transmission losses by scattering can occur through pores, second phases, grain boundaries and surfaces(43,44). The transmission depends on the index of refraction difference between the materials and the scattering center, the size and the density of the scatters. Usually a size distribution exists and therefore the transmission is very sensitive to the type of distribution(45). Because of the fabrication process of $CdCr_2Se_4$ and $(1-x)CdCr_2S_4 \cdot x\ CdCr_2Se_4$, knowledge about the physical properties of the scatterers is very important.

In some hot-pressed materials because of the large size of second phase or pores Mie scattering must be used to interpret the transmission data. J.G.J. Peelen et alia(43) used Mie scattering to determine the influence of pores on the transmission of hot-pressed and sintered

alumina. They found that a lognormal distribution of pore sizes was necessary to fit the transmission data. For this research because of the more difficult problems such as decomposition and free-carrier absorption no effort was made to investigate scattering processes.

3.1.3. Magnetic Properties

The magnetic properties of $CdCr_2Se_4$ have been studied extensively in the past fifteen years. The reason being that $CdCr_2Se_4$ is very close to being an ideal Heisenberg ferromagnet and it is therefore an ideal system to test the theories of critical phenomena of magnetic materials(46). Ferromagnetism in spinels occurs in the absence of high conductivity. The type of exchange interactions between the magnetic ions occurs by a superexchange interaction via the oxygen or chalcogenide anions.

In $CdCr_2Se_4$ the distance between Cr^{3+} cations is 3.84Å. This separation between the Cr^{3+} is too large for direct overlap of the Cr^{3+} orbitals(47). Exchange interactions therefore take place via the selenium anions. Magnetic measurements and neutron diffraction also show that there is a simple alignment of all the magnetic moments in $CdCr_2Se_4$. The ferromagnetic behavior in chromium chalcogenide spinels can be accounted for on the basis of a Heisenberg spin

Hamiltonian of the form(48,49)

$$H = -2J \sum_{ij} S_i \cdot S_j - 2K \sum_{ik} S_i \cdot S_k - g\mu H_z \cdot \sum_i S_{iz}$$

The sum over ij includes all nearest-neighbor pair interactions (Cr_i - Se - Cr_j). J represents the strength of the nearest-neighbor interactions and it is assumed to be positive; the number of nearest neighbors z is 6, S_i and S_j are the total spin-magnetic moments of the Cr^{3+} ions, S = 3/2 according to Hund's rules. The sum over ik includes all pair interactions of the type Cr_j - Se - Cd - Se - Cr_k. The number of next-neighbor included in this interaction is 30 and they are assumed to have an identical strength K. The sign of K may be either positive or negative. The final term in the spin Hamiltonian is the usual Zeeman energy in an external field H_z.

Baltzer et al.(48) have found that for $CdCr_2Se_4$ $J = 1.93 \times 10^{-15}$ ergs and $K = -1.37 \times 10^{-17}$. Thus showing that $J > 0$ is associated with ferromagnetic ordering of the Cr^{3+} spin magnetic moments and $K < 0$ indicates antiferromagnetic ordering of the next-nearest neighbors.

Magnetic moments of $CdCr_2Se_4$ as well as $CdCr_2S_4$ have been found to be highly dependent on stoichiometry(50). Anionic deficiencies for example have been found to decrease

the net magnetic moments per unit cell. The decrease in magnetic moment was found to be due to the presence of divalent chromium cations to charge compensate for anionic deficiencies. Cr^{2+} decreases the net ferromagnetic interactions because of a lower magnetic moment per unit cell ($4\mu_B$ vs $6\mu_B$ for Cr^{3+}) and because Cr^{2+} couple antiferromagnetically to the nearest Cr^{3+} neighbors. Magnetic properties of $CdCr_2Se_4$ single crystals are given in Table 3.3.

In $(1-x)CdCr_2S_4 \cdot x\ CdCr_2Se_4$, the ferromagnetic behavior is also explained by a superexchange interaction mechanism where the Cr^{3+} ions align in neutral directions(18). The Heisenberg spin Hamiltonian can be used to explain the ferromagnetic behavior as in the case of the individual phases $CdCr_2S_4$ and $CdCr_2Se_4$. In the solid solution however, the superexchange interactions occur via both the sulfur and selenium anions. The Curie temperature does not vary linearly with temperature as shown in Figure 3.2a. This is due to the non-monotonic dependence of the nearest neighbor interaction, $\tilde{J}$, and next-nearest neighbor interaction $\tilde{K}$ on the compositional parameter x. $\tilde{J}$ and $\tilde{K}$ can be expressed in terms of the compositional parameter x and on the different neighbor interactions depending on whether sulfur or selenium ions are involved in the interaction(18, 51, 52), Figure 3.4b.

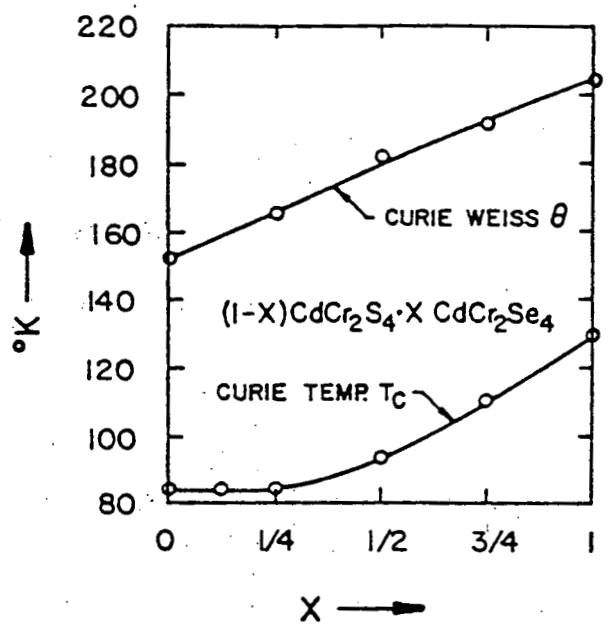

(a)

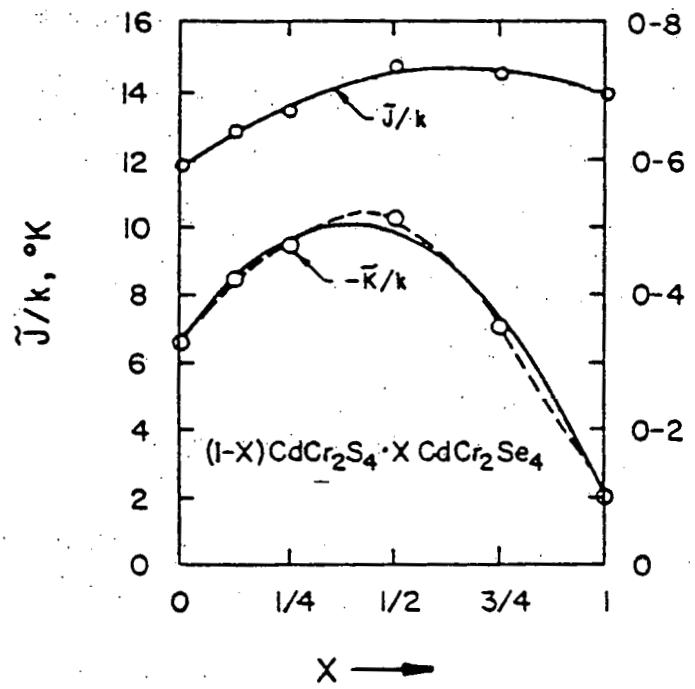

(b)

Figure 3.4. (a) Curie temperature and Curie-Weiss parameters as a function of composition within the system (1-x) $CdCr_2S_4 \cdot x\ CdCr_2Se_4$, and,
(b) the composition dependent effective exchange parameters, $\tilde{J}$ and $\tilde{K}$ as functions of composition within the system (1-x) $CdCr_2S_4 \cdot xCdCr_2Se_4$.

The experimental value of μ as measured by P.J. Woetowicz et alia(18) varies with composition as shown in Table 3.3. The deviation from theoretical value of $6\mu_B$ is most probably due to a selenium and/or sulfur deficiency as in the case of the constituents $CdCr_2Se_4$ and $CdCr_2S_4$. That is, anionic deficiencies would be charged compensated by the formation of Cr^{2+} thus lowering the net magnetic moment.

3.1.4. Magneto-Optical Properties

The Faraday effect is the rotation of the plane of polarization of a light beam as it is transmitted through a magnitized dielectric. At normal incidence a linearly polarized beam may be resolved into left hand circularly polarized and a right hand circularly polarized components. The induced birefringence causes these components to see different indices of refraction(53,54), resulting in a phase shift between the two components and thus a rotation of the plane of polarization of the radiation upon transmission. Phenomenologically the Faraday rotation can be expressed as:

$$\theta_F = VB\ell\cos\phi \qquad 3.3$$

where V is the Verdet constant, B is the applied

magnetic field, ℓ is the thickness of the sample, and ϕ is the angle that the light beam makes with the direction of the applied magnetic field.

In non-magnetic semiconductors the origin of the Faraday rotation is due to the interaction of non-magnetic electrons with the magnetic field. In magnetic semiconductors such as $CdCr_2Se_4$ this effect does not contribute measurably to the Faraday rotation. In chromium chalcogenide spinels the Faraday rotation has two origins. The first arises from the high energy crystal field transition and/or charge-transfer transition which are electric dipole transitions. These occur in the visible and near infrared part of the spectrum. The second arises from magnetic dipole transition having resonance frequencies in the far infrared or microwave frequencies. The latter contribution in the wavelength region of interest (1-18μm) is independent of wavelength(36,19).

In $CdCr_2Se_4$ the Faraday rotation due to the electric dipole transitions is determined by the spin-orbit splitting of the excited state. The large negative rotation observed due to electric dipole transitions has been attributed to a $Se \rightarrow Cr$ charge transfer band at 0.481μm having the form(36).

$$\Theta'_F = K' \frac{M}{M_s} \ell \frac{\lambda^2}{(\lambda^2 - \lambda_o^2)^2} \qquad 3.4$$

to Equation 3.4 the magnetic dipole transition terms must be added. This second term depends only on the magnetization M and gyromagnetic ratio γ eq. 3.5.

$$\theta'_F = \frac{2\pi\ell}{c}\sqrt{\varepsilon_o}\ \gamma\ M \qquad 3.5$$

Adding Eq. 3.4 to Eq. 3.5 we get:

$$\theta_F = \theta'_F + \theta'_F = k\frac{M}{M_s}\ell\frac{\lambda^2}{(\lambda^2-\lambda_o^2)^2} + \frac{2\pi\ell}{c}\sqrt{\varepsilon_o}\ \gamma\ M \qquad 3.6$$

The deviation of Eq. 3.6 has been reviewed by S. Jacobs(1) and therefore it will not be reproduced here.

Bongers and Zanmarchi(36) have determined the Faraday rotation of $CdCr_2Se_4$ from 1 to 18μm and have also fitted Eq. 3.6 to their data with the magnetic dipole term equal to =193 degrees/cm (measured), M = 286 G, and $(K\frac{M}{M_s}) = 1.11 \times 10^{-4}$ degrees cm. The Faraday rotation calculated from Eq. 3.6 is given in Figure 3.5. At short wavelengths the largest Faraday rotation of-9200 deg/cm was measured at 1.17μm indicating that for an optical isolator at this wavelength an element thickness of only 49μm is needed. At 5μm, θ_F = -263 deg/cm and an element thickness of 0.171cm is needed.

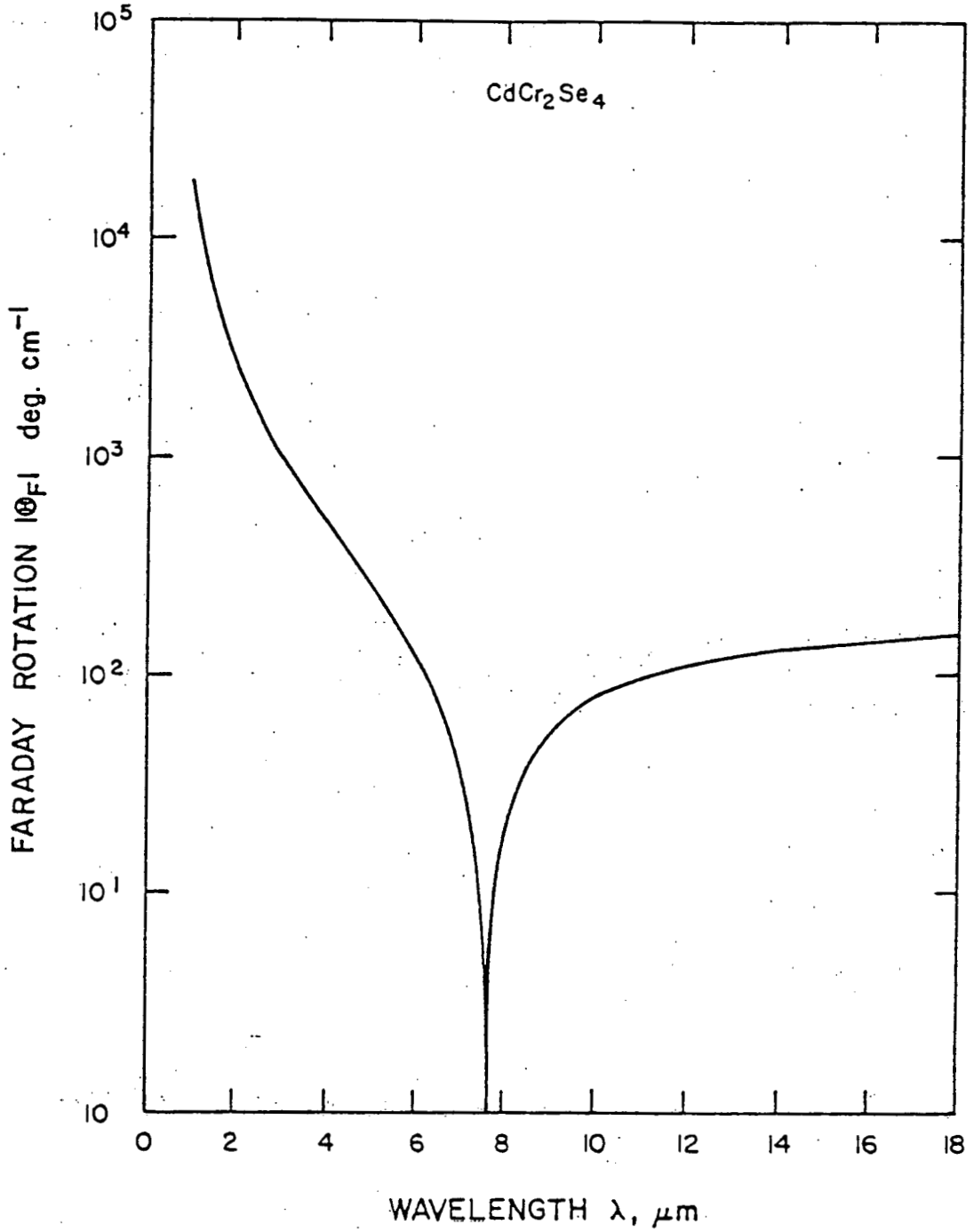

Figure 3.5. Saturated Faraday motion vs wavelength of $CdCr_2Se_4$.

The Faraday rotation in chromium chalcogenide spinels at 10.6μm, for example, can be varied from a minimum of ~94 degrees/cm at $M = M_s$ to ~1000 degrees/cm for $HgCr_2Se_4$(55). However, because intrinsic electronic absorption in $HgCr_2Se_4$ occur at much longer wavelength and because of the apparent technological problems, as will be described in Chapter 3.2, $HgCr_2Se_4$ is not investigated. However, solid solutions of $HgCr_2Se_4$ and $CdCr_2Se_4$ may be a viable system. Figure 3.6 shows a schematic of a Faraday isolator in a laser system.

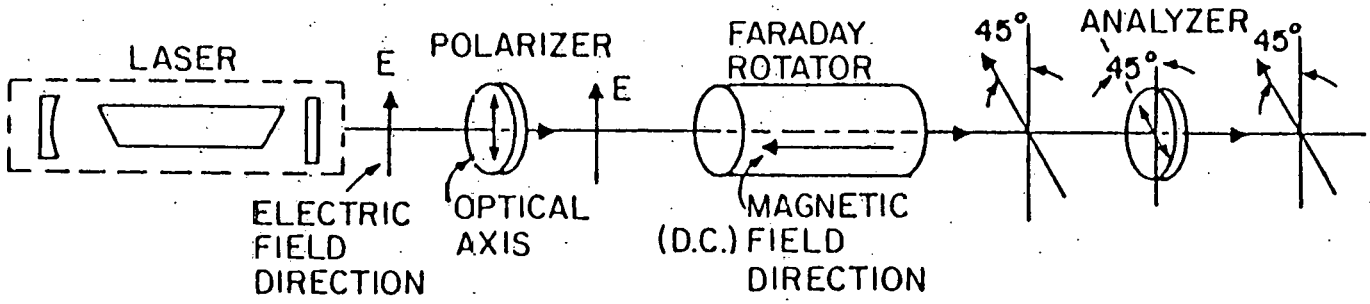

(a) FORWARD DIRECTION

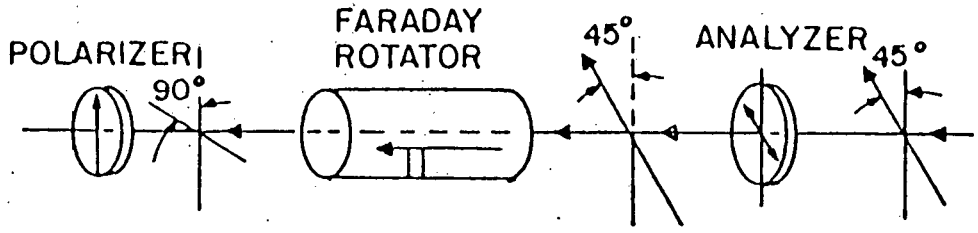

(b) REVERSE DIRECTION

Figure 3.6. Schematic of a Faraday isolator.

3.2. Consolidation of Ceramic Powders by Hot-Pressing.

3.2.1. Introduction

Hot-pressing is a fabrication process whereby a ceramic or metal powder is subjected to a high pressure and temperature for a time t in order to densify the powder to near theoretical densities. Hot-pressing as a fabrication process has been finding increasing utility in the ceramic industry in the past years with particular emphasis on the preparation of materials with improved properties through composition, microstructure and density control.

Many researchers have devoted much of their time to the understanding of densification mechanisms of powders during various stages of densification. However, there is still no complete theory that can describe the densification processes during the various stages of densification. The major difficulty being that densification occurs by many concurrent and sequential processes(56).

During the past 20 years or so a lot of research has been done on optimizing and understanding the densification of oxides, borides, nitrides and alkali halides. However, very little work has been done on the chalcogenides with the exception of the work of Ed Carnall (57) at Kodak Research Laboratories. The reason for the scarsity of data has been due to a limited demand for ternary chalcogenide optical elements. But, this is slowly increasing as infrared and millimeter wave technology is being developed. A second reason for the lack of data is that chalcogenides, and especially chalcogenide spinels,

tend to be non-stoichiometric and therefore it is difficult to test densification theories.

However, because of a recent interest in infrared active optical elements, more effort should be devoted to the understanding of densification mechanisms and defect structure of these materials. This section is devoted mainly to the description of various mechanisms that can occur in chalcogenide spinels.

3.2.2.. Driving Force During Consolidation and Stages of Densification

The driving force (D.F.) during hot-pressing is expressed as the sum of three terms:

$$D.F. = g\sigma_a + C\gamma - p$$

where g is a stress correction factor which depends on the porosity Figure 3.7 (58), σ_a is the applied pressure, C is a pore structure sensitive parameter. (During hot-pressing the shape of the pores changes; while during the initial stages the shape may be approximated by a cylinder and $C = \frac{1}{r}$ where r is the radius of the cylinder, during the final stages the pores can be approximated by a sphere and $C = \frac{2}{r}$ where r is the radius of the sphere), γ is the surface free energy and p is the internal gas pressure which exerts a negative pressure on the plunger.

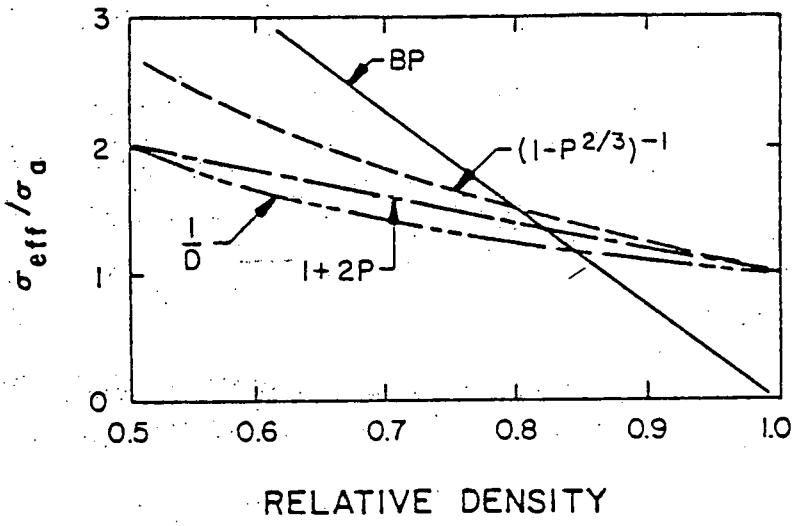

Figure 3.7. Stress correction factor g as a function of relative density (adopted from (58)).

The stress correction factor g is a very important parameter at low relative densities. At high relative densities the effective applied pressure is very close to the applied pressure and therefore no correction is needed. In reality a correction should be made but the scatter in most experimental data makes it difficult to test the functional relation of g shown in Figure 3.4.

The densification process can be divided in three stages: (1) initial, (2) intermediate, (3) final. During the initial stage, densification can occur by a combination of particle size rearrangement by sliding at the grain boundaries(59), by particle fracture, by grain shape changes by plastic deformation and by diffusion. Rearrangement occurs by sliding of the grains over each other along their surfaces to accommodate the applied stress. Rearrangement can also be aided by the presence of a liquid phase with a $T_{b.p.}$ lower than the hot-pressing temperature. Particle fracture usually occurs in brittle materials and in large crystals below the brittle to ductile transition temperature. Rearrangment by grain boundary shape changes by plastic flow is especially important in compacts of large non-uniform particle size. In stoichiometric crystalline materials with a low brittle to ductile transition temperature, e.g. alkali halides, large particles can be densified to near-theoretical densities >99.9%. However in materials with a high brittle to ductile transition temperature, submicron

particles are desirable.

Densification during the intermediate and final stages is dominated by diffusional creep mechanism as described by Coble(60, 61) and power-law creep(62).

3.2.3. Rate Equations

There are several mechanisms that have been invoked to descirbe densification during hot-pressing. The driving force as already mentioned, can cause rearrangement of the particles(59), it may induce plasticity and/or fracture; and it may increase the effects of surface tension as a driving force for diffusion. But, no single mechanism in any material is responsible for complete densification. The dominant mechanisms depend on the internal parameters such as neck size, gas pressure in the pores, and compact density. Therefore the relative contribution of each mechanism changes as densification proceeds.

The densification rate, $\dot{\rho}$, can be expressed in terms of the pressing parameters, internal parameters and physical constants.

$$\dot{\rho} = \dot{\rho}(\rho, T, \sigma_a, r, d, \text{physical constants})$$

where

ρ = relative density of the compact

T = absolute temperature

σ_a = applied pressure

r = pore radius

d = average particle size

The rate equation does not include the initial stage of densification because there are too many mechanisms taking place to determine the kinetics(63). D.L. Johnson et al.(64) have proposed mechanisms of initial stage of sintering for non-isothermal densification but it only takes into account grain boundary diffusion and lattice diffusion. More work is warranted in determining the mechanisms and formulation of models of the initial stages of hot-pressing.

During the intermediate and final stages of hot-pressing seven mechanisms can contribute to the densification: (1) lattice diffusion from the boundary, (2) grain boundary diffusion from the boundary, (3) power-law creep, (4) plasticity, (5) lattice diffusion from the surface, (6) surface diffusion and (7) vapor transport. Of these only (1-4) lead to neck-growth and thus influence the rate of densification(75).

A. Diffusional creep.

When a stress is applied to a polycrystalline material at elevated temperatures, movement of vacancies can occur from the regions in compression to those in tension. This process can occur through the lattice in which case it is a lattice diffusion mechanism usually referred to as Nabarro-Herring diffusional creep(65,66) or through the grain boundaries in which case it is called

Coble diffusional creep(60).

The creep rate or in our case the densification rate through the lattice has been calculated originally by Nabarro(65) and Herring(66) independently. The strain rate is given by:

$$\dot{\varepsilon}_{NH} = \frac{B\Omega\,\sigma D_\ell}{kTd^2} \qquad 3.7$$

where B is a constant which depends on the grain shape(67,68) (for a sphere in tensile stress $B = 13.3$, in shear stress $B = 40$), D_ℓ is the lattice diffusion coefficient, σ is the applied uniaxial stress, d is the grain size, k is the Boltzmann constant, T is the absolute temperature and Ω is the vacancy volume or the volume of the diffusing atoms. The temperature dependences for lattice diffusion can be expressed as:

$$D_\ell = D_\ell^{\,o}\, e^{-Q_\ell/kT} \qquad 3.8$$

where $D_\ell^{\,o}$ and Q_ℓ are the pre-experimental and activation energy for the lattice diffusion process, respectively.

Grain boundary diffusional creep or densification has been calculated by Coble(61). The strain rate is expressed by

$$\dot{\varepsilon}_C = \frac{47.5W\Omega\,\sigma D_b}{kTd^3} \qquad 3.9$$

W is grain boundary, D_b is the boundary diffusion coefficient. The temperature dependence for boundary diffusion can be expressed as:

$$D_b = D_b^{\circ} e^{-Q_B/kT} \qquad 3.10$$

where D_b° and Q_B are the pre-exponential and the activation energy for boundary diffusion respectively.

Since grain boundary diffusion and lattice diffusion are independent they can occur concurrently during densification. In concurrent processes the densification or strain rate can be expressed as a sum

$$\dot{\varepsilon} = \dot{\varepsilon}_{N-H} + \dot{\varepsilon}_C \qquad 3.11$$

substituting for $\dot{\varepsilon}_{N-H}$ and $\dot{\varepsilon}_C$ we get:

$$\dot{\varepsilon} = \frac{\Omega\sigma}{kTd^2} \left[D_\ell \, 13.3 + \frac{47.5 D_b W}{d}\right] \qquad 3.12$$

Equation 3.12 has important consequences.

The activation energy of grain boundary diffusion has a lower activation energy and thus it will dominate at low temperatures. Also, the transition temperature from grain boundary diffusion to lattice diffusion is a function of particle size(65).

B. Power-Law Creep

In materials where creep or densification during the

final stage is controlled by dislocations, the steady state creep rate is proportional to the stress to the power of n, Eq. 3.13, as observed in alkali nalides and as LiF, NaCl, and NaBr(69,70).

$$\dot{\varepsilon} = A\sigma^n \qquad 3.13$$

where A is a constant which depends on the diffusion for dislocation creep, temperature, shear modulus and Burgers vector. The grain size has little influence on the rate of this mechanism which will continue to operate even after abnormal grain growth has occured.

As pointed out by Wilshire(68), n is highly dependent on stoichiometry and it is only valid for a particular temperature range; n can vary from ~3 for dislocation glide/climb controlled by climb to ~5 for pipe diffusion occuring along dislocations cores(71). In determining n from experimental data a sufficiently wide temperature range must be used to avoid ambiguity of n due to a mechanism transition, that is, regions where parallel or concurrent process take place(56).

C. Plasticity

Plasticity has been observed to occur in many materials during hot-pressing. Such materials are InSb(72), GaAs(73) and alkali halides, to name a few. Phenomenologically Murray et al.(74) calculated the densification rate by substituting the applied pressure for surface force

energy as the driving force and with appropriate simplification for the rate of densification

$$\frac{dD}{dt} = \frac{3}{4}\frac{\sigma_a}{\eta}(1-D)$$

$$\frac{dD}{(1-D)} = \frac{3}{4}\frac{\sigma_a}{\eta}dt$$

$$\ell n(1-D) = -\frac{3}{4}\frac{\sigma_a}{\eta}t + c \qquad 3.14$$

where η is the viscosity and D is the relative density. Plasticity can be easily observed by the presence of texture by x-ray analysis, and by alignment of the grains along the tensile direction microstructurally.

Densification by plastic flow occurs instantaneously if the flow strength σ_y is high enough:

$$\dot{\varepsilon} = \begin{cases} 0 & \sigma_y > \sigma_a \\ \infty & \sigma_y < \sigma_a \end{cases} \qquad 3.15$$

also if a critical density D_c is reached plastic deformation does not take place even if $\sigma_a > \sigma_y$.

IV. EXPERIMENTAL TECHNIQUES

4.1. Materials Preparation

Materials preparation is of utmost importance in the fabrication of optical elements by hot-pressing. In this section the procedures for powder preparation and sample fabrication by hot-pressing are described. In order to optimize the optical properties of $CdCr_2Se_4$ and investigate the densification mechanisms, powders with varying particle sizes were formed. Materials preparation is presented in two parts; the first describes the powder preparation and the second the sample fabrication by hot-pressing.

4.1.1. Powder Preparation

There are several ways of preparing $CdCr_2Se_4$ each giving different crystal sizes. Single crystals with sizes 0.1 to several millimeters on the side can be grown by liquid-vapor transport(11), liquid transport (8, 9, 10), flux growth(13) and vapor transport(12). Powders with a particle size less than 0.1mm can be grown by the direct reaction of the binary selenides in a selenium atmosphere and by the reaction of the elements(15). Submicron powders can be grown by the reaction of metal chlorides or co-precipitated metal hydroxides with excess selenium in a hydrogen gas stream(17). In our investigation the following methods were used to grow $CdCr_2Se_4$ with varying particle sizes:

(1) Liquid - transport of CdSe and $CrCl_3$

(2) Direct reaction of CdSe and Cr_2Se_3

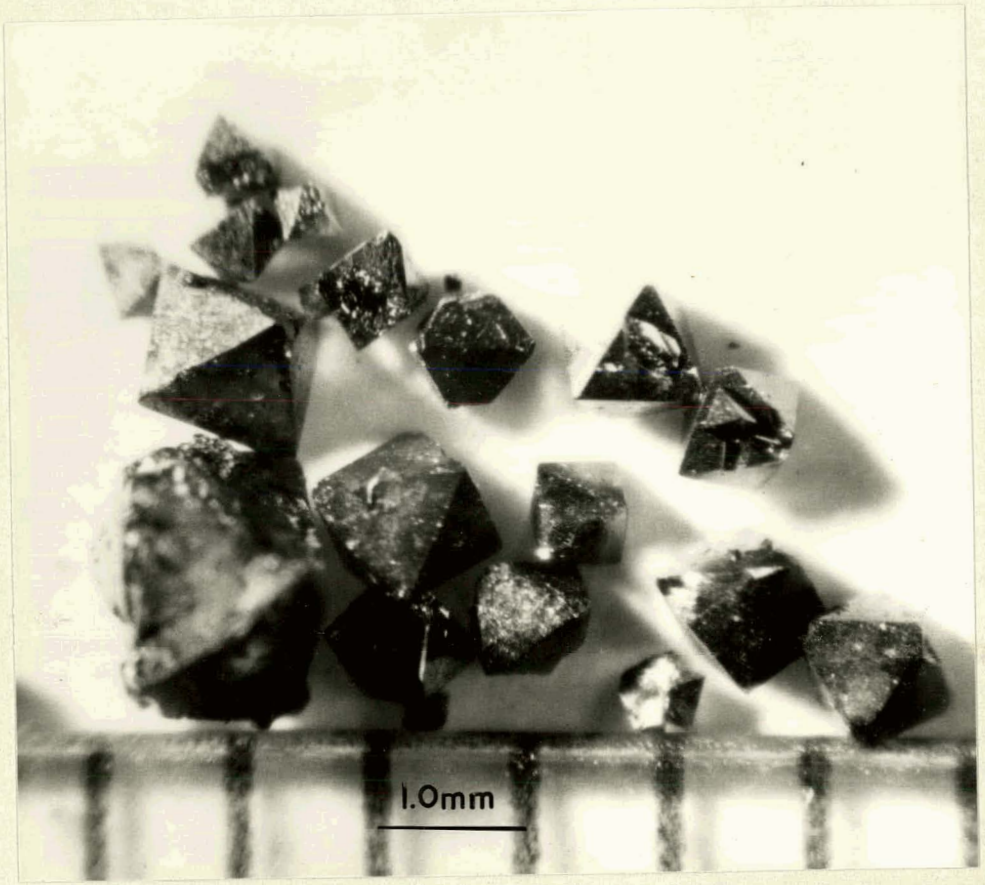

Figure 4.1. Optical micrograph of $CdCr_2Se_4$ single crystals grown by the liquid transport method.

(3) Reaction of co-precipitated chromium and cadmium hydroxides in H_2 + x Se.

A. Single crystals

Single crystals with a particle size 0.1-2.0mm were grown by the liquid-transport method developed by H. von Philipsborn(8, 9, 10) and Tung Cheng(75). In this method CdSe (99.999%, -325mesh), and $CrCl_3$ (99.8%, -80mesh) in a 2:1 ratio by weight are individually cold pressed into pellets approximately 13mm in diameter and 14mm in length at 20MPa. The pellets are placed in a platinum or cadmium boat next to each other in the order $CrCl_3$-CdSe-CdSe-C_2Cl_3. The symmetric arrangements of the four pellets doubles the interface which is of importance. Platinum or cadmium are used to prevent Cr_2Se_3 formation. Initially platinum was used, however cadmium was later used as suggested by von Philipsborn and by T. Cheng. Cadmium is used over platinum because of its economic advantage. The pellets in the platinum or cadmium boat are then placed in a quartz tube evacuated to 10^{-6}torr, sealed off and put in a horizontal tube furnace. The furnace is then heated to 695-705°C in 4 hours and kept at this temperature for 3-5 days. The furnace is then cooled to room temperature and the quartz tube withdrawn. Upon breaking the quartz ampule and analysis of the pellets, $CdCr_2Se_4$ octahedra Figure 4.1., were observed in the CdSe pellets but not in the $CrCl_3$ pellets. The crystal growth is thought

to occur by liquid-transport, but the exact kinetics are still not understood.

B. Powders with a Particle Size <100μm

CdSe (99.999%, -325mesh) and Cr_2Se_3 (99.99% -325mesh) powders were used as the starting materials. CdSe was commercial high purity from Cerac Inc. Cr_2Se_3 on the other hand was freshly synthesized in our laboratory from the elements according to Equation 4.1.

$$2Cr(s) + \frac{3}{2}Se_2(g) \xrightarrow[5\text{-days}]{600°C} Cr_2Se_3(s) \qquad 4.1$$

The reaction of the powders was carried in quartz ampules (15mm I.D., 17mm O.D., 200mm long). The ampules were sealed off at one end using an oxygen torch and necked as shown in Figure 4.2b to facilitate sealing under vacuum. The ampules were cleaned in a 40%HF solution followed by a 70%HNO_3 and ethyl alcohol wash. The ampules (Figure 4.2a) were subsequently outgassed in vacuum with the aid of an oxygen flame. The vacuum system is shown in Figure 4.2b.

The binary powders are mixed in an automatic mortar for one hour. They are then placed in a freshly cleaned ampule and evacuated to $\lesssim 10^{-6}$torr in 5 to 6 hours. The ampule is then sealed with an oxygen torch, placed in a horizontal furnace and heated to 650°C to react for 5 days, according to Equation 4.2.

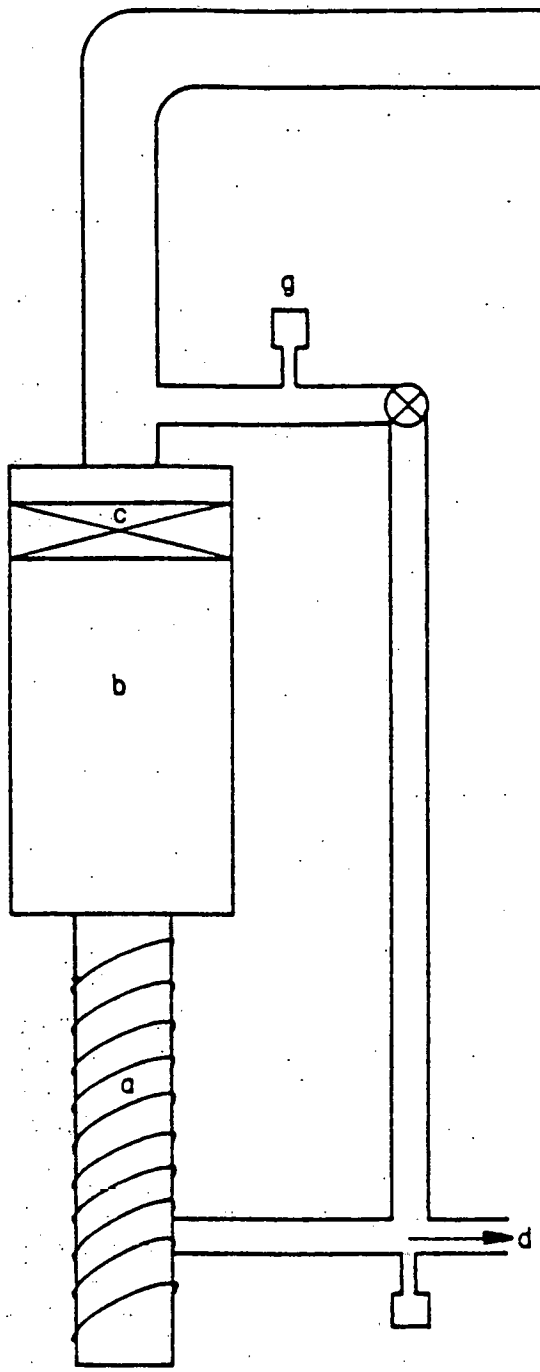

a Diffusion pump
b Liquid nitrogen cold trap
c Butterfly valve
d Mechanical vacuum pump
e Ampule
f Powder
g Thermocouple gauge

(a)

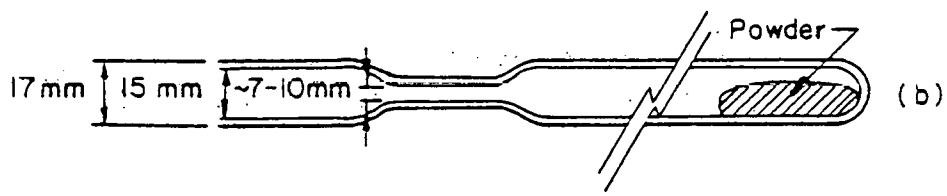

Figure 4.2. (a) Schematic of the vacuum system used to evaluate ampules shown in (b).

$$CdSe(s) + Cr_2Se_3(s) + 0.002gm/cm^3 Se_2(g) \xrightarrow{650°C} CdCr_2Se_4(s) + xSe_2(g) \qquad 4.2$$

(Excess selenium was found to be necessary to achieve 100% reaction).

The reacted powders were then taken out of the ampule, a sample was taken out for analysis, the rest was reground, put in a freshly cleaned ampule, evacuated, sealed and reacted at 650°C for an additional week. This procedure was repeated until x-ray diffraction showed a single phase. Usually three reaction periods were necessary to obtain a single phase material according to x-ray diffraction.

The fully reacted powders were ground and sieved through a 625mesh sieve ($\leq$20μm) and placed in a dessicator ready for hot-pressing.

C. Reaction of Co-precipitated hydroxides.

Don Pearlman and Ed Carnall(36) used a dilute solution of hydrazine (N_2H_4) to co-precipitate a finely divided mixture of cadmium and chromium hydroxides uncontaminated by salts from a solution of CrO_3 and CdO in a molar ratio of 2:1, Equation 4.3.

$$CdO + 2CrO_3 \cdot x\,H_2O + (NH_2)_2 \cdot xH_2O \rightarrow 2Cr(OH)_3 + Cd(OH)_2 + H_2O \qquad 4.3$$

The co-precipitated hydroxides are subsequently dried at

105-110°C in air overnight. The seleno spinel are then formed by reacting the co-precipitated hydroxides with excess selenium in a quartz firing tube as shown in Figure 4.3 under a hydrogen gas stream using an incremental temperature increase. The quartz firing tube was arranged for cooling the powder rapidly in the firing atmosphere. For conversion to $CdCr_2Se_4$ the powders were treated for one hour at 200°C, 2 hours at 400°C, 3 hours at 600°C and 3 hours at 700°C. At the end of each period the product is cooled to room temperature, sampled for analyses and the remainder processed further according to the program. The resulting powders had submicron particle sizes.

The corresponding sulfide powders, $CdCr_2S_4$, were also made using the same method except that the maximum temperature used was ~925°C and H_2S gas was used instead of H_2 and sulfur.

The solid solutions of $(1-x)CdCr_2S_4 \cdot x\ CdCr_2Se_4$ were formed by reacting $CdCr_2S_4$ and $CdCr_2Se_4$ powders in an evacuated quartz ampule at 670°C for 3 days. The resulting material had a particle size $\leq 1\mu m$.

4.1.2. Sample Fabrication by Hot-Pressing

A. Apparatus

Vacuum hot-pressing of $CdCr_2Se_4$ and $(1-x)CdCr_2S_4 \cdot x\ CdCr_2Se_4$ was carried out in the apparatus shown in Figure 4.4. The vacuum hot-pressing apparatus consists basically of a mechanical pump, a two inch diffusion pump, a chamber

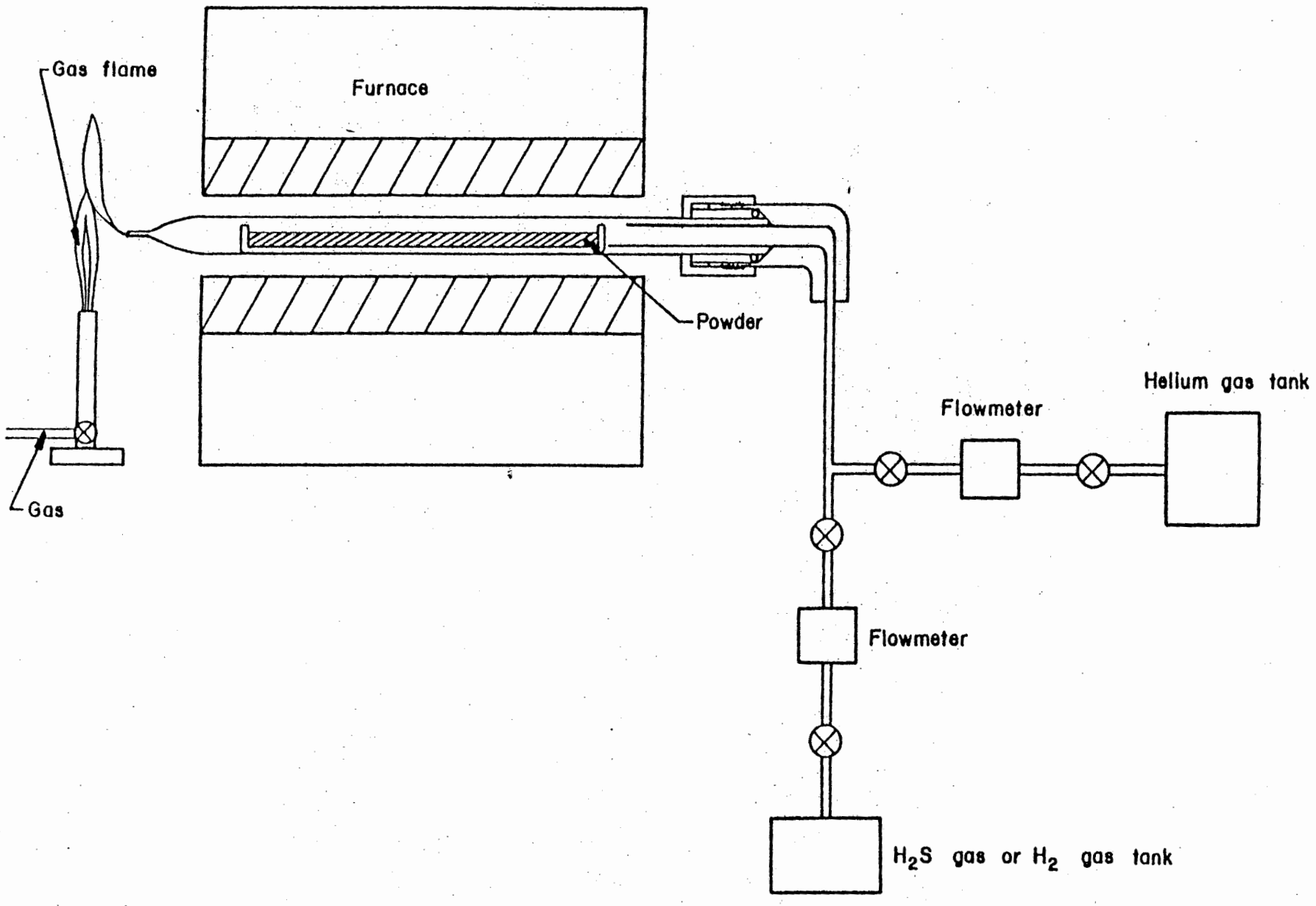

Figure 4.3. Apparatus used to grow submicron chromium chalcogenide spinel powders and powder treatment after growth in a helium gas atmosphere.

with the hot-pressing die, a radio frequency coil to heat the die by induction and a press capable of applying 120,000kg on a six inch diameter ram. The pressure can be applied uniaxially through two vertical rams; the upper ram being fixed and the lower is connected to a hydraulic acuator. The die was heated by means of a 7.5Kw 200-480KH_z Lepel radio-frequency generator and the temperature was controlled manually to ±3°C. The vacuum during hot-pressing was maintained at ~5 x 10^{-5}torr. The hot-pressing die is made of a Molybdenum titanium zirconium* alloy which allowed a pressure of 380MPa at $T \leq 900°C$. The die was coated with aquadag prior to all runs to allow easy removal of the hot-pressed material. Also, two pyrolithic graphite discs were placed below and above the powder to maintain a uniform temperature within the powder and allow easy removal of the hot-pressed material. The displacement of the powder during the hot-pressing was monitored by a dial gauge that could be read to ±2.5μm.

B. Hot-Pressing

The powder is placed in the hot-pressing die shown in Figure 4.5 between the two pyrolithic graphite discs and put in the hot-pressing chamber to evacuate for 2-3 hours. The die was then heated to 350°C-450°C at a heating rate of 30-35 deg/min. and outgassed for 15-60 minutes at zero

---

*TZM - Molybdenum Alloy, Climax Molybdenum Company of Michigan, Detroit Michigan.

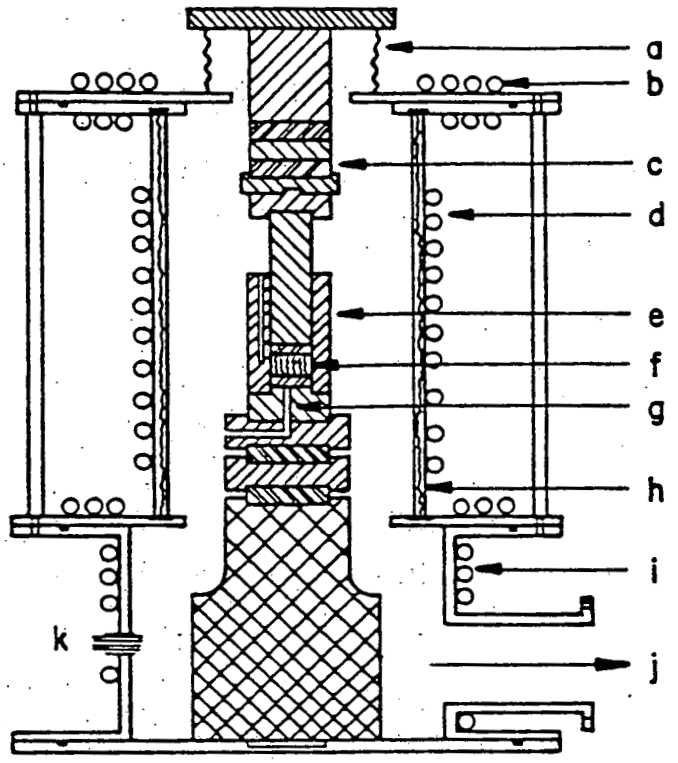

TZM-Mo ALLOY
HPG-PYROLITHIC GRAPHITE
ALUMINUM
STEEL
BRASS

a BELLOWS
b COOLING COILS
c SPACER
d RADIO FREQ. COILS
e H-P DIE
f POWDER
g THERMOCOUPLE WELL
h FUSED QUARTZ TUBE
i COOLING COILS
j TO VACUUM PUMP
k THERMOCOUPLE FEEDTHRU

Figure 4.4. Vacuum hot-pressing apparatus.

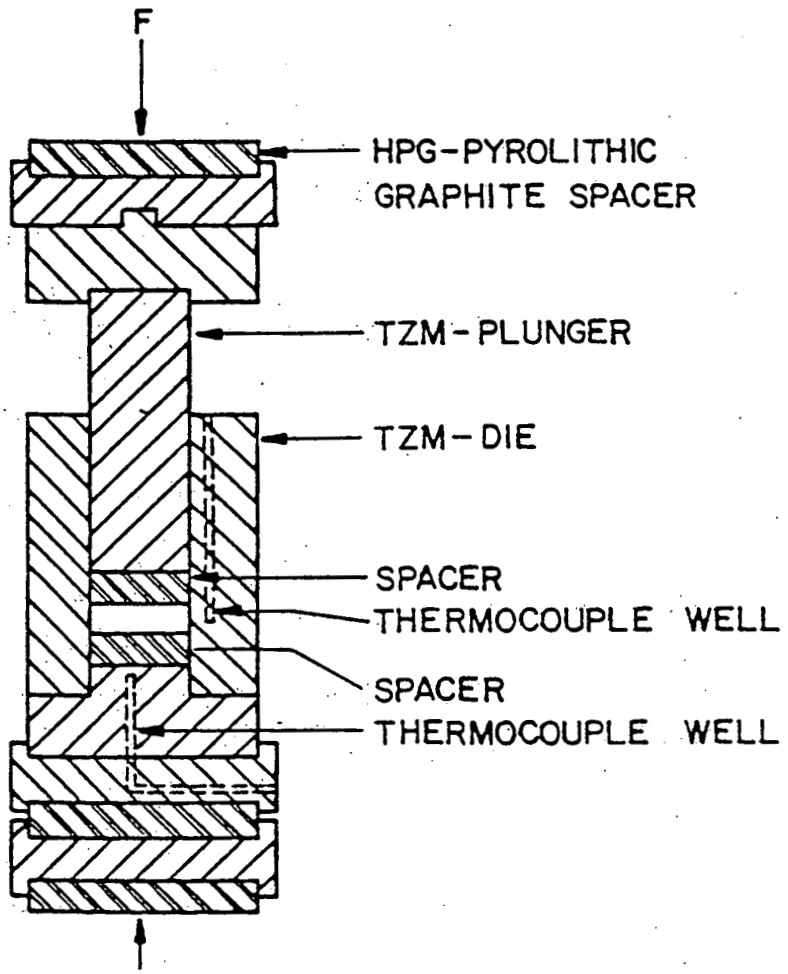

Figure 4.5. "TZM" Molybdenum alloy hot-pressing die.

applied pressure. After the outgassing period a partial pressure varying from 19-78MPa was applied to the powder and the die heated to 650-700°C at rates varying from 13-18deg/min. At 700°C the powder is brought to equilibrium under an applied pressure of 78MPa in ten minutes after which a final pressure is applied (150-344MPa) at 40MPa/min. and the powder is hot-pressed for 5-240 minutes. At the end of the run the radio-frequency generator is shut off and the pressure is released slowly to 100MPa between the maximum temperature and 500°C. At 500°C the pressure is released to zero and the chamber is back filled with nitrogen gas and cooled to room temperature. A flow chart of the hot-pressing procedure is shown in Figure 4.6.

4.1.3. Sample Preparation

Hot-pressed samples were ground and polished using conventional metallurgical techniques for optical observation of the surfaces electrical resistivity measurements and for optical transmission measurements.

The surfaces of the hot-pressed samples were etched at room temperature in a 70% solution of HNO_3 plus two or three drops of H_2O_2 for 30-60 seconds to prevent staining to show the grain boundaries and etch out any CdSe found at triple points. Grain boundaries were further etched by removing both CdSe and Cr_2Se_3 with boiling 70%HNO_3 + 2-3 drops of H_2O_2.

4.2. Materials Characterization

4.2.1. Chemical Analyses

Chemical analyses of both the powders and hot-pressed

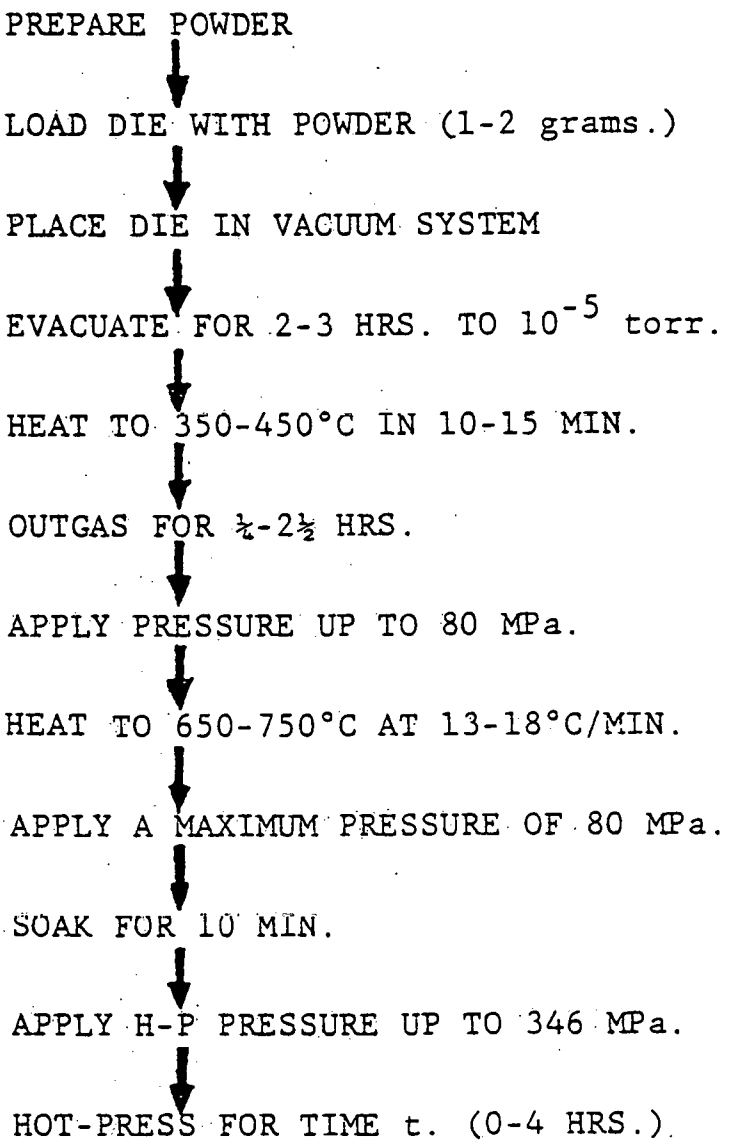

Figure 4.6. Flow chart of the hot-pressing procedure of $CdCr_2Se_4$ and $(1-x)CdCr_2S_4 \cdot x\ CdCr_2Se_4$.

$$CdSe(s) + Cr_2Se_3(s) = 0.002\ gm/cm^3 Se_2(g) \xrightarrow{650^\circ C} CdCr_2Se_4(s) + xSe_2(g)$$

(Excess selenium was found to be necessary to achieve 100% reaction.

The reacted powders were then taken out of the ampule, a sample was taken out for analysis, the rest was reground, put in a freshly cleaned ampule, evacuated, sealed and reacted at 650°C for an additional week. This procedure was repeated until x-ray diffraction showed a single phase. Usually three reaction periods were necessary to obtain a single phase material according to x-ray diffraction.

The fully reacted powders were ground and sieved through a 625 mesh sieve ($\leq$20μm) and placed in a dessicator ready for hot-pressing.

C. Reaction of Co-precipitated hydroxides.

Don Pearlman and Ed Carnall (17) used a dilute solution of hydrazine (N_2H_4) to co-precipitate a finely divided mixture of cadmium and chromium hydroxides uncontaminated by salts from a solution of CrO_3 and CdO in a molar ratio of 2:1, Equation 4.3.

$$CdO + 2CrO_3 \cdot x\ H_2O + (NH_2)_2 \cdot xH_2O \quad 2Cr(OH)_3 + Cd(OH)_2 + H_2O \qquad 4.3.$$

The co-precipitated hydroxides are subsequently dried at

samples was accomplished by x-ray diffraction. The as formed powders were routinely analyzed by x-ray diffractometry in order to determine the second phase concentration. The second phase concentration of Cr_2Se_3 and CdSe, the most prominent second phases in $CdCr_2Se_4$ that could be detected by x-ray diffractometry was calculated by taking the ratio of the 100% x-ray line of the second phase and 100% x-ray line of $CdCr_2Se_4$. X-ray diffraction using a Debye-Scherrer camera was also used to determine the lattice parameter, as of $CdCr_2Se_4$. The lattice parameter was calculated from the x-ray data using the Nelson Riley method(7). Table 4.1 lists the lattice spacings of $CdCr_2Se_4$ powder; within the experimental error no difference was found between the lattice parameter of the powders and that of the hot-pressed samples. The values of our lattice parameter agree with the values of a_o reported by other researchers (48,76).

Hot-pressed samples were also analyzed by optical microscopy to locate the second phase and determine quantitatively the amount of second phases. Observation of second phases was also done by scanning electron microscopy and analyzed by electron microprobe.

4.2.2. D.C. Electrical Resistivity Measurements

D.C. resistivity measurements were made by using the van der Paw method(77). The apparatus used is shown schematically in Figure 4.7. Stainless steel wristwatch

TABLE 4.1. X-RAY DATA OF $CdCr_2Se_4$

hkl	I/I_o	d $\overset{o}{A}$	a_o $\overset{o}{A}$	$\frac{1}{2}\left[\frac{\cos^2\theta}{\sin\theta} + \frac{\cos^2\theta}{\theta}\right]$
220	53	3.7935	10.7296	4.7013
CdSe	4	3.4998		
β(311)		3.2376		
CdSe	4			
β(222)		3.0998		
CdSe	6			
311	63	3.2376	10.7379	3.9426
222	49	3.0998	10.7380	3.7526
β(400)		2.6827	10.7308	
Cr_2Se_3(101)	7	2.7467		
400	55	2.6827	10.7308	3.1701
331	18	2.4630	10.7360	2.8577
β333(511)	2.7	2.0650(β)	10.7302	
422	15	2.1916	10.7366	2.4644
β(440)	3	1.8946	10.7177	
333(511)	56	2.0650	10.7302	2.2135
440	100	1.8972	10.7321	2.0221
442	3	1.7873	10.7243	
620	5.4	1.6966	10.7302	1.7144
533	8	1.6343	10.7167	1.6144
622	10	1.6182	10.7340	1.5898
444	8	1.5500	10.7387	1.4796
711(511)	8.6	1.5033	10.7357	1.4031

TABLE 4.1. X-RAY DATA OF $CdCr_2Se_4$ (cont'd.) 2.

hkl	I/I_o	d Å	a_o Å	$\frac{1}{2}\left[\frac{\cos^2\theta}{\sin\theta} + \frac{\cos^2\theta}{\theta}\right]$
642	11	1.4338	10.7296	1.2872
731(553)	12	1.3976	10.7352	1.2261
800	8	1.3418	10.7344	1.1304
733	6	1.3115	10.7351	1.0776
822(660)	6	1.2656	10.7390	0.9965
555(751)	7	1.2411	10.748	0.9526
804	12	1.2006	10.7385	0.8790
931	19	1.1251	10.7320	0.7385
844	27	1.0960	10.7382	0.6829

$$a_o = 10.738 \pm 0.005 \text{Å}$$

$$\rho_{x\text{-ray}} = 5.714 \pm 0.007 \text{ gm/cc}$$

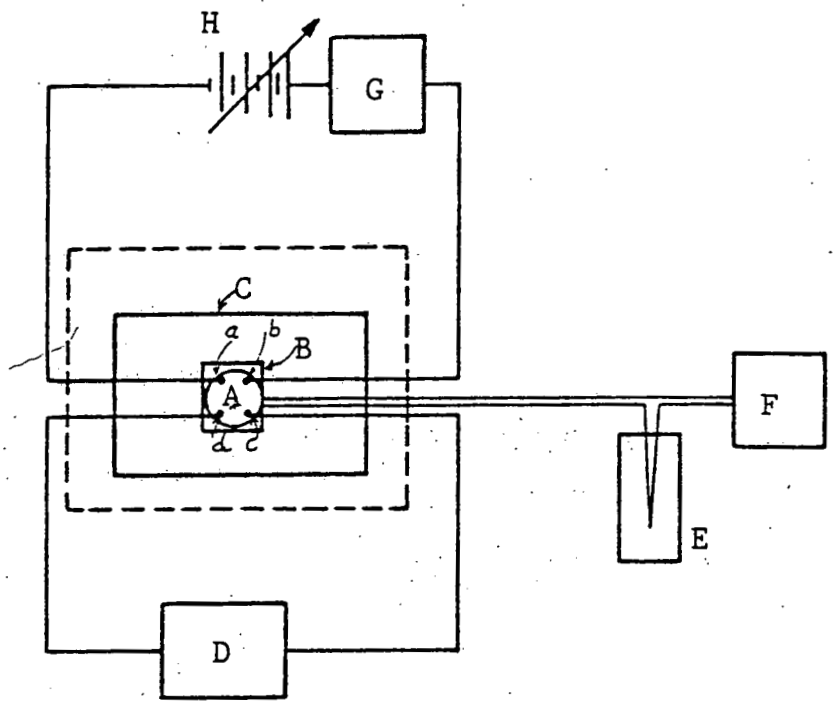

A Sample
B Fused quartz slide
C Copper block (350g)
D Keithley voltmeter
E Thermocouple reference junction at 273K
F Digital voltmeter
G Micro-microammeter
H D.C. Power supply (0-3000V)
I Liquid nitrogen dewar

Figure 4.7. Schematic of the electrical resistivity measurement apparatus.

single sided spring bars were used as pressure contacts and silver amalgam was used to ensure an ohmic contact at both room temperature and liquid nitrogen temperature. The silver amalgam was placed on the tip of the pressure contacts and on the samples at the point of contact. Prior to all measurements the hot-pressed samples were polished by standard metallurgical techniques with 0.05μm alumina, they were lightly etched with HCl to remove any oxide layer and cleaned with ethyl alcohol. A Fluke variable D.C. power supply (0-3000v) was used as the voltage source and the current flowing through ab was measured using a Keithley micro-microammeter. The voltage across cd was measured by using a Keithley high impedance nullmeter. The sample holder was a 350gram Cu-block in order to ensure thermal equilibrium at every reading. The sample was kept in a nitrogen gas atmosphere above liquid nitrogen and allowed to warm to room temperature in 4-5 hours; care was taken in preventing water condensation on the sample. The sample temperature was measured by a chromel constantan thermocouple referenced to 273K placed in close contact with the sample. The readings were taken every ~2 degrees celsius.

The probes were placed symmetrically around the sample edge so that $R_{ab,cd} = R_{bc,da}$. The resistivity was calculated by using the van der Paw formula, Equation 4.3.

$$\rho = \frac{\pi d}{\ell n 2} \left[\frac{R_{ab,cd} + R_{bc,da}}{2} \right] f(R_{ab,cd}/R_{bc,da}) \quad 4.3$$

where d is the sample thickness in centimeters, the resistance Rab,cd is defined as the potential difference $V_d - V_c$ between contacts d and c per unit current through the contacts a and b. The current enters the sample through the contact a and leaves it through contact b; similarly Rbc,da is defined. f(Rab,cd/Rbc,da) is defined in Equation 4.4.

$$f \approx 1 - \left[\frac{R_{ab,cd} - R_{bc,da}}{R_{ab,cd} + R_{bc,da}}\right]^2 \frac{\ell n 2}{2} - \left[\frac{R_{ab,cd} - R_{bc,da}}{R_{ab,cd} + R_{bc,da}}\right]^4 \frac{(\ell n 2)^2}{4} \left\{\frac{(\ell n 2)^2}{4} - \frac{(\ell n 2)^3}{12}\right\} \qquad 4.4$$

Since $R_{ab,cd} = R_{bc,da}$ f( ) ≈ 1 and Equation 4.3. . becomes

$$\rho = \frac{\pi d}{\ell n 2} [R]$$

$$R = \frac{V_{cd}}{I_{ab}} \qquad 4.5$$

$$\rho = \frac{\pi d}{\ell n 2} \left(\frac{V_{cd}}{I_{ab}}\right)$$

where V_{cd} is the voltage across cd and I_{ab} is the current flowing through ab.

4.2.3. Infrared Transmission Measurements

Transmission measurements at 10.6μm were made on all hot-pressed samples (116 in total). routinely using

the apparatus shown in Figure 4.8a. The apparatus consists of a CO_2-laser, a photoacoustic detector(78), a lock-in amplifier and a chopper. The transmission measurements at 10.6μm for samples with an attenuation coefficient less than $50cm^{-1}$ were made on samples with a thickness varying from 0.15 to 0.2cm; whereas samples with attenuation coefficients greater $50cm^{-1}$ had to be polished down to a thickness of 0.05-0.1cm. From the value of the transmittance the attenuation coefficient $(\alpha+\tau)$ was calculated from Equation 4.6.

$$\frac{I_{out}}{I_{in}} = \frac{(1-R)^2 e^{-(\alpha+\tau)\ell}}{1-R^2 e^{-2(\alpha+\tau)\ell}} \qquad 4.6$$

where R is the reflectivity for two surfaces

$$R = \left(\frac{n-1}{n+1} \right)^2$$

n is the index of refraction. Table 4.2 lists the values of the index of refraction of $CdCr_2Se_4$ and $CdCr_2S_4$ as a function of wavelength in the infrared.

Room temperature and liquid nitrogen spectra from 2.5μm and 30μm were obtained using a Beckmann 4250 spectrophotometer. The spectra at liquid nitrogen temperature were made using the cryostat with NaCl windows shown in Figure 4.8b. The NaCl windows were kept at approximately 10°C above room temperature to prevent water condensation. The samples used to obtain infrared spectra were polished

TABLE 4.2. REFRACTIVE INDEX vs WAVELENGTH FOR $CdCr_2S_4$ AND $CdCr_2Se_4$ (Adopted from (17))

$CdCr_2S_4$		$CdCr_2Se_4$	
Wavelength (μm)	Index	Wavelength (μm)	Index
0.633	3.57	1.18	3.33
0.800	3.86	1.22	3.30
0.850	3.75	1.45	3.23
0.900	3.58	1.70	3.20
0.950	3.46	2.56	3.15
1.00	3.37	2.97	3.14
1.20	3.13	3.33	3.14
1.50	2.97	4.45	3.14
2.00	2.89	5.33	.14
2.50	2.86	6.68	3.14
5.00	2.84	8.94	3.16
10.00	2.84	13.53	3.18
15.00	2.84	15.01	3.17
		22.62	3.18
		26.95	3.17

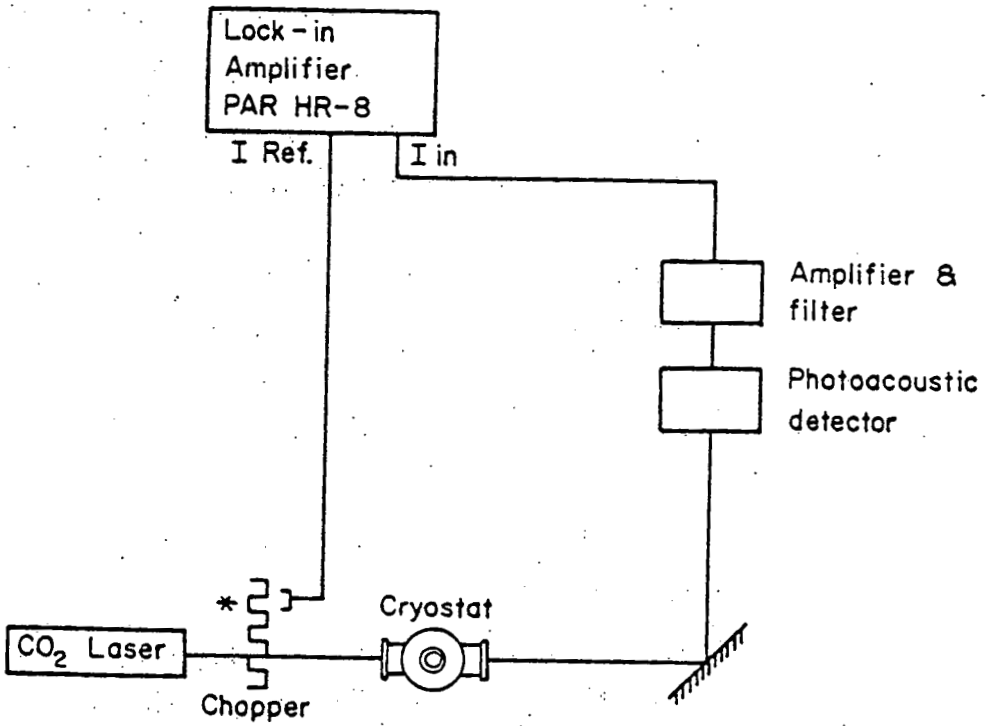

(a)

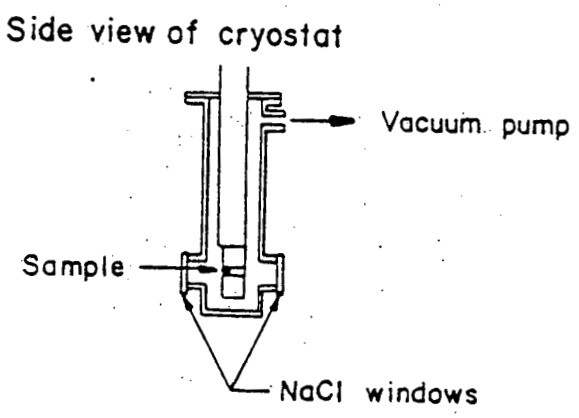

(b)

Figure 4.8. (a) Schematic of the optical transmission apparatus at $\lambda = 10.6\mu m$,
(b) schematic of the cryostat used for low temperature transmission measurements.

down to a thickness of 100-250μm. Care was taken in preventing wedging.

4.2.4. Physical Density Measurements

The physical density of hot-pressed discs averaging a mass of 1-1.5 grams was measured by a liquid displacement method using air-free distilled water as the fluid(79,80). A constantan or chromel wire 12.7μm thick was used to suspend a nichrome basket into the water. Wires with a thickness larger than 20μm caused large fluctuations in the weight during each weighing period and also caused a systematic error due to the large surface tension of water. The distilled water was always boiled prior to all measurements to remove air bubbles if it had been sitting for more than twelve hours. A copper block with plastic legs was used as the base of the water beaker containing the wire basket since charging effects were also found to cause severe fluctuations in the Sartorius semi-microbalance.

Samples to be measured were polished with 0.05μm alumina and cleaned with acetone. The as cleaned samples were weighed in air and then placed in air-free distilled water. The samples were heated in the water to the boiling point of water and boiled until all air bubbles trapped at the surface disappeared. The samples were then transferred to the beaker with the basket without exposing the sample to air. The sample and wire were then weighed suspended in water. Precautions were taken to minimize the air-water temperature differences and corrections were made for effects on air and water densities. This procedure

yielded densities with a standard deviation of ±0.05%.

The procedure for high precision density determinations by hydrostatic weighing has been described by(79,80). They calculate the density of the material ρ_x from Equation 4.7.

$$\rho_x = \frac{\bar{W}_A\rho_w - \bar{W}_w\rho_A}{\bar{W}_A - \bar{W}_w} \qquad 4.7$$

where $\bar{W}_A$ is the average weight of the sample in air, ρ_w is the density of water at the prevailing temperature and barometric pressure, $\bar{W}_w$ is the weight of the sample in water and ρ_A is the density of air at the prevailing temperature and barometric pressure.

The x-ray density of $CdCr_2Se_4$ was calculated using the lattice parameter measured, See Table 4.1, by using Equation 4.9.

$$D = \frac{M}{\bar{V}} \qquad 4.8$$

where M = is the molecular weight (532.232grams/mole for $CdCr_2Se_4$) and $V = \frac{a_o^3 N}{Z}$, where a_o is lattice parameter, N is Avogadro's number (6.02×10^{23}) and z is the number of molecules per unit cell.

$$D = \frac{M_z}{a_o^3 N} \quad (gm/cm^3) \qquad 4.9$$

4.3. Photoacoustic Spectroscopy

This report is concerned with the measurement of the photoacoustic signals generated in highly transparent solids, thin films and powders using both laser and infrared blackbody sources of radiation. Due to the transparent nature of these materials, however, only a minute fraction of the incident light will be absorbed and converted into an acoustic disturbance. Consequently, it may be anticipated that the photoacoustic signals generated from these materials will be rather weak, even when using a laser source.

The employment of an IR blackbody radiation source magnifies the problem. In contrast to the UV and visible regions of the spectrum where tunable lasers are readily available, broadband sources of flux in the IR are basically limited to blackbody radiators, whose optical power per unit wavelength interval is orders of magnitude lower than their visible counterparts. As a result, the photoacoustic signals generated in the infrared region by the blackbody source will also be extremely low.

In this investigation, it was therefore of critical importance to optimize as many photoacoustic parameters as was possible in an effort to maximize the signal to noise ratio. In this report, the results of the optimi-

zation procedures used in this study will be presented. The various trade-offs encountered between the optical, thermal electronic, and photoacoustic cell design parameters will be thoroughly discussed. Finally, a characterization of the frequency response, noise equivalent power, waveform, temporal response, and linearity properties of the photoacoustic signal using carbon black powder in an optimal cell design will be presented.

4.3.1. Photoacoustic cell design

A diagram of the basic design of photoacoustic cells used in this investigation is illustrated in Figure 4.9. The interior dimensions of the cell were 12.7 mm in diameter by 1.2 mm thick. The microphone chamber and cell were connected by an 11 mm by .89 mm diameter channel. The microphone chamber dimensions were 25.4 mm diameters by .29 mm high. The total enclosed volume of the cell including microphone chamber was approximately 300 mm^2. In some cells, the thickness was reduced to .74 mm, in which case the total enclosed volume was roughly 240 mm^3. Aluminum was chosen as the cell material and Harshaw polycrystalline polished NaCl flats were used for the window. The window and samples were clamped against the cell body to form an airtight seal. Alternatively, when a greater degree of permanence was desired, the window and cell were sealed onto the cell with beeswax.

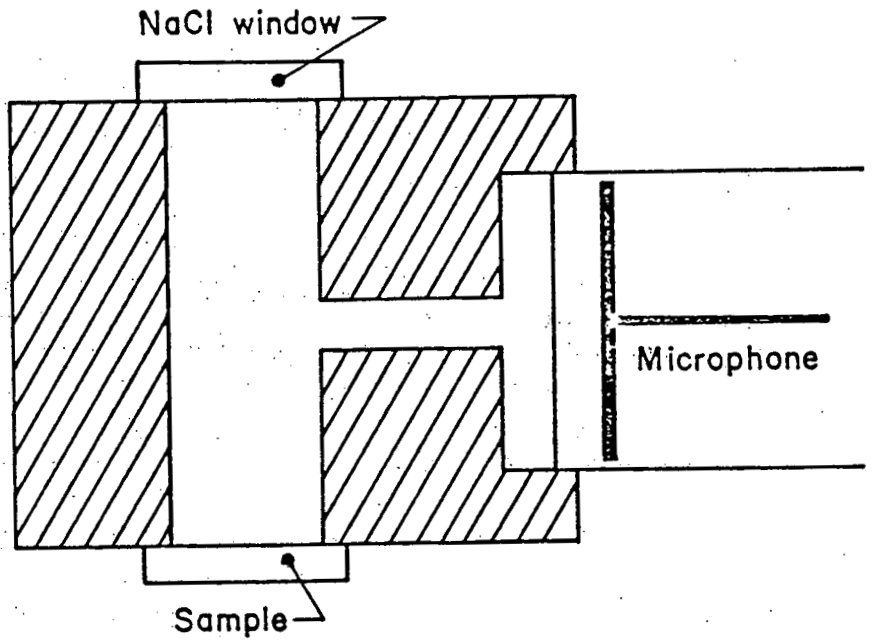

Figure 4.9. Diagram of the photoacoustic cells used in this investigation.

Several considerations went into the design of the photoacoustic cell, and various different configurations were built and tested using opaque carbon black samples. Of primary concern was the maximization of the magnitude of the photoacoustic signal, accomplished mainly by reducing the total cell volume.

From the theoretical analysis presented earlier, we discovered that the photoacoustic signal and cell volume were inversely related. This relationship was tested experimentally using five cells whose volumes ranged from a maximum of 10^8 mm^3 to a minimum of 150 m^3. A plot of the photoacoustic responsivity at 100 Hz vrs. cell volume for the five cells is presented in Figure 4.10. Inspection of this graph shows that an inverse relationship does indeed exist for volumes greater than approximately 300 mm^3. Thus, it is seen that, in contrast to the theoretical prediction, the photoacoustic signal does not tend to infinity as the volume goes to zero. It also appears that there is an optimal cell volume which results in the greatest photoacoustic responsivity at a particular modulation frequency.

There are several reasons which might explain this behavior. First and most importantly, we note that if we neglect the microphone chamber volume, the physical distance between the sample and cell windows, ℓ/g decreases linearly with decreasing cell volume. For cells whose

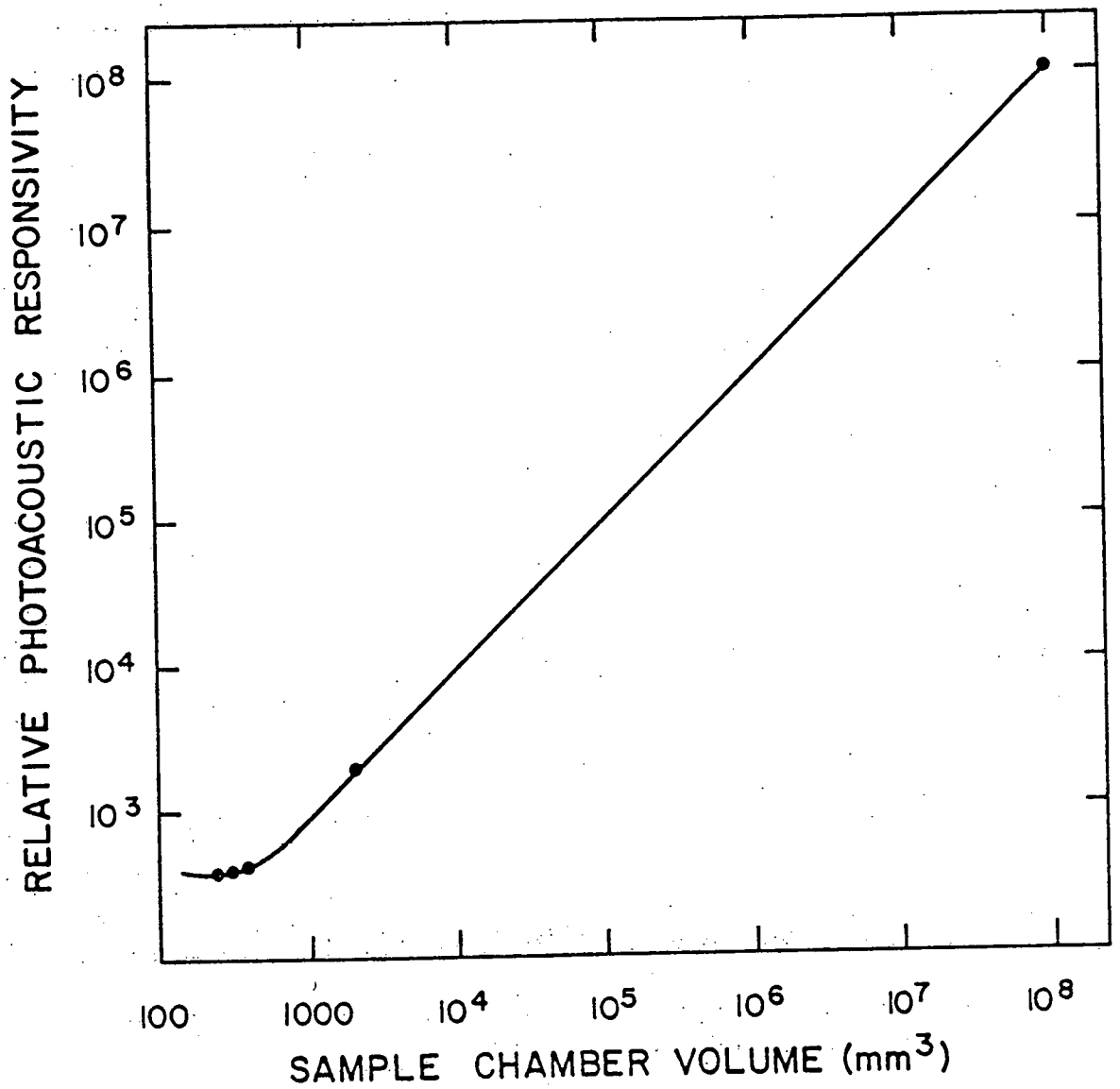

Figure 4.10. Photoacoustic response vrs. cell volume.

volumes are less than 300 mm^3, this distance is less than 1.2 mm. At the same time, inspection of Table 4.3 shows that the length of the acoustic piston ℓ/g, is .4 mm greater than ℓ/g at a modulation frequency of 100 Hz in air. Thus, it is important to note that assumptions made in our theoretical model are no longer valid in the small volume regime. We also see that a significiant amount of heat may be transferred by the gas to the cell window since the acoustic piston is larger than the buffer gas length. In this respect, we may consider the buffer gas as a thermal short which conducts heat from the sample to the exterior ambient environment. As a result, the average temperature fluctuation in the gas is diminished and the magnitude of the photoacoustic signal reduced.

This hypothesis may be tested by employing the same cell and carbon black sample to monitor the photoacoustic responsivity as a function of buffer gas. Inspection of Table 4.3, for example, shows that helium has a thermal diffusion length 2.85 times that of air. Thus, according to (78), an <u>increase</u> in the photoacoustic signal of ~ 2.84 should be observed if helium were substituted for the buffer gas. This prediction was tested with the cell described above where $\ell/g = .74$ mm. The responsivity of the cell was first measured using air as the buffer gas. The cell was then disconnected from the microphone to allow an exchange of buffer gases, and left in a helium

environment for one hour. At the end of this period, the cell was re-attached in the microphone inside the helium environment and its responsivity measured. This procedure was repeated three times. The results of this experiment were that the photoacoustic response of the cell was smaller using helium as a buffer gas by approximately 690. Thus, it would seem that the increase in the photoacoustic signal, anticipated primarily as a result of the decreased density of helium, has been more than cancelled out as a consequence of the increased thermal shorting. Similar trends verifying this behavior have recently been independently verified (81).

Additional confirmation of the thermal short hypothesis may be made by monitoring the photoacoustic response of a particular cell as ℓ/g is reduced. In practice this was accomplished by adding more and more carbon black powder to the cell and monitoring the responsitivity. Our theoretical predictions based on the thermal short hypothesis would be that the responsivity would decrease when the powder virtually filled the cell. The experiment was performed in a cell whose microphone channel was connected to the cell at the NaCl window. When the carbon black powder was added to the cell so that it touched the window in several locations, the photoacoustic response decreased by a factor of more than 2, in agreement with our thermal short hypothesis.

Table 4.3. Thermal Sampling Depths for Various Materials

Substance	Sampling Depth .01 Hz	1 Hz	100 Hz	10 KHz
Air	26 mm	2.6 mm	260 μm	26 μm
Helium	.74 mm	7.4 mm	740 μm	74 μm
Germanium	34 mm	3.4 mm	340 μm	34 μm
Glass	4 mm	400 μm	40 μm	4 μm
$CdCr_2Se_4$	8.9 mm	890 μm	89 μm	9 μm
$CdCr_2S_4$	11 mm	1.1 mm	113 μm	11 μm
ZnSe	21 mm	2.1 mm	206 μm	21 μm
NaCl	11 mm	1.1 mm	108 μm	11 μm

Additional damping mechanisms should also be considered. Viscosity and similar losses will be important when the dimensions of any acoustic propagation apertures approach the dimensions of the damping skin depths (82) which are given by:

$$l_d = \frac{\sqrt{2\eta}}{\sqrt{\omega\rho_o}} + \frac{\sqrt{2k}}{\sqrt{\omega\rho_o}} \qquad 4.10$$

where η is the viscosity of the gas (Kg/m-sec). Table 4.4 lists the values of l_d as a function of frequency for air and helium. At 100 Hz, we see that the skin depths are 47 μm and 139 μm for air and helium, respectively. Since the minimum dimensions in the cell are 290 μm in the microphone chamber, we see that viscous damping may also have contributed to the decrease in photoacoustic responsivity as the buffer gas was changed to helium. For air, however, the viscous damping forces may be neglected since the minimum acoustic aperture is a factor of six greater than the damping skin depth. It should be noted that equation 4.10 represents a limit on the size of the microphone chamber volume and the connecting tube. Unfortunately, efforts to decrease the volume of the microphone chamber by reducing its height to $\sim 2l_d$ were not successful, due to the mechanical strength and stability of the aluminum. As such, a total photoacoustic cell

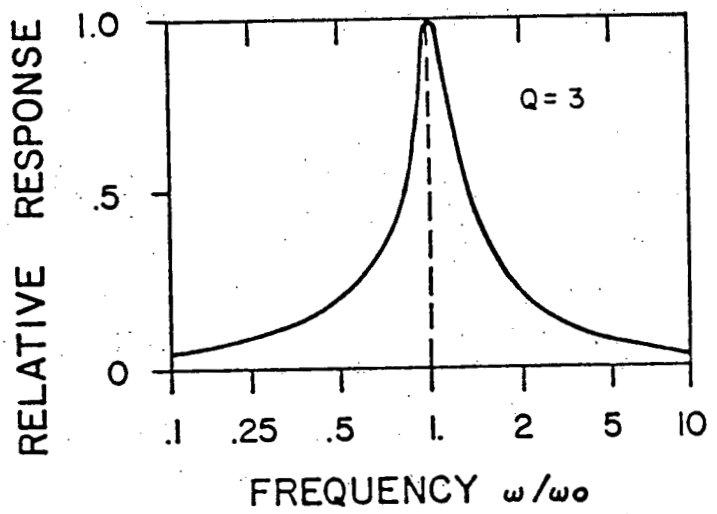

Figure 4.11. Acoustical gain vrs. frequency for a resonant cell.

Table 4.4 Acoustic Damping Skin Depths for Helium and Air

Substance	Skin Depth			
	.01 Hz	1Hz	100 Hz	10KHz
Air	4.7 mm	470 μm	47 μm	4.7 μm
Helium	13.9 mm	1.39 mm	139 μm	13.9 μm

volume of ~250-300 mm^3 for sample diameters of 17.6 mm may be considered as optimal.

Photoacoustic cells may be acoustically resonant or non-resonant. The selection of one or the other is dependent primarily upon the intended application. In the acoustically resonant cell, the minimum dimensions of the cell must be approximately half the acoustic wavelength of sound in the buffer gas. For air at 100 Hz, these dimensions are roughly 1.5 meters. Thus, we see that in the resonant cell design, the total cell volume may increase by as much as a factor of 10^3 over the non-resonant cell. Since acoustical gains in resonant cells may typically be on the order of 5 to 300 at the design frequency, the net result is a reduction in the total photoacoustic response by a factor of ~10 or more. However, it should be noted that using appropriate designs, such as a long narrow tube connected to the cell, the response may be enhanced to the point where the resonant and non-resonant responses are approximately equal at the design frequency.

Alternatively, one might hope to increase the resonant response by reducing the cell dimensions and increasing the resonant frequency. However, from our theoretical analysis of the photoacoustic effect, we found that the magnitude exhibited either at f^{-1} or $f^{-1.5}$ modulation frequency dependence. Since the response is inversely proportional to the cell volume we thus see that the high

frequency resonant response may actually be lower than that for the low modulation frequency case.

In this investigation, the non-resonant cell design was used exclusively for several reasons. From our analysis above, it is readily concluded that there is little to gain in the photoacoustic response by employing resonant type cells. We also note that the resonant cell, in most cases, does not significantly improve the signal to noise ratio, since the cell provides acoustical gain for both the photoacoustic effect and any acoustical noise which may be present in the environment. Any substantial improvement in the signal to noise ratio may only be realized if the photoacoustic system is limited by factors other than environmental acoustic vibrations. Unfortunately, as we shall see, most photoacoustic systems are acoustically noise limited, in which case the improvement in the signal to noise ratio will be minimized.

The non-resonant cell configuration was also chosen for modulation frequency considerations. In this investigation, it will be important to monitor the magnitude of the photoacoustic signal as a function of modulation frequency. In the non-resonant cell design, the acoustical gain of the cell is, to a good approximation, a constant independent of chopping frequency. However, in the resonant cell, the gain is a strong function of frequency, particularly around the resonance frequency as is shown

in Figure 4.11. This presents several problems. First, the gain function affects not only the amplitude of the photoacoustic signal, but also its phase. Thus, calibration and interpretation of results obtained in a modulation frequency study would be extremely difficult, if not impossible, to accurately interpret. Second, we note that for frequencies sufficiently removed from the resonance, the photoacoustic signal is strongly damped. Thus, while the resonant frequency response may be large, the off resonant response may decrease significantly. Consequently, for the highly transparent samples investigated in this thesis, the resonant photoacoustic signal detection problems would be more severe. Finally, the stability of the chopper would become extremely important since a small change in the modulation frequency around the resonance would give rise to a large fluctuation in the photoacoustic signal. Additional stability problems may also be encountered as a result of ambient temperature variations changing the location of the resonant frequency.

Suppression of spurious photoacoustic background signals is another major consideration in the cell design. Spurious photoacoustic signals originate from the incident light flux being absorbed at several sources including the cell walls, cell window, and the microphone membrane.[84] These "false absorption" signals are extremely important, especially in the highly transparent sample regime, since

they: 1) are at the same frequency as the "true" signal, 2) tend to be at the same phase since both signals arise primarily as a consequence of surface absorption, and 3) may be much stronger than the "true" signal. Thus, the spurious signal is not only indistinguishable from the true signal, but the latter may be entirely masked by the photoacoustic background generated within the cell.

Several photoacoustic cell parameters were selected in order to minimize the spurious background signal. First of all, Harshaw infrared window quality NaCl flats were employed as cell windows. The total absorption of these flats at 10.6 μm within a diffusion length of the buffer gas is ~ 1×10^{-5} at 100 Hz. As we shall see, this is approximately two orders of magnitude lower than the absorptances we will measure in the germanium samples. Thus, the NaCl windows may be considered to be essentially transparent in the infrared wavelengths of interest. Additionally, we note that the Fresnel reflection loss for NaCl is small (4%/ surface) due to its 1.50 index of refraction at 10.6 μm. As such, light which strikes the NaCl window on the interior surface at an angle of incidence less than the critical angle (42.1°) will be transmitted out of the cell into the ambient environment. The main contribution of the scattered light, which originates from the Fresnel reflection off the first surface of the sample, will consequently be shunted out of the photo-

acoustic cell without generating an appreciable background signal.

The material with which the photoacoustic cell is made of may also be used to minimize background signals. The cells used in these investigations were made of aluminum, which is highly reflective in the infrared region. At 10.6 μm, the reflectance of aluminum is 99%(83). Thus, only 1% of the light scattered onto the walls can be absorbed. The small fraction which is absorbed will simultaneously be heat sunk away from the buffer gas due to the extremely large thermal conductivity of aluminum. From (78) the relative magnitude of the photoacoustic effect for a cell wall absorption is given by the product $(\mu_b/\mu_s)(k_s/k_b)$. For a germanium sample and aluminum cell, we find that the photoacoustic signal generated from an absorption at the cell walls would be a factor 6.8 smaller than the photoacoustic signal generated by an equivalent absorption on the surface of the germanium sample. Thus, the cell walls may be considered to have an effective reflectance of 99.85%.

The total amount of light incident upon the cell walls can also be minimized by reducing the total cell wall area and by decreasing the aspect ratio, l_g/D, of the cell. In the latter case, the total solid angle subtended by the cell walls is reduced. It is interesting to note that again it is advantageous to employ the non-

resonant cell design since the total interior cell surface area is necessarily larger for the resonant cell configuration.

An interesting observation may also be made regarding the role of the buffer gas in reducing the background signal. Consider the case where $l_g = 2\pi\mu_g$ for two otherwise identical cells filled with helium and air, respectively. From our previous analysis, we note that the photoacoustic cell responsivities should be equal in the two cases. However, it is still advantageous to use air as the buffer gas, since the background signal will be significantly lower due to the smaller total surface area and the reduced aspect ratio encountered in the latter case.

A portion of the interior surface in the photoacoustic cell consisted of the steel microphone diaphragm. The absorptance of steel at 10.6 μm is ~7% (reflectance = 93%)(83). Even though the effective photoacoustic reflectance is somewhat higher, the increased absorptance of steel may generate a significant background signal. Furthermore, we note that microphone diaphragm absorptions will create an additional electrical signal due to the thermal expansion of the diaphragm itself. As such, it is important to shield the microphone from scattered radiation. This was accomplished by using a small channel oriented perpendicular to the incident irradiation to connect the microphone and sample chambers. Although it

is not diagrammed in this location in Figure 5-1, the top portion of the microphone channel often consisted of the NaCl window itself. In this manner, scattered light which would otherwise be waveguided into the microphone was allowed to escape through the window. It should also be noted that an additional right angle in the connecting channel was added for the powder analysis, since the diffuse reflectance of the powder is far greater than that of the polished germanium flats used in the photoacoustic scanning experiments.

The total background contribution to the photoacoustic signal may be estimated if we assume that the incident irradiance is perpendicular to the sample and that the latter is a Lambertian diffuse reflector (exhibits a $\cos^2\theta$ reflectance). Expressed in absorptance units, the false absorption, A_F, is given by:

$$A_f = A_l + A_w + A_m \qquad 4.11$$

where

$$A_l = R_d \, (1 - R_{al}) \int_{\xi_1}^{90} \cos^2\xi \, d\xi \qquad 4.12$$

where A_w is the false absorptance due to the window, A_l is the false absorption contribution due to the cell walls, ξ is the angle of the reflected light relative to

the sample surface, $\xi_1 = \sin^{-1}(D/l_g)$ is the angle subtended by the cell walls, $R_d = (n-1)^2/(n+1)^2$ is the normal Fresnel reflectance off of a sample whose index of refraction is n, R_{al} is the effective reflectance of the aluminum walls, and is the false absorption contribution due to the microphone. In practice, $A_m << A_l$ and can be therefore neglected.

Using $\xi_1 = 79.1°$ for the photoacoustic cells employed in these investigations, we find that A_w is 1.2×10^{-6} and 1.5×10^{-7} for germanium and sodium chloride samples, respectively. Comparison of these results with the $\sim 1 \times 10^{-5}$ effective absorptance of the NaCl window reveals that the photoacoustic cell used in these investigations will have a background signal which is window absorptance limited. A summary of the photoacoustic cell design considerations is presented in Table 4,5.

4.3.2. Electronics

The photoacoustic signal generated within the photoacoustic cell is converted into an electrical signal and amplified by means of a microphone and preamplifier. Due to the extremely high input impedances required by microphones, the electrical noise of the preamplifier may become the dominant source of noise in photoacoustic systems. In this section, we describe the microphone and preamplifier circuits used in our investigations and discuss

Table 4.5. Photoacoustic Cell Design Considerations

Parameter	Minimize/Maximize	Constraints
Volume	minimize	thermal diffusion length viscous damping length microphone size sample size
Interior surface area	minimize	thermal diffusion length viscous damping length microphone size sample size resonant/nonresonant cell
cell thermal conuctivity; density	maximize	material selection
cell reflectivity	maximize	material selection
microphone response	maximize	microphone size cell volume
preamp noise	minimize	Johnson, 1/f noise Brownian motion of mike
window absorption	minimize	material selection

steps which were taken to minimize the electrical noise contribution.

A B&K model 4144 25.4 mm diameter condenser microphone was used to detect the photoacoustic signal. Condenser microphones operate on the principle that acoustic waves, which are incident upon a parallel plate capacitor, will cause the distance between the two plates to vary as a function of time. Since the capacitance is inversely related to the separation of the plates, the moving membrane creates an a.c. voltage fluctuation. For small amplitudes, the voltage fluctuation is directly proportional to the amplitude of the pressure wave, and a linear conversion from the acoustic domain to the electrical signal domain is achieved.

The B&K model 4144 was chosen primarily for the ultra high, 5mV/μbar(50mV/N/m^2) sensitivity. The minimum detectable pressure in a microphone is most often limited by the electrical noise in the preamplifier. The electrical noise in the preamplifier, in turn, increases as the gain of the preamplifier increases. Thus, a high sensitivity in the microphone is extremely desirable since it effectively decreases the electrical gain necessary to be able to detect the electrical signal. Consequently, the electrical noise contribution is diminished and the amplitude of the minimum detectable acoustic signal is reduced.

The frequency response of the B&K model 4144 microphone(84) which is presented in Figure 4.12 is also important to consider. Inspection of Figure 5-4 shows that the response is completely flat from 20 Hz to 2KHz. At 5 KHz, we notice an increase in responsivity due to a microphone resonance. Above the resonance, the microphone membrane becomes too massive to respond to the high frequencies, and the sensitivity decreases. In our investigations, only the 10Hz to 2 KHz regime is used, and corrections to the photoacoustic signal due to the microphone frequency response will be unnecessary.

A microphone preamplifier serves two main purposes. First, it provides an impedance match for the microphone in that it converts the high output impedance of the condenser microphone into a low output impedance. Second, it provides electrical amplification of the extremely weak a.c. signal, thus enabling the output to be connected to more conventional signal detectors, such as oscilloscopes and lock-in amplifiers. Both functions reduce the electrical noise signal since they minimize the contributions of noisy amplifiers and reduce the antenna pick-up of the high impedance microphones. The design of the preamplifier, however, is often critical, since the main electrical noise contribution will originate from this source. In our studies, where the photoacoustic signals are extremely weak, it was necessary to design a

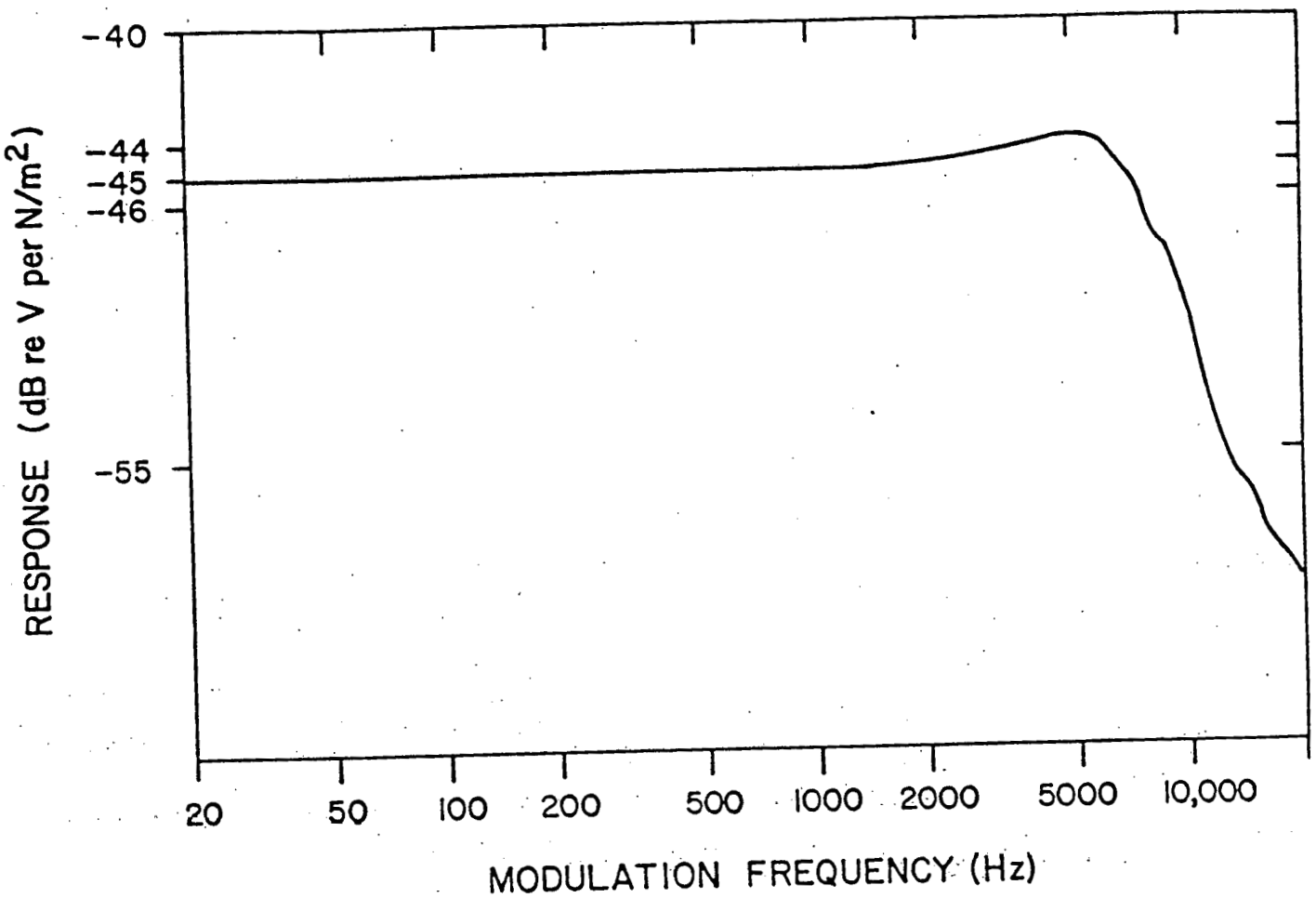

Figure 4.12. B & K 4144 microphone frequency response.

special low noise preamplifier in order to prevent electrical noise from masking the photoacoustic signal. The electrical diagram of the preamplifier is shown in Figure 4.13.

There are several features of the preamplifier design which warrant attention. The heart of the preamp is a BF 800 low leakage (3×10^{-16} amp $\sqrt{Hz}$), low noise (25 nV $\sqrt{Hz}$), high input impedance (10^{14} Ω) FET, whose purpose is mainly to provide an impedance match to the microphone. The output of the FET is then, supplied to an emitter-follower transistor combination, which reduces the output impedance farther and provides a feedback loop to fix the electrical gain at 10. The microphone itself is supplied with a heavily filtered 200 VDC polarization voltage, while the transistors are supplied with a filtered 20 VDC power source. All of the resistors are either wire wound or metal film. With the electrical gain of 10, the overall microphone response is 50 mV/μbar (.5 mV/N/m^2)

A unique feature of the preamplifier design involves the use of two 100 GΩ resistors between the microphone and the FET input. The purpose of the ultra large resistors is twofold. First, they prevent charge from leaking from the microphone. Second, they reduce the electrical noise contribution of the preamplifier. The latter result is best illustrated by considering sources of electrical noise in an equivalent circuit diagram, shown in

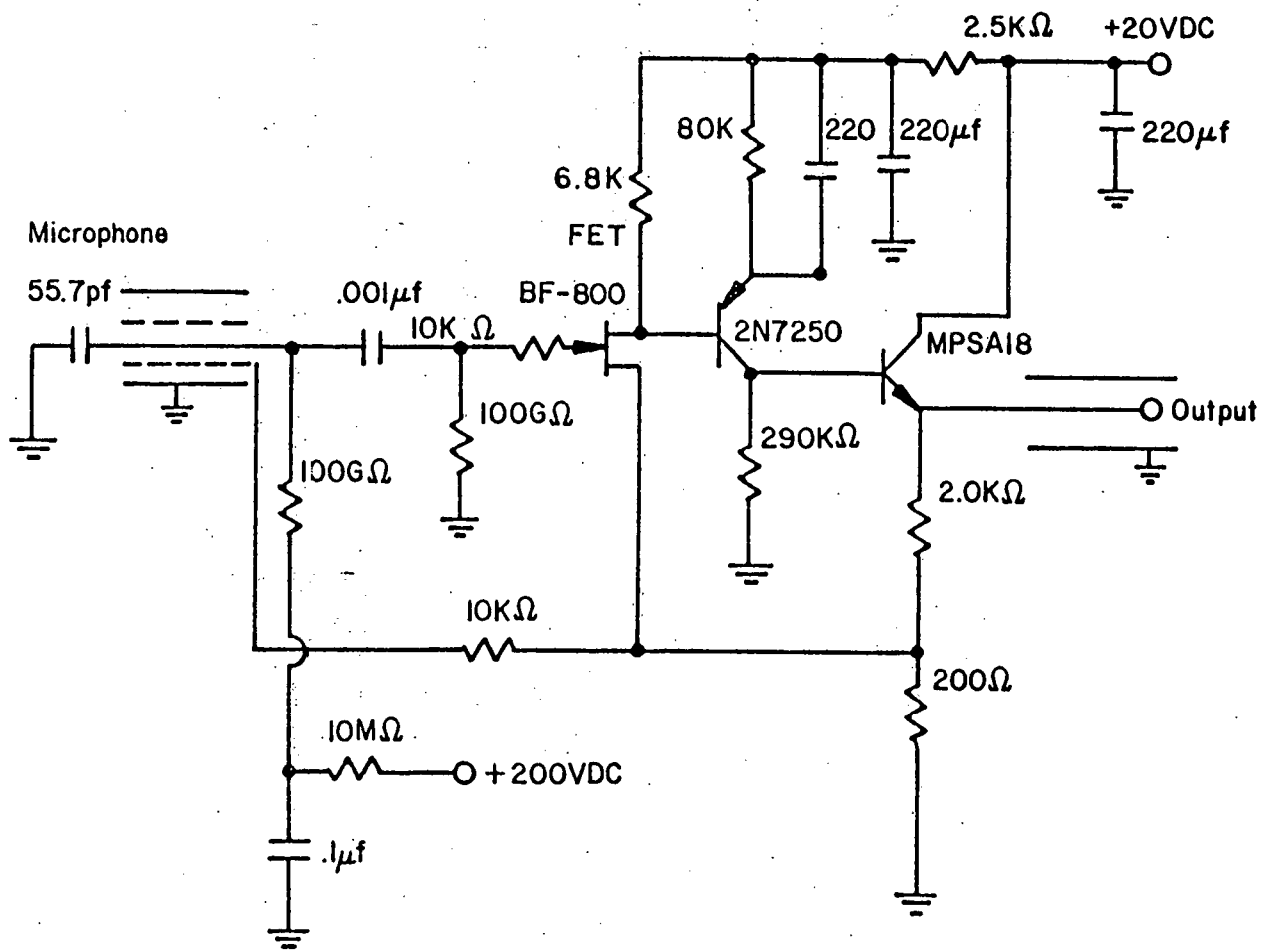

Figure 4.13. Low noise preamplifier circuit diagram.

Figure 4.14a. Here, V_s is the a.c. photoacoustic electrical signal, V_n is the voltage noise of the FET, $i_L R$ is the noise voltage caused by the FET leakage current i_L, and V_J is the Johnson noise of the resistor. Inspection of Figure 4.14a shows that V_s encounters a high pass RC circuit to the FET whose -3db point is at $\omega_o = 2\pi f = (RC)^{-1}$, shown in Figure 4.14b. However, the Johnson and leakage noise contributions see a high pass RC filter circuit to ground. As such, the noise voltage contributions of the latter two sources is attenuated by 20 db (a factor of 10) per decade above ω_o. At 260 Hz, for example, these sources have been attenuated by 10^3 while the microphone signal remains uneffected.

The total electrical noise at the output of the preamplifier (including the electrical gain of 10), V_T, is given by:

$$V_T = 10\left(V_n^2 + \frac{i_L^2}{\omega^2 C^2} + \frac{4kT\Delta B}{\omega^2 C^2 R} + V_{eff}^2 \right) \qquad 4.13$$

where k is the Boltzmann constant (J/K), ΔB is the bandwidth (Hz), T is the temperature of the 100 GΩ resistors (K), and V_{eff} is the effective noise voltage of the rest of the preamplifier (V).

Inspection of 4.13 reveals the surprising result that the electrical output noise decreases as R increases.

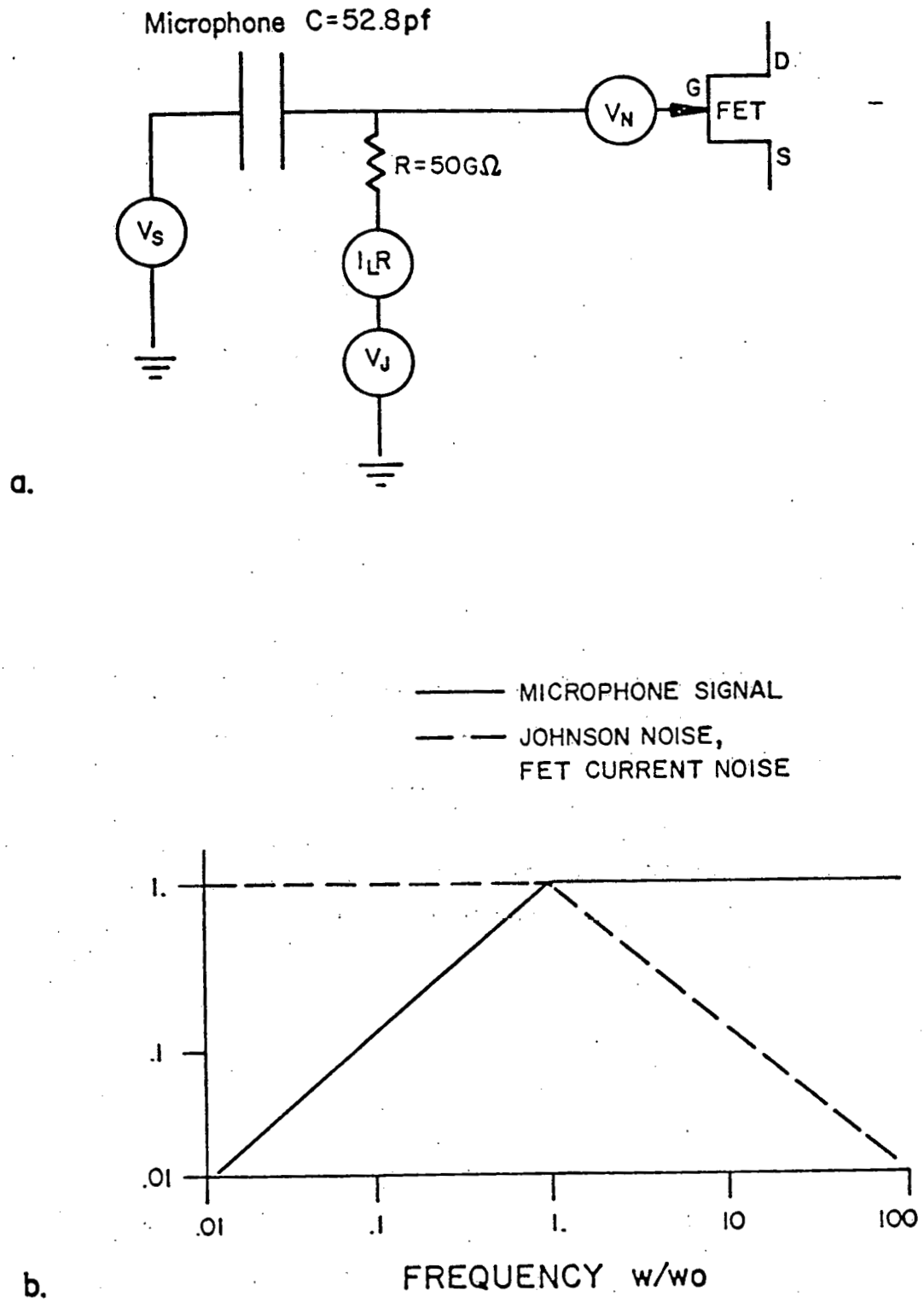

Figure 4.14. Low noise preamplifier equivalent input circuit diagram (a) and frequency response (b).

However, we note that as $R \to \infty$, only the Johnson noise contribution (the third term) goes to zero. As such, a practical limitation on the value of R is arrived at when the Johnson noise contribution is much less than the other sources. In the case under consideration, this limit is reached when R = 100 GΩ.

The frequency spectrum of the electrical noise in the preamplifier was tested experimentally by substituting an equivalent 50 pf capacitor for the microphone and monitoring the output with a lock-in amplifier. The experimental result obtained is compared with the theoretical design curve (given by (4.13)) in Figure 4.15. Agreement between the two is seen to be generally good. At low frequencies, the experimental result is higher due to the 1/f noise in the electronics. At higher frequencies, we see that the experimental values are lower than the theoretical curve. This may be explained as a consequence of the frequency dependence of the V_n term in 4.13 for the BF-800, which was unknown and could not be taken into account in the theoretical curve.

It is interesting to compare the performance of the preamplifier to the theroetical noise limit dictated by the Brownian motion of the microphone diaphragm, V_B. The latter is given by (85):

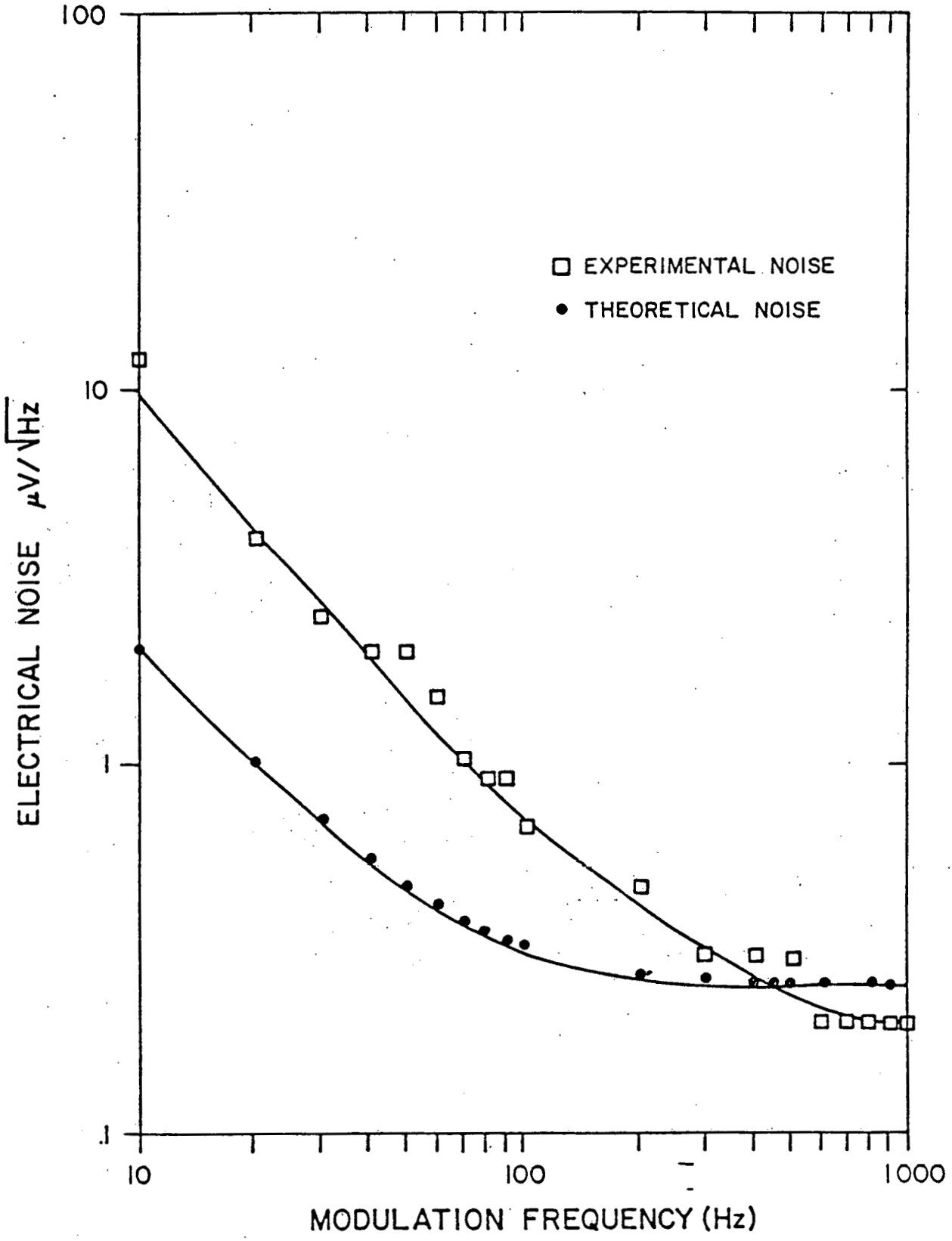

Figure 4.15. Electrical output noise of the low noise preamplifier.

$$V_B = R \left(\frac{8\ kT\ \sigma\ \Delta B}{A\ \tau}\right)^{\frac{1}{2}} \qquad 4.14$$

where σ is the mass density of the microphone (g/cm^2), τ is the microphone response time (sec), and R is the responsivity of the microphone and preamplifier (V/μbar). Substituting the values appropriate for the B&K 4144 microphone, we find that the Brownian noise voltage limit is 100 $nV/\sqrt{Hz}$. Inspection of Figure 4.15 shows that the preamplifier electrical noise is 200 $nV\sqrt{Hz}$, or a value which is only a factor of ~2 greater than the microphone Brownian noise limit.

Finally, we note that the use of 100 GΩ resistors required that adequate shielding be maintained in order to prevent antenna-like pick-up. To minimize these difficulties, the preamplifier was enclosed in a metallic case and the distance between the microphone and the FET reduced to ~3 cm. For similar reasons, careful attention was also paid to the grounding circuit, which was laid so that all grounds were connected together at one physical point.

4.3.3. Acoustical noise

The minimum detectable photoacoustic signal is often a function of the magnitude of environmental vibrations

and sounds. The origin of these detrimental signals may be traced to a variety of sources. A few of the most important are: building vibrations and sounds originating from trains, planes, voices, air conditioners and fans, doors slamming, chopper blades, and vacuum pumps. In the present investigation, where photoacoustic signals are rather weak, it is important to minimize the effect of these random signals. Reduction of the influence of acoustical noise on the photoacoustic signal may be accomplished using several techniques.

The most effective method of noise reduction involves phase sensitive or lock-in amplifier detection of the photoacoustic signal. Lock-in amplifiers measure only the frequency component of the total microphone signal which is within ΔB of the referenced chopping frequency. Thus, acoustic noises at frequencies different from that of the modulation frequency will be severely attenuated and their detrimental influence reduced. The bandpass of the lock-in may also be varied so that the effect of the random background signal may be decreased to an acceptable level.

The noise rejection capabilities of the lock-in detection scheme may be best illustrated by considering the vicinity of the laboratory in which this investigation was performed. A frequently used railroad track is located approximately 50 meters from the lab, and an airport ap-

proachway for the local airport brings large aircraft within ~500 meters of the room. In spite of the fact that both of these sources emit large quantities of low frequency large amplitude acoustic waves, neither was found to have any significant influence on the photoacoustic signal for modulation frequencies from 100 Hz to 2 KHz at bandwidths of 10 Hz. Similar results were obtained for most other identifiable sources of acoustic noise whose noise spectrum was broad. These included an air conditioner, vacuum pump, radio, and oscilloscope fan.

Vibrations transmitted through the building to the microphone were effectively minimized by placing the photoacoustic apparatus on top of a Newport Research Honeycomb optical table. Vibrations in the table resulting primarily from the mechanical chopping motor, however, proved to be more difficult to eliminate. The effect of this source was most acutely felt at high frequencies, where the chopper motor was rotating at speeds up to 10,000 rpm. Consequently, chopper blades with up to 52 teeth were used to obtain high modulation frequencies while maintaining low chopper motor rotation rates. In this manner, the vibrations of the optical table were kept to a minimum. It should be noted, however, that chopper noises and vibrations could be virtually eliminated by using an alternate source of amplitude modulation, such as an electro-optic acoustic-optic modulator. Unfortunate-

ly, infrared materials and economic considerations prevented their use in this investigation.

Coherent sources of noise, which have the identical frequency and a fixed phase relationship to the photoacoustic signal, should also be mentioned since the lock-in amplifier cannot alone discriminate between these sources and the true photoacoustic signal. In this study, the dominant source of coherent noise was the chopper, whose rotating fan blades generated acoustic disturbances at the same frequencies as the photoacoustic signal. In principle, these effects could be eliminated by using a reflection mask evaporated onto a transparent disk, or by employing an electro-optic or acousto-optic modulator. In the infrared region, however, material costs are high and prevented the implementation of these measures. As such, the effect of the chopper was reduced by placing it as far away from the photoacoustic cell as possible. In this manner, the strength of the acoustic wave would be reduced both by atmospheric absorption and diffraction losses. While extremely simple, such measures proved to be satisfactory in most of our experiments, since the coherent noise contribution was most often masked by other sources of noise. Additionally, it should be noted that it is possible to discriminate between the photoacoustic signal and the coherent noise by measuring the magnitude and phase of the coherent signal alone, and vectorally sub-

tracting the contribution from the total signal. In practice, this may be accomplished by momentarily blocking the radiation source from the photoacoustic cell and measuring the coherent noise signal. The true photoacoustic signal can then be related to the total measured signal by:

$$A = (Q^2 = (I_o - I)^2)^{\frac{1}{2}} \qquad 4.15$$

$$\Phi_r = \Phi_m - \delta \qquad 4.16$$

$$\delta = \tan^{-1} (Q/(I - I_o)) \qquad 4.17$$

where A is the in phase amplitude of the true signal

Q is the in quadrature amplitude of the signal when the beam is blocked.

I_o is the in phase amplitude of the total signal

I is the in phase amplitude of the signal when the beam is blocked

Φ_r is the phase angle of the true signal

Φ_m is the phase angle of the total signal

δ is the correction to the phase angle due to the noise signal

Finally, we note that the photoacoustic cell itself acts to reduce the external acoustic noise. Aluminum is

a relatively dense material. As such, the acoustic waves transmitted through the cell are attenuated by absorption mechanisms. Also, the acoustic impedance mismatch between aluminum and the air is large, resulting in the reflection, a major portion of the incident sound wave in an analogous manner to the optical Fresnel reflection for highly refractive materials.

A plot of the frequency spectrum of the total noise in the photoacoustic cell and electronics is presented in Figure 4.16. Inspection of Figure 4.16 shows that the acoustic noise is more than an order of magnitude larger than the preamplifier electrical noise, and thus will be the dominant mechanism limiting the minimum detectable photoacoustic signal. We also note that the noise decreases in an approximately linear fashion as the bandwidth of the lock-in amplifier is decreased. Thus, it is possible to reduce the total noise of the system by increasing the time constant of the lock-in amplifier.

The noise level decreases as the modulation frequency increases. This is a result of the fact that low frequency environmental sounds have much lower acoustic absorption coefficients than higher frequencies. Thus, higher frequencies are more severely attenuated as they travel to the microphone membrane. A least squares fit to the data presented in Figure 4.16 reveals that the total noise varies roughly as $f^{-1.3}$. The analysis

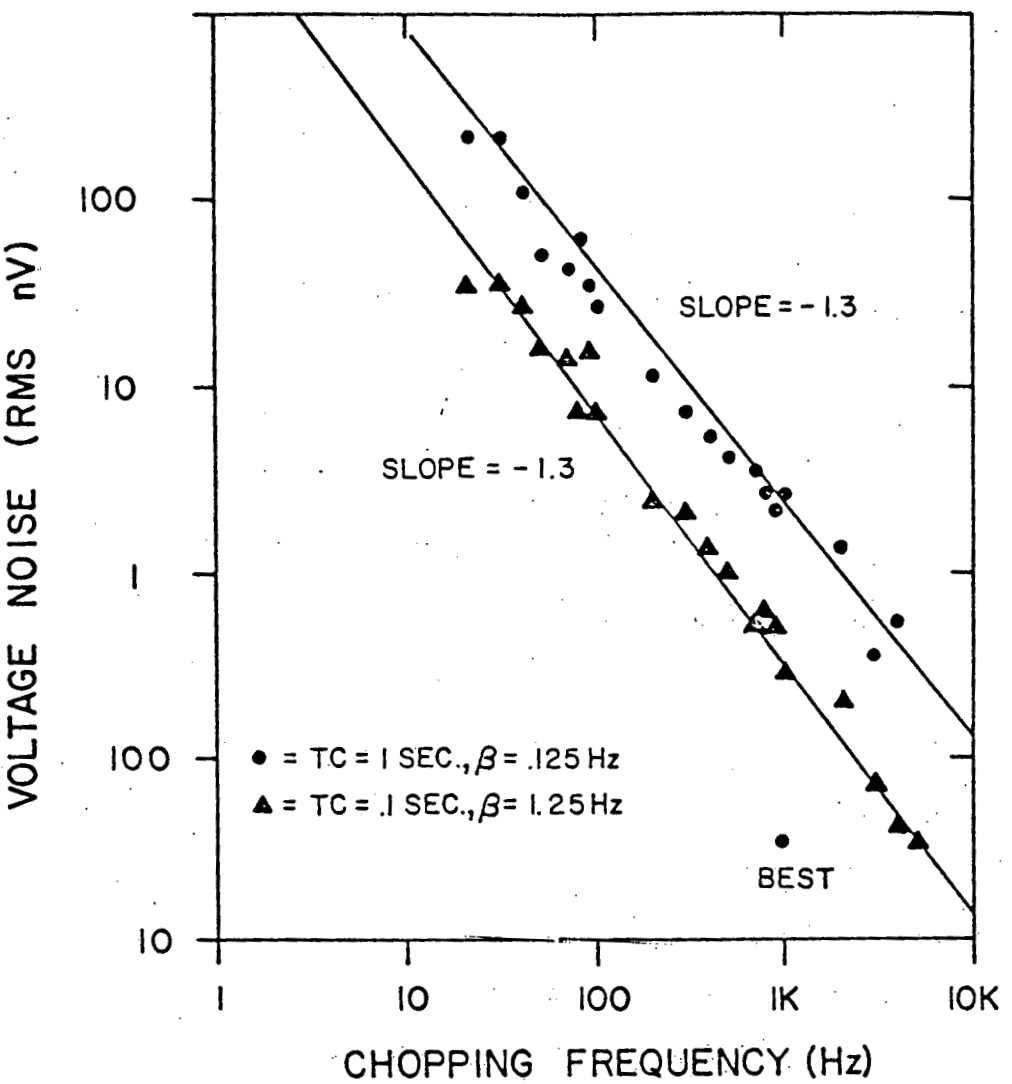

Figure 4.16. Total output noise of the photoacoustic system.

presented in (78) indicated that the photoacoustic signal will vary as f^{-1} or $f^{-1.5}$, depending on the nature of the material. Consequently, we see that in the first case, the optimum photoacoustic modulation frequency which results in the greatest signal to noise ratio will tend toward high (~100 Hz) frequencies. In contrast, if the photoacoustic signal varies as $f^{-1.5}$, the optimum frequency will be at lower modulation rates. These considerations will become extremely important when the optimum chopping frequencies are selected for the dual beam photoacoustic spectrometer and scanning systems.

It should be noted that Figure 4.16 represents data obtained on a given day at a given time. Depending on the exact time of analysis, the magnitude of the acoustic noises was found to decrease almost an order of magnitude from the values in Figure 4.16. This is illustrated in Figure 4.17 where we monitor the acoustic noise at 500 Hz as a function of time. During the quiet period, the rms noise voltage was approximately 180 nV for a bandwidth of .125 Hz. However, during the noisier five minute span, the rms signal increased by a factor of two or three. Unfortunately, efforts to locate the source of the additional noise were often unsuccessful, possibly because of the sensitivity and non-discriminatory nature of the human ear. For example, inspection of Table (82) which relates the output of the preamplifier with common noise

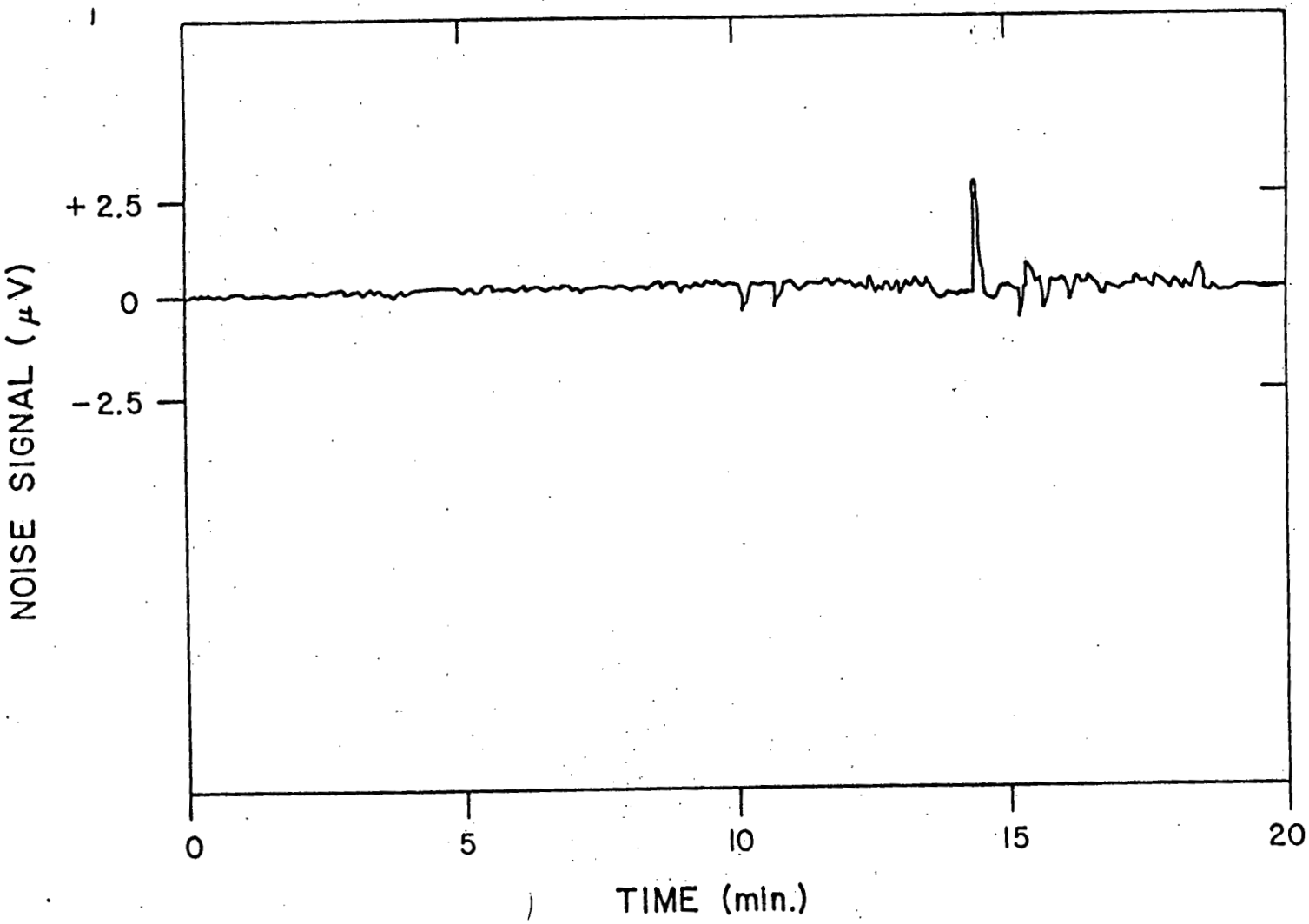

Figure 4.17. Total output noise of the photoacoustic system as a function of time.

Table 4.6. Output Amplifier Signal Levels Related to Common Noises (adapted from ref. 6.3.).

Output Signal	ΔP/P	dB	Common noise
100 nV	2×10^{-12}	-40	Brownian noise limit
10 μV	2×10^{-10}	0	Threshold of hearing
50 μV	10^{-9}	13	Quiet forest
500 μV	10^{-8}	33	Library
5 mV	10^{-7}	53	Conversational speech
50 mV	10^{-6}	73	Heavy truck
500 mV	10^{-5}	93	Pneumatic chopper
5 V	10^{-4}	113	Jet take-off (100m away)

levels, shows that a 300 nV signal would be lower than the threshold of hearing. Comparison of Table 4.5 and Figure 4.16 also gives a feel for the tremendous sensitivity of the photoacoustic apparatus used in these experiments, and a physical feeling for the magnitude of the photoacoustic effect.

4.3.4. Characterization of the Photoacoustic Signal

A block diagram of the apparatus used to characterize the photoacoustic signal is presented in Figure 4.18. The flux from a 300 mW TEM_{oo} linearly polarized CO_2 laser was amplitude modulated by a variable frequency chopper and directed onto a photoacoustic cell filled with commercial grade carbon black powder. A diagram of the cell is given in Figure 4.19 and is identical to the cells which were used to obtain the infrared photoacoustic spectra of powders, described later. The variable speed chopper was controlled by a Heathkit regulator power supply, and could be set for modulation frequencies from 10 Hz to 2 KHz using two different chopper blades. The photoacoustic signal was fed into a PAR HR-8 lock-in amplifier, and the output monitored with either a strip chart recorder, or an oscilloscope. Fluctuations in the laser power were monitored using a Scientech model 380-102 calorimeter which was placed in the beam at frequent intervals.

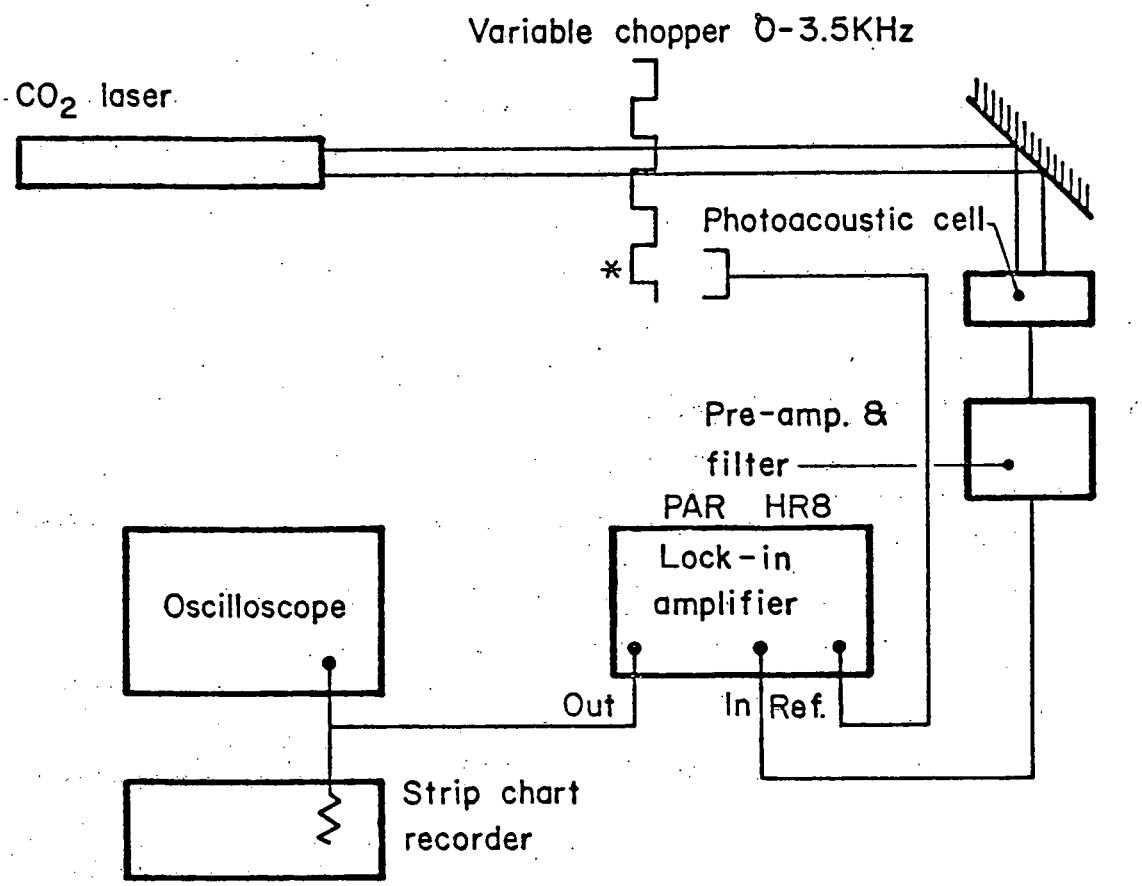

Figure 4.18. Apparatus used to characterize the photoacoustic effect.

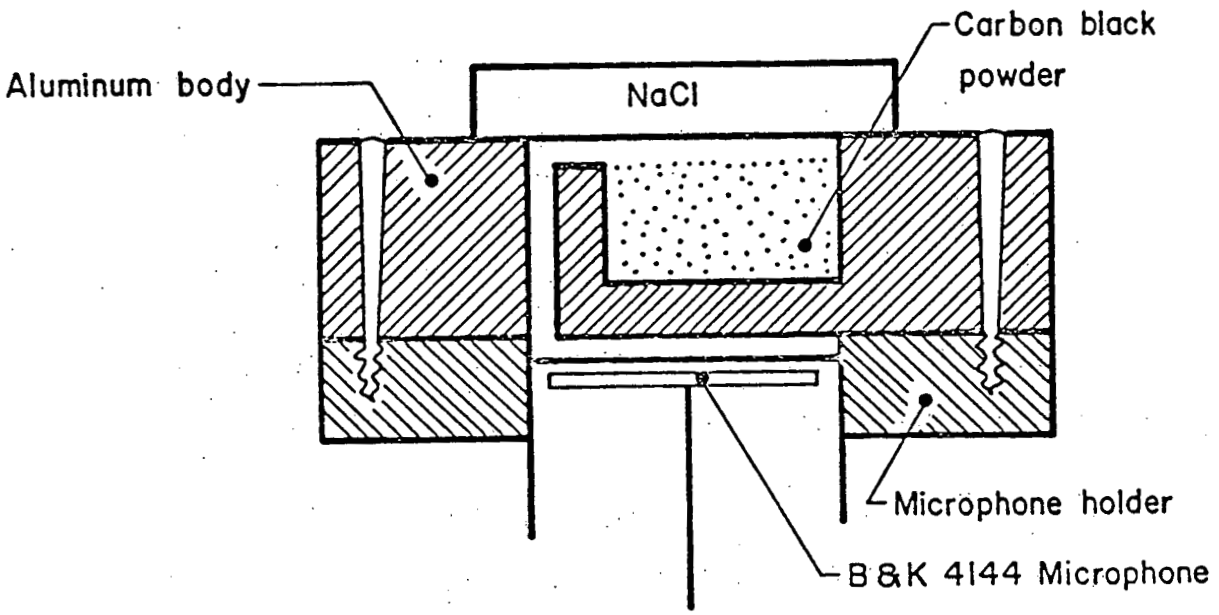

Figure 4.19. Photoacoustic cell employed for powder samples (including carbon black).

A. Frequency Response

A plot of the responsivity of the photoacoustic cell as a function of modulation frequency is presented in Figure 4.20. There are several features of interest. First and most importantly, we see that the photoacoustic amplitude decreases monotonically with frequency until 1-2 KHz, where it increases dramatically. The phase undergoes a 100 degree shift in the same region. Such behavior is strongly reminiscent of an acoustic resonance, even though the largest dimensions of the cell are much smaller than half of the 16 cm acoustic wavelength present at 1 KHz in gas at STP. However, closer inspection of the non-resonant cell design reveals that the microphone and sample chambers form a configuration known as a Helmholz resonator, which is shown in Figure 4.21. The Helmholz resonance behavior is well known in acoustics, and the resonance frequency of the cell, f_o, is given by (86).

$$f_o = \frac{\nu}{2\pi} \{ (1/V_1 + 1/V_2)\pi r^2 / (L + \pi r/2) \}^{\frac{1}{2}} \qquad 4.18$$

where V_1 and V_2 are the volumes of the microphone and sample chambers (cm^3), r is the diameter of the connecting tube (cm), and L is the length of the connecting tube (cm). For the photoacoustic cell under consideration, $V_1 = 150$ mm^3, $V_2 = 150$ mm^3, L = 11 mm, and r = .445 mm. Substitution of

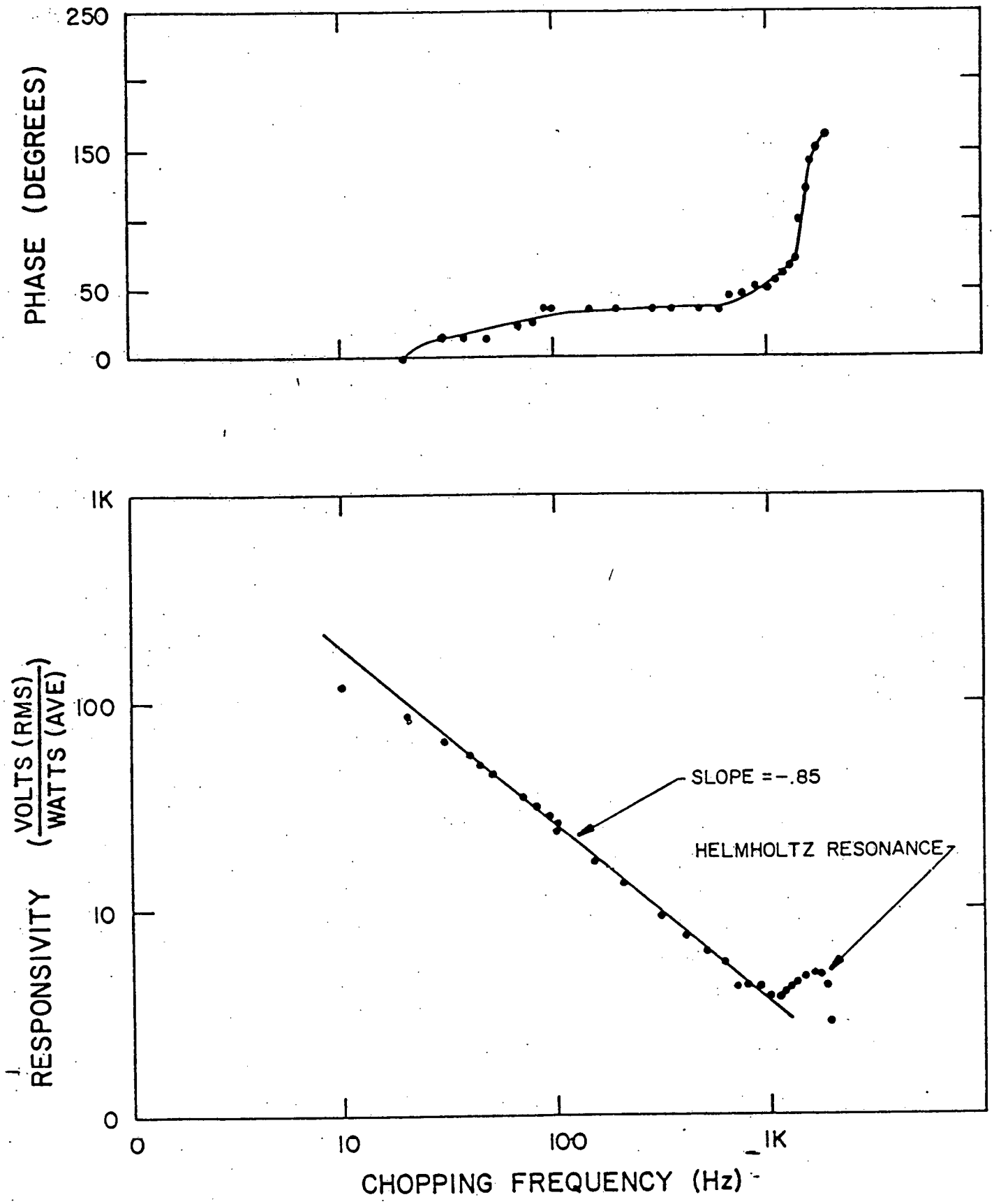

Figure 4.20. Photoacoustic cell response as a function of modulation frequency.

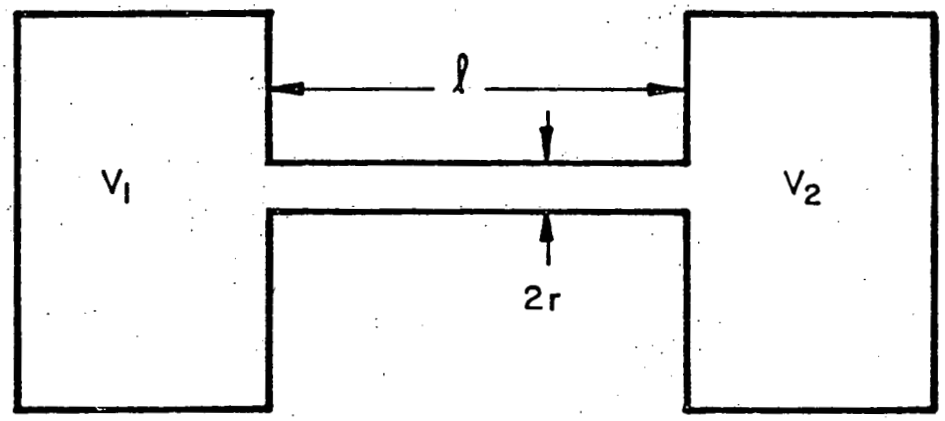

Figure 4.21. Helmholz resonator configuration geometry.

these values into equation 4.18 yields a resonance frequency of 1.36 KHz, in excellent agreement with the 1.5 KHz resonance observed.

The Helmholz resonance observed is a broad and weak effect, providing an acoustical gain at 1.5 KHz at not a factor of 3 over what might be expected in a completely non-resonant cell. As such, the analysis presented earlier for non-resonant cells may be applied with only minor modifications. It should be noted, however, that the resonance behavior may significantly effect the interpretation of photoacoustic signal dependences on the modulation frequency, especially at frequencies greater than 1 KHz.

A least squares fit to the data presented in Figure 4.20 reveals a $f^{-.85}$ frequency dependence of the photoacoustic signal for frequencies between 30 Hz and 1 KHz. This dependence is slightly less than the -1.0 dependences anticipated from theoretical analysis presented in (78) for highly opaque materials, and may be accounted for if we assume that the photoacoustic signal experiences a slight gain as a result of the tail of the photoacoustic resonance. Similar behavior has recently been observed by Fernilius (86).

At frequencies less than 30 Hz, the amplitude of the photoacoustic signal trails off from the -.85 frequency de-

pendence, and the phase again experiences a significant shift. This is not likely the result of thermal shorting from the carbon black to the window and photoacoustic cell. At 10 Hz, the thermal diffusion length in the gas is approximately 840 μm, and the acoustic piston becomes significantly larger than ℓ/g. Also, the effect of a three dimensional flow of heat may begin to appear at low frequencies, since a significant amount of heat may now be transferred to the cell walls instead of the buffer gas.

It is important to note the extremely high responsivities measured in the photoacoustic cell using carbon black. At 100 Hz, for example, the response is 25 volts rms/watt. Since carbon black exhibits strong absorption throughout the infrared, the photoacoustic cell may be thought of as a broadband room temperature wide aperture detector of infrared radiation. This fact, which we will make extensive use of in the photoacoustic spectrometer, was recognized by Freese and Teegarden (86). Their results are summarized in Table 4.6.

B. Noise equivalent power of the photoacoustic cell

The noise equivalent power (NEP) of the photoacoustic cell may be obtained by combining Figures 4.20 and 4.16 and is presented as a function of frequency in Figure 4.22. The noise equivalent power of the photoacoustic cell represents the amount of optical radiation necessary to produce

Table 4.7. Photoacoustic Detector Characteristics

Operating temperature	300K
Linear response	0 to 500 mW, limited by preamp saturation
Detector area	2.85 cm^2
Uniformity	$\pm$ 5% over entire detector
Frequency response	1Hz to ~10 KHz
Time constant	limited by chopping frequency 1.4 msec demonstrated
Responsivity (10.6 μm, 1KHz)	3.8 V/W incident upon window, constant to within $\pm$ 3% at .6328 μm and 1.06 μm.
NEP (1KHz, B=1Hz) "best"	75 nW
NEP (1KHz, B=1KHz) "best"	3.7 μW
NEP (1KHz, B=1Hz) "typical"	1 μW

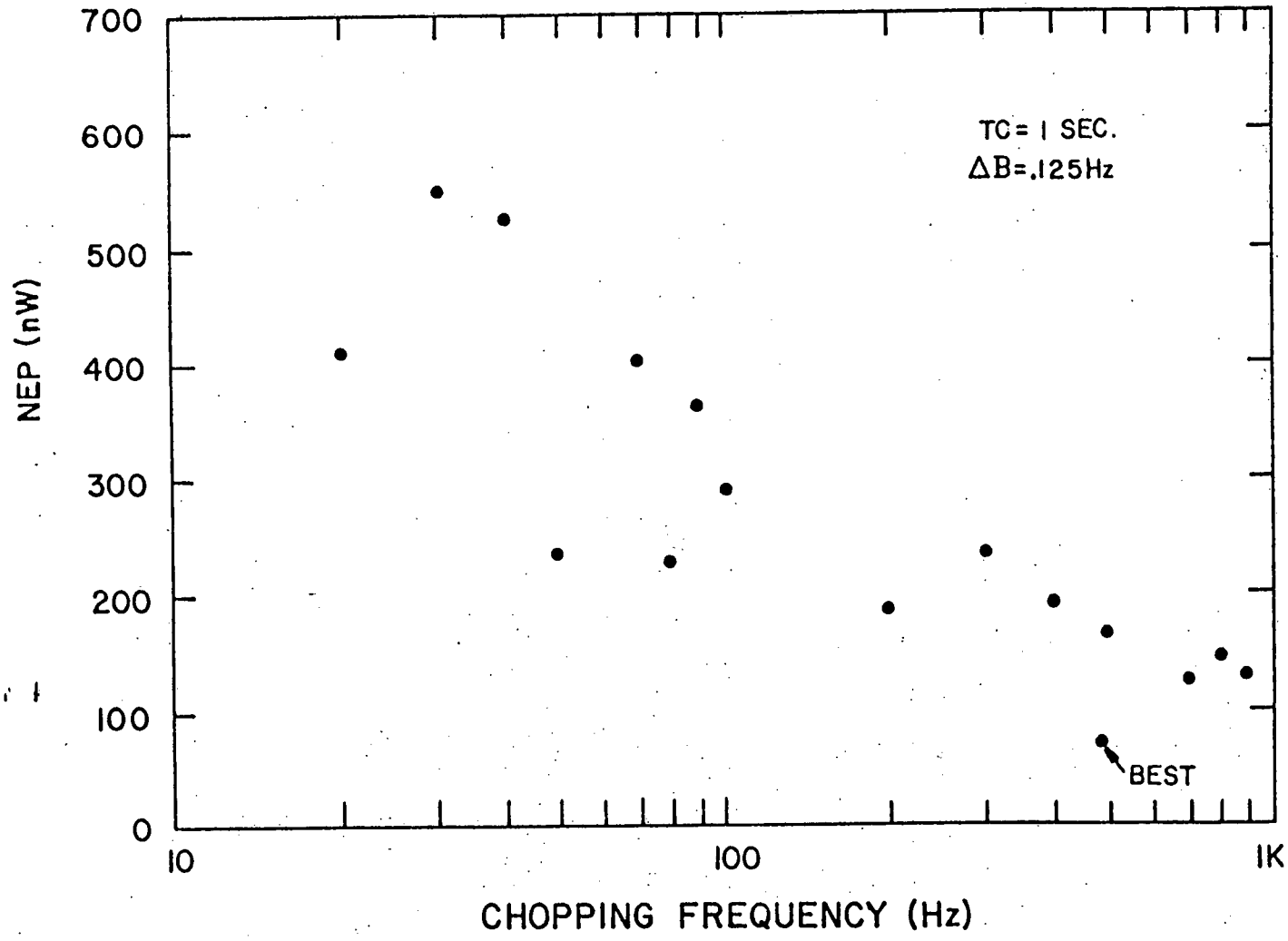

Figure 4.22. NEP of the photoacoustic detector as a function of frequency.

a 1:1 signal to noise ratio, and is important to consider since the NEP effectively sets a lower limit on the optical powers which may be used in photoacoustic investigations. In the infrared, where blackbody sources are orders of magnitude lower than their visible counterparts, the NEP is of particular importance.

Inspection of Figure 4.22 reveals that the lowest NEP is found to occur at frequencies between 100 Hz and 1 KHz. This is a result of the fact that the noise decreased as $f^{-1.3}$ while the signal only decreased as $f^{-.85}$ At higher frequencies, the vibrations of the chopper motor became excessive, and the NEP decreased. Thus, it would seem that, when given a choice, the optimum chopping frequency lies around 500 KHz for this cell.

C. Waveforms

The waveforms of the photoacoustic signal were investigated by feeding the output of the microphone directly into an oscilloscope. The resulting oscillographs as a function of frequency are presented in Figure 4.23 a-h. At 20 Hz, we see that the photoacoustic signal rises and falls in a manner characteristic of thermal excitation and de-excitation. The signal also seems to have approached saturation while the source was still on. This type of behavior would be indicative of other non-photoacoustic energy transfer mechanisms, such as thermal shorting to

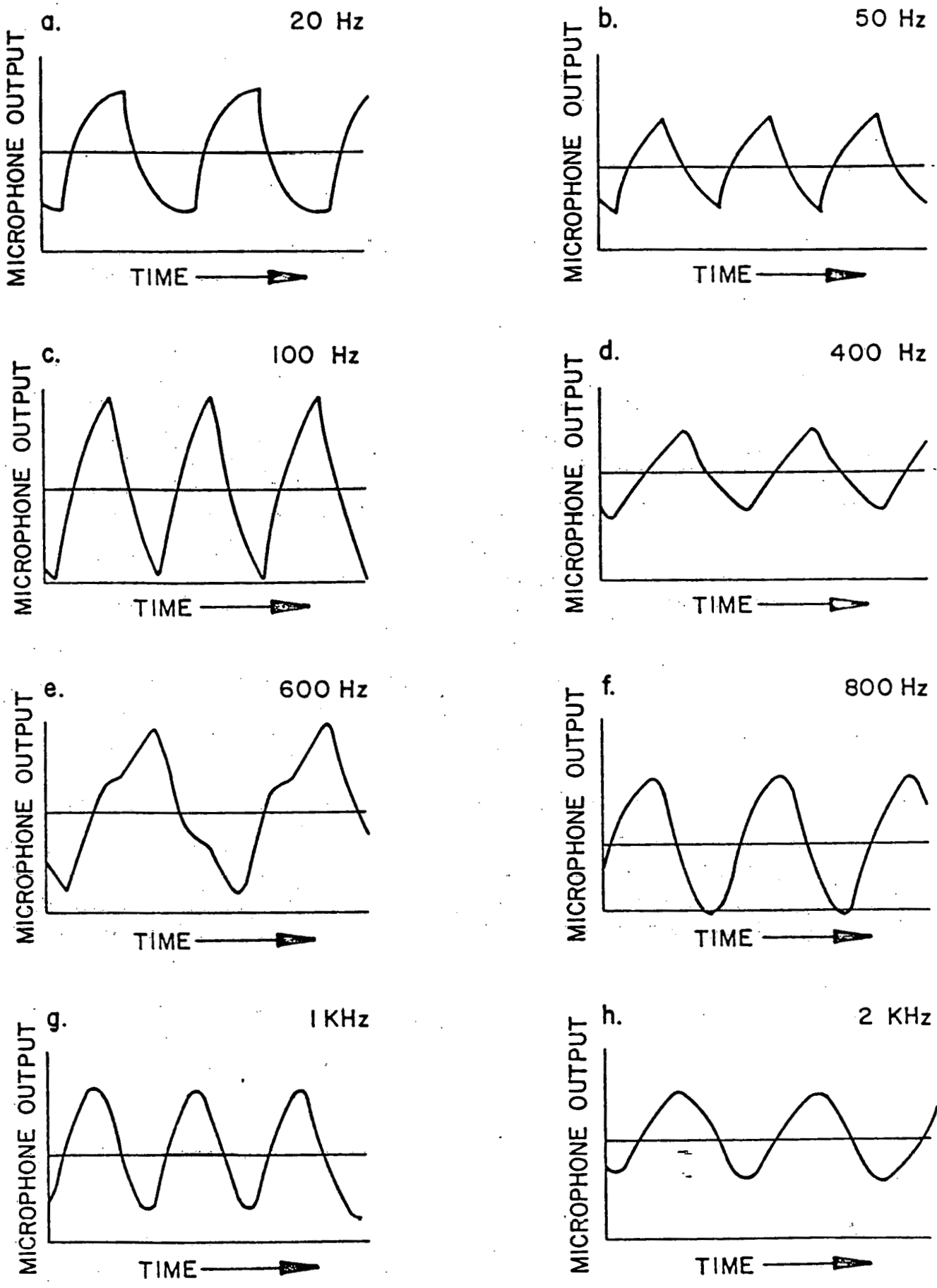

Figure 4.23. Photoacoustic signal waveforms: a)20 Hz, b)50 Hz c) 100 Hz, d)400 Hz, e)600 Hz f)800 Hz,g)1KHz, h)2KH

the photoacoustic cell. At 50 Hz, we notice that the saturation effects are nearly gone and the waveform now approximates that of a triangular wave. Thus, it would seem that the thermal shorting is no longer significant for frequencies greater than 50 Hz. This supports earlier arguments regarding the decrease in photoacoustic response at low frequencies.

Around 400 Hz, on the triangular waveform has started to degrade, and there is evidence to suggest that an additional signal at approximately three times the modulation frequency has been added. At 500 Hz, the behavior is not only magnified, but the 3f signal also appears to have been phase shifted with respect to the fundamental. This initially unexpected behavior may be explained by considering the 3f Fourier component of the incident square wave pulse. At 400 Hz, 3f = 1.2 KHz and the Fourier component encounters the Helmholz cell resonant frequency. As such, it is amplified, and shifted in phase. At 600 Hz, 3f = 1.8 KHz, and the Fourier component not only experiences acoustic gain, but its phase has been shifted by 100° from the fundamental. As a result, the total waveform is noticeably asymmetric at 600 Hz.

At 800 Hz, we notice that the 3f component has almost completely disappeared, a result which may be expected since the Fourier component is beyond the cell resonances. At 2 KHz, only the fundamental frequency

component remains, since the other Fourier components are all too high for the microphone to respond. Thus, the total waveform is nearly a perfect sinusoid.

D. Temporal response

The speed of the photoacoustic response was tested by inserting a rotating shutter in the optical beam and monitoring the output of the lock-in amplifier with an oscilloscope, as is shown in Figure 4.24. The speed of the rotating shutter was measured independently using a Molectron P-1 pyroelectric detector, and was found to have a 10% to 90% risetime of 100 μsec. The modulation frequency was set at 1.3 KHz, and the lock-in time constant set at 1 msec at 6 db/octave. The output of the lock-in as a function of time is shown in Figure 4.25. The 10% to 90% risetime was found to be 1.4 msec. At lock-in time constants faster than 1 msec, the output of the amplifier fluctuated dramatically due to the 1.8 KHz modulated signal. Thus, we see that the speed of response for the entire lock-in photoacoustic detection system is limited to times less than the period of the modulation frequency. This fact will be useful in the next chapter, where we consider photoacoustic scanning rates.

E. Linearity

The linearity of the photoacoustic signal was examined by inserting a wire grid polarizer in the polarized

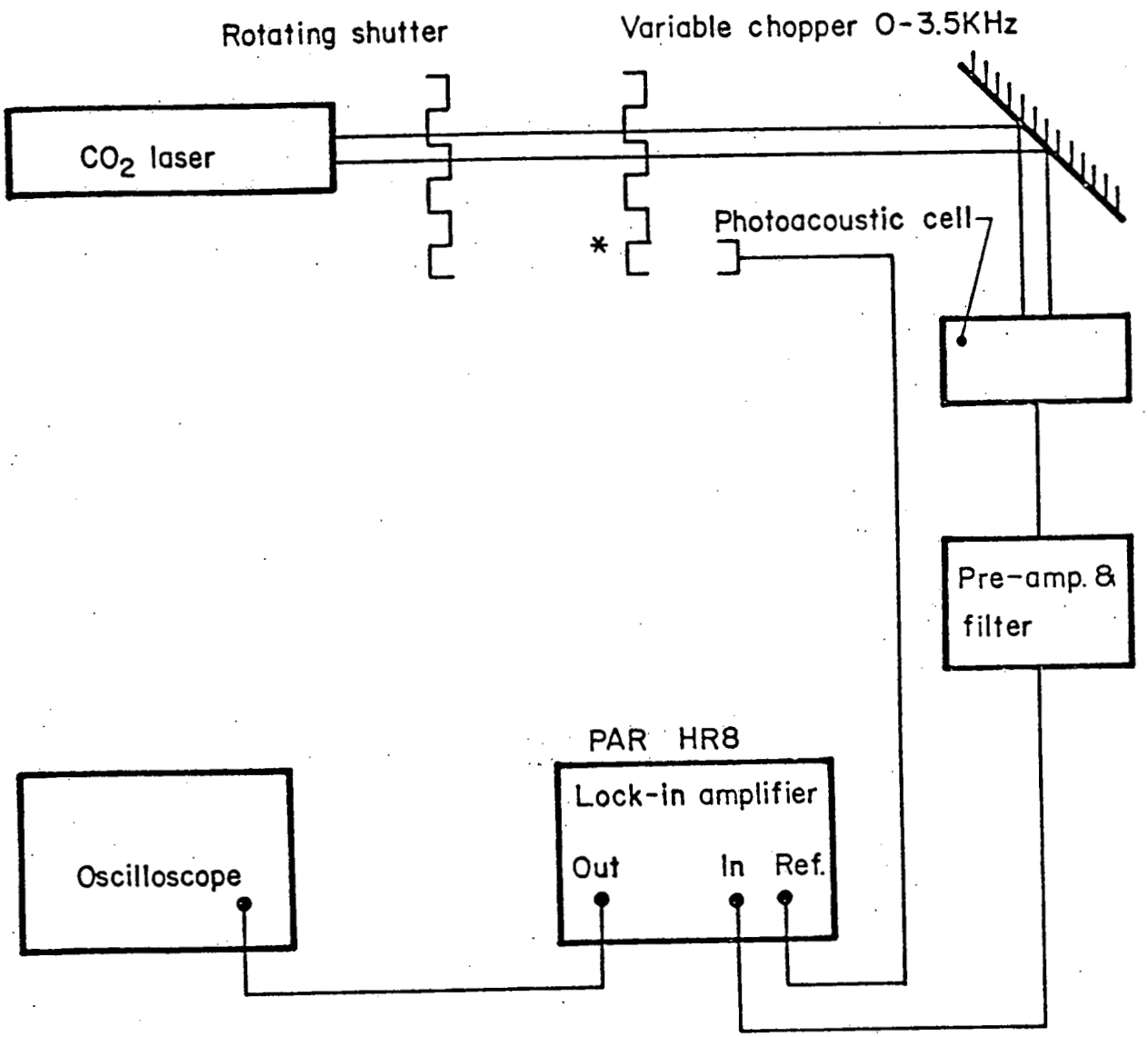

Figure 4.24. Photoacoustic detector temporal response apparatus.

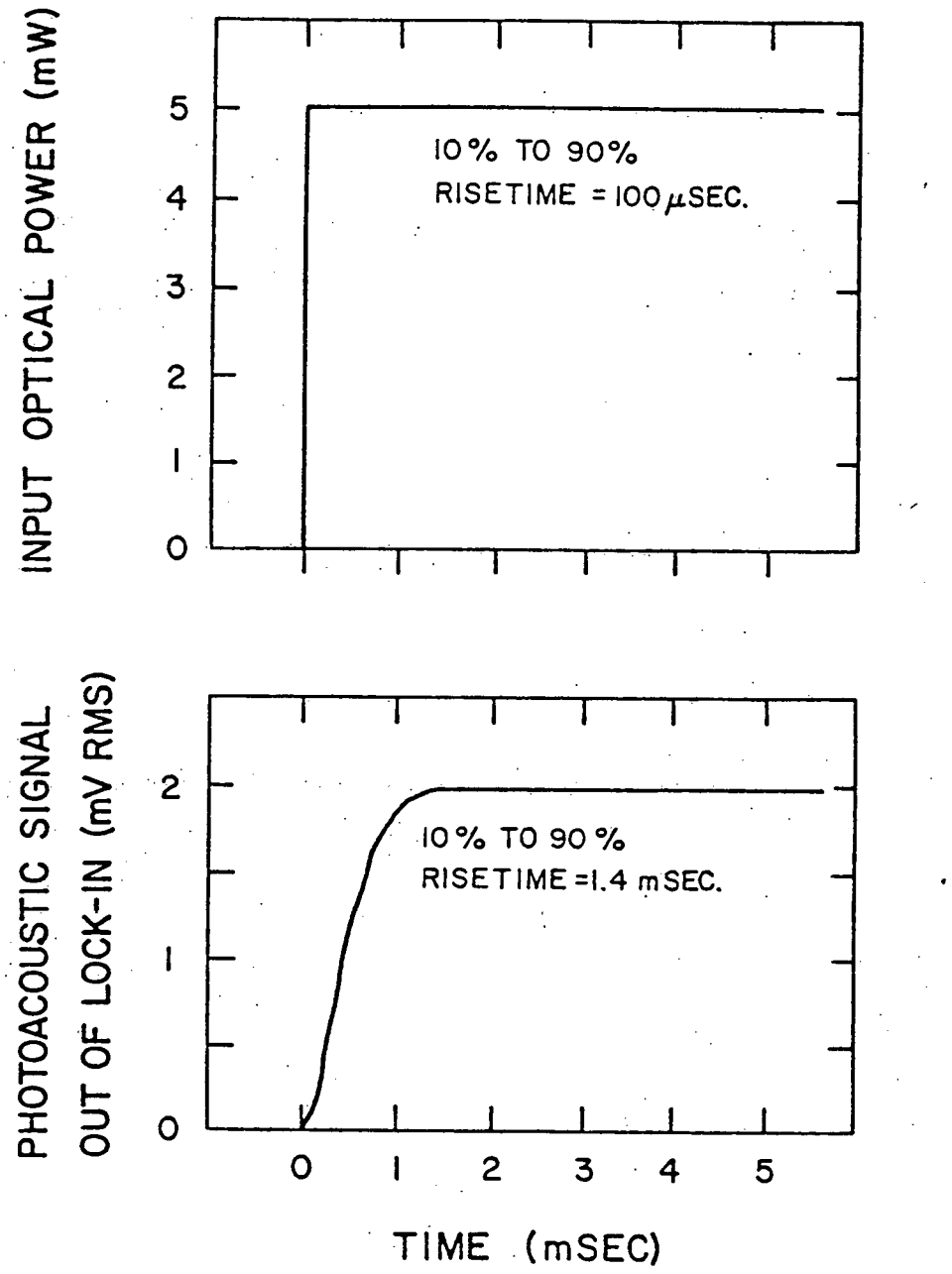

Figure 4.25. Photoacoustic detector temporal response.

CO_2 beam, and monitoring the output of the lock-in as a function of incident laser power. The results are shown in Figure 4.26 for laser powers up to 500 mW. Inspection of Figure 4.26 shows that the photoacoustic signal is completely linear with power within experimental error. This indicates that the sample is not being heated up to a significant amount above ambient temperature, in agreement with our theoretical predictions presented in (78). These results also imply that, up to powers of ~500 mW, non-linear absorption mechanisms do not play a significant role in carbon black powder at 10.6 μm.

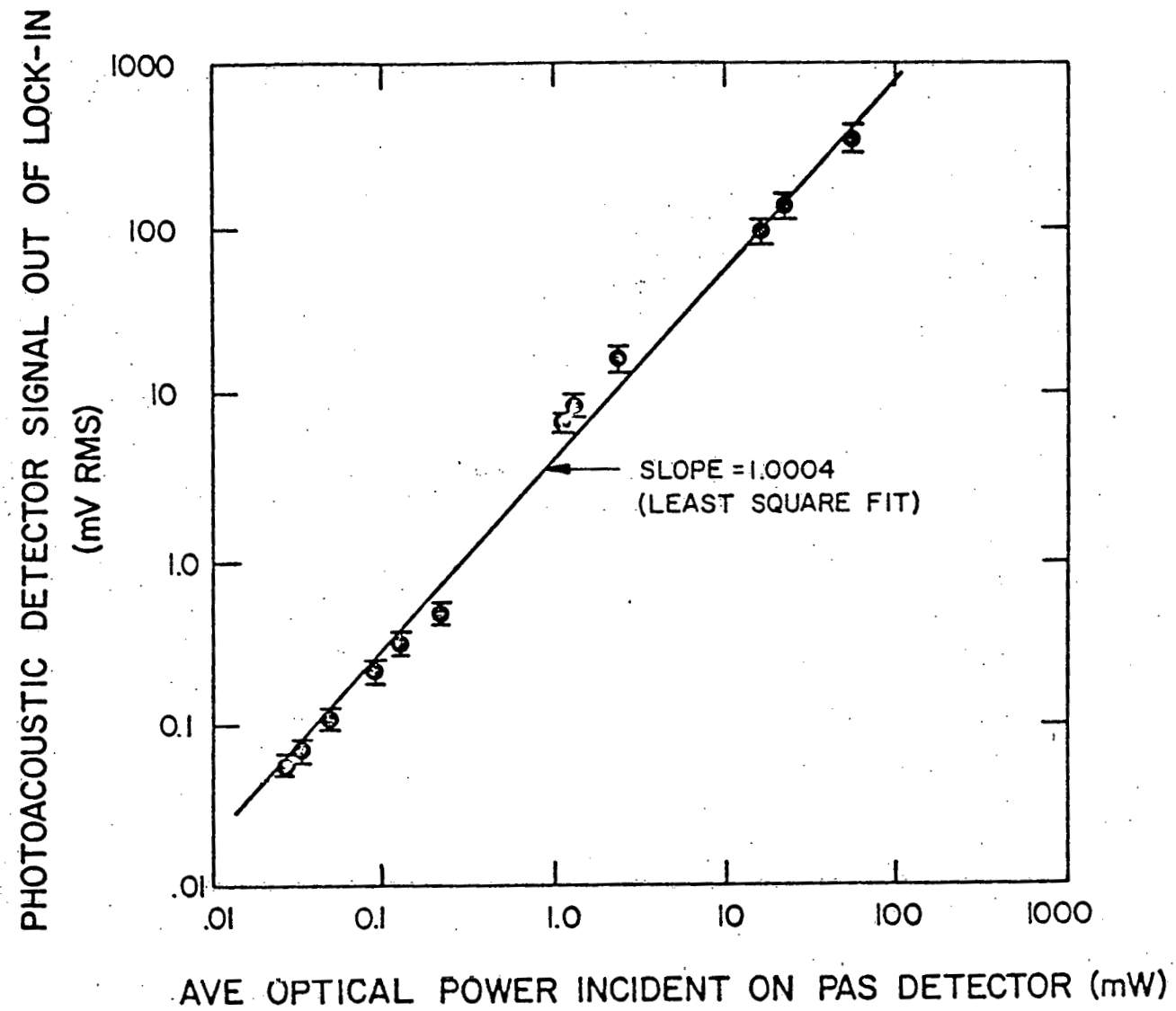

Figure 4.26. Photoacoustic cell response as a function of incident optical power.

V. RESULTS

5.1. Densification of $CdCr_2Se_4$

In this section the densification of $CdCr_2Se_4$ will be described and results presented. Densification of powders can occur by several mechanisms, either concurrent and sequential. Also, three stages of densification can be distinguished as shown in Figure 5.1.

Figure 5.1 shows a typical compaction curve during hot-pressing of $CdCr_2Se_4$ with a particle size <1μm. The first region (1) is referred to as the initial stage, where densification occurs non-isothermally and isobarically between 350 and ~710°C. Region II is the intermediate stage at constant temperature and pressure (~80MPa), and the third, region III, is the final stage of densification at the highest temperature ($T_{max} \simeq 750^{\circ}C$) and pressure ($P_{max} \simeq$ 350MPa).

5.1.1. Initial Stage

During the initial stage of hot-pressing, after the clamping pressure has been applied, the temperature is increased linearly to the final hot-pressing temperature.

During the heating period, rearrangement and fragmentation of the particles occurs. The densification rate or shrinkage rate of $CdCr_2Se_4$, $\dot{\varepsilon}$, during the initial stage is greatly enhanced by the presence of selenium as shown in Figure 5.2. Here the initial stage compaction of two samples with different selenium concentration is shown. The increased

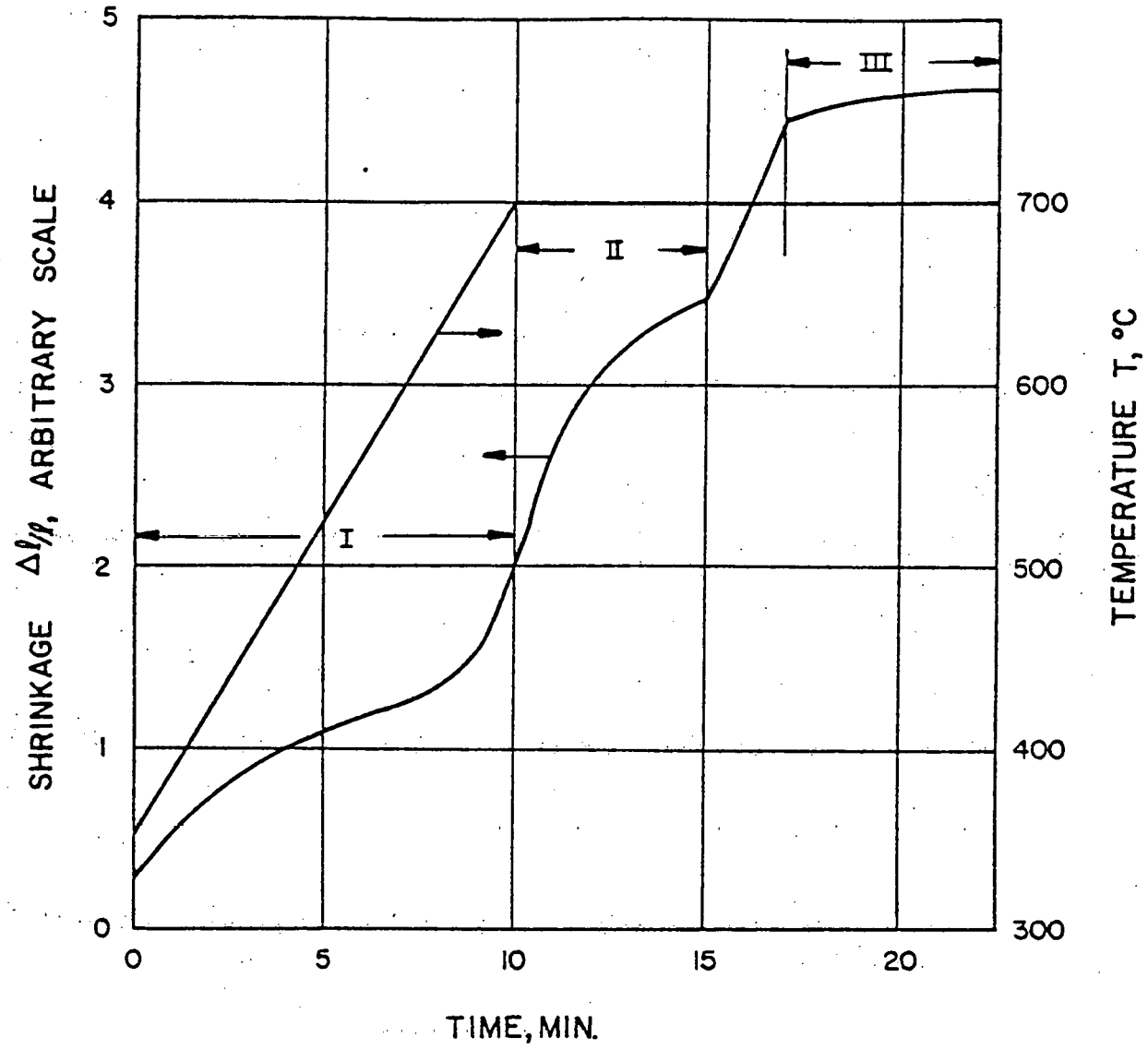

Figure 5.1. Typical shrinkage vs time curve for $CdCr_2Se_4$ showing three stages of densification.

densification rate of sample a is attributed to a selenium liquid phase at 217°C = T ≤ 685°C. Liquid selenium facilitates the rearrangement of the particles and therefore acts as a lubricant. At T ≥ 500°C selenium has a vapor pressure of $\geq 4.3 \times 10^3$ torr and it begins to evaporate rapidly. This leads to the decrease in densification rate as indicated by plateau A in Figure 5.2. Also, thermodynamic considerations of the pseudo-binary system $CdCr_2Se_4$:Se rule out the possibility of the reaction of selenium with $CdCr_2Se_4$ to form a liquid phase since this does not occur until about 890°C (16). Therefore during the initial stage densification does not occur by a liquid phase mechanism but by a rearrangement and fragmentation of the powders.

The absence of selenium in the virgin powders resulted in a decrease in densification rate and final density at the end of the initial stage. A decrease in densification rate is also observed in samples hot-pressed at lower clamping pressures, as expected, See Figure 5.3. It has been observed that more selenium evolves from the powder at lower clamping pressures. In samples free of a selenium liquid phase, fragmentation by brittle fracture is believed to occur in all powders as it is observed in hot-pressed single crystals with a particle size 0.1-1.0mm, Figure 5.4. (Fragmentation during the initial stage is detected by a "clicking noise" only in samples without free selenium).

Fine powders (<1μm) are found to have lower densities

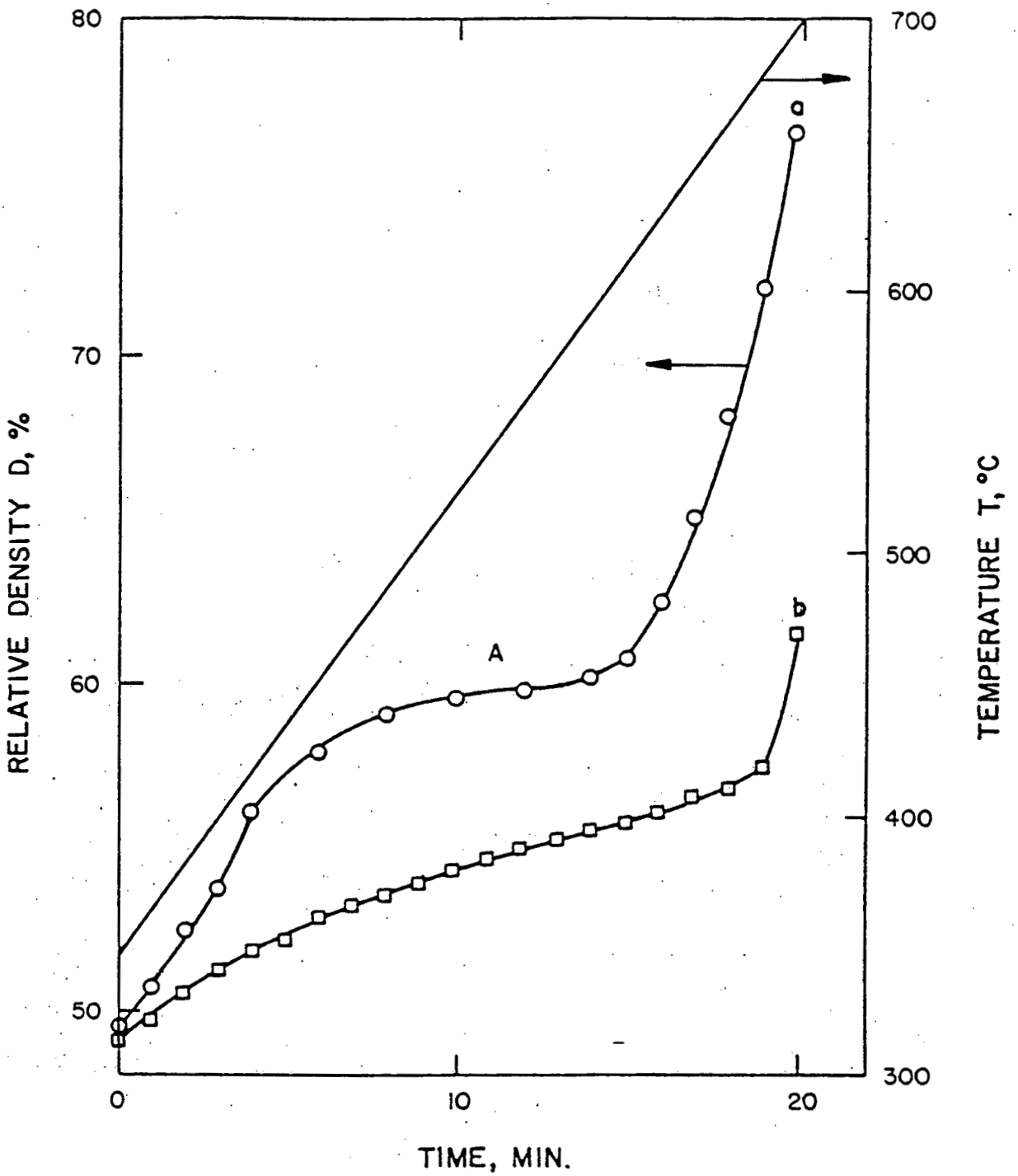

Figure 5.2. Effect of selenium on the densification behavior of $CdCr_2Se_4$ (p.s. $\leq$ 1μm) during the initial stage; (a) virgin powder containing selenium and (b) excess selenium was removed in flowing He (99.999% pure) gas at 400°C for 2 hours.

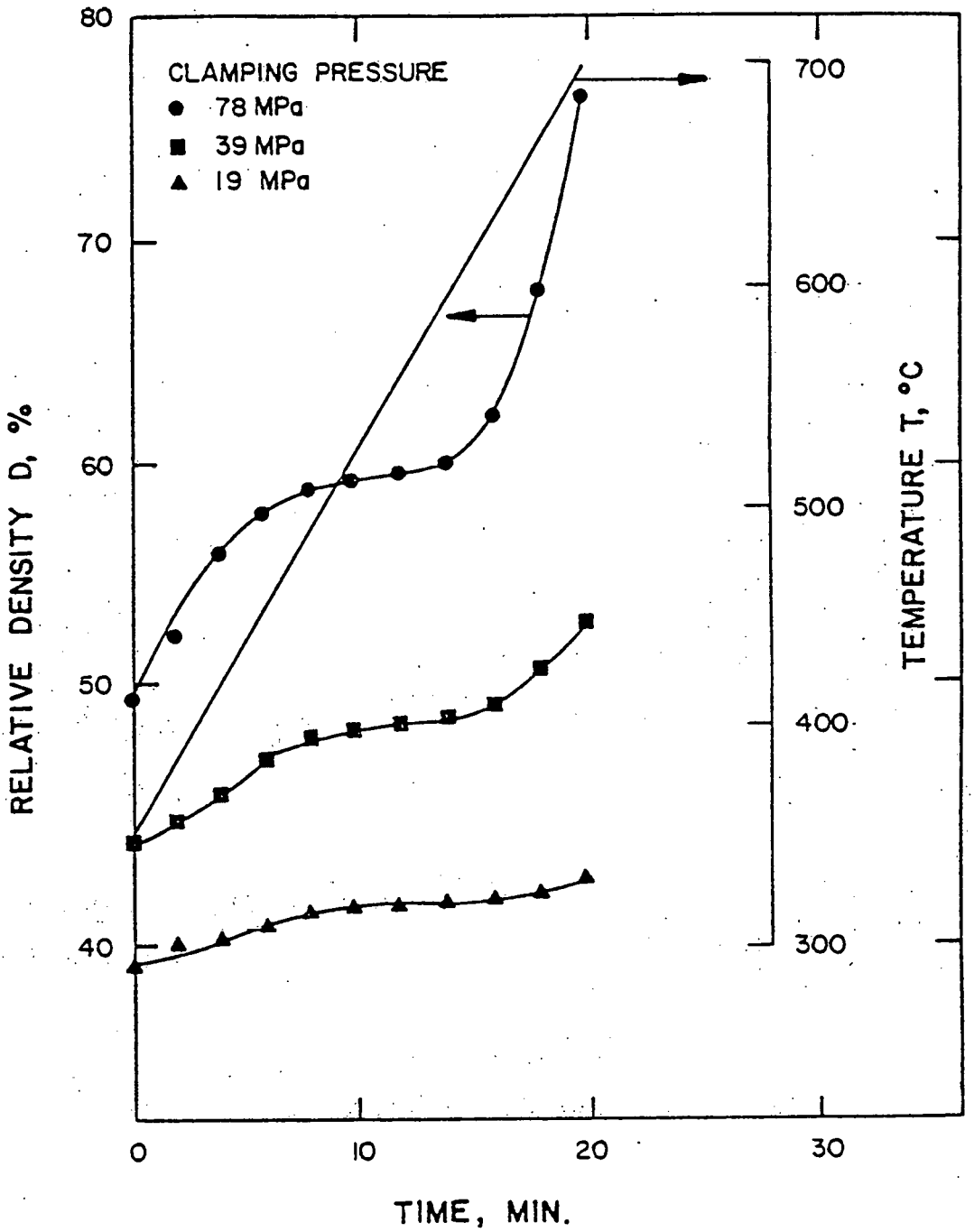

Figure 5.3. Relative density, D, of $CdCr_2Se_4$ (p.s. < 1μm) during the initial stage as a function of clamping pressure.

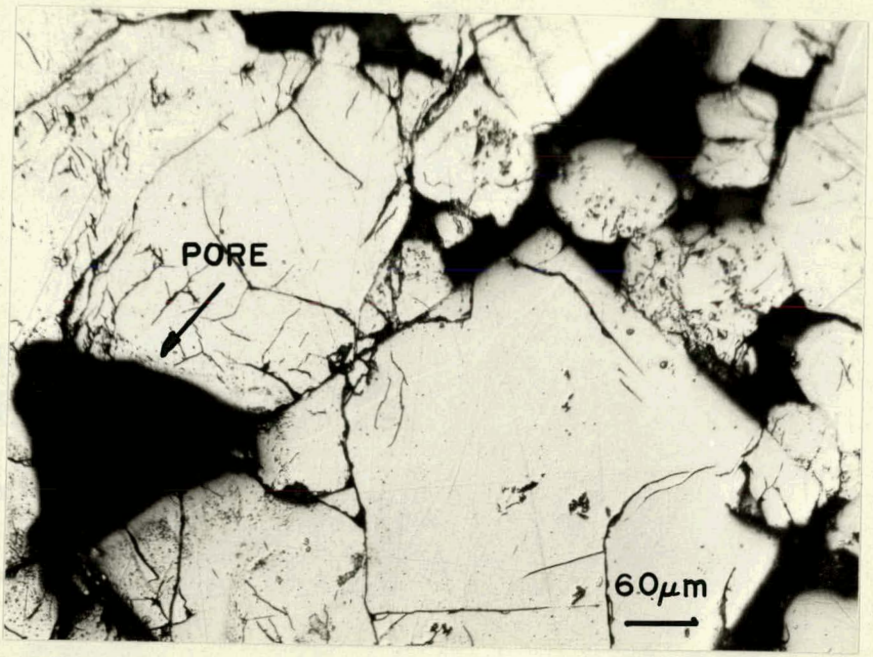

Figure 5.4. Microstructure of hot-pressed $CdCr_2Se_4$ single crystals.

throughout the initial stage in comparison to the powders with a p.s. $\leq$ 20μm and 10^2 - 10^3μm, Figure 5.5. However, the pure powders have higher densification rates because of the larger number of interparticle contacts and the higher surface free energy term γ/r to the driving force.

In conclusion, selenium is found to enhance the densification rate of $CdCr_2Se_4$ during the initial stage and fine powders densify at higher rates during this stage. The coarse powders have higher initial densities but their densification rate goes to zero after the first few minutes implying the absence of high surface reactivity. However, although selenium increases the densification rate and decreases the amount of decomposition, as will be seen in Section 5.2.2, it cannot be used as an inhibitor of decomposition and to increase the densification rate because it is deleterious to the optical properties.

5.1.2. Intermediate Stage

During the intermediate stage of densification the powders have relative densities ranging from 50% to 80% and densify at rates ranging from 10^{-4} to 10^{-5} per second depending on the particle size, temperature and applied pressure. Figure 5.5 shows that the relative density at the end of the intermediate stage increases with decreasing particle size. Also Figure 5.6 shows that densification at $T > 650°C$ is a function of temperature.

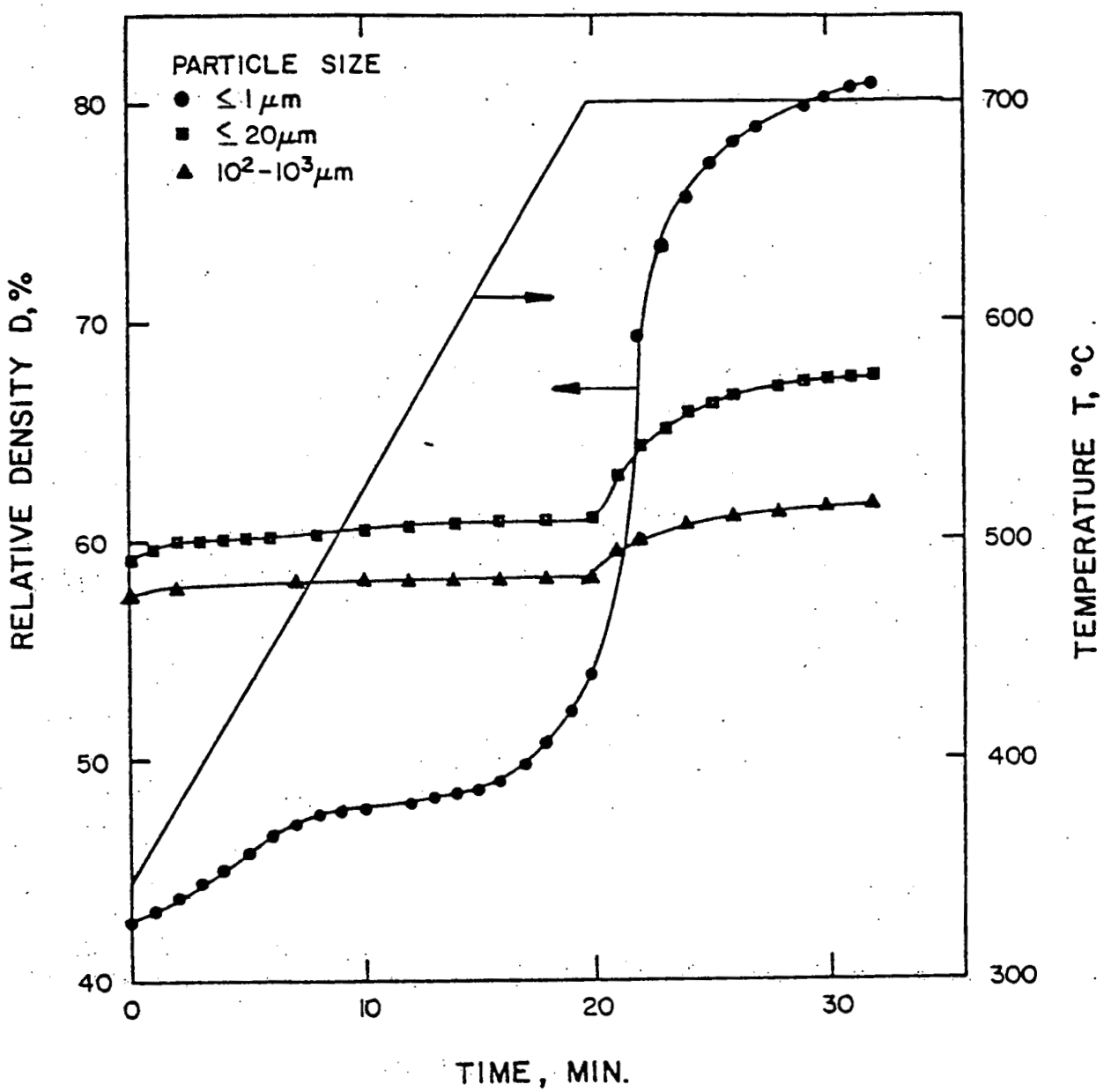

Figure 5.5. Relative density, D, of $CdCr_2Se_4$ during the initial and intermediate stages of densification for three particle sizes.

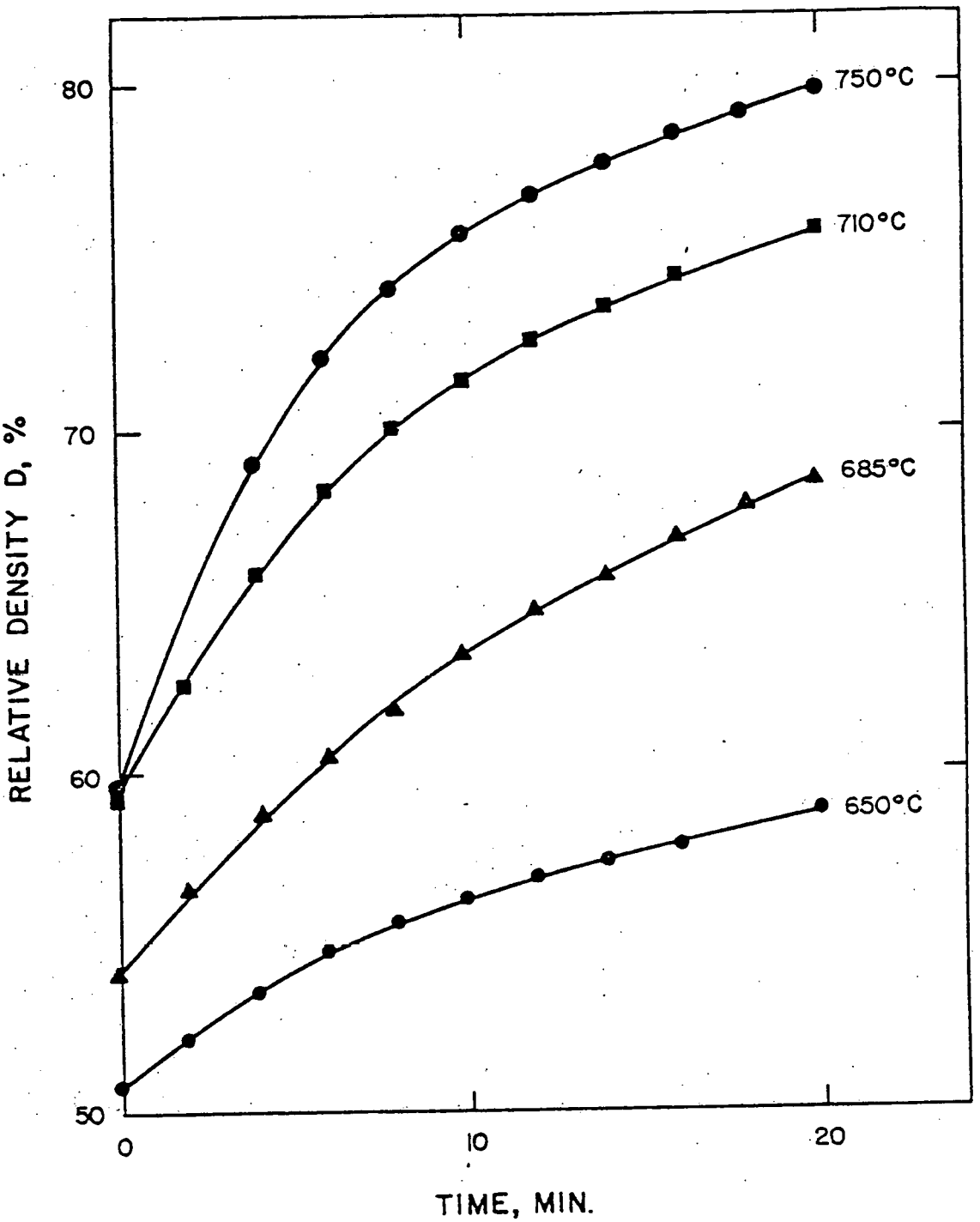

Figure 5.6. Relative density, D, of $CdCr_2Se_4$ (p.s. $\lesssim$ 1μm) during the intermediate stage of densification at T = 650°C, 685°C, 710°C, and 750°C.

It is found that during this stage, decomposition of $CdCr_2Se_4$ into the binary phases occurs according to Equation 5.1a,b

$$CdCr_2Se_4(s) \xrightarrow{700°C} Cd_{1-x}Cr_2Se_{4-y}(s) + xCd(g) + y/2Se_2(g) + yV''_{Se} + xV^{\cdot\cdot}_{Cd} \qquad 5.1a$$

$$xCd(g) + y/2Se_2(g) \xrightarrow{\sim 700°C} xCdSe(s) + \tfrac{1}{2}(x-y)Se_2(g) \qquad 5.1b$$

The amount of decompositon is found to be a function of relative density at 700°C as shown in Figure 5.7. As the relative density increases the amount of second phase decreases. In samples with relative densities greater than 75% the second phase concentration is too low to be detected by x-ray diffractometry. Decompositon occurs in all samples hot-pressed with an initial particle size $\geq 5\mu m$ under all hot-pressing conditions in the absence of a selenium vapor pressure. The excessive decomposition in large particle size powders is attributed to the presence of large voids at all stages of densification, even during the final stage at $D > 90\%$. Figure 5.8 shows the x-ray diffraction pattern of $CdCr_2Se_4$ powder and hot-pressed, $CdCr_2Se_4$.

The decomposition mechanism of $CdCr_2Se_4$ during hot-pressing was verified by annealing experiments of the powders and the hot-pressed samples. $CdCr_2Se_4$ powder and hot-pressed samples were annealed in a continuous vacuum and sealed ampules at $500°C \leq T \leq 700°C$. These

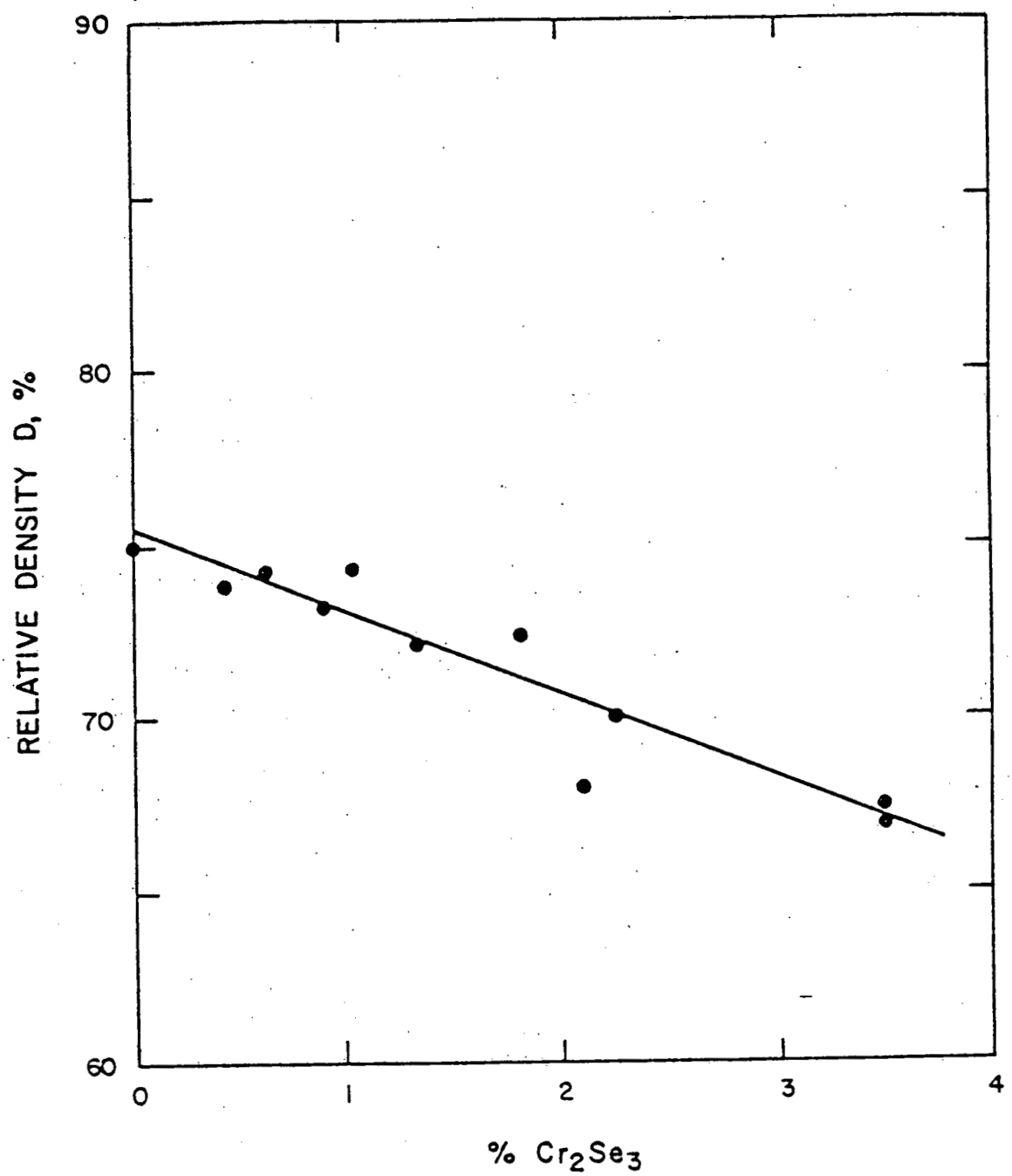

Figure 5.7. Relative density, D, of $CdCr_2Se_4$ (p.s. ≤1μm) at the end of the intermediate stage vs % Cr_2Se_3 ($I(101)Cr_2Se_3/I(440)$ $CdCr_2Se_4$).

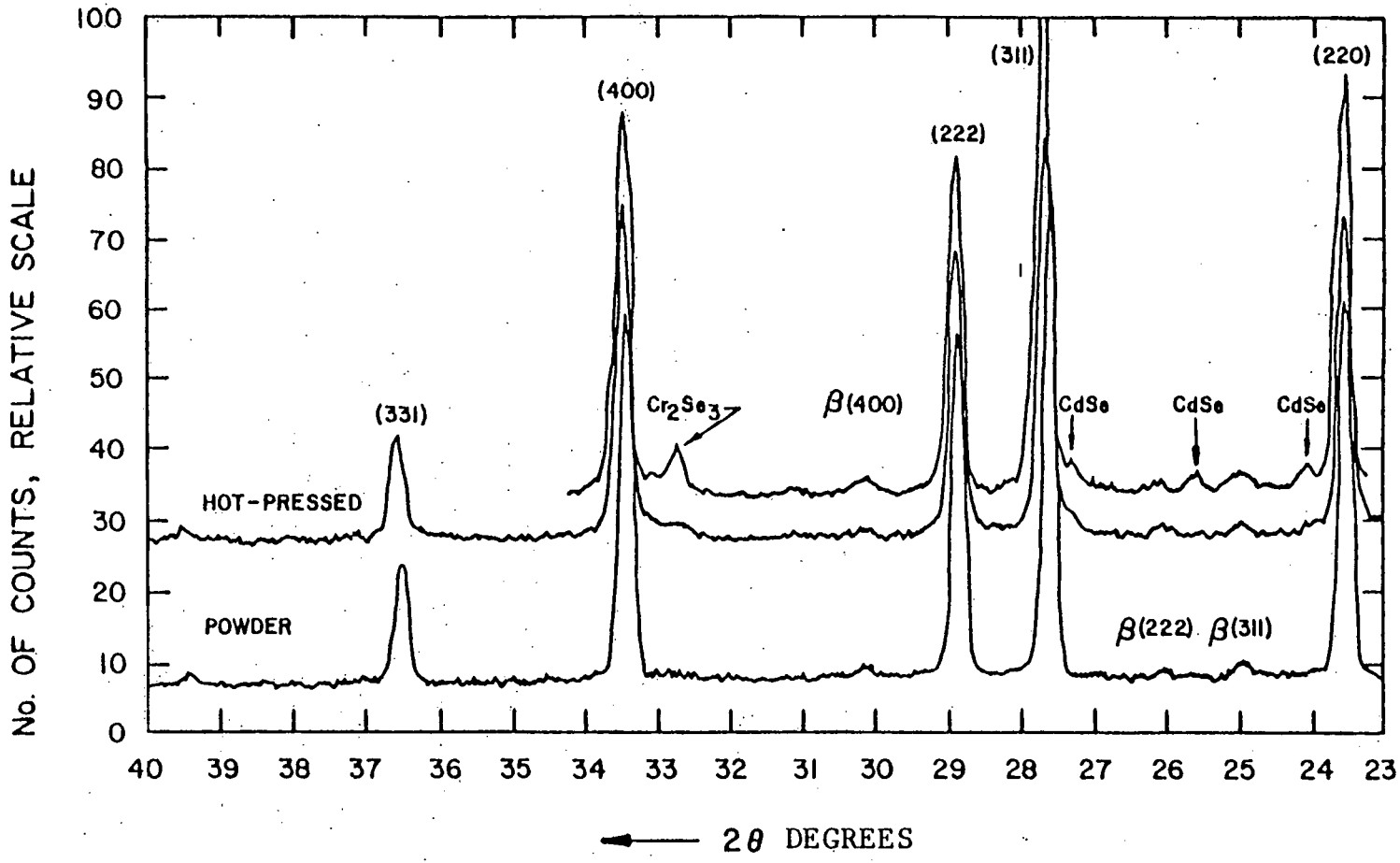

Figure 5.8. X-ray diffraction pattern of $CdCr_2Se_4$ powder and hot-pressed $CdCr_2Se_4$ at small 2θ values.

experiments showed that selenium and cadmium sublimed individually onto the cold parts of the firing tube in a continuous vacuum. In the sealed ampules selenium and cadmium reacted to form CdSe after evaporation at the cold ends of the ampule. X-ray diffractometry of annealed powders and hot-pressed $CdCr_2Se_4$ always showed the presence of the spinel phase and Cr_2Se_3 but very little CdSe thus indicating that selenium and cadmium evaporate individually and not as CdSe.

Figure 5.9a,b shows that decomposition of $CdCr_2Se_4$ occurs between large grains. Also, once decomposition takes place, unless there is a selenium vapor pressure to drive Equation 5.2

$$CdCr_2Se_4 \underset{+Se}{\rightleftharpoons} CdSe(s) + Cr_2Se_3(s) \qquad 5.2$$

to the left, long densification times during the final stage do not re-react the binary phases into the spinel phase. Therefore the presence of second phases can only be reduced by trying to achieve higher densities at the end of the intermediate stage for submicron powders.

Figure 5.10 shows an x-ray spectrum of CdSe at a grain intersection as shown in Figure 5.11. Figure 5.12 shows the x-ray spectrum of the $CdCr_2Se_4$ surface for comparison purposes. Cr_2Se_3 was not observed at grain boundary intersections and was not observed in the microstructure except in highly decomposed samples and in samples highly etched in boiling 70%HNO_3. Figure 5.13a,b shows an

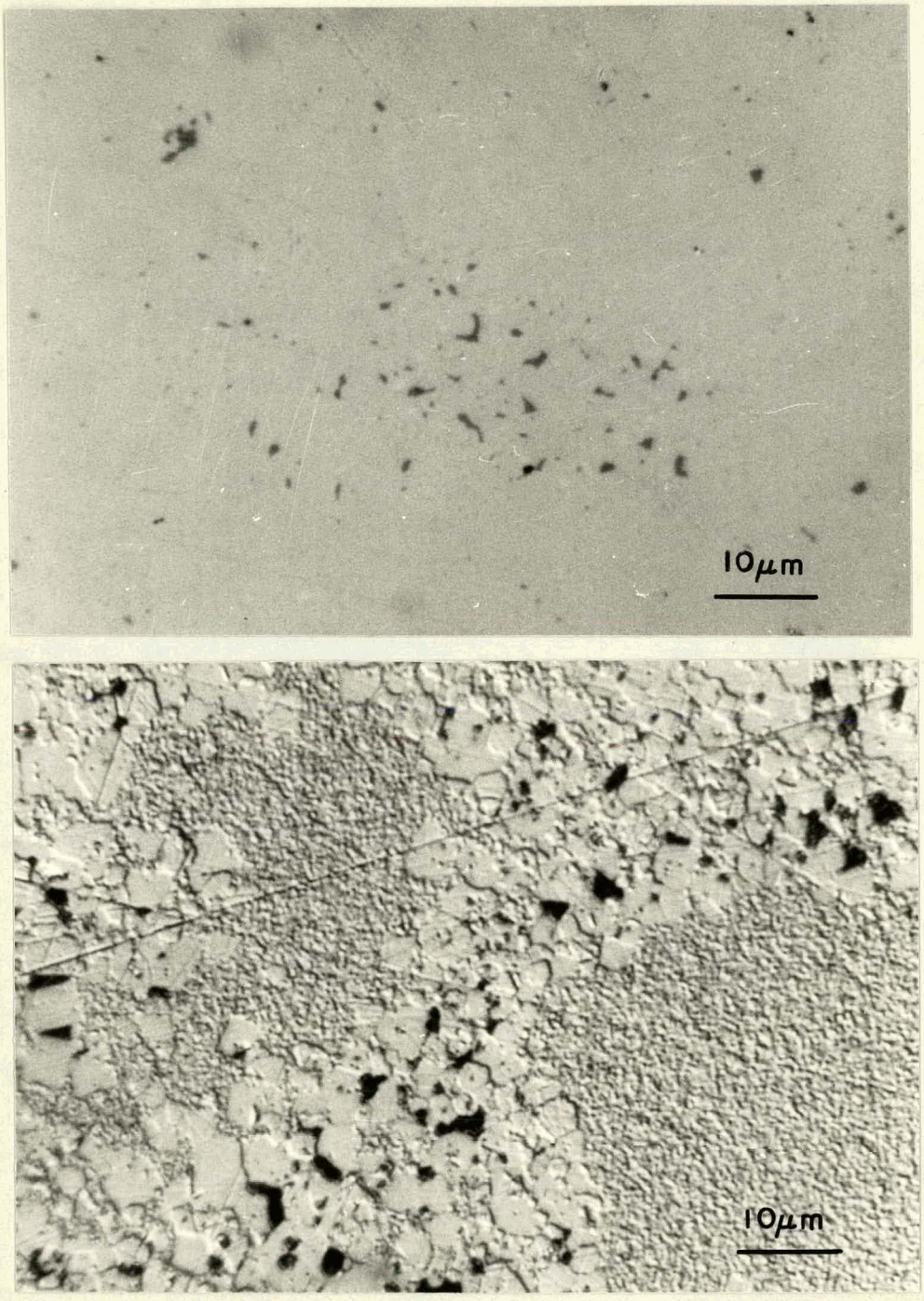

a

b

Figure 5.9. Optical micrographs of (a) polished surface of hot-pressed $CdCr_2Se_4$ (p.s. ≤ 5μm) and (b) of the etched surface in 70% HNO_3+H_2O_2 at room temperature.

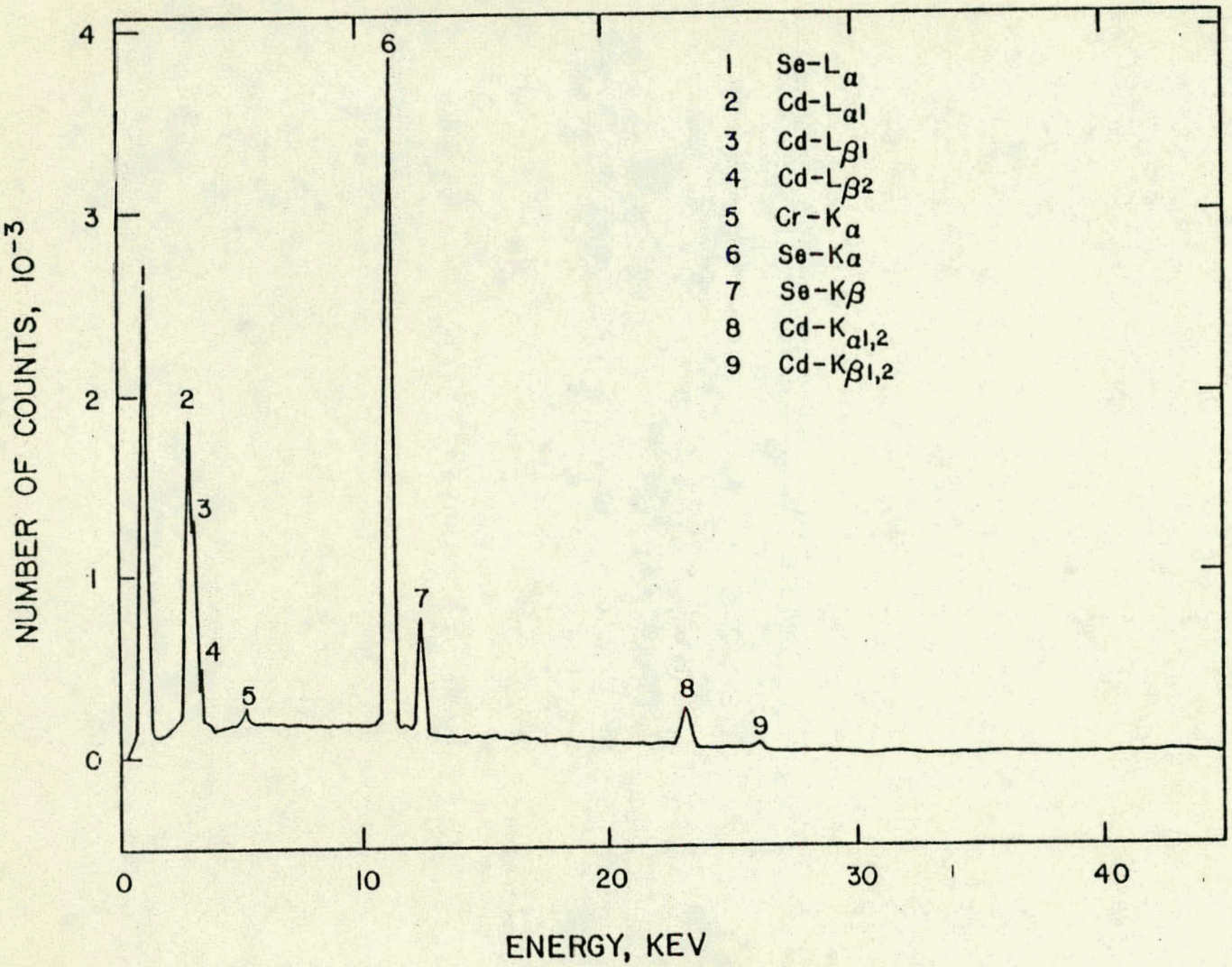

Figure 5.10. X-ray spectrum of CdSe in hot-pressed $CdCr_2Se_4$.

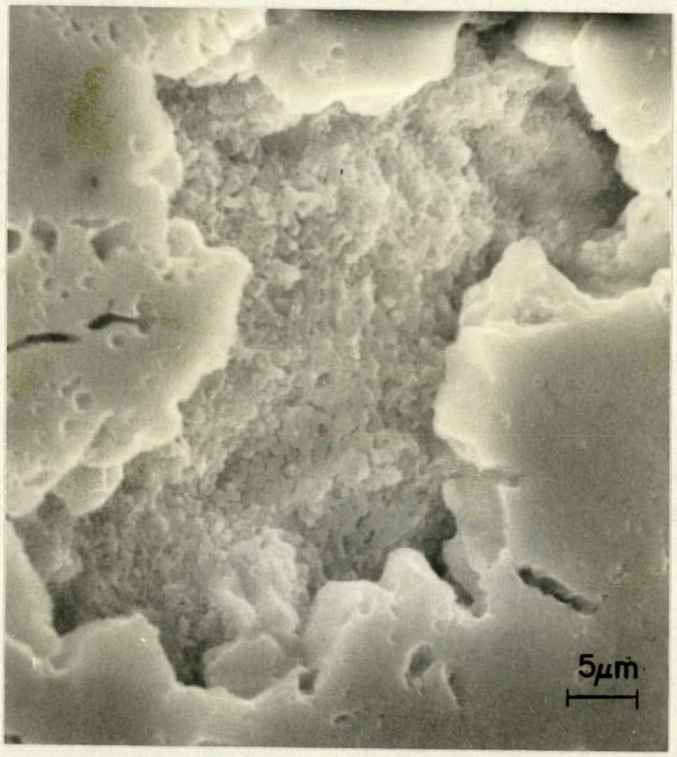

Figure 5.11. SEM micrograph of CdSe in hot-pressed $CdCr_2Se_4$.

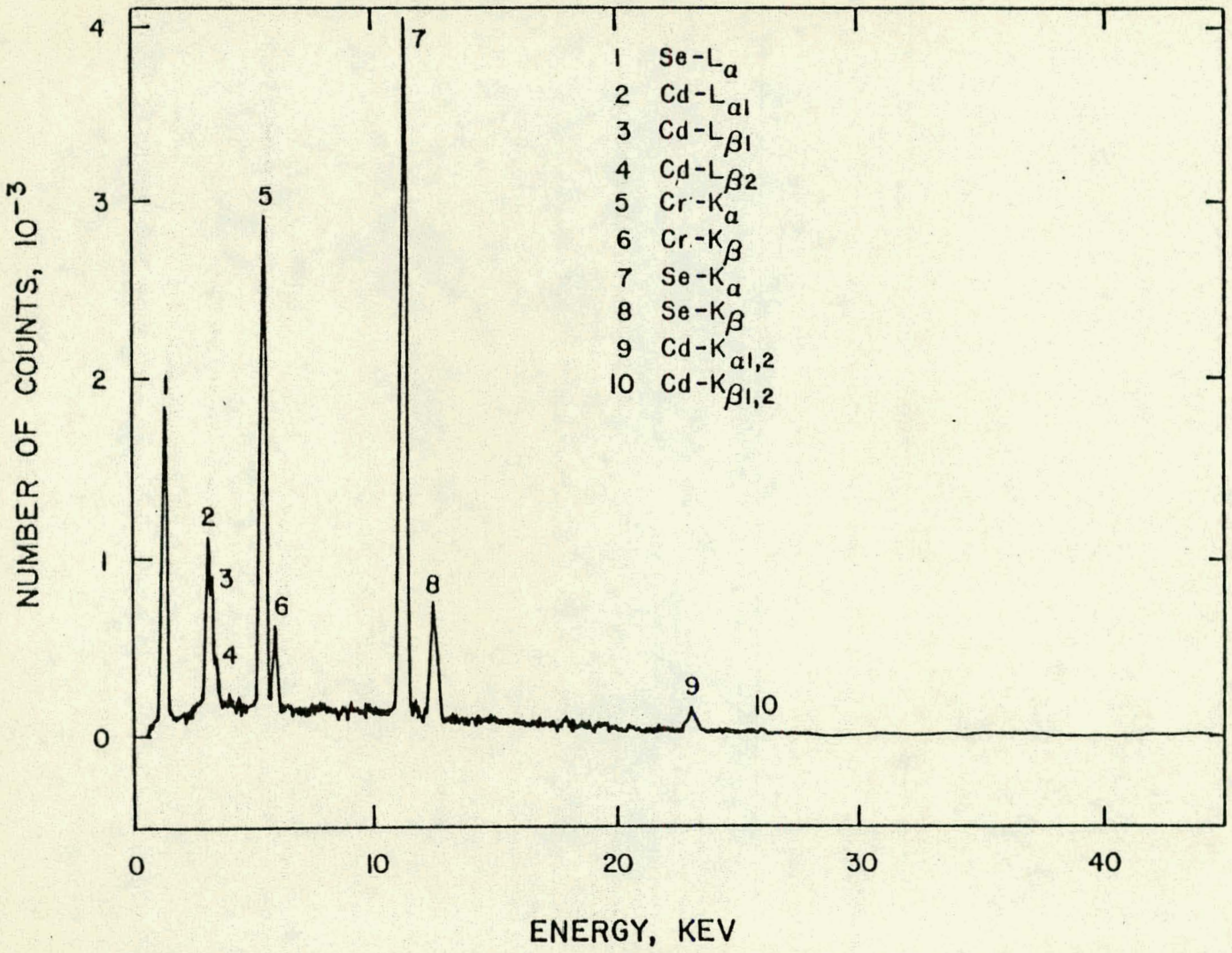

Figure 5.12. X-ray spectrum of hot-pressed $CdCr_2Se_4$.

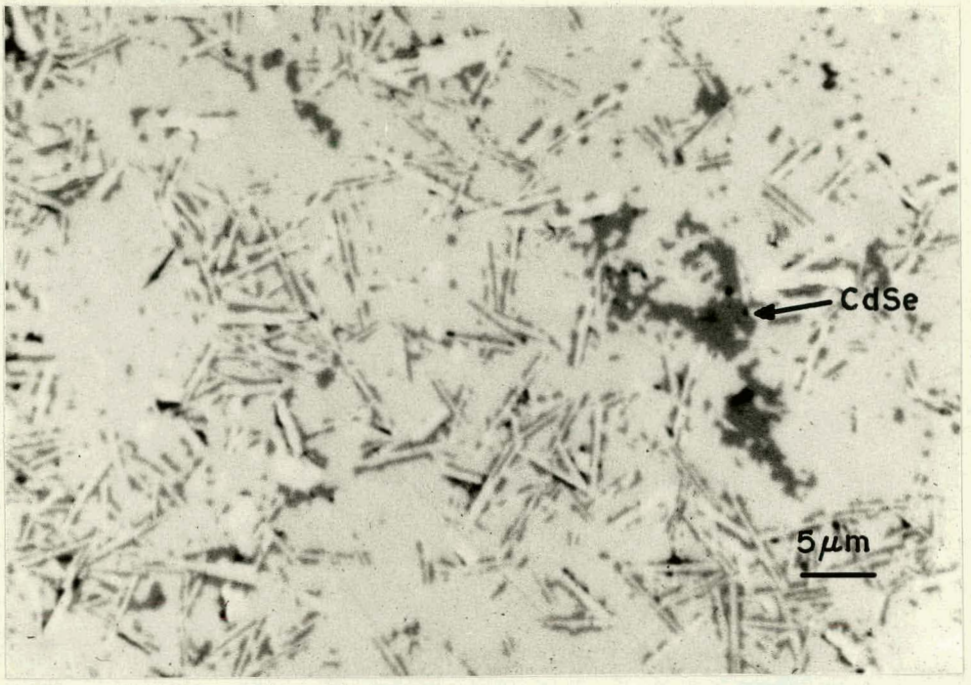

(a)

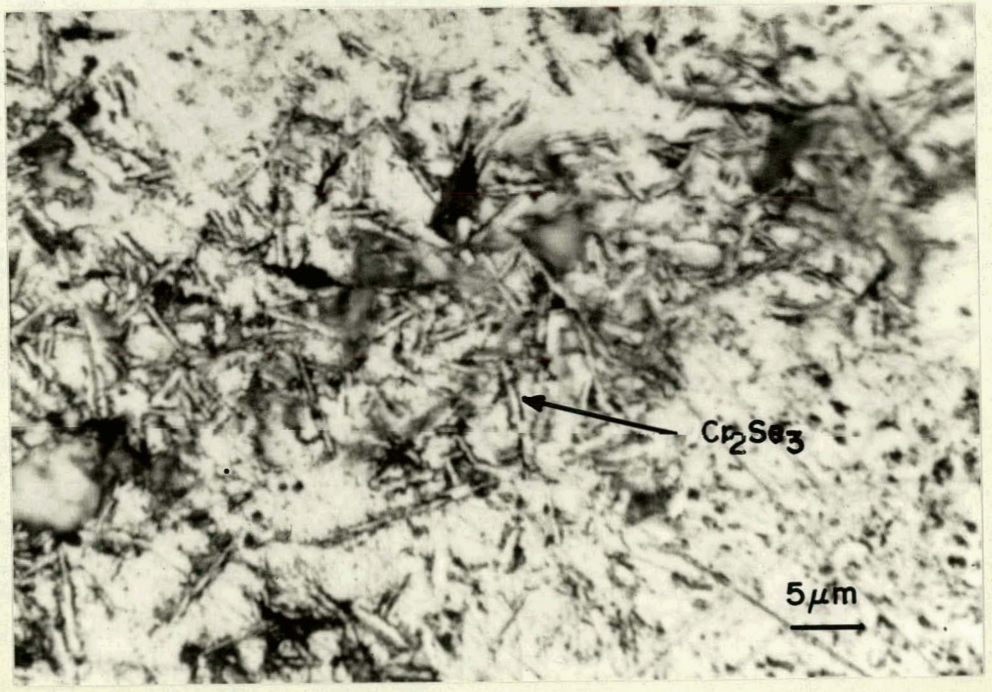

(b)

Figure 5.13. Optical micrographs of (a) polished surface of over decomposed hot-pressed $CdCr_2Se_4$ and (b) etched surface in 70%HNO_3+H_2O_2 at room temperature.

overdecomposed region with both CdSe, as the light phase, and Cr_2Se_3 with the plate-like structure. Even in samples with ~3.5% Cr_2Se_3, the Cr_2Se_3 was not detected by optical microscopy. Overetched samples however show that Cr_2Se_3 forms at the surfaces of the grains as is required by charge neutrality since cadmium and selenium evaporate to the pores (87).

In summary, during the intermediate stage two processes occur concurrently:

(1) densification aided an evaporation condensation mechanism of the selenium and cadmium atoms at the grain boundaries.

(2) decomposition of $CdCr_2Se_4$ into Cr_2Se_3, Cd(g) and Se_2(g) with the eventual reaction of Cd and Se into CdSe if the densification rate is not high enough.

5.1.3. Final Stage

The densification rate during the final stage depends strongly on the particle size of the starting powders, the hot-pressing temperature and the applied pressure. Figure 5.14 shows the densification behavior of $CdCr_2Se_4$ as a function of particle size. The large particles (0.1 - 1.0mm) densify at very low rates (~10^{-6}/sec) and reach a final relative density of $\leq$90%, whereas the fine powders densify at rates ~10^{-4}/sec to densities greater than 99%, Figure 5.14. The incomplete densification for large grain sizes is attributed to low material transport because of the small surface areas and thus small driving force and inefficient packing. Also, it is evident from

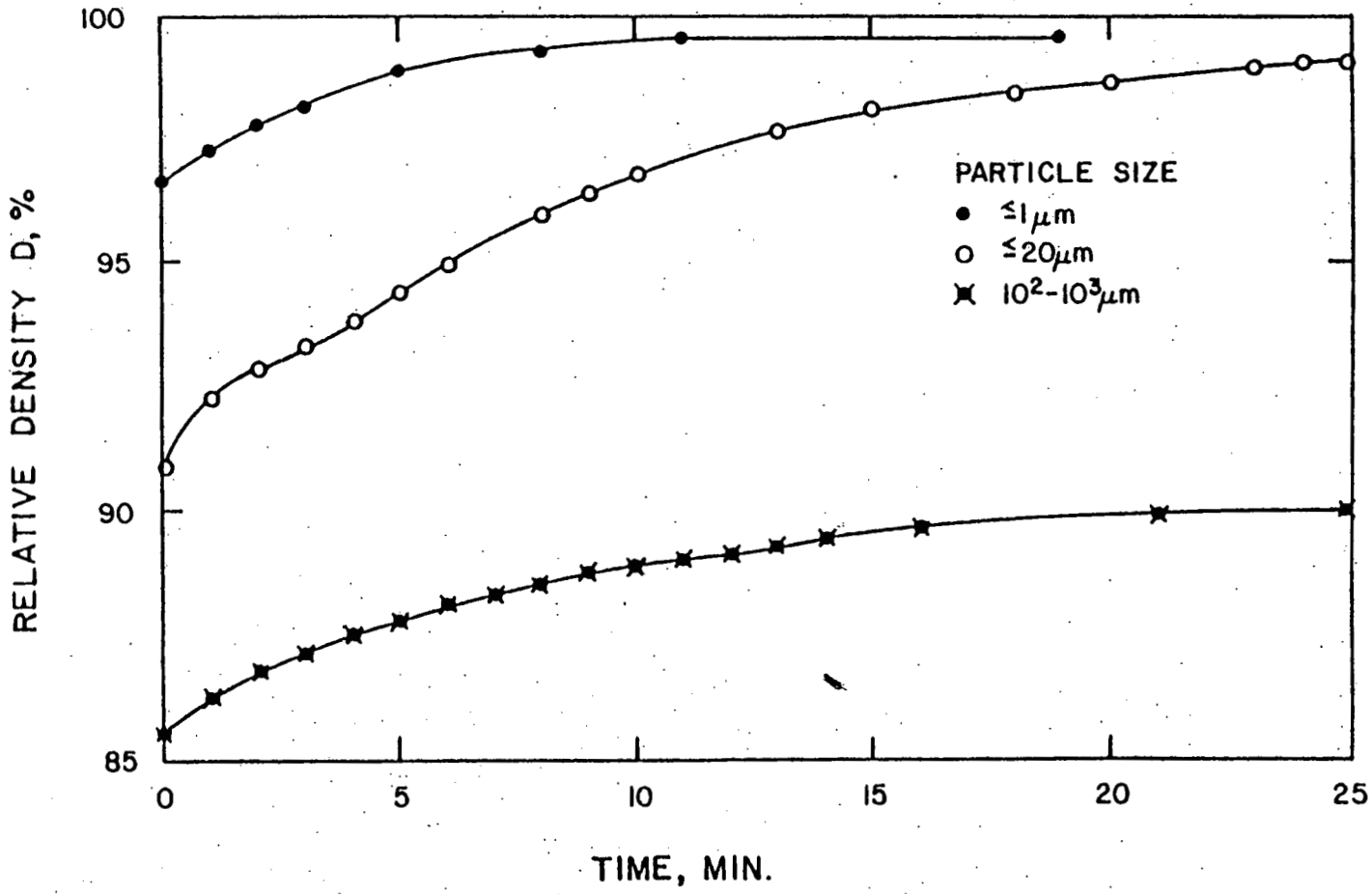

Figure 5.14. Relative density, D, during the final stage of densification for three particles size of $CdCr_2Se_4$.

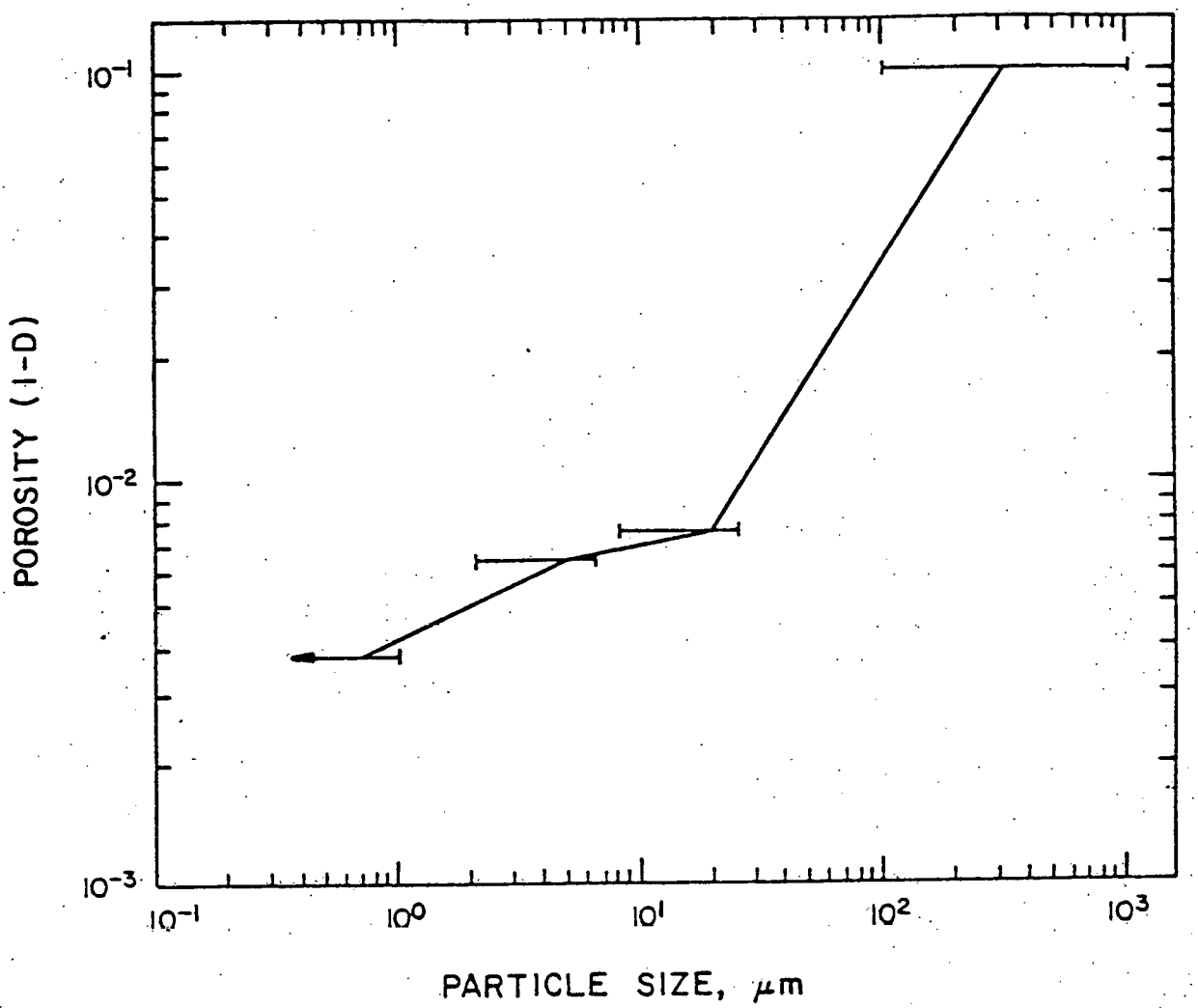

Figure 5.15. Porosity of hot-pressed $CdCr_2Se_4$ vs particle size.

the optical micrographs, Figure 5.16a,b, of regions parallel to the applied pressure that no plastic deformation occurs in single crystals hot-pressed at effective stresses as high as 575MPa. The absence of plastic deformation indicates that the transition from brittle to plastic behavior at $T \leq 750°C$ has not occured. X-ray diffraction further supports the absence of plastic deformation. X-ray relative intensities of the (220), (222), and (400) lines of powders and hot-pressed samples vary only slightly, Figure -5.8, within the experimental error, indicating that crystallographic texture is absent, (no pole figure plot was obtained). Figure 5.17 shows that for particles $\leq 20\mu m$ hot-pressed at 282MPa and 710°C, very slight grain alignment along the tensile direction is observed. However, since densification of these powders to $D = 99.25\%$ took 45-90 minutes and since large single crystals do not show plastic deformation, the observed alignment is attributed to a movement of atoms from regions in compression to region in tension by a diffusion mechanism.

It is difficult at this point to say what the main densification mechanism for $CdCr_2Se_4$ is at these temperatures and pressures. But from the experimental data presented here, plastic deformation can be eliminated in all stages of densification. Power-law creep as a possible densification mechanism can also be eliminated since densification rates as a function of pressure, Figure 5.18, show that for applied pressures between 192-282MPa, the stress

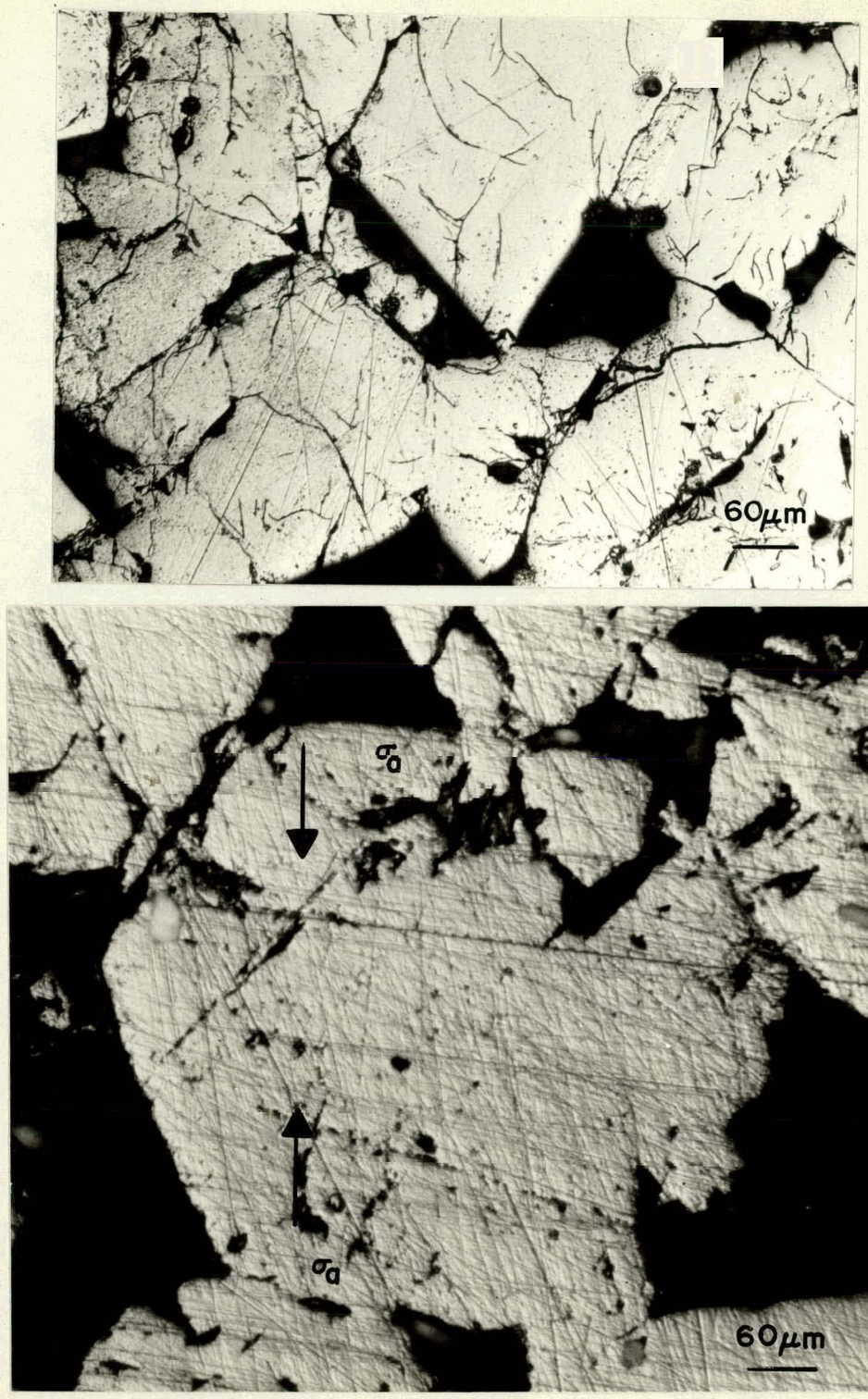

(a)

(b)

Figure 5.16. Optical micrographs of hot-pressed $CdCr_2Se_4$ single crystals (a) perpendicular to σ_a and (b) parallel to σ_a.

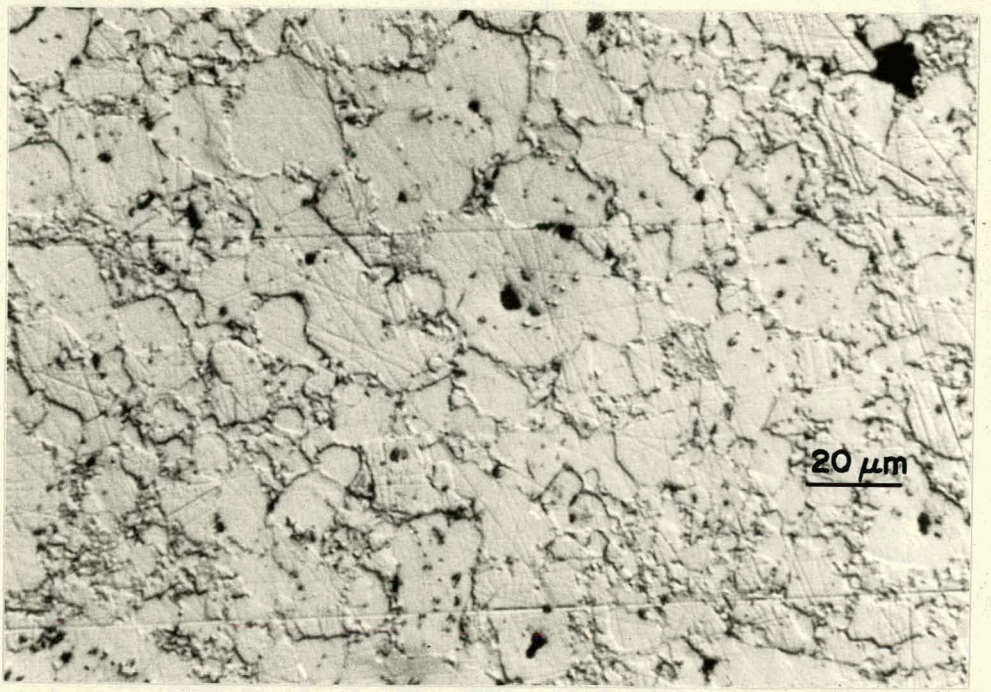

(a)

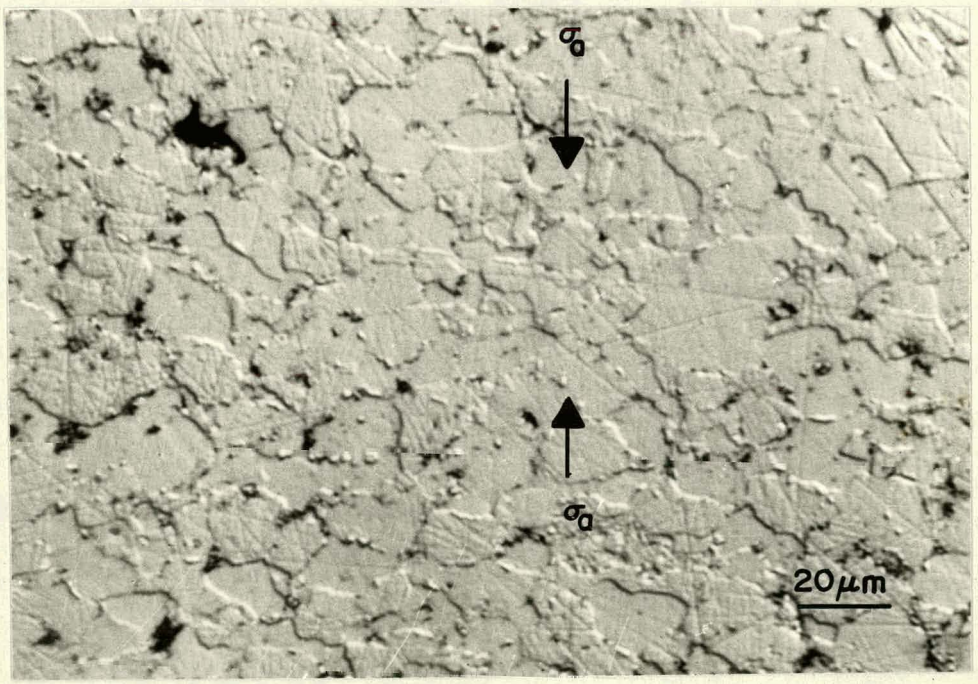

(b)

Figure 5.17. Optical micrographs of hot-pressed $CdCr_2Se_4$ (p.s. $\leq 20\mu m$) (a) perpendicular to σ_a, (b) parallel to σ_a.

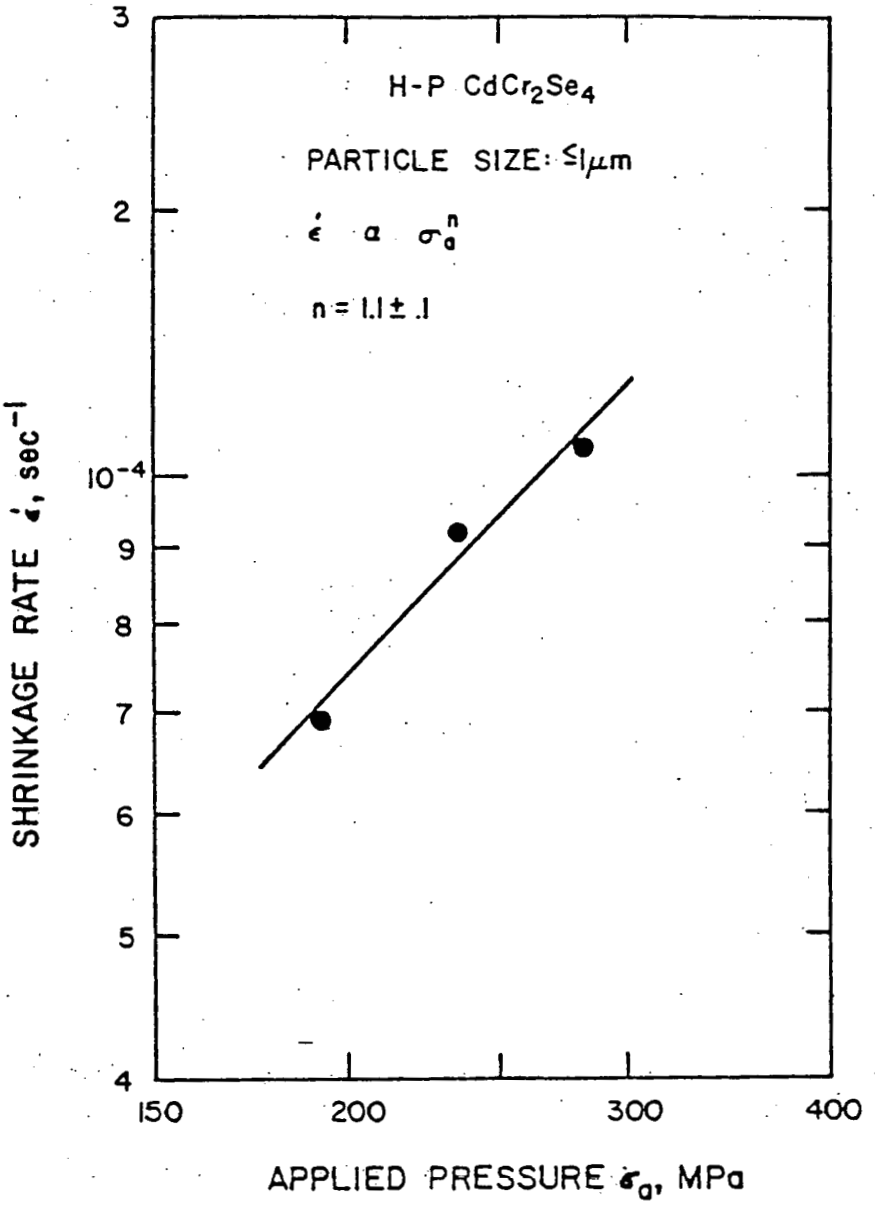

Figure 5.18. Shrinkage rate, $\dot{\epsilon}$ at D = 97.5% and T = 710°C vs applied pressure, σ_a, of $CdCr_2Se_4$.

exponent n, Equation 5.3, at a relative density D = 97.5% is 1.1±.1.

$$\dot{\varepsilon} = \frac{A\sigma^{1.1} \exp^{-Ea/KT}}{d^m} \qquad 5.3$$

The value n = 1.1±.1 is in agreement with Newtonian flow and hence diffusional creep. However, the grain size exponent m determined for our material is ~0.75, Figure 5.19, in disagreement with both the Coble grain size exponent of 2 and the Nabarro-Herring grain size exponent of 3. The disagreement is believed to be due to the contribution of several mechanisms to the densification and also the presence of second phases and non-stoichiometry.

Further, it is found that during the final stage the densification rate, $\dot{\varepsilon}$, determined by $\frac{1}{D}\frac{dD}{dt}$ where D = relative density, decreases with second phase concentration, Figure 5.20. The decrease in the steady state densification rate is due to second phase concentration at the grain boundaries and grain intersections. The separate effect of the second phases has not been determined. But, because of the more refractory nature of Cr_2Se_3 (Tmp $\gtrsim$ 1500°C) compared to CdSe (Tmp $\gtrsim$ 1280°C) and its non-cubic structure, Cr_2Se_3 is more likely to have a larger effect. Also, microstructural observations indicate that Cr_2Se_3 forms mainly at the grain boundaries due to the decomposition mechanisms and thus decreases material transport across the boundary (88).

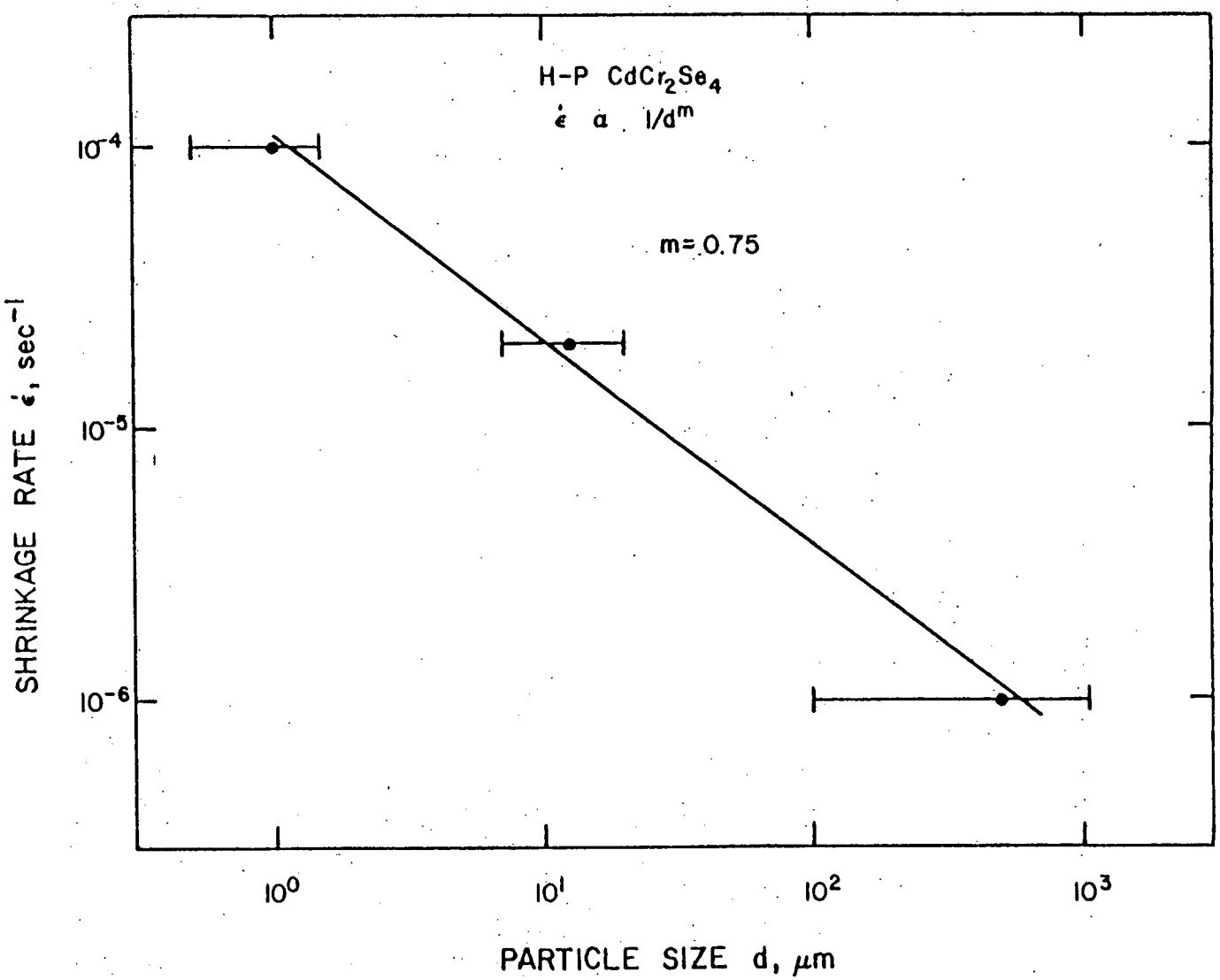

Figure 5.19. Shrinkage rate, $\dot{\epsilon}$, at D = 97.5% at T = 710°C and σ_a = 234MPa vs particle size of $CdCr_2Se_4$.

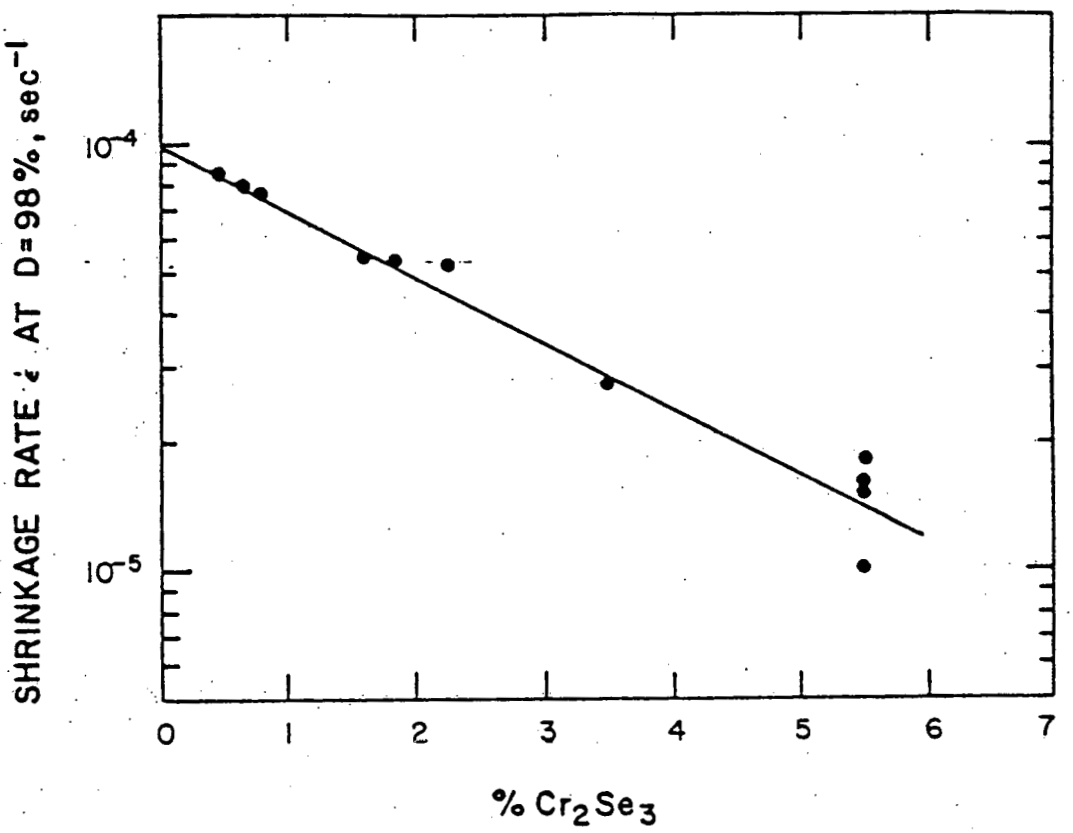

Figure 5.20. Shrinkage rate, $\dot{\varepsilon}$, at D = 98% vs %Cr_2Se_3 ($I(101)Cr_2Se_3/I(440)CdCr_2Se_4$).

Densification is a thermally activated process as shown in Figure 5.21. The activation energy for densification for the $\leq$1μm particles and $\leq$20μm particles is 27.5cal/mole and 29.1Kcal/mole respectively. The disagreement of the activation energy for the two particle sizes is attributed to non-stoichiometric effects and/or to the relative contributions of the grain size sensitive mechanisms. Figure 5.22 shows that temperatures of 700-750°C and fine powders are necessary to achieve high relative densities.

In conclusion, densification of $CdCr_2Se_4$ occurs by rearrangement and fragmentation during the initial stage. At $T \geq 500°C$ an evaporation-condensation of cadmium and selenium ions takes place with re-ordering of the grains. During the intermediate stage, evaporation and condensation of selenium and cadmium leads to decomposition with the formation of CdSe.

During the final stage, the high atomic mobility of selenium and cadmium along the grain boundaries is thought to contribute to the densification and also to decomposition if the densification rate is not high enough. Also a stress exponent of $n = 1.1 \pm .1$ is found for the $\leq$1μm powders in close agreement with Newtonian mechanisms. The activation energy for densification in 27.3Kcal/mole and 29.1Kcal/mole for $\leq$1μm and $\leq$20μm particles respectively. Further, it is found that second phases decrease the densification rate and also prevent complete densification of $CdCr_2Se_4$.

Considering the experimental data obtained so far submicron particles of $CdCr_2Se_4$ free of second phases

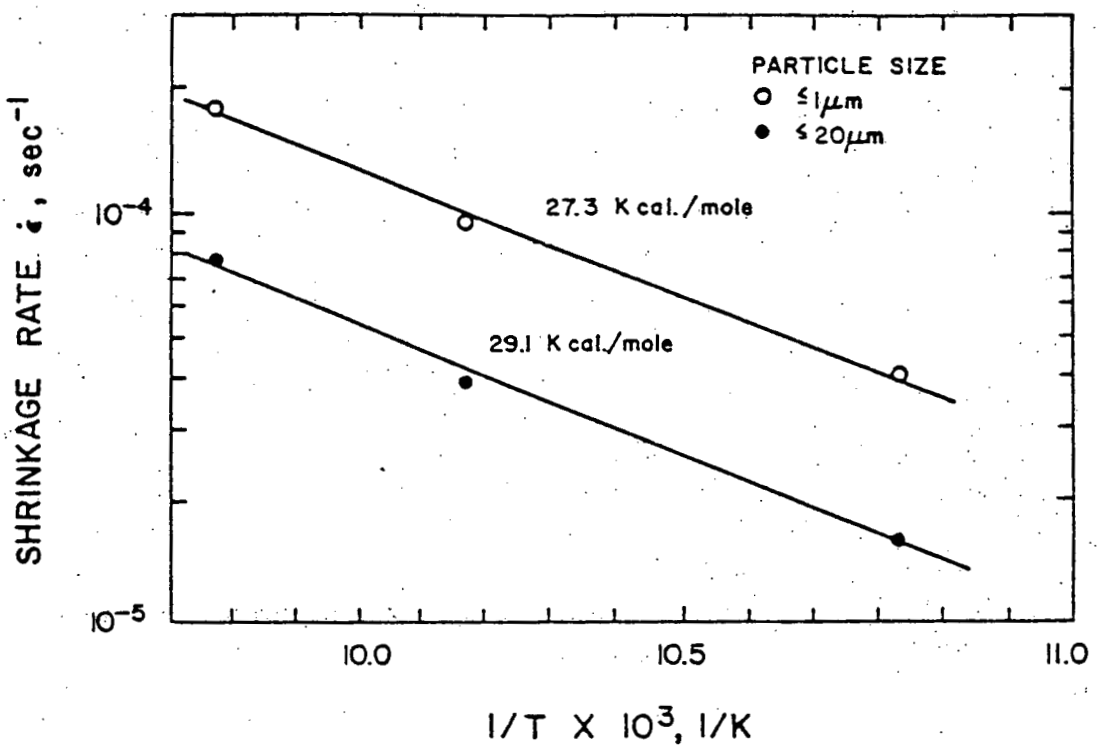

Figure 5.21. Temperature dependence of the shrinkage rate, $\dot{\epsilon}$, of $CdCr_2Se_4$ during the final stage of densification at D = 97.5%.

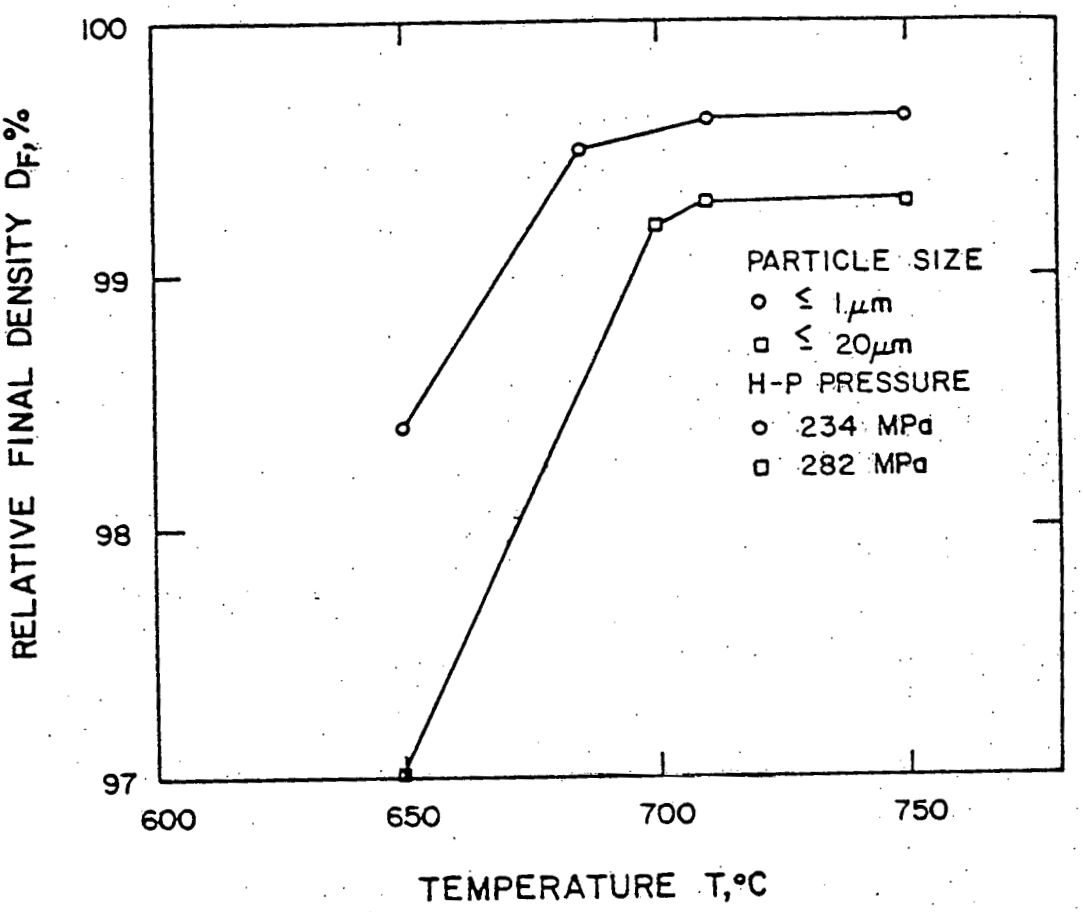

Figure 5.22. Final relative density, D_F, vs temperature for two particle sizes.

are needed to achieve relative densities greater than 99.6%.

5.2. Optical Properties of $CdCr_2S_4$, $CdCr_2Se_4$ & $(1-x)CdCr_2S_4 \cdot xCdCr_2Se_4$

5.2.1. Hot-Pressed $CdCr_2S_4$

Figure 5.23 shows the infrared spectra of hot-pressed $CdCr_2S_4$ at T = 297K and 77K. There are three main features to be noted. The first occurs at short wavelengths. At room temperature there is a broad absorption band from 2.8μm to 5.2μm (0.24ev - 0.44ev). As the temperature is lowered to ~140K the absorption band sharpens into three distinct bands A, B and C at energies 0.4ev, 0.35ev and 0.28ev respectively as shown in Figure 5.23. Then as the temperature is lowered below the Curie temperature (84.5K) to 77K the 0.4ev band decreases as shown in Figure 5.24. These bands are associated with sulfur deficiencies introduced during hot-pressing at a temperature of 900°C and an applied pressure of 234MPa. Since the bands are believed to be due to sulfur deficiencies they are most probably donor bands, Equation 5.5, as also seen by Miyatami(59).

$$CdCr_2S_4(s) \xrightarrow{900°C} CdCr_2S_{4-x}(s) + \frac{x}{2} S_2(g) + 2e^- \qquad 5.5$$

The charge compensation as already discussed in Chapter 3. is accomplished by the formation of Cr^{2+}, Equation 5.6, on the octahedral sites.

$$CdCr_2S_{4-x}\ (s) + 2e^- \rightarrow CdCr_{2-2x}^{3+}Cr_{2x}^{2+}\ S_{4-x}(s) \qquad 5.6$$

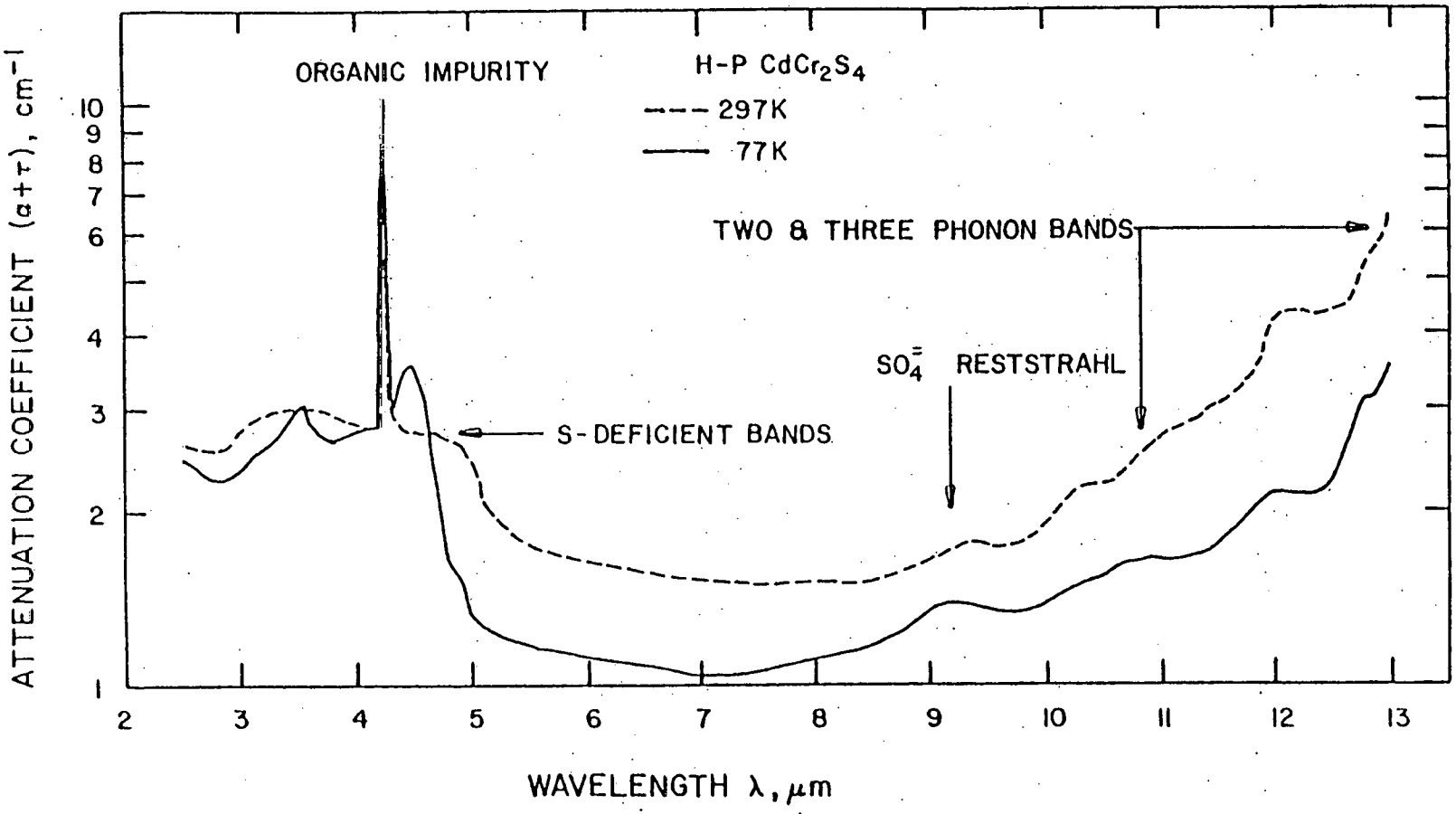

Figure 5.23. Infrared absorption spectrum of hot-pressed $CdCr_2S_4$.

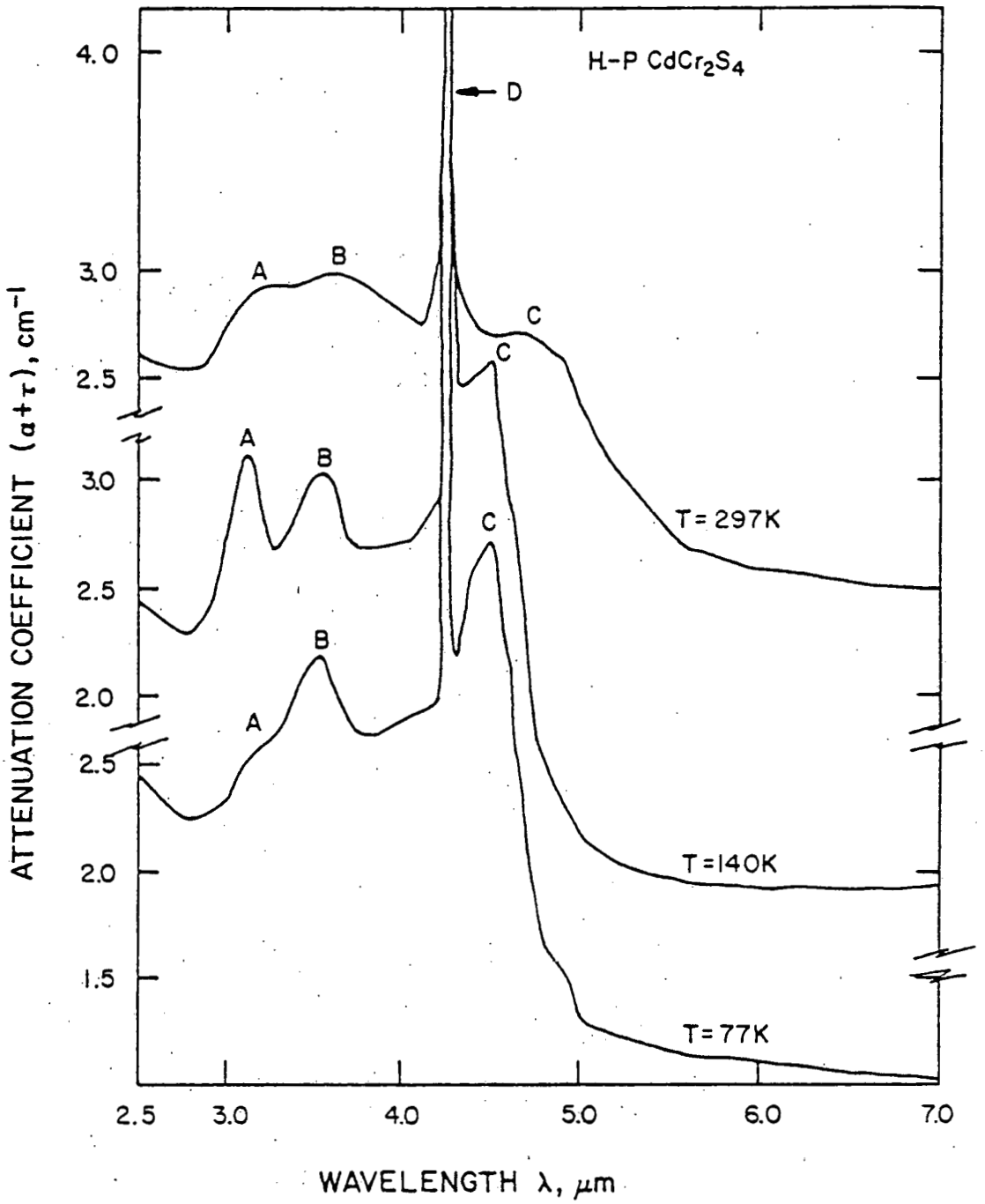

Figure 5.24. Infrared absorption spectra of hot-pressed $CdCr_2S_4$ as a function of temperature showing the sulfur deficient bands.

A second feature that is observed in many samples of hot-pressed $CdCr_2S_4$ is a very sharp absorption band, D, at 0.29ev. This absorption band is attributed to carbon monoxide trapped in the powder. The origin of the CO is most probably from the mechanical pump oil. Samples hot-pressed in a vacuum system with $P \leq 10^{-4}$torr and a liquid nitrogen cold trap did not show the sharp absorption band.

A third feature that is observed at longer wavelengths is an impurity reststrahl band at 9.3μm. This band is attributed to the reststrahl of the $SO_4^{=}$ complex. The sulfate ions are thought to form at high temperature by the reaction of sulfur trapped at pores and oxygen present in the powder because of an improper outgassing procedure prior to hot-pressing.

Finally, the fourth and most important features are the intrinsic multiphonon absorption bands at $\lambda > 10\mu m$. Two-phonon absorption bands have already been observed (35) and combination phonon frequencies assigned to them. In this work additional absorption bands due to three-phonon absorption were observed and a new assignment is made to the reported two-phonon absorption band occuring at $\lambda = 12.5\mu m$ ($800cm^{-1}$). Figure 5.25 shows the spectrum of hot-pressed $CdCr_2S_4$ at $\lambda > 9.5\mu m$ showing the multiphonon absorption bands from 10.24μm to 15.55μm. Table 5.1 lists the two- and three-phonon sum frequencies assignments to the absorption bands shown in Figure 5.24. The values of

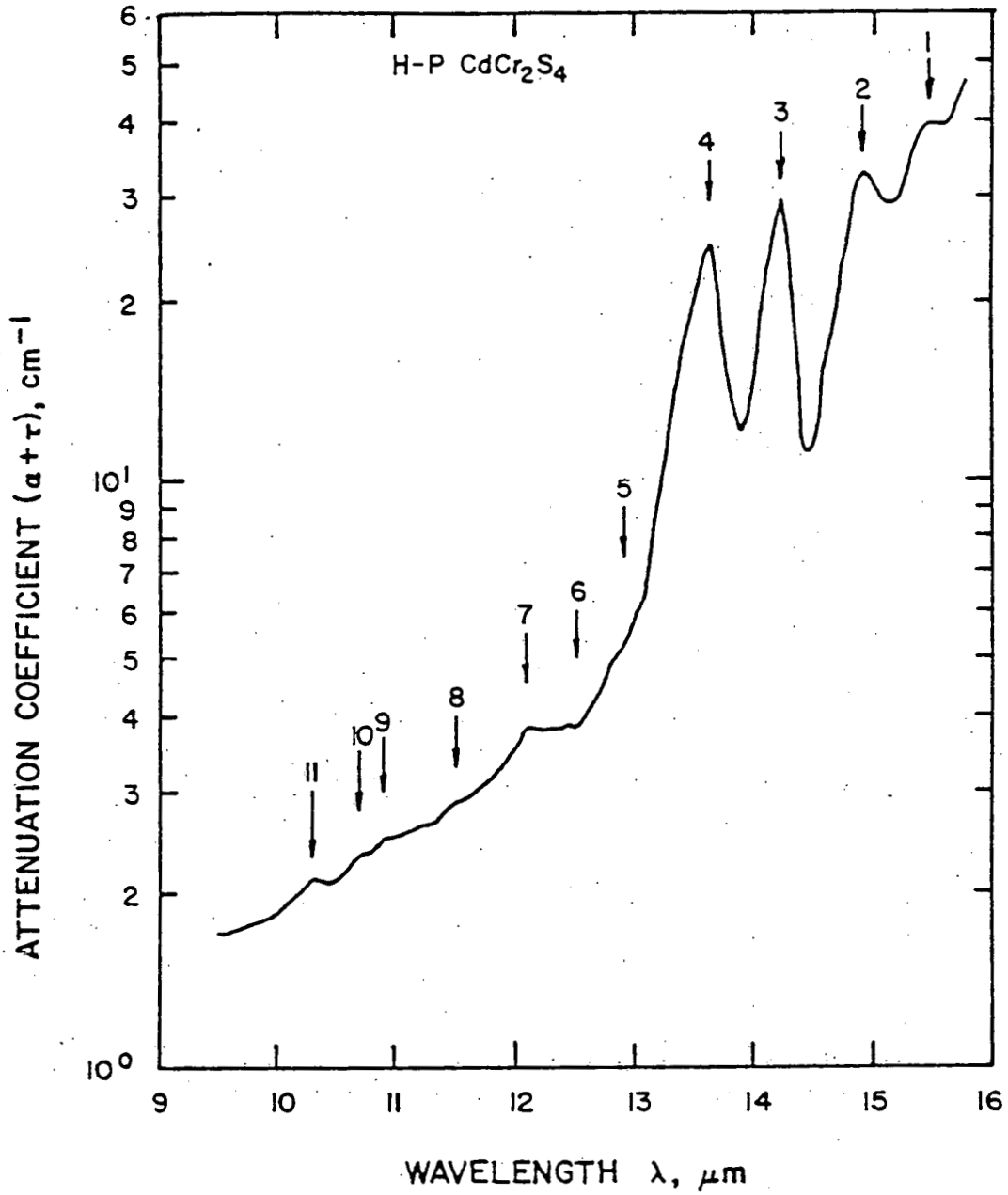

Figure 5.25. Infrared absorption spectrum of hot-pressed $CdCr_2S_4$ showing two and three-phonon absorption bands listed in Table 5.1.

TABLE 5.1. MULTIPHONON ABSORPTION BANDS IN HOT-PRESSED $CdCr_2S_4$

ABSORPTION BAND NUMBER (Fig. 5.25)	PHONON COMBINATION	WAVENUMBER/WAVELENGTH $cm^{-1}/\mu m$ THEORETICAL	WAVENUMBER/WAVELENGTH $cm^{-1}/\mu m$ MEASURED
1	$2T.O._2$	643.2/15.55	640/15.63
2	$L.O._2 + T.O._2$	668.2/14.97	670/14.93
3	$T.O._1 + T.O._2$	698.8/14.31	700/14.29
4	$T.O._1 + L.O._2$	724.1/13.81	725/13.79
5	$2L.O._1$	779.8/12.82	775/12.90
6	$T.O._1 + T.O._2 + T.O._4$	795.5/12.57	800/12.5
7	$L.O._1 + L.O._2 + T.O._4$	834.1/11.99	830/12.05
8	$T.O._1 + L.O._1 + T.O._4$	863.5/11.58	870/11.5
9	$T.O._2 + L.O._2 + T.O._3$	908.8/11.0	915/10.93
10	$T.O._1 + T.O._2 + T.O._3$	938.5/10.66	935/10.70
11	$L.O._1 + L.O._2 + T.O._3$	977/10.24	971/10.30

the transverse and longitudinal optical phonon frequencies are listed in Table 3.4.

Therefore, in addition to the two-phonon absorption bands three-phonon absorption bands are found to intrinsically limit $CdCr_2S_4$ at $\lambda > 10\mu m$. Thus, it is necessary to investigate other materials that are not intrinsically limited. In the next sections the optical properties of $CdCr_2Se_4$ and $(1-x)CdCr_2S_4 \cdot x\ CdCr_2Se_4$ are described.

5.2.2. Hot-Pressed $CdCr_2Se_4$

Figure 5.26 shows a typical infrared spectrum of hot-pressed $CdCr_2Se_4$. At long wavelengths the wavelength dependence of the transmission is indicative of free-carrier absorption. Also, a very strong absorption band at $\lambda \geq 16.3\mu m$ is present. This as already observed in $CoCr_2S_4$ and $CdCr_2S_4$ (89) is most probably due to the Cr_2O_3 reststrahl. At short wavelengths the wavelength dependence is indicative of scattering.

In this section the sources of optical attenuation in hot-pressed $CdCr_2Se_4$ are described and the attenuation coefficient reduced.

A. Electronic Absorption

Our experiments indicate that free-carriers contribute to the increase in absorption at $\lambda \geq 4.5\mu m$ with wavelength. The temperature dependence of the absorption at $\lambda \geq 4.5\mu m$ is consistent with free-carrier quenching

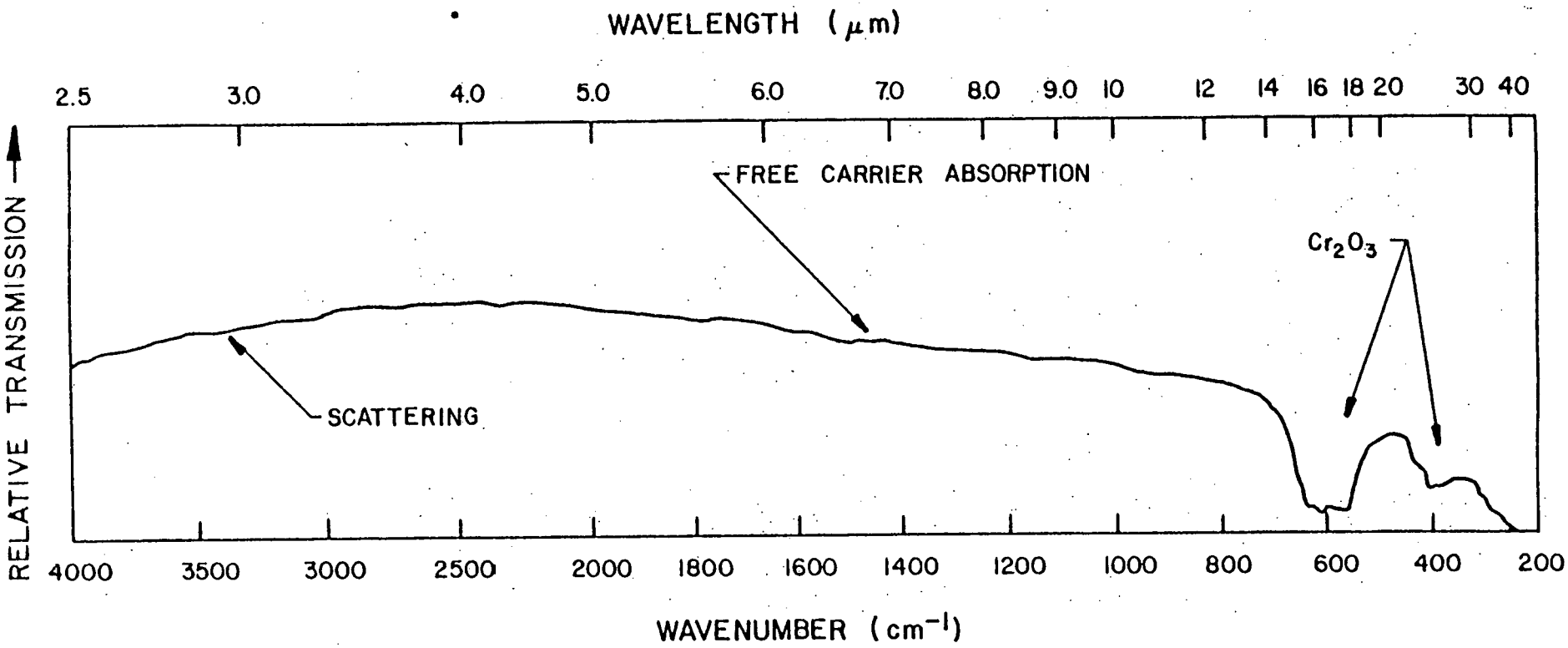

Figure 5.26. Infrared transmission of hot-pressed $CdCr_2Se_4$ of as grown powders (p.s. ≤ 1μm).

at liquid nitrogen temperature as shown in Figure 5.27. Room temperature resistivity measurements also indicate that free-carriers are responsible for the high absorption at long wavelengths. Figure 5.28 shows that the attenuation coefficient at $\lambda = 10.6\mu m$ increases with decreasing resistivity as expected. However, the attenuation coefficient does not follow the classical λ^2 dependence. This is due to a number of factors. The most important in our case are the optical scattering, which will be described in Section 5.2.2B, and Cr_2O_3 reststrahl contributions to the attenuation coefficient.

Our experiments further indicate that the free-carriers responsible for absorption at long wavelengths are associated with excess selenium present in the virgin powder. We have shown that $CdCr_2Se_4$ powders formed by the co-precipitation of hydroxides and by the direct reaction of the binary phases contain free selenium. Upon hot-pressing free selenium gets trapped at grain boundaries and reacts with $CdCr_2Se_4$ at high temperature. The reaction occurs as shown in Equation 5.6a.

$$CdCr_2Se_4(s) + \frac{x}{2}Se_2(g) \overset{\sim 710°C}{} CdCr_2Se_{4+y}(s) + (\frac{x}{2} - \frac{y}{2})Se_2(g) + 2h^{\cdot} \qquad 5.6a$$

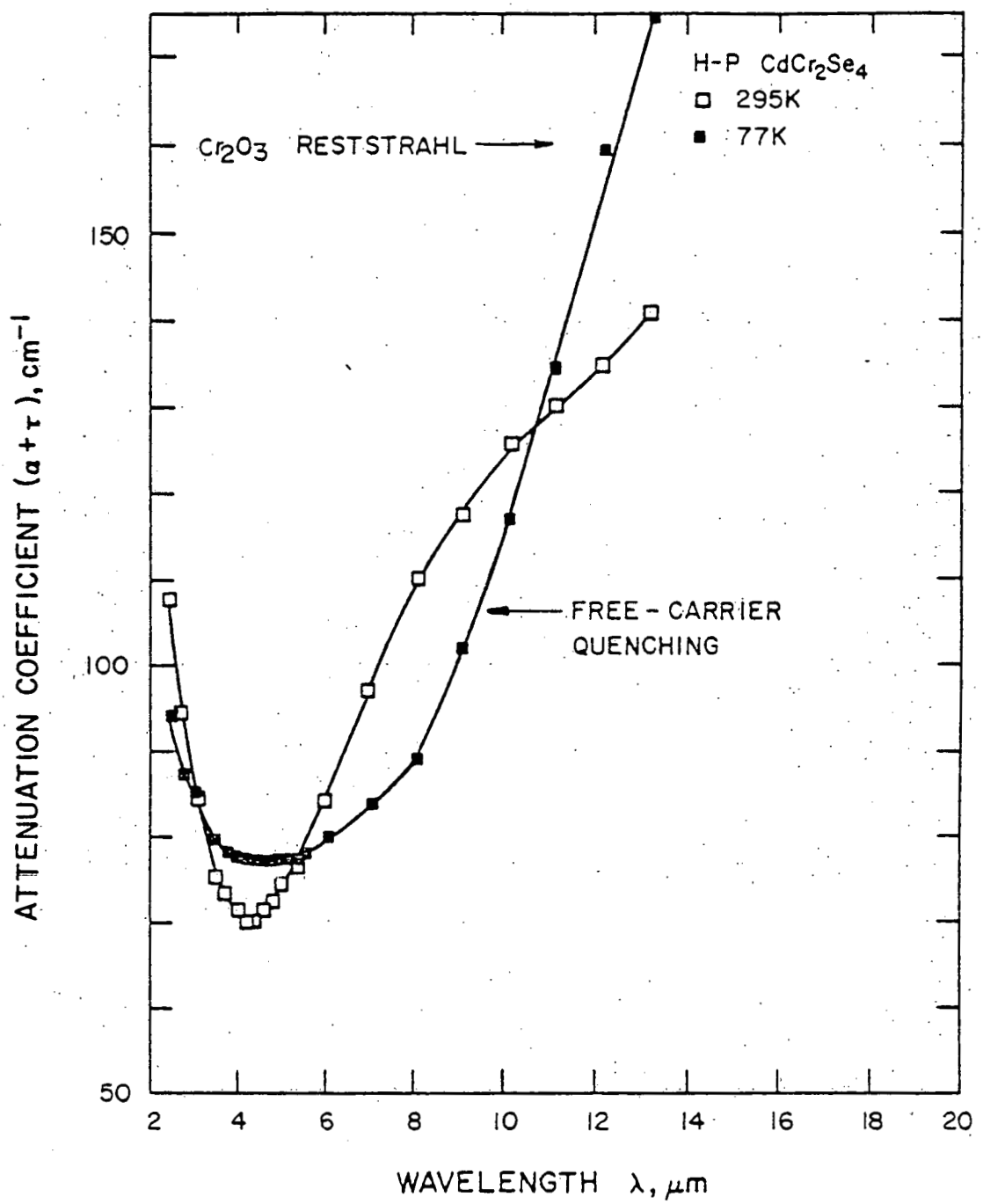

Figure 5.27. Infrared absorption of hot-pressed $CdCr_2Se_4$ (as grown) containing excess selenium at 297 K and 77 K.

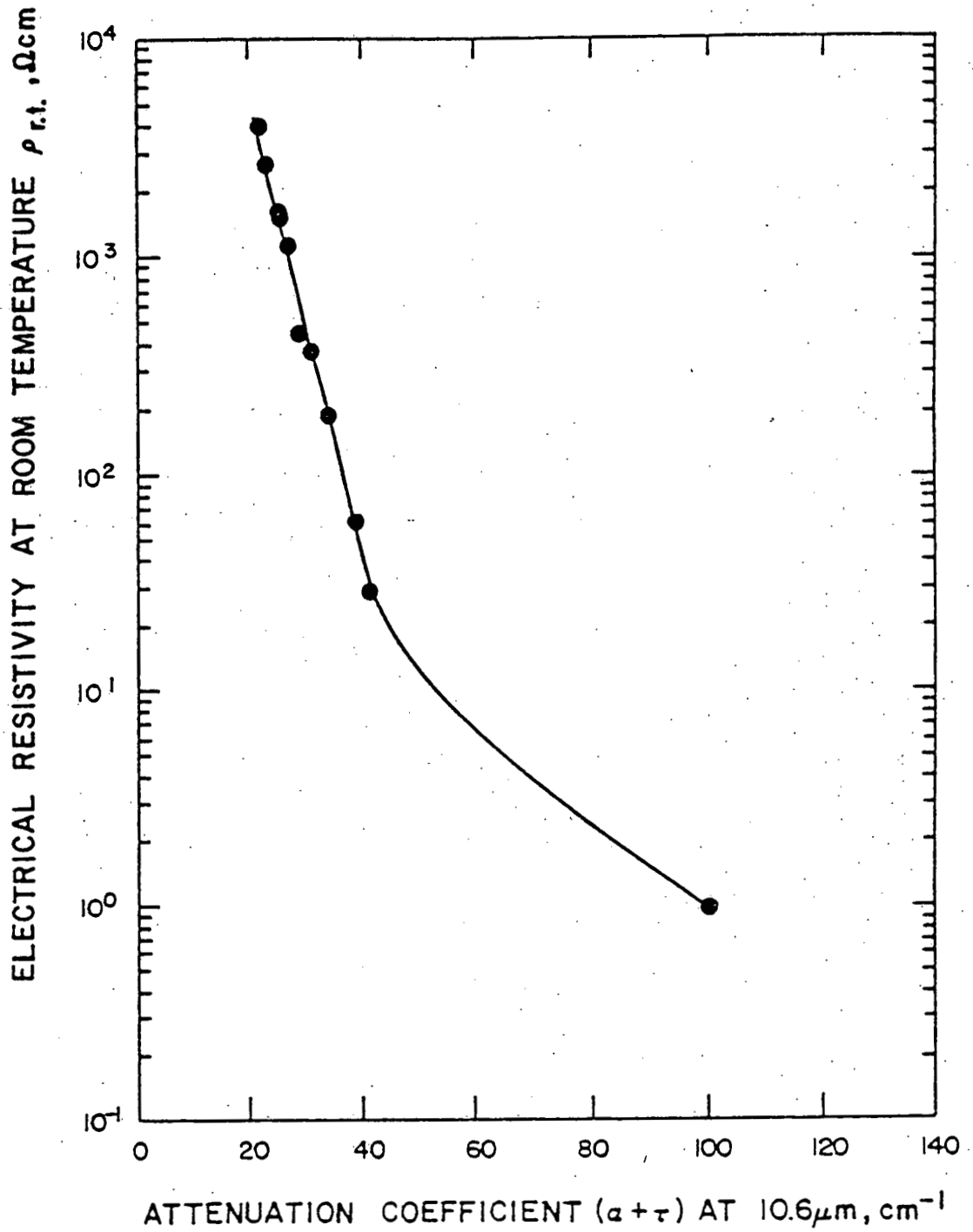

Figure 5.28. Room temperature electrical resistivity vs attenuation coefficient at λ = 10.6μm.

$$CdCr_2Se_{4+y}(s) + 2h^{\cdot} \rightarrow CdCr^{3+}_{2-2y}Cr^{4+}_{2y}Se_{4+y}(s) \qquad 5.6b$$

As shown in Equation 5.6b charge compensation is believed to occur by the formation of Cr^{4+}.

Excess selenium was observed by SEM in conjunction with an electron microprobe. Figure 5.29 shows an x-ray spectrum of a pore filled with selenium. Also, since free selenium has a high vapor pressure and reacts readily with H_2 it was always detected as a foul odor during the grinding and polishing of the hot-pressed samples.

Electronic absorption due to free-carriers was reduced by removing selenium from the virgin powders by two methods.

(1) by treating the powders at T ~400°C in a flowing dry helium gas for 2 hours prior to hot-pressing;

(2) by lowering the clamping pressure after the outgassing period from 78MPa to 19MPa during the heating period from 350-710°C.

Removal of selenium during the heating period proved to be more successful and faster. Removal of free selenium from the powders caused a decrease in attenuation coefficient at long wavelengths with decreasing clamping pressure as shown in Figure 5.30. The decrease in attenuating coefficient was found to be directly related to the free-selenium evolution during the initial stage of densification. As

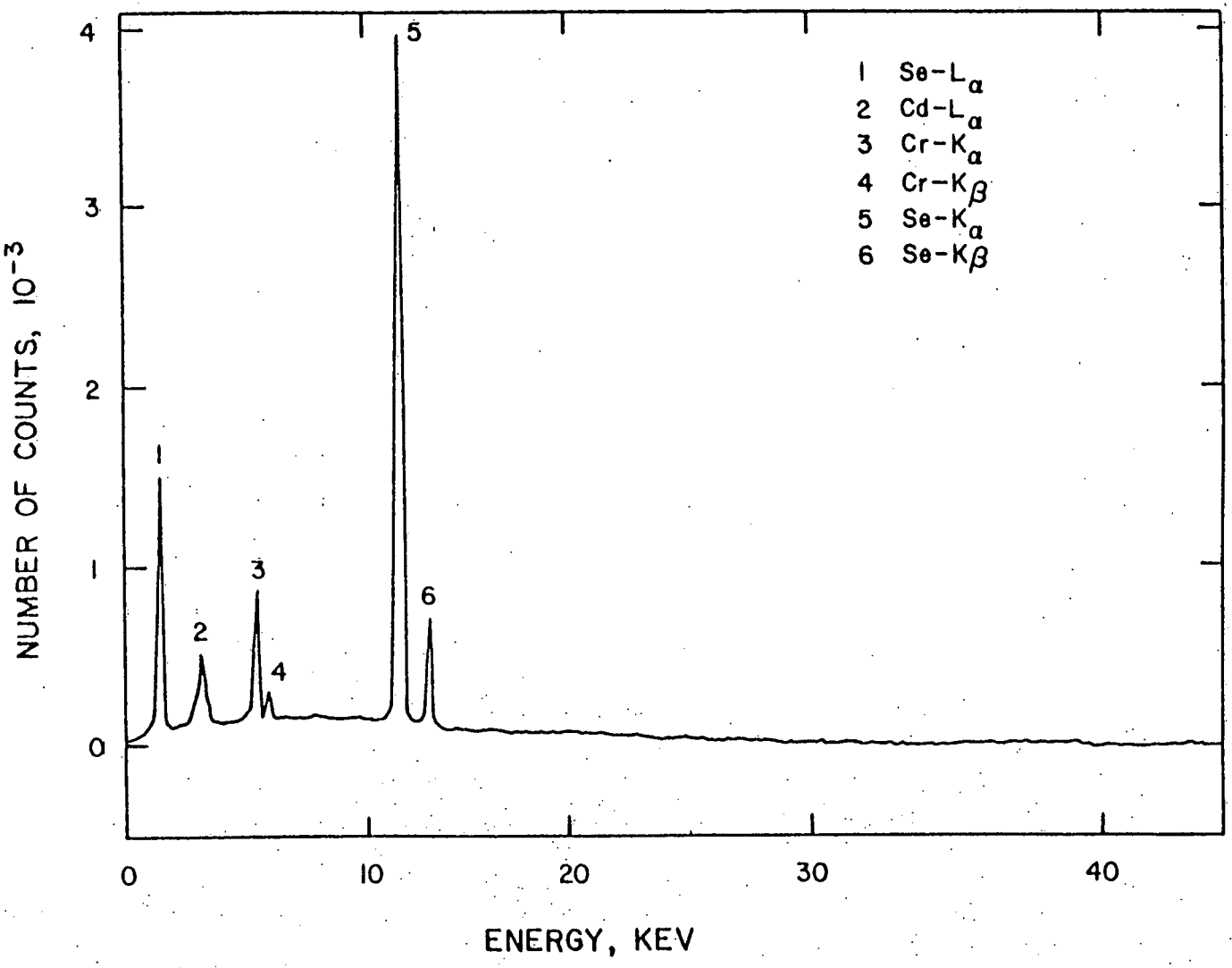

Figure 5.29. X-ray spectrum of selenium in hot-pressed $CdCr_2Se_4$.

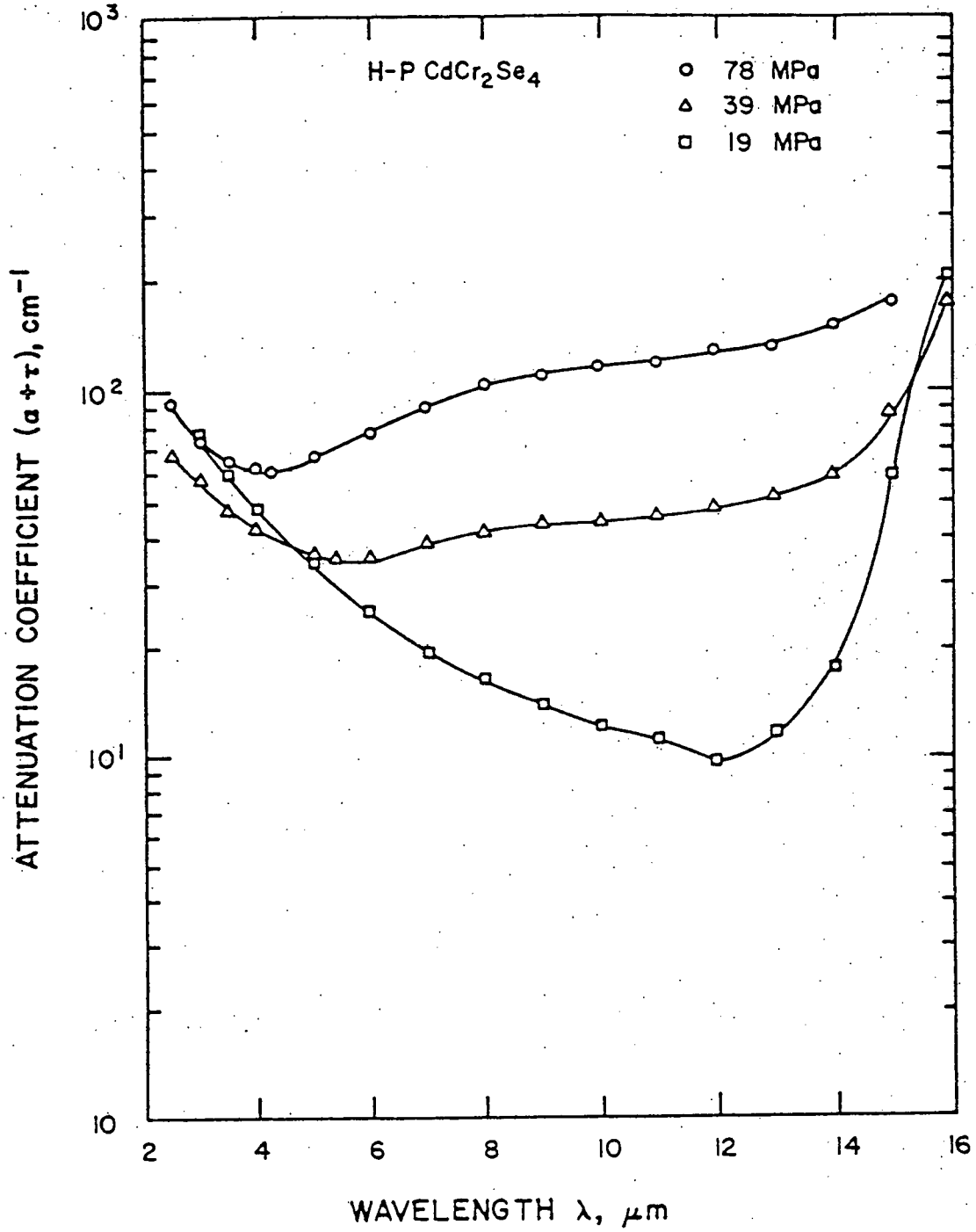

Figure 5.30. Room temperature infrared absorption spectra of hot-pressed $CdCr_2Se_4$ (σ_a = 234MPa, T = 710°C) as a function of clamping pressure.

further evidence that free-selenium reacts with $CdCr_2Se_4$ during hot-pressing to create free-carriers is the absence of free-carrier absorption in the virgin powders. Photoacoustic spectroscopy was recently used to obtain infrared spectra of as grown powders (78). Figure 5.31 shows a typical infrared spectrum of $CdCr_2Se_4$ (p.s. $\leq$ 1μm) showing a broad electronic absorption band at short wavelengths but no free-carrier is observed. Thus indicating that selenium doping occurs during the hot-pressing process. However in powders formed from the binary second phases (p.s. $\leq$ 20μm) free-carrier at long wavelengths is observed, Figure 5.32. This is attributed to the long reaction times to form the powders and the eventual trapping of selenium during the growth process. Treatment of the powders in flowing He at 500°C removed some selenium and reduced free-carrier absorption as shown in Figure 5.33.

Hot-pressing time at the optimum hot-pressing temperature and pressure has been found to have an effect on the electrical resistivity behavior of hot-pressed $CdCr_2Se_4$ below the Curie temperature. Figure 5.34 shows the temperature dependence of the electrical resistivity. At low temperatures approaching the Curie temperature the resistivity changes slope and it increases with decreasing hot-pressing time. This behavior indicates that the slope is dependent on the cadmium and selenium deficiency. Also, since the electrical resistivity behavior is indicative

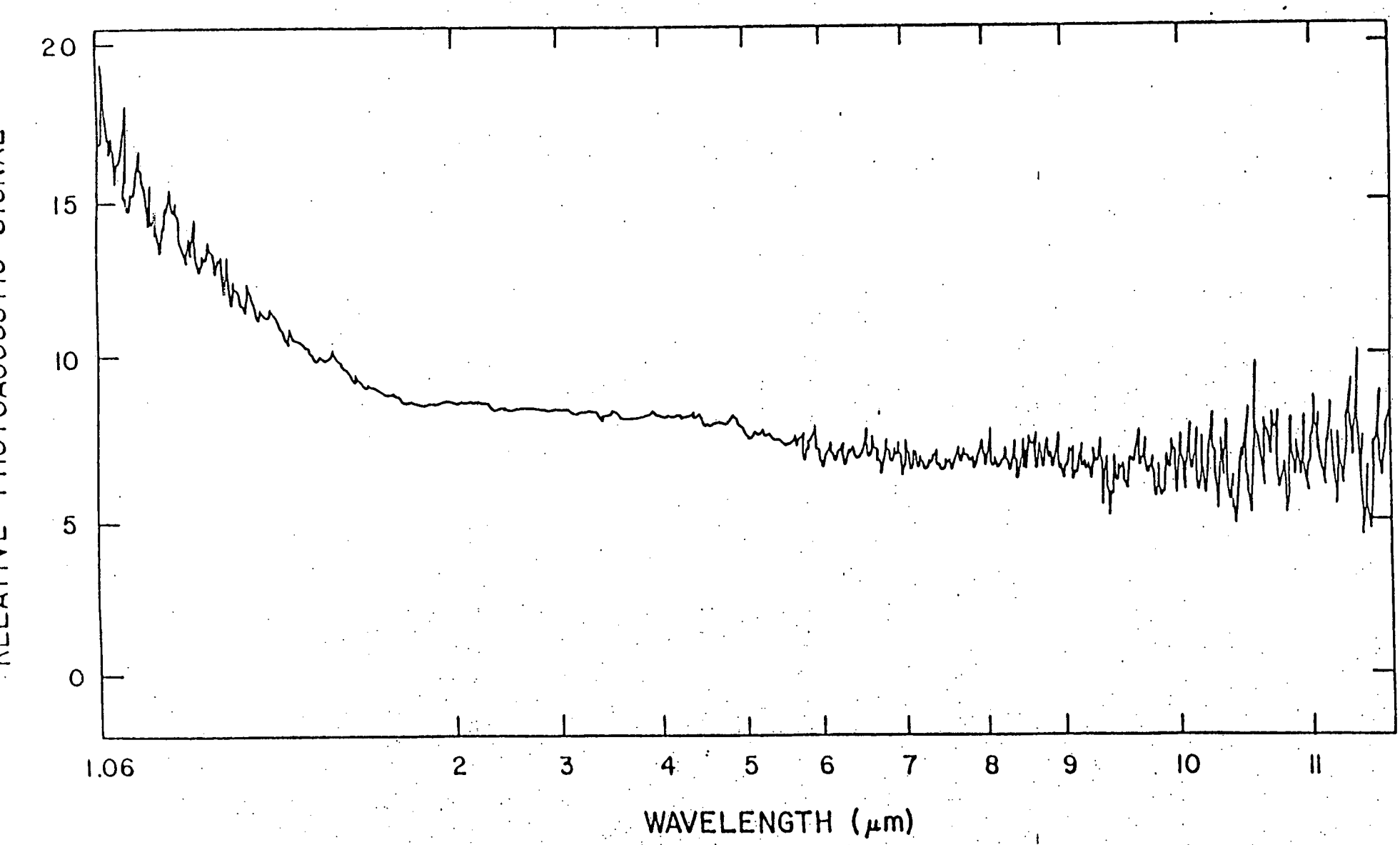

Figure 5.31. Photoacoustic spectrum of (as grown) $CdCr_2Se_4$ (powder) (p.s. ≤ 1μm) (adopted from(78).

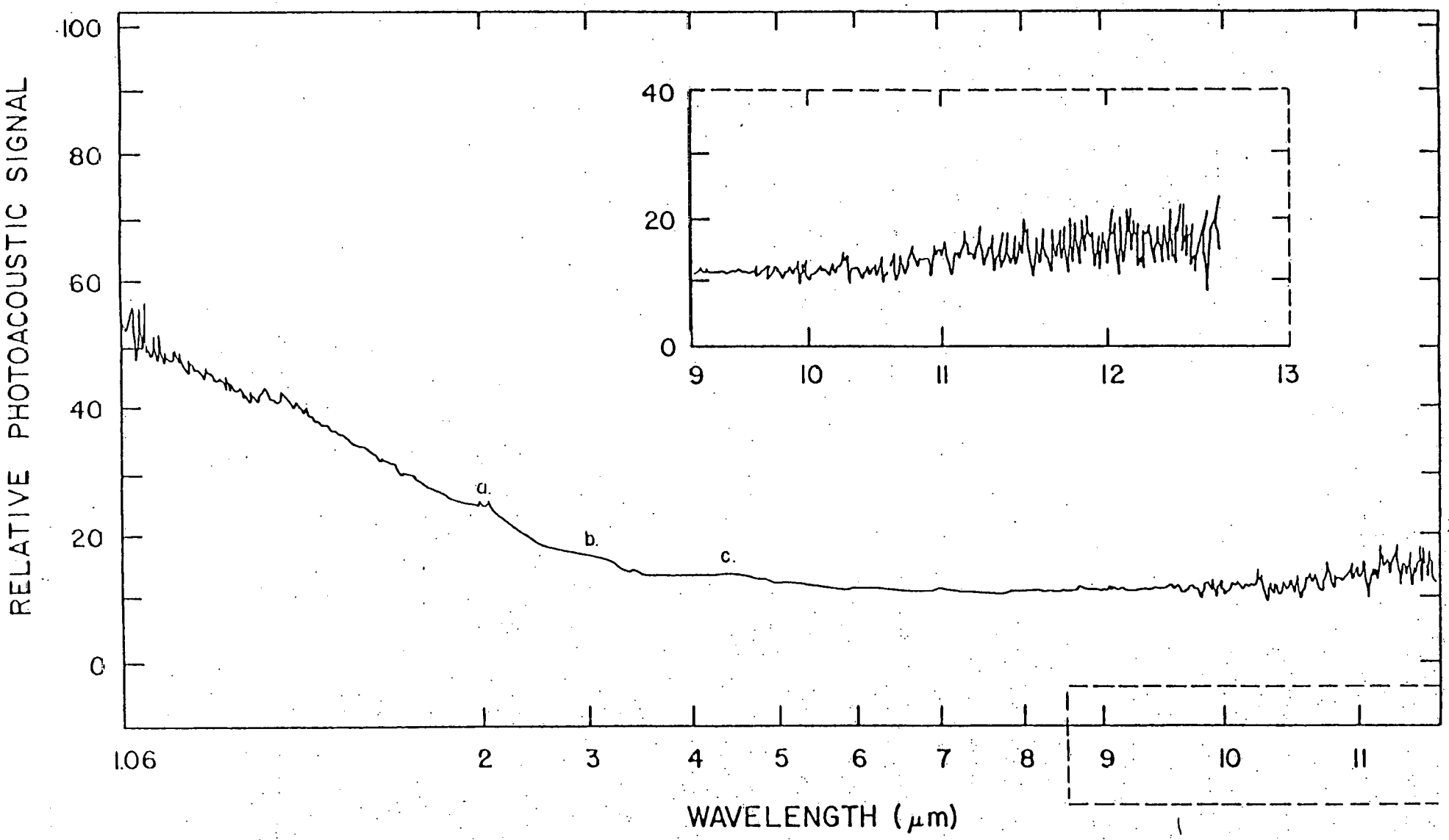

Figure 5.32. Photoacoustic spectrum of as grown $CdCr_2Se_4$ powder (p.s. $\leq$ 20μm) (adopted from (78).

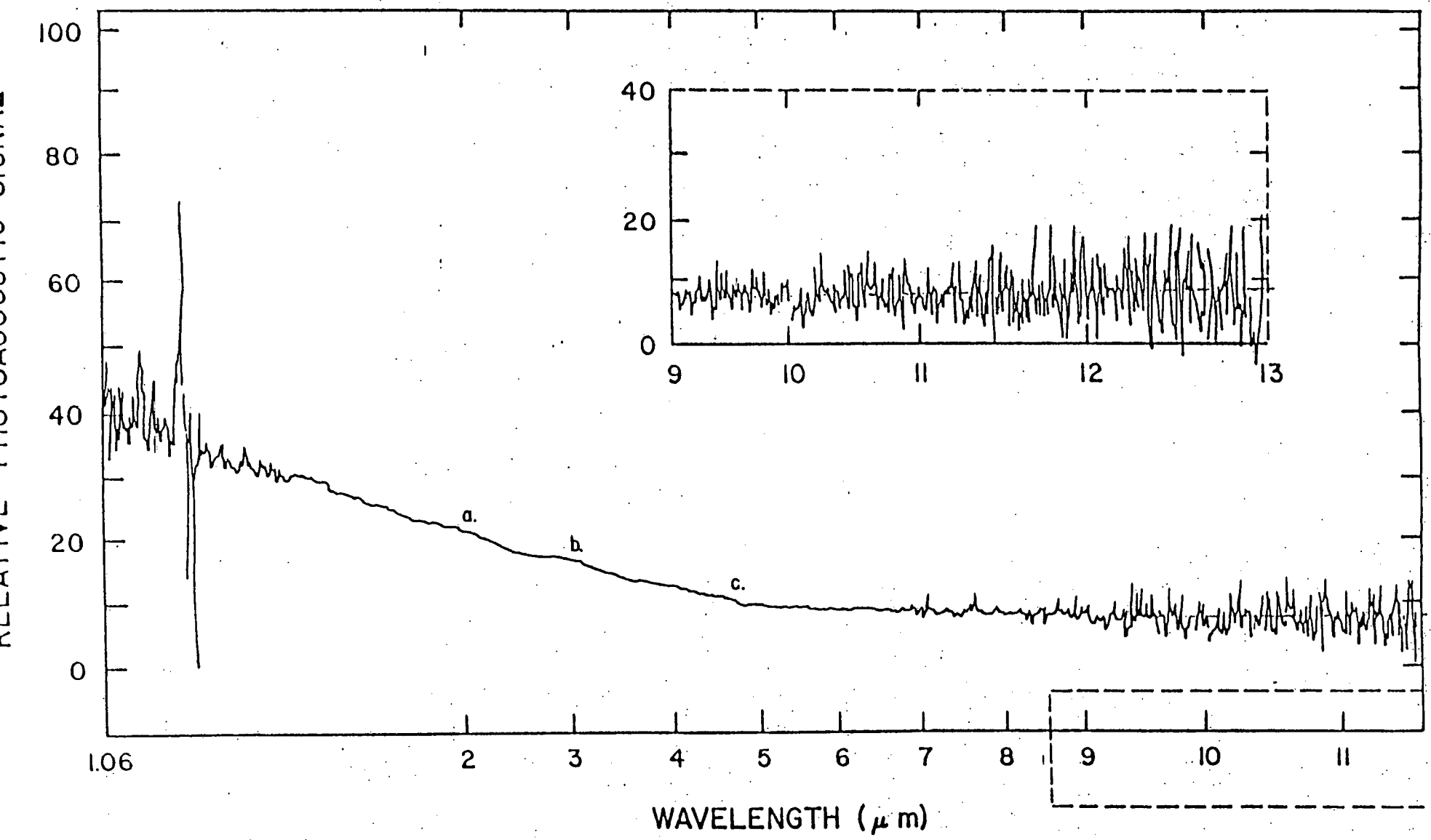

Figure 5.33 Photoacoustic spectrum of heat treated CdCr Se powder (p.s. < 20μm)(adopted from (78),

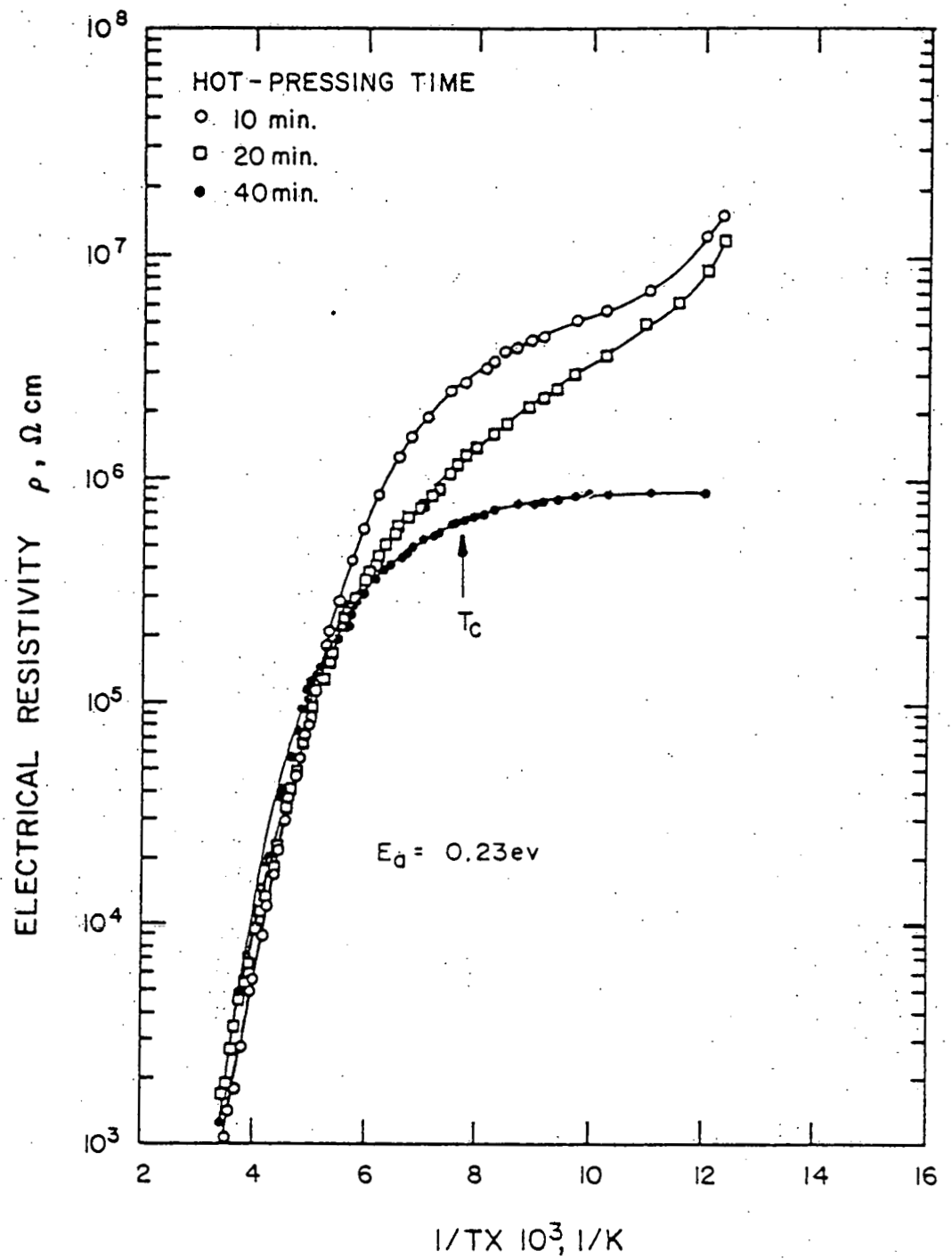

Figure 5.34. Electrical resistivity as a function of temperature for samples hot-pressed at σ_a = 234MPa, T = 710°C and three different times.

of n-type conduction (27) selenium loss must be higher than that of cadmium. Calculations of the activation energy for extrinsic conduction(90) show that the activation energy of $CdCr_2Se_4$ hot-pressed for t = 20 minutes is 0.23ev. The value of E_a = 0.23ev is in excellent agreement with the activation energy of selenium deficient $CdCr_2Se_4$ single crystals(91).

Figure 5.35 shows the infrared spectrum of hot-pressed $CdCr_2Se_4$ with a room temperature resistivity greater than 1.5 x $10^3\Omega$cm at 297K and 77K. Two important features must be noted here. The first is the absorption band at E ~0.23ev at liquid nitrogen temperature. This band is associated with a selenium deficient band. This is again, in excellent agreement with the published data(26,91) on single crystals and with the electrical resistivity measurements of the same sample. The second feature to be noted is a decrease of ~6cm^{-1} in absorption coefficient at liquid nitrogen temperatures if the index of refraction is kept constant. The decrease can be attributed to a decrease in number of free-carriers at grain boundaries and/or a decrease in index of refraction. If it is assumed that the increase in transmission is due to a decrease in index of refraction a dn/dT of ~7 x 10^{-4}/K is obtained. S. Jacobs(1), however, found that dn/dT for $CdCr_2S_4$ was very small and not enough to account for the change in transmittance. This may also

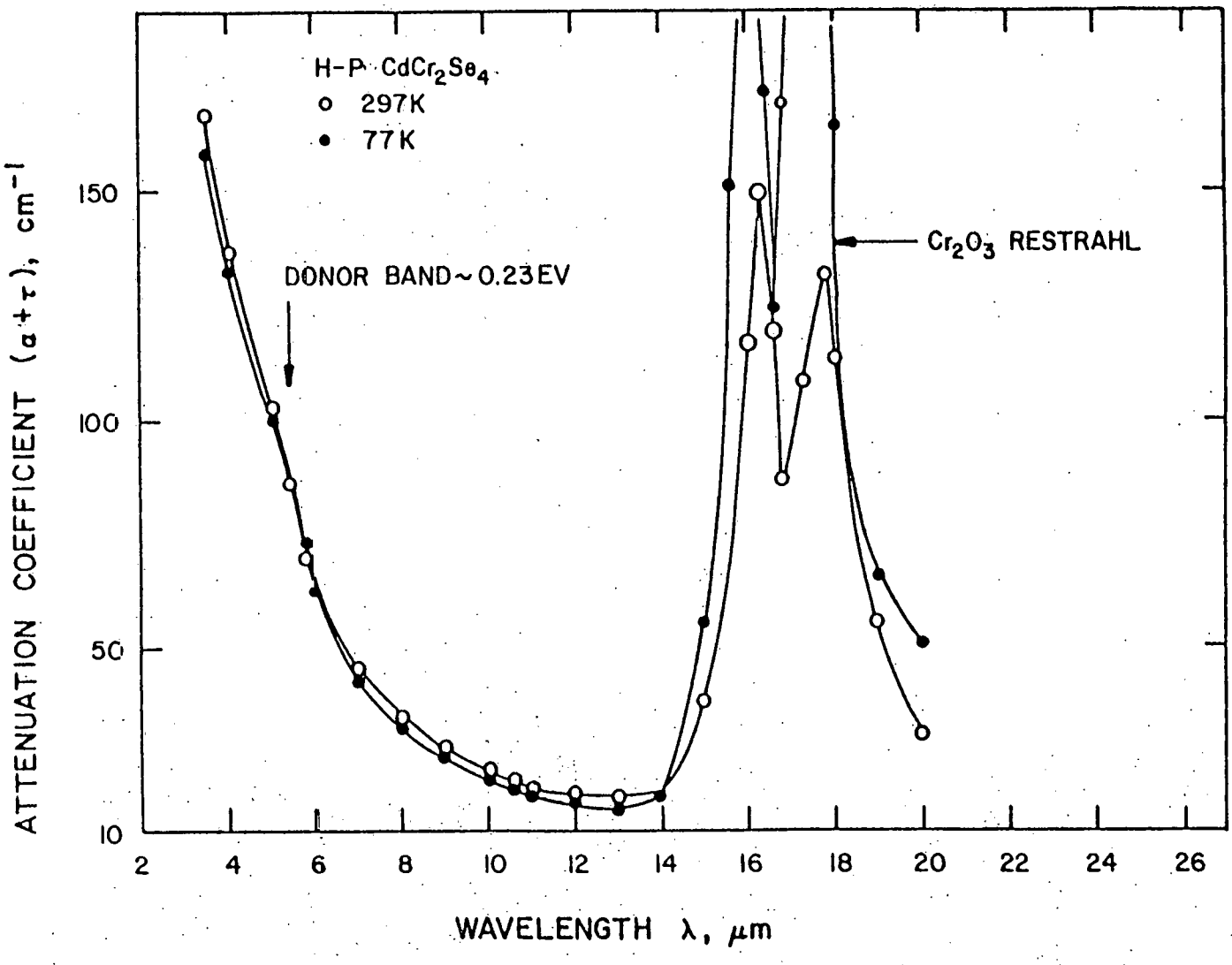

Figure 5.35. Infrared absorption spectra of hot-pressed $CdCr_2Se_4$ (p.s. $\leq 1\mu m$) at room temperature and liquid nitrogen temperature.

be true in $CdCr_2Se_4$ in which case the increase in transmission cannot be accounted for a decrease in n. And the decrease in attenuation can be attributed to carrier quenching.

In summary, the large absorption in hot-pressed $CdCr_2Se_4$ at long wavelengths indicative of free-carrier absorption was found to be due to holes introduced by excess selenium present in the virgin powders. Free-carrier absorption was reduced by removing selenium from the powders during the initial stage of densification. The lowest absorption coefficient obtained at 10.6μm was $12.1cm^{-1}$ at room temperature. Also, samples with absorption coefficients lower than $25cm^{-1}$ at 10.6μm were found to have room temperature electrical resistivities greater than $1.5 \times 10^3 \Omega cm$. In addition, these samples had an electrical resistivity behavior indicative of n-type conduction with an activation energy for electrical conduction of 0.23ev between 200K-297K.

B. Scattering

In the last section it was shown that the infrared attenuation of hot-pressed $CdCr_2Se_4$ varies very little with temperature for samples with room temperature electrical resistivities higher than $1.5 \times 10^3 \Omega cm$ as shown in Figure 5.35. This indicates that the residual attenuation is due to a temperature insensitive mechanism such as scattering. Microstructural and x-ray diffraction studies

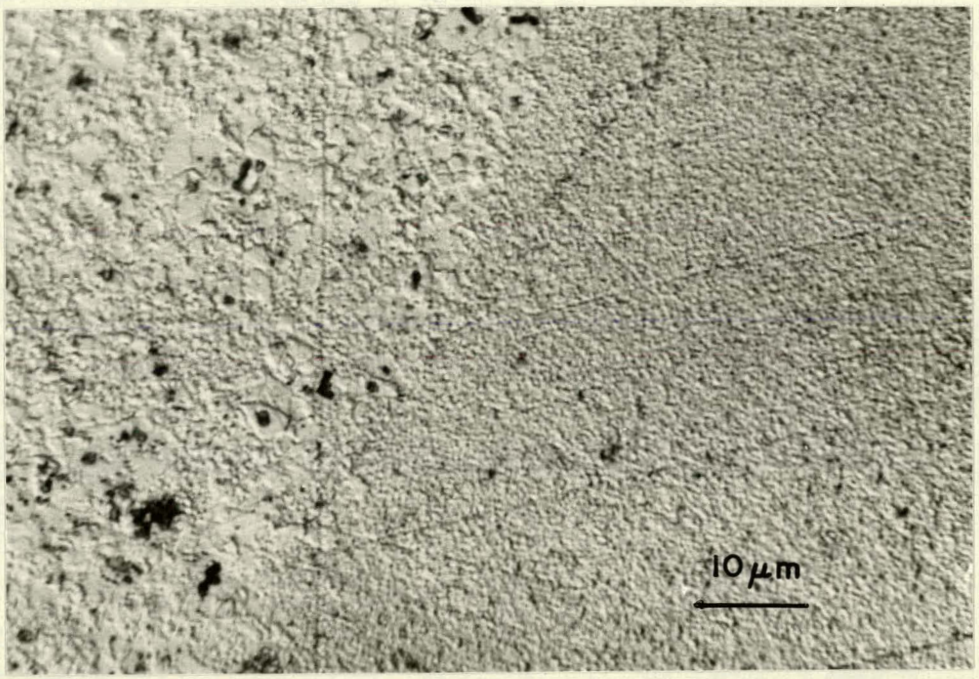

Figure 5.36. Etched surface of hot-pressed $CdCr_2Se_4$ ($\leq$1μm).

of hot-pressed $CdCr_2Se_4$ show that pores and second phases, CdSe and Cr_2Se_3, are present as shown in Figure 5.36 and Figure 5.8. Also infrared spectrophotometry shows two strong absorption bands at 16.3μm and 18.9μm. These bands were found to be due to Cr_2O_3 reststrahl processes, Figure 5.35. The values of $T.O._1$ and $T.O._2$ are in close agreement with the published values of $T.O._1$ and $T.O._2$(92,93) of 16.2μm ($618cm^{-1}$) and 18.2μm($550cm^{-1}$). Therefore it is most likely that the residual absorption observed is due to scattering by pores due to incomplete densification, second phases, CdSe and Cr_2Se_3, introduced mainly by the decomposition of $CdCr_2Se_4$ during hot-pressing and Cr_2O_3 present in the as grown powders.

Figure 5.37 shows that the attenuation coefficient at 10.6μm decreases with increasing porosity and that densities greater than 99.8% are necessary for attenuation coefficient $\leq 1cm^{-1}$ at 10.6μm. As shown in Chapter 5.1, porosity in hot-pressed $CdCr_2Se_4$ arises from incomplete densification due to second phases in the as grown powders and from decomposition during the intermediate stage of densification. Figure 5.38 shows that the attenuation coefficient at 10.6μm increases with second phase concentration. A least squares fit shows that at zero concentration, according to x-ray diffractometry, the attenuation coefficient is $14cm^{-1}$. This value however is high because x-ray diffractometry is not

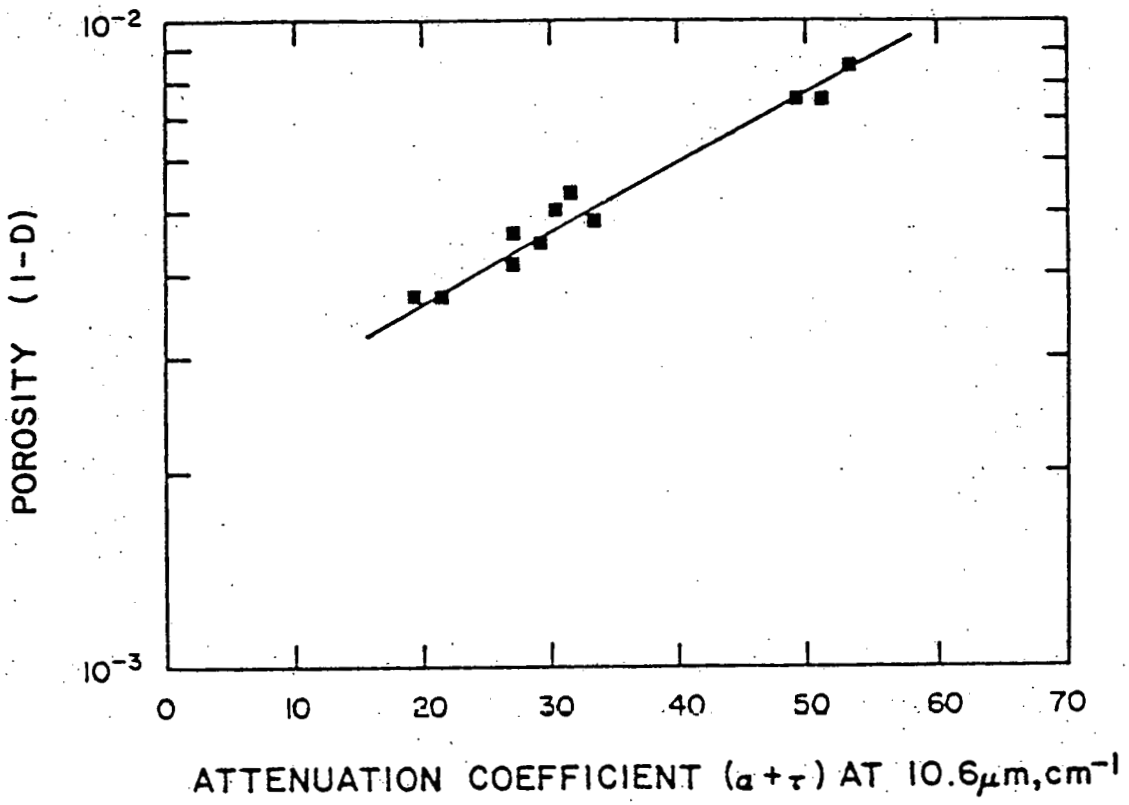

Figure 5.37. Attenuation coefficient ($\alpha + \tau$) at $\lambda = 10.6\mu m$ vs porosity of hot-pressed $CdCr_2Se_4$ (p.s. $\leq$ 1μm).

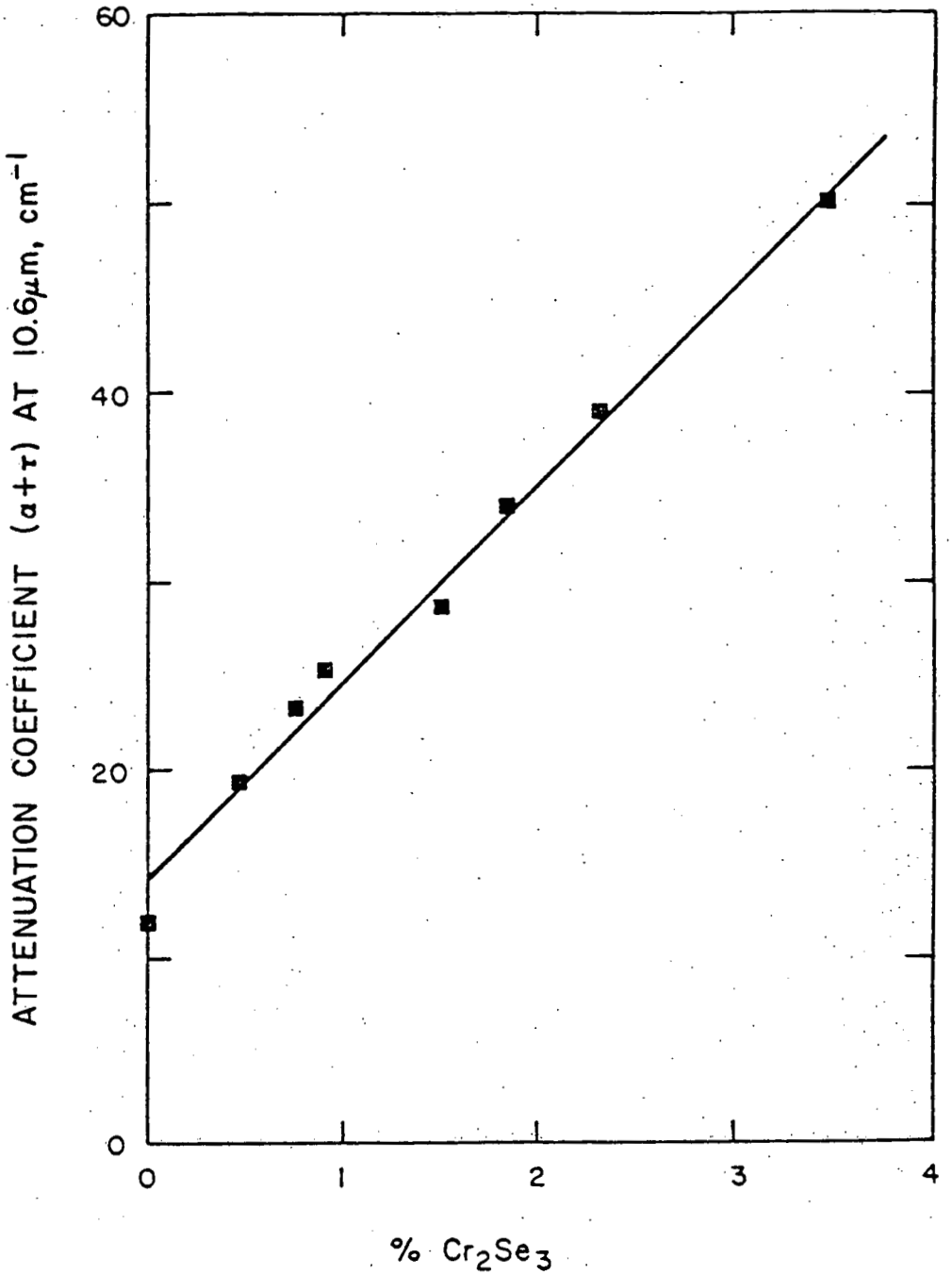

Figure 5.38. Cr_2Se_3 concentration, (I(101) Cr_2Se_3/ I(440)$CdCr_2Se_4$), vs attenuation coefficient at 10.6μm in hot-pressed $CdCr_2Se_4$.

sensitive to concentrations less than ~1%. Figure 5.39 further shows that decomposition which is responsible for the incomplete densification and therefore scattering, occurs during the intermediate stage of densification. The effect of incomplete densification can also be seen in samples hot-pressed at temperatures lower than 710°C. Figure 5.40 shows that the attenuation coefficient at 10.6μm is a minimum at a hot-pressing temperature of ~710°C. At temperatures less than 710°C the material does not densify completely and less free-selenium evaporates during the soaking period. At temperatures ~750°C more decomposition occurs and thus the increase in attenuation. The effect of density and decomposition is also seen in samples hot-pressed at lower final pressures as shown in Figure 5.41. At lower final pressures more selenium and cadmium evaporate thus increasing the amount of decomposition. At higher pressures on the other the high attenuation is attributed to gas entrappment and a lower electrical resistivity.

As shown in Section 5.1 fine powders (p.s. $\leq$ 1μm) densify to higher relative densities than coarse particles ($\leq$ 20μm) and single crystals (0.01 - 0.1cm). Figure 5.42 shows that in hot-pressed $CdCr_2Se_4$ with two particles sizes and resistivities higher than $1.5 \times 10^3 \Omega cm$ scattering is much larger in coarse powders. This is attributed to the incomplete densification and presence

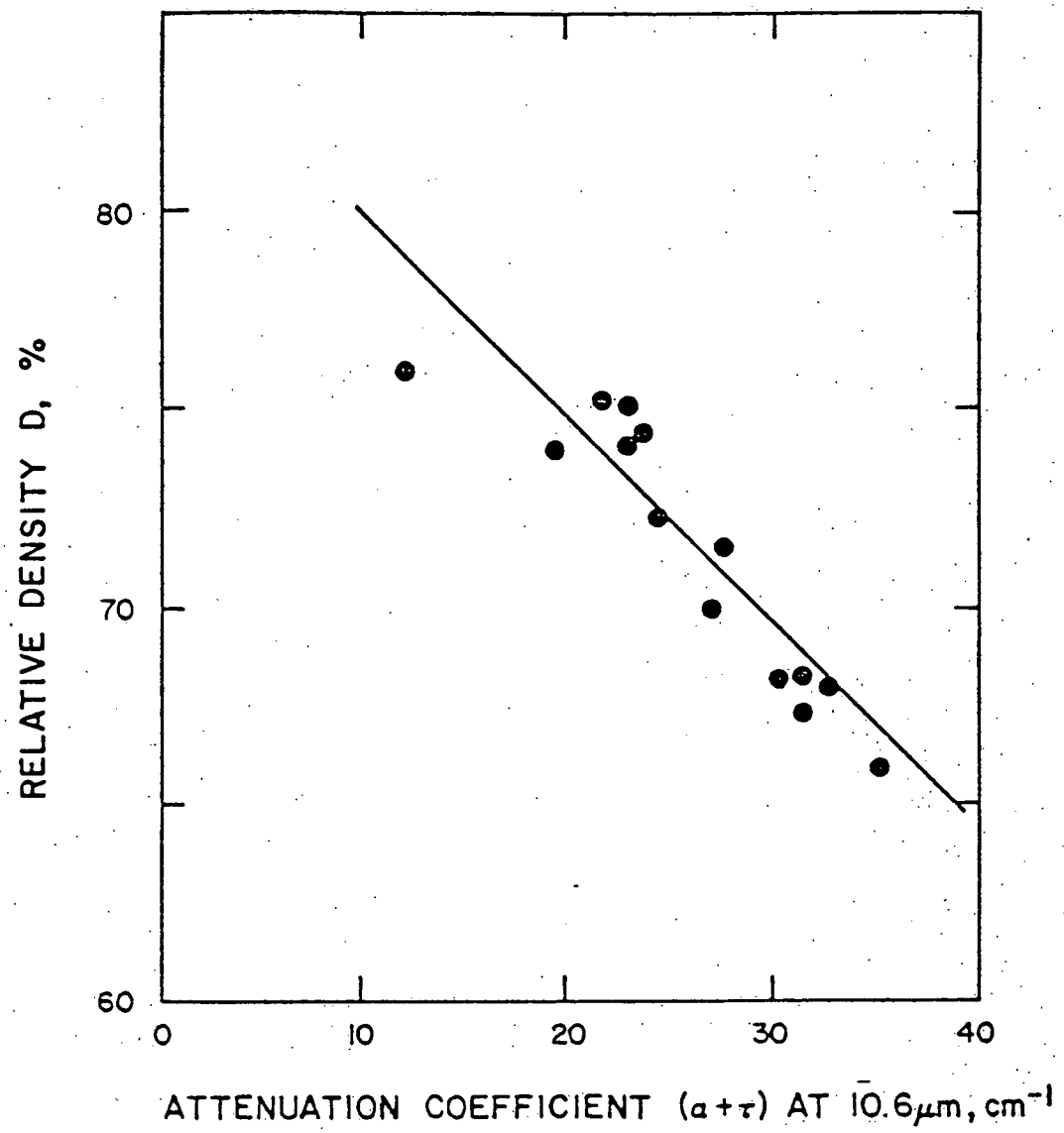

Figure 5.39. Attenuation coefficient ($\alpha + \tau$) at λ =10.6μm vs relative density, D, at the end of the intermediate stage of densification.

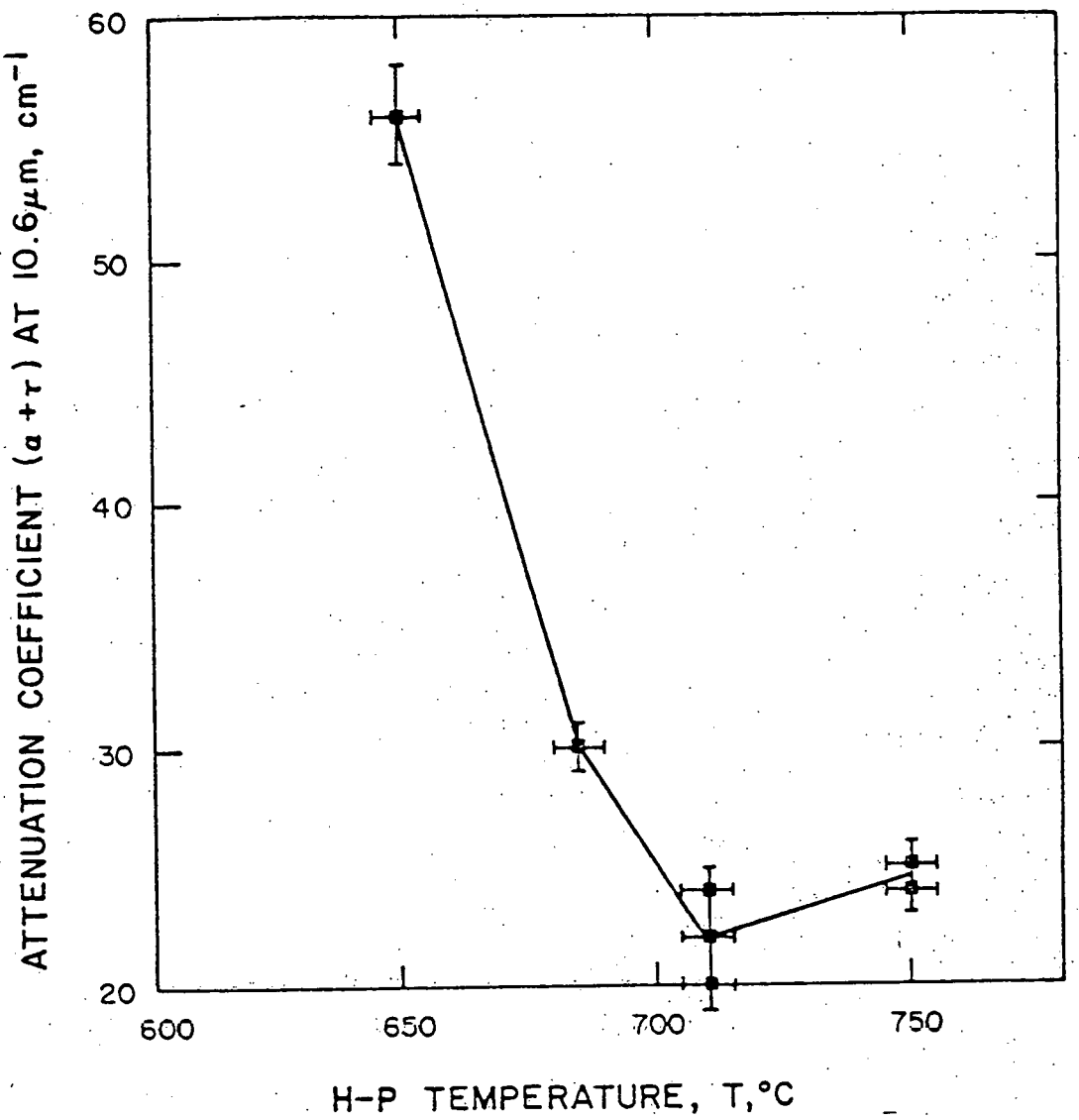

Figure 5.40. Attenuation coefficient ($\alpha + \tau$) at $\lambda = 10.6\mu m$ of hot-pressed $CdCr_2Se_4$ vs hot-pressing temperature.

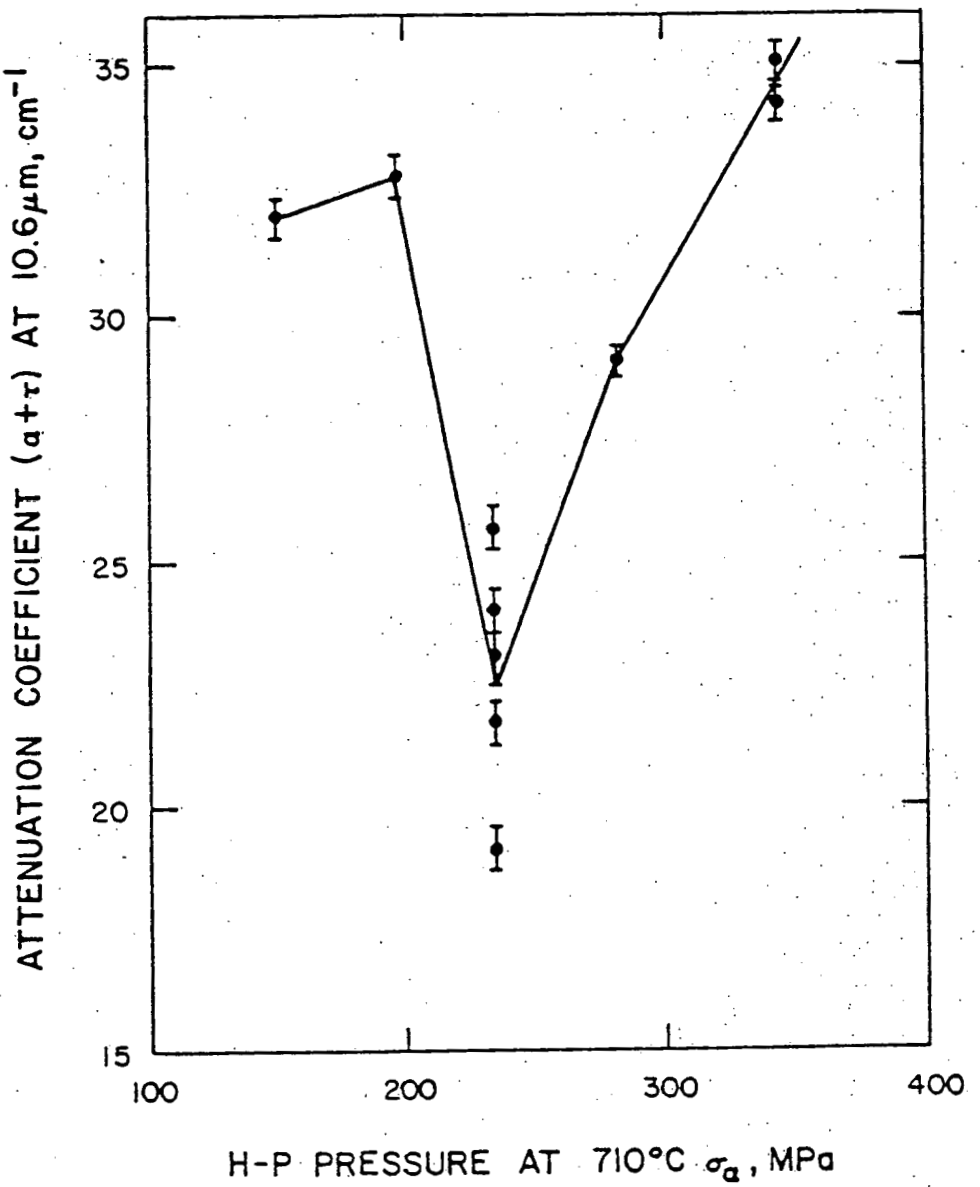

Figure 5.41. Attenuation coefficient ($\alpha + \tau$) at $\lambda = 10.6\mu m$ of hot-pressed $CdCr_2Se_4$ vs hot-pressing pressure.

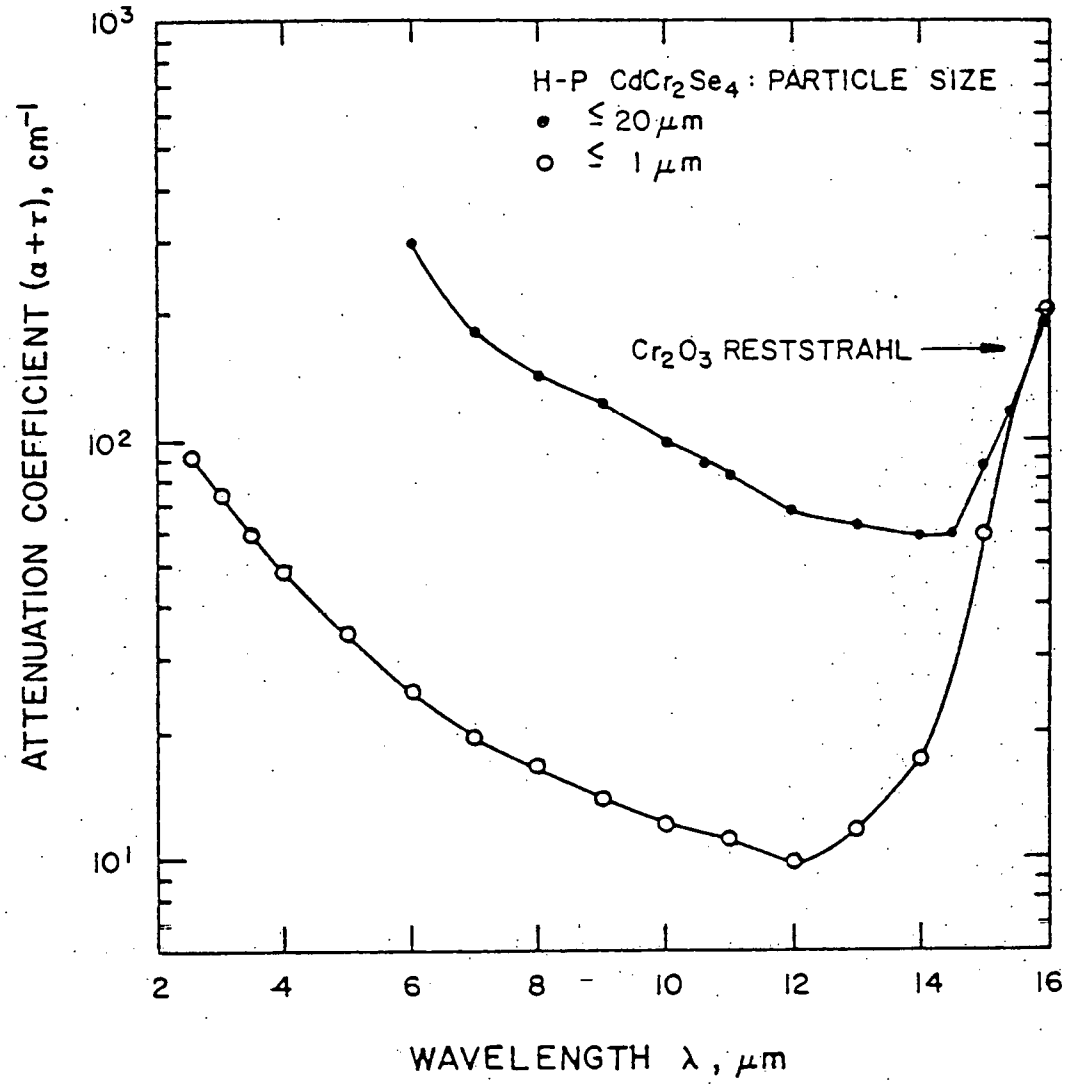

Figure 5.42. Infrared absorption spectra of hot-pressed $CdCr_2Se_4$ with two particle sizes.

of second phases at grain boundaries.

A further indication that second phases cause severe scattering in hot-pressed $CdCr_2Se_4$ is seen in Figure 5.43. In these samples the second phase concentration was changed by increasing the outgassing time thereby losing selenium and aiding decomposition. The selenium deficiency is clearly seen in the spectra, Figure 5.4, showing the wide absorption band centered at ~0.23ev. The scattering at short wavelengths is attributed to the higher concentration of second phases and also to the larger size of CdSe as microstructureal observations show. Cr_2Se_3 is not detected by optical microscopy nor is it detected by SEM with an electron microprobe attachment.

In summary, residual attenuation in hot-pressed $CdCr_2Se_4$ is caused mainly by pores and second phases present mostly as a consequence of decomposition during hot-pressing.

5.2.3. Hot-Pressed $(1-x)CdCr_2S_4 \cdot x\, CdCr_2Se_4$

Figure 5.44 shows the infrared spectra of the physical mixtures of as grown $CdCr_2Se_4$ and $CdCr_2S_4$ fine powders (p.s. $\leq$ 1μm). Three features can be observed. As the compositional parameter x increases the attenuation coefficient decreases. Also, the increase in absorption at long wavelengths with increasing wavelengths has a different wavelength dependence. The decrease in attenuation

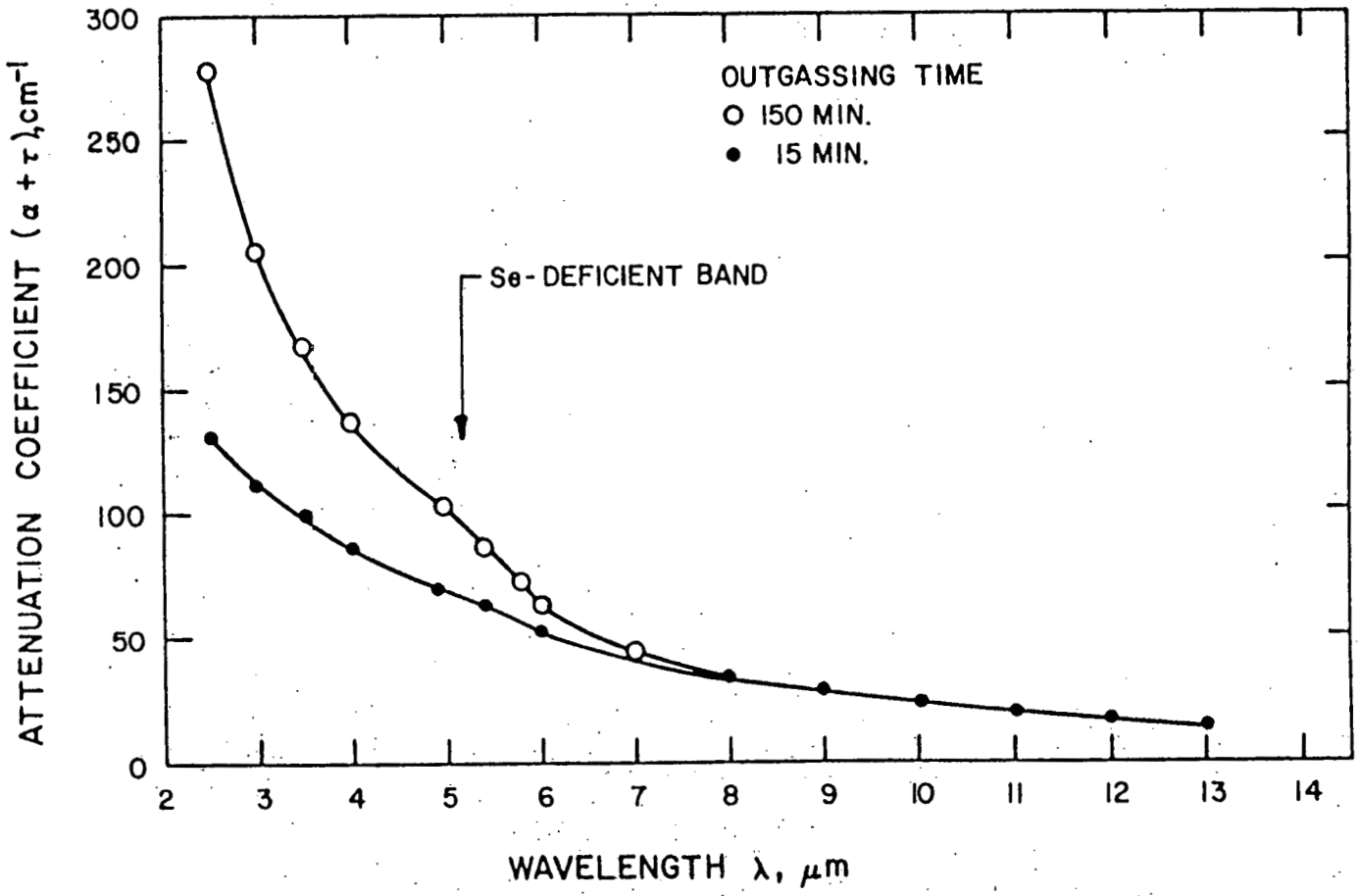

Figure 5.43. Infrared absorption of hot-pressed $CdCr_2Se_4$ showing the increased attenuation of short wavelength caused by second phases.

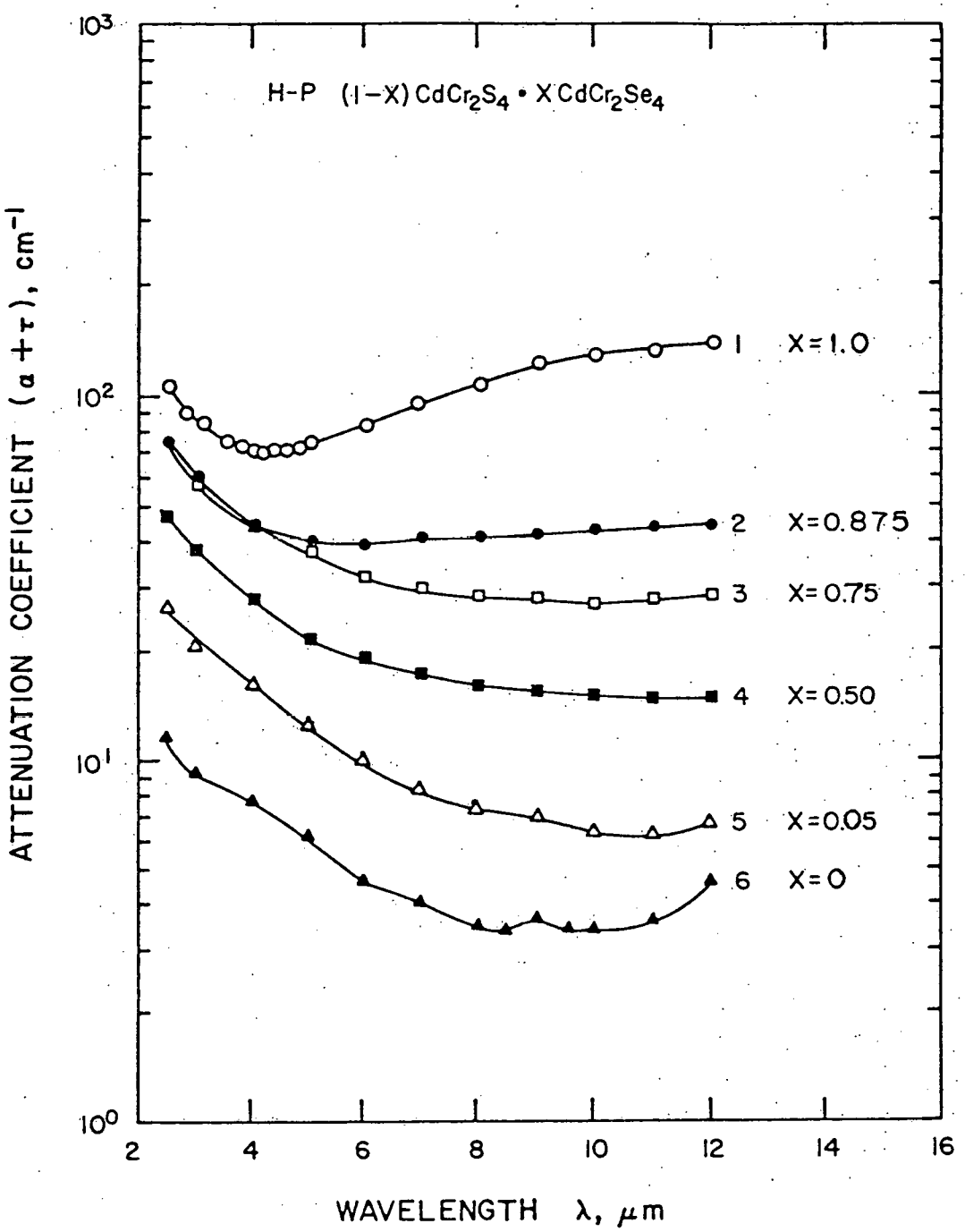

Figure 5.44. Infrared absorption spectra of hot-pressed $(1-x)CdCr_2S_4 \cdot xCdCr_2Se_4$ as a function of composition.

coefficient and the change in the wavelength dependence is attributed to a dilution effect of the free selenium in $(1-x)CdCr_2S_4 \cdot x\ CdCr_2Se_4$. Since $CdCr_2S_4$ is formed by flowing H_2S over the co-precipitated metal hydroxide powders at temperatures as high as 925°C(17) it is most likely that the it is more stoichiometric, i.e. it does not contain excess sulfur. Chemical analyses of similar as grown powders of $CdCr_2S_4$ carried out at Kodak Research Laboratories show that there is ~0.2% excess sulfur. However, upon hot-pressing at 900°C and 234MPa $CdCr_2S_4$ becomes sulfur deficient as Figure 5.24 shows. Therefore, upon the formation of the physical mixtures some excess selenium ions are incorporated in $CdCr_2S_4$. As a consequence the number of free-selenium ions produced at the grain boundaries is reduced and free-carrier absorption decreases with composition. The third feature to note is the scattering at short wavelengths. For x=0 the amount of scattering is much lower than the mixed powders. This, as x-ray diffraction of the hot-pressed materials show is due to the incomplete reaction of the two compounds to form a solid-solution and decomposition of $CdCr_2Se_4$ into CdSe and Cr_2Se_3 as shown in Figure 5.45. In addition, physical density measurements show that the powders were not completely densified. Relative densities of 99.5 - 99.7% were achieved for all compositions. Whereas, relative densities greater than 99.9% were not unusual for hot-pressed $CdCr_2S_4$.

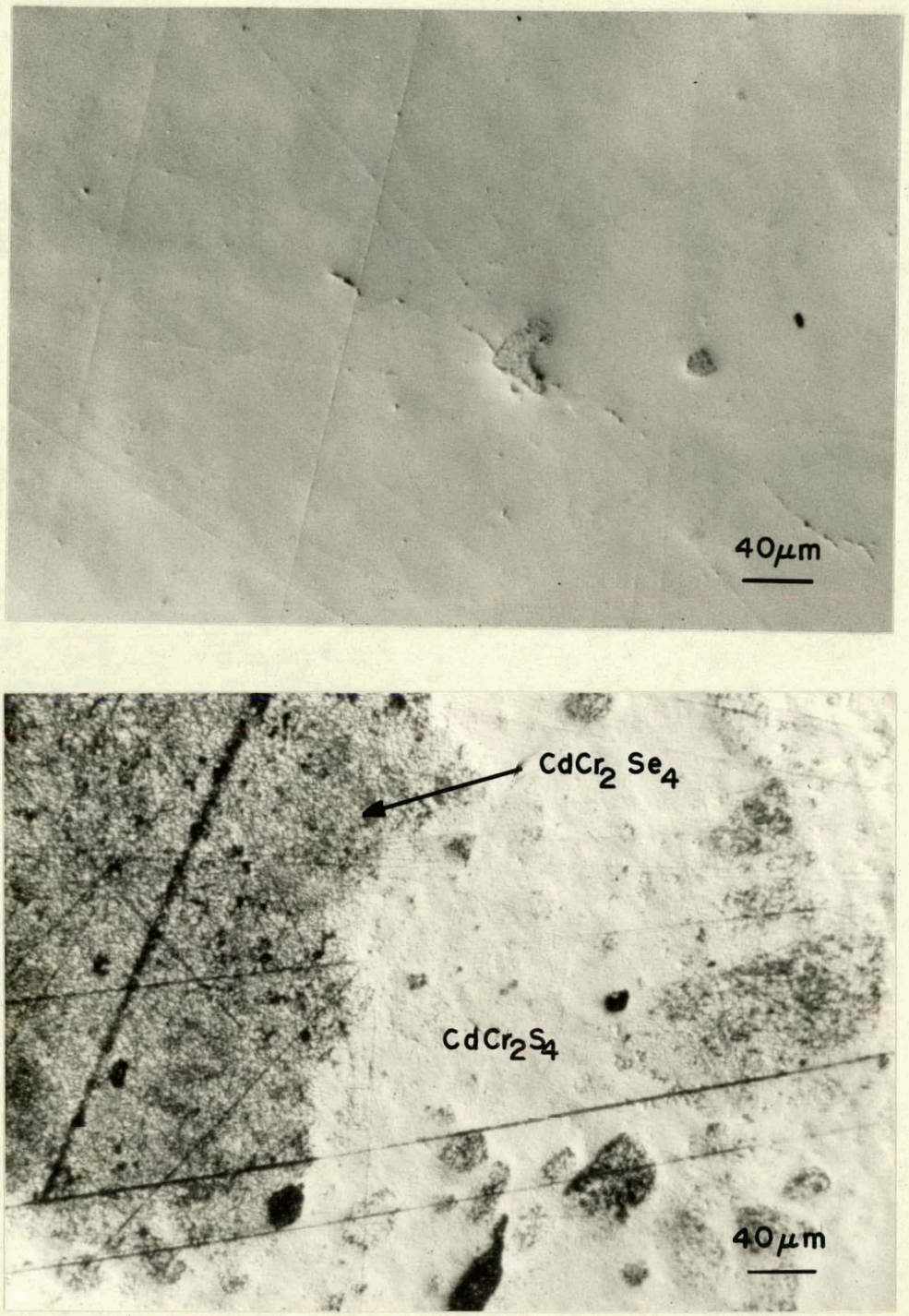

(a)

(b)

Figure 5.45. Optical micrographs of hot-pressed $\frac{1}{2}CdCr_2S_4 \cdot \frac{1}{2}CdCr_2Se_4$; (a) polished surface, (b) etched surface.

The mixed system $(1-x)CdCr_2S_4 \cdot x\ CdCr_2Se_4$ was hot-pressed using the same procedure as for $CdCr_2Se_4$ as indicated in Figure 4.6, with the exception of the final hot-pressing temperature and the clamping pressure. The hot-pressing temperature varied from 710°C for x=0 to 900°C for x=1, see Table 5.1. The clamping pressure was maintained at ~80MPa both during the heating period and the intermediate stage of densification. The solid solutions with x=0.5 were hot-pressed under the same conditions

Two-phonon absorption bands observed in hot-pressed $CdCr_2S_4$ were reduced and shifted to longer wavelengths by forming the solid solutions and physical mixtures. Figure 5.44 shows the infrared absorption spectra with the two-phonon absorption bands slightly shifted and reduced for x=0.95. For values greater than 0.95 the two-phonon absorption bands were not observed because of the Cr_2O_3 reststrahl at 16.3μm. Also, since Cr_2O_3 could not be removed from the samples, the analysis of reststrahl and multiphonon absorption was not possible.

Presently the absorption coefficient of $(1-x)CdCr_2S_4 \cdot x\ CdCr_2Se_4$ is limited by scattering by pores, second phases, possibly free-carrier absorption at long wavelengths and by the Cr_2O_3 reststrahl.

Thus, our experiments show that $(1-x)CdCr_2S_4 \cdot x\ CdCr_2Se_4$ is extrinsically limited, addition of $CdCr_2Se_4$ reduces phonon absorptions but its decomposition must be reduced in order to decrease the attenuation coefficient.

TABLE 5.2. HOT-PRESSING TEMPERATURE OF $(1-x)CdCr_2S_4 \cdot x\ CdCr_2Se_4$
(σ_a = 234MPa, t = 20min.)

SAMPLE NO.	$(\alpha + \tau)$ at 10.6μm cm^{-1}	H-P T °C	COMPOSITION x
LKSSe01	7.3	900	0.05
LKSSe05	14.9 - 18.0	800	0.5
LKSSe06	19.6	775	0.75
LKSSe07	43	750	0.875
LKRSSe08*	18.0	900	0.5

*Solid-solution formed at 670°C in vacuum for three days.

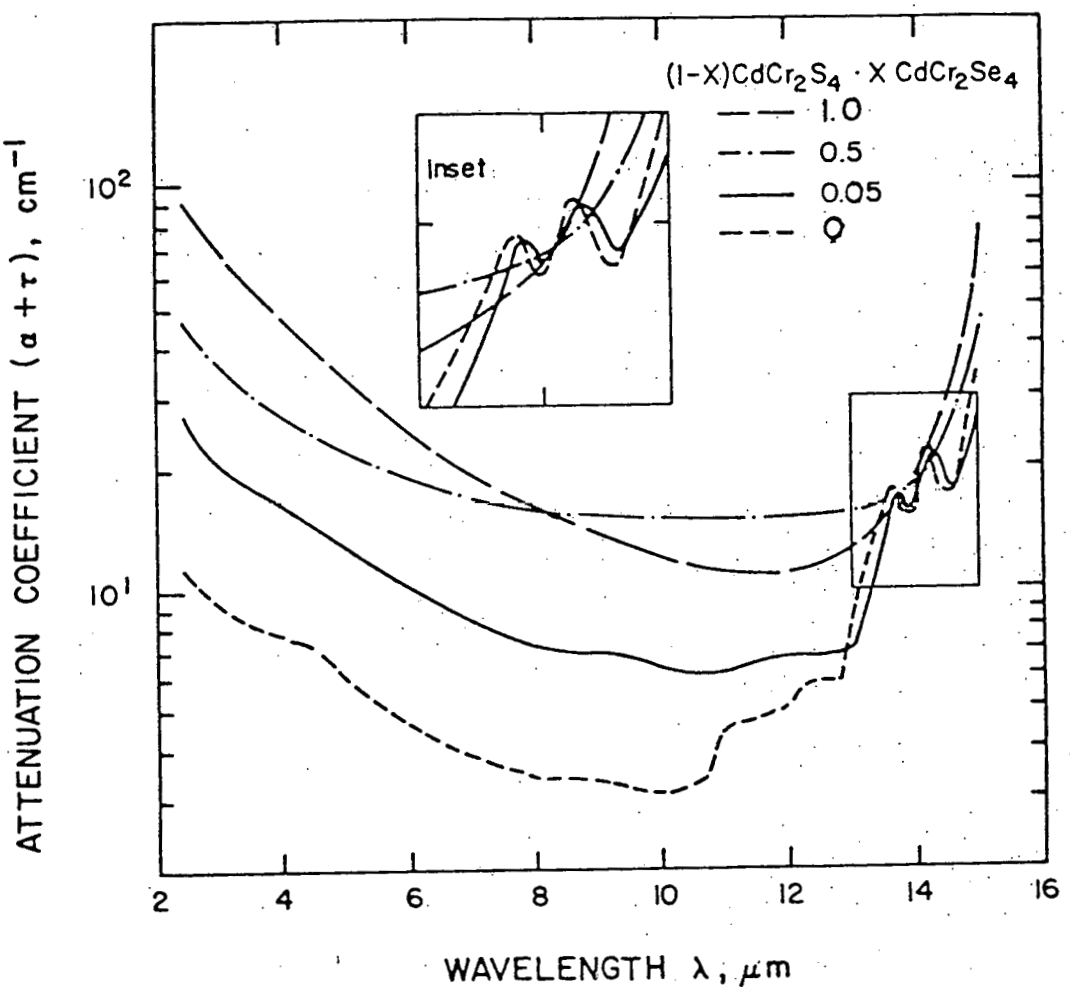

Figure 5.46. Infrared absorption spectra of hot-pressed $(1-x)CdCr_2S_4 \cdot xCdCr_2Se_4$ showing scattering at short wavelengths and two-phonon absorption bands at longer wavelengths.

5.3. Conclusions

$CdCr_2Se_4$ and $(1-x)CdCr_2S_4 \cdot x\ CdCr_2Se_4$ have been hot-pressed to relative densities of 99.6% and 99.7% respectively. The minimum attenuation coefficient of hot-pressed $CdCr_2Se_4$ obtained at 10.6μm was $12.1cm^{-1}$ at room temperature. In $(1-x)CdCr_2S_4 \cdot x\ CdCr_2Se_4$ a minimum attenuation coefficient of $14.9cm^{-1}$ was obtained for $x=\frac{1}{2}$.

At long wavelengths, the major absorbing mechanisms in hot-pressed $CdCr_2Se_4$ were found to be free-carrier absorption and Cr_2O_3 reststrahl absorption. Free-carrier absorption was found to be induced by free-selenium present in the as grown powders. Suppression of free-carrier absorption was achieved by removing selenium from the powders during the initial stage of densification. The residual attenuation in hot-pressed $CdCr_2Se_4$ and $(1-x)CdCr_2S_4 \cdot x\ CdCr_2Se_4$ was found to be due to scattering by pores and second phases (CdSe, Cr_2Se_3, Cr_2O_3) and Cr_2O_3 reststrahl absorption. The pores are present because of incomplete densification due to the presence of second phases in the as grown powder and from decomposition mainly during the intermediate stage of densification.

The data presented in this report show that materials preparation is indeed very important. Submicron single phase powders are necessary to achieve complete densification. Also, it was shown that the hot-pressing procedure is critical in improving the optical properties. Specifically, the hot-pressing process must be optimized in order to

prevent excessive selenium and cadmium loss. This would be especially important for short wavelength applications since the selenium and cadmium deficiency bands occur at short wavelengths. This is also the case in $CdCr_2S_4$ where a very broad band is observed from 2.8-5.2μm.

Materials preparation can be improved using higher purity starting materials (CrO_3, CdO), optimizing the co-precipitation process and most important optimize the treatment of the co-precipitated hydroxides in $H_2 + \frac{1}{2}Se_2$ in order to decrease the second phase concentration.

Solid-solutions and physical mixtures of $CdCr_2S_4$ and $CdCr_2Se_4$ with $x \leq \frac{1}{2}$ were shown to be extrinsically limited by scattering and possibly free-carrier absorption. Further, it was shown that two-phonon absorption bands were shifted and reduced in intensity with increasing selenide concentration.

In addition, it was shown that $CdCr_2S_4$ is limited not only by two-phonon absorption but also by three-phonon absorption near 10.6μm and a new three-phonon sum frequency combination was assigned to the band occuring at 800cm^{-1} instead of a two-phonon combination.

As a consequence of the data presented in this report $CdCr_2Se_4$ and the solid solutions of $(1-x)CdCr_2S_4 \cdot x\ CdCr_2Se_4$ with $x \leq \frac{1}{2}$ would be better candidates for applications up to $\lambda = 10.6\mu m$. However extrinsic absorption still needs to be reduced further.

VI. INFRARED PHOTOACOUSTIC SPECTRA OF TRANSPARENT SEMICONDUCTORS IN THE POWDER STATE FROM 1 μm - 15 μm

Quantitative absorption spectra of highly transparent material in the powder form are often difficult or impossible to obtain using standard techniques available today. This is due to a variety of reasons including: 1) the highly scattering nature of the powders, 2) the minute size of the individual particles, and 3) the high optical transparency of the grains themselves ($\beta\delta << 1$ where δ is the mean particle diameter). For the high refractive index ($n = 2.8 - 4.0$) materials of interest in this investigation, the problem is particularly serious since the Fresnel reflection coefficients are large, the powder particle sizes may be on the same order as infrared wavelengths, and $\beta\delta$ may be less than 10^{-4}. In this section we investigate the ability of the photoacoustic method to overcome these difficulties and obtain both qualitative and quantitative information regarding the infrared absorption properties of three highly transparent semiconductors in the powder form in the 1 - 15 μm region of the infrared.

6.1. Samples

Infrared photoacoustic spectra were obtained on three transparent infrared semiconductors in the powder form:

germanium, $CdCr_2Se_4$ and $CdCr_2S_4$. The intrinsic grade germanium powders, which were obtained from Eagle Pitcher Industries, were examined primarily because of their well known optical properties. As such, the photoacoustic spectra of germanium may be used to investigate and verify the ability of the photoacoustic method to obtain information regarding the physical and optical properties of the powder.

Initial efforts to investigate the optical properties of the spinel powders in the 1 - 15 μm region of the infrared using standard transmission and pellet techniques have not been successful. In most cases, the single crystals were too small to be able to employ standard spectrophotometric microsampling methods. Attempts to implant a small concentration of the powders in either KBr Nujol, or selenium pellets also proved to be unsuccessful. Pellets made in this fashion were often too opaque or too scattering to analyze, mainly due to the extremely high spinel indices of refraction (3.15 and 2.85 for $CdCr_2Se_4$ and $CdCr_2S_4$ respectively). When the powder concentration was reduced to yield transparent pellets, the quantity of powder used was not large enough to yield any spectral information. Additional problems including the destructiveness and the non-quantitative information capability of the technique also made the method undesirable.

The successful application of photoacoustic methods to the analysis of the optical properties of $CdCr_2Se_4$ and $CdCr_2S_4$ would eliminate the three main difficulties en-

countered in the transmission studies: size, sensitivity, and scattering. From our earlier results, we found that it is desirable to work with small sample sizes, since the photoacoustic signal is stronger for small cell volumes. We discovered that the photoacoustic method is one of the most sensitive techniques for measuring optical absorption. Also, since only the absorbed radiation contribute to the photoacoustic signal, highly scattering samples present no major difficulties. Additionally, as we shall see, the photoacoustic method is able to provide quantitative information regarding the optical properties of the powders. Thus, infrared photoacoustic spectra would not only assist in the understanding and optimization of the hot-pressing procedures, but also provide the first quantitative measurements of the optical absorption coefficients of these materials in powder form in the infrared. The latter capability is particularly important for studies concerned with the assessment of the suitability of $CdCr_2Se_4$ for Faraday rotation isolator and other magneto-optical applications.

6.2. Apparatus

In this section we report the first photoacoustic spectra ever obtained in the 1 - 15 μm region of the spectrum. Obviously, infrared photoacoustic spectrometers were not yet commercially available, and it was necessary

The bottom disk supported the weight of the glower, while the top disk maintained the glower in a vertical position. Additionally, the top disk was constructed in a manner which allowed the glower to expand during heating, thus reducing thermally induced mechanical stress. Asbestos was chosen to reduce the thermal contact between the 1500 K glower and the aluminum holder.

Preheating of the ceramic rod was accomplished using two tungsten heater wires wrapped around two ceramic cylinders and mounted symmetrically on either side of the glower. During the initial start-up procedure, current was allowed to flow through the tungsten wires. After the glower was sufficiently heated, the heater wires were then disconnected from the power supply.

The heater coils, asbestos disks, and Nernst glower were all mounted in a cylindrical aluminum cell with an open window drilled out. In this manner, the glower was protected from temperature variations (and thus variations in the output flux) caused by local air currents.

The leads of the glower were connected in series with a 150 watt light bulb across line voltage (120 vac). The light bulb, which has a positive temperature coefficient of resistance, provided a convenient ballast for the Nernst glower. During operation, the glower consumed 70 watts of power at an a.c. current of ~.8 amps. Finally, we note that the 60 Hz line voltage could be used in place of a

to construct our own. The design, operation, and calibration of the photoacoustic spectrometer will therefore be described in the following sections.

A block diagram of the apparatus is presented in Figure 6.1. Generally speaking, broadband laser sources of radiation are not tunable over the 1 - 15 μm region of the infrared. As a result, a 24 mm long by 2 mm wide PE-2 Nernst glower obtained from Buck Scientific was employed as the broadband source of infrared radiation. The Nernst glower is a thermal source of radiation and operates at a temperature of approximately 1500 - 1800 K with an emissivity of approximately .5. Thus, its output strongly resembles that of a 1500 K blackbody. The glower itself is comprised of a proprietary mixture of zirconium, yttrium and thorium oxides formed into a hollow rod (83). It is an extremely fragile device and must be mounted in a manner which minimizes the effect of mechanically or thermally induced stress. The glower also exhibits a large negative temperature coefficient of resistance and requires a ballasted power supply of approximately 70 watts at 70 VAC. At room temperature, the electrical resistance of the glower is greater than 10^9 Ω. Thus, it is necessary to preheat the rod in order to turn the device on.

The Nernst glower was mounted in a specially designed holder, diagrammed in Figure 6.2. The ends of the ceramic rod were positioned in holes drilled in two asbestos disks.

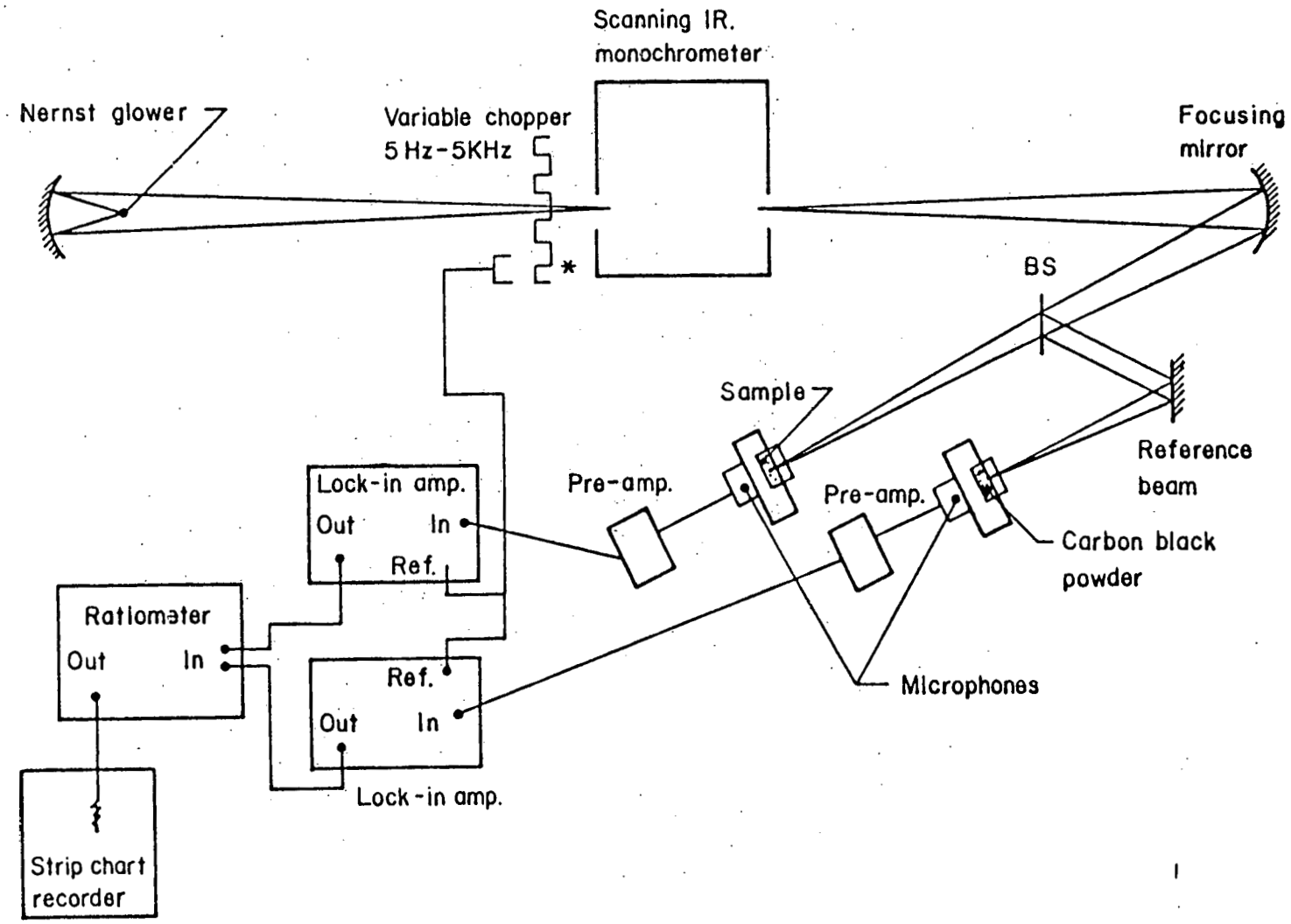

Figure 6.1. Diagram of the dual beam IR photoacoustic spectrometer.

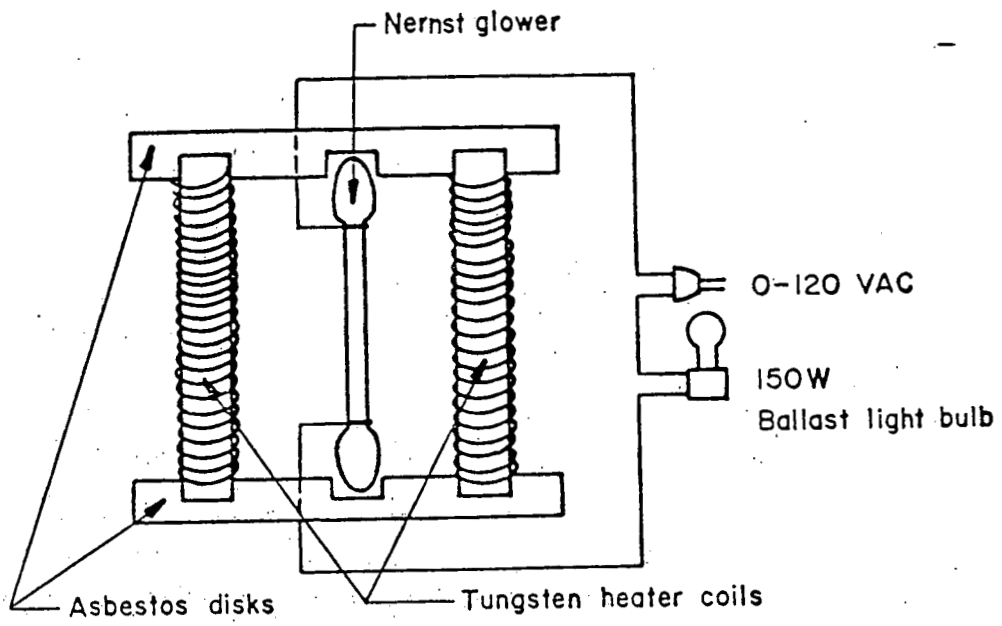

a.

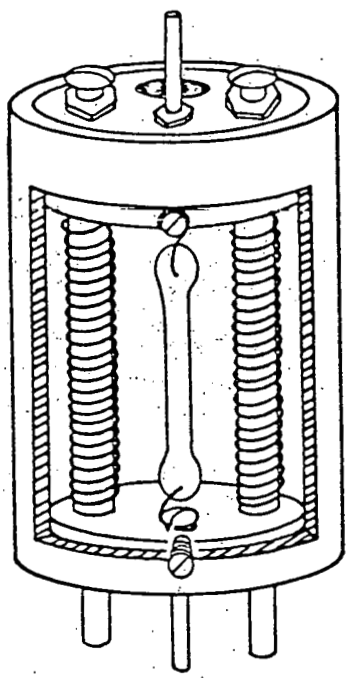

b.

Figure 6.2. Nernst glower housing and mountin geometry.

d.c. power supply since the large thermal mass of the glower prevented the emittence of the device from following the a.c. electrical power fluctuations.

The output of the Nernst glower was collected by a f/2.8 Al coated front surface mirror, modulated by a synchronous motor driven chopper, and imaged 1:1 on the input slots of a f/5.6 collection optics Zeiss double prism monochromator. The dispersive element in the double monochromator consisted of two KBr prisms, which were used for their high transmission in the 1 - 15 μm transmission region of interest. The KBr prisms, which are highly hygroscopic and subject to atmospheric degradation, were kept 5 °C above room temperature and enclosed in a steel shell to prevent their degradation. It should also be noted that, due to the size of the prisms, only a f/9 cone angle of light could be dispersed in spite of the f/5.6 collection optics of the monochromator. This fact will be important later when the subject of photoacoustic spectrometer optimization is addressed, since the smaller collection angle implies that less total dispersed radiation power is available for use in the generation of the photoacoustic signal.

The wavelength of the radiation available at the exit slits of the monochromator could be varied by turning a dial which altered the angle of incidence of the KBr prisms. This system was modified for continuous scanning by at-

taching a reduction gear train to the dial and driving the former with a synchronous motor. In this manner, the time necessary to complete an entire photoacoustic spectrum could be varied as circumstances dictated. Under normal operation, the gear train was set so that a 1 μm to 15 μm spectrum could be obtained in ~ 75 minutes.

The output of the monochromator was collected by an f/4 40 cm focal length front surface coated mirror, split into two equal beams, and focused onto the front surface of two photoacoustic cells. The electrical output of the two photoacoustic cells was then sent into two Ithaco 391A Dynatrac lock-in amplifiers, normalized by a ratiometry and displayed on a Honeywell strip chart recorder. During normal operation, one of the photoacoustic cells was filled with carbon black powder in a manner similar to that discussed in ref. (78) and acted as a detector of optical radiation. Employment of the carbon black cell thus enabled the photoacoustic signal from the opposite cell to be normalized for incident power fluctuations resulting from either atmospheric absorption or Nernst glower instabilities. A photoacoustic detector was selected primarily because it was the most sensitive large aperture room temperature broadband infrared detector available.

6.3. Procedure

Approximately 100 mg of sample powder was placed in

the optimized photoacoustic cell whose design was described earlier (78) and Fig. 6.3 . The powder and cell were then heated to approximately 150 °C for ~ 15 minutes to reduce the detrimental influences of any water which might be present on the cell or in the sample itself. A new Harshaw NaCl window was then waxed into place, and the cooled cell attached to the microphone in a manner which oriented the cell window up. In this way, the powder did not come in contact with the NaCl window. Also, by placing different samples in separate but nearly identical photoacoustic cells, we were able to double check such factors as reproducibility and long term chemical decomposition without disturbing the sample itself.

In a dual beam spectrometer which employs an inhomogeneous source (i.e., a source whose radiance and wavelength dependence of radiance is a function of position on the source; e.g., a Nernst glower), it is extremely important to insure that the beamsplitter divides the optical beam symmetrically in order to maintain a flat 100% line as a function of wavelength. For example, consider a hypothetical case where the hotter center portion of the Nernst glower was imaged onto one detector, while the cooler outer portion of the glower was imaged onto an identical detector. The radiance of the two beams as a function of wavelength would not be identical, since the blackbody radiation of the first beam would correspond to

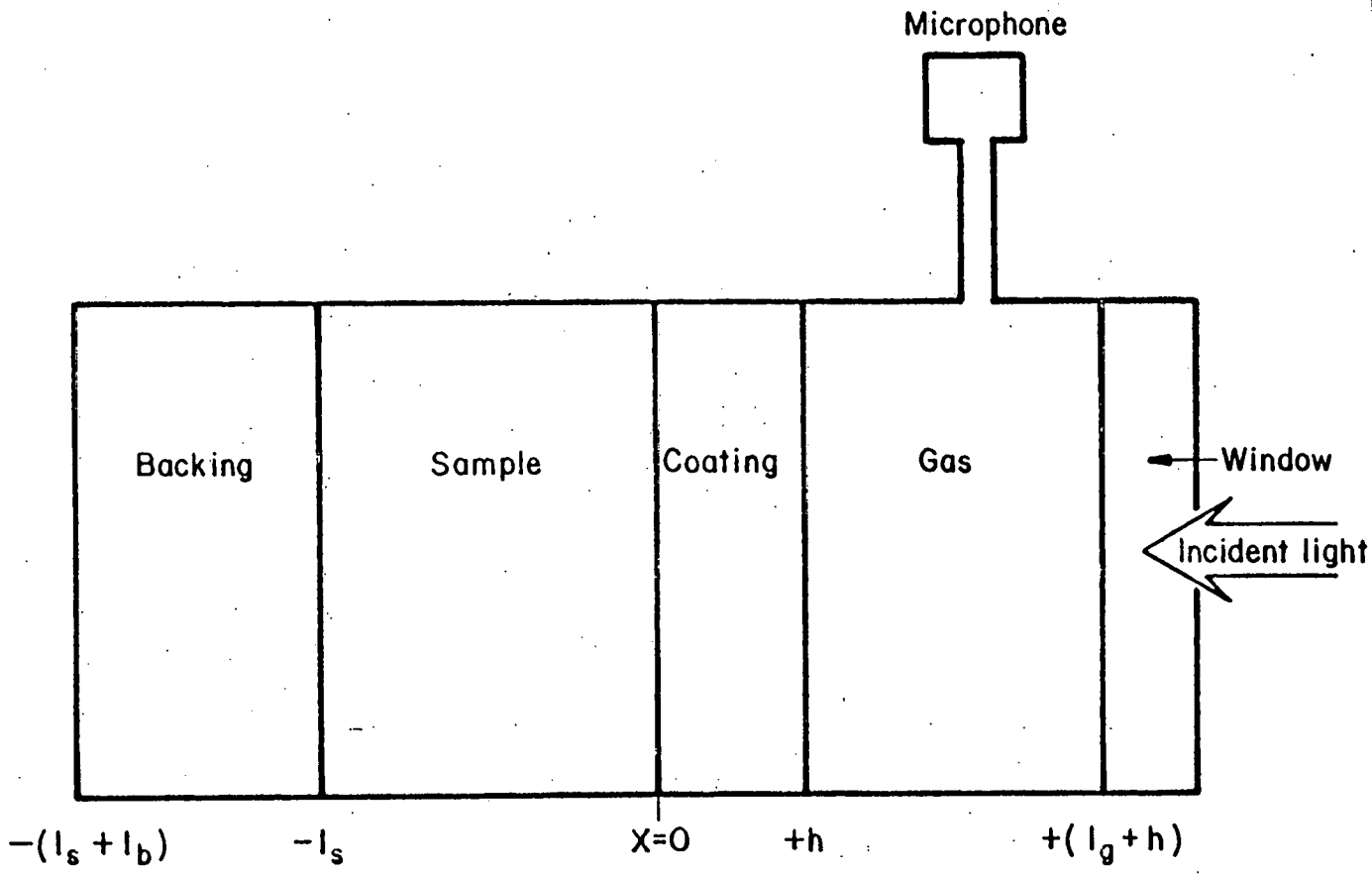

Figure 6.3. Photoacoustic cell sample geometry.

a significantly hotter blackbody than the second beam. Thus, the ratio of the two beams would vary as a function of wavelength.

This problem was minimized in the photoacoustic spectrometer by careful selection of the position and orientation of the reflective beamsplitter and Nernst glower. In order to maximize the etendue of the entire system, the glower was oriented in a vertical manner such that its long axis was parallel to the long axis of the monochromator slits. It was therefore optimal to orient the reflective beamsplitter in a manner which sent the top portion of the exit slits to one beam, while allowing the symmetric bottom portion of the exit slits to propagate as the second beam. The precise location of the beamsplitter was determined by measuring the total flux in the second beam, and then positioning the beamsplitter at a height which yielded exactly half the response as was measured from the full beam.

Once the beamsplitter was in place, the position of the photoacoustic sample cell was determined by visually inspecting the image of the source while the monochromator was set for green wavelengths of light. Since all of the optics in the photoacoustic spectrometer were reflective and thus achromatic, the position of the visible image corresponded to the position of the invisible infrared images. It should be noted that alignment of the monochro-

mator optics was also accomplished using a similar technique only using a HeNe laser as the visible source.

Due to the dispersion of the KBr prisms which were used, the resolution of the monochromator was a function of both the slit width and the average wavelength at the slits. Thus, it would be desirable to change the slit width as a function of wavelength in order to maintain constant resolution over the entire scan. Unfortunately, the construction, use, and location of the three slits on the Leiss monochromator made this goal impractical and photoacoustic spectrum were recorded at a fixed slit width. In the regions of low dispersion, or in the cases where higher resolution was desired, two separate spectrum using different slit widths were often recorded. For the semiconductor powders investigated in this study, most of the spectral features of interest were broad and well separated. Consequently, the normal slit width employed during photoacoustic spectra analysis was set for a resolution of $\Delta\lambda/\lambda = .1$ at 10.6 μ m.

Photoacoustic spectra were obtained by monitoring the amplitude of the photoacoustic signal as a function of wavelength at constant phase. The optimum phase angle was determined by setting the phase dial to force a null reading on the lock-in amplifier, then adding (or subtracting) 90° to this value. Once determined, the phase angle was not altered during a particular run. It should

also be noted that the lock-in parameters were set while the photoacoustic signal was at a maximum in order to reduce lock-in amplifier errors. In almost all of the photoacoustic spectra taken, a time constant of 1 sec was employed. Finally, we note that the spectra were recorded at a constant lock-in amplifier setting (i.e., the dials were not changed during a run).

6.4. Spectrometer calibration

Calibration of the dual beam photoacoustic spectrometer was accomplished using two well known sources of absorption: 1) the atmosphere and 2) polystyrene. A CO_2 laser beam (λ= 10.6 μm) and Nd:YAG laser beam (λ= 1.06 μm) were also employed. In the atmospheric absorption experiments, the beamsplitter was totally removed and the output of the monochromator allowed to fall incident upon the photoacoustic detector. The resulting spectra, obtained at fixed slit width, is shown in Figure as a function of the wavelength dial setting.

Inspection of Figure 6.4 reveals several features of interest. First of all, we see that the general envelope function of the spectrum resembles that of a blackbody curve. Since the Nernst glower approximates a blackbody source, the single beam spectrum indicates that our assumption regarding the carbon black and its role as an optical detector appears to be valid. The peak of the spectrum

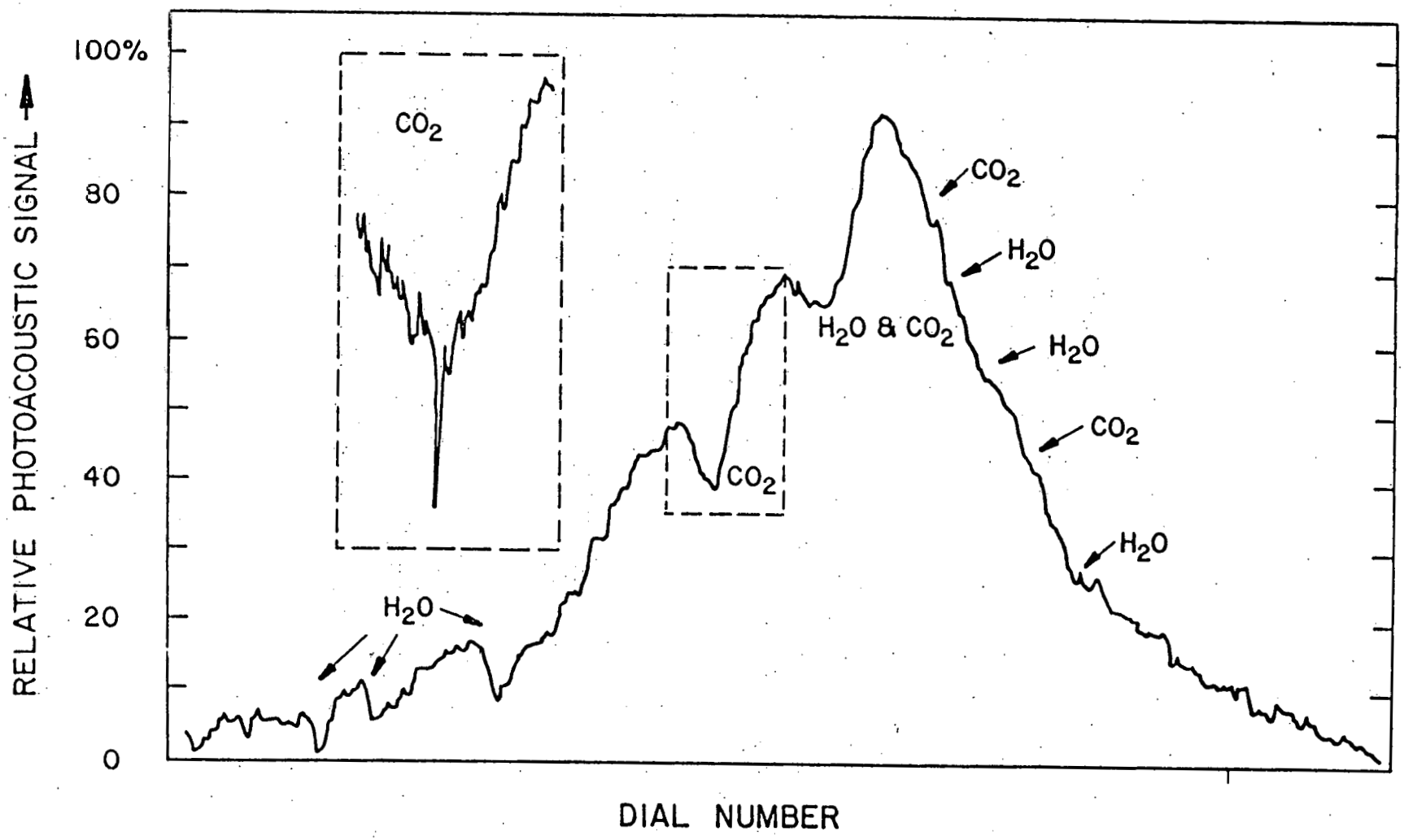

Figure 6.4. Single beam spectrum of air using the photoacoustic detector.

lies around 2.5 μm which is a significantly longer wavelength than the 1.9 μm value indicative of a 1500 K blackbody. However, it must be remembered that the output flux is a function of both the blackbody spectrum and the dispersion of the KBr prisms. Inspection of the latter, which is presented in Figure 6.5. reveals that the minimum dispersion of KBr is at 4 μm. Thus, the wavelength of maximum radiation will be shifted toward longer wavelengths in agreement with our experimental findings.

We also note that the short wavelength side of the spectrum appears to be much broader than a typical blackbody curve. However, this is a result of the extremely high dispersion of the KBr prisms in the 1 - 2 μm region. As such, the shorter wavelengths are "stretched" out to the right.

Several atmospheric absorption bands are clearly seen in Figure 6.4. These bands have been identified by comparing the transmission spectrum of the atmosphere(97) with the experimental spectrum, and the absorbing species have been noted on the figure. Of particular interest is the extremely strong CO_2 band at 4.3 μm, which is resolved better using a narrower slit width. This band is readily identified by its sharp peak and its common persistence in unequal path length dual beam spectrophotometers. The 6.0 μm and 2.7 μm water bands are also clearly resolved. At shorter wavelengths, the atmospheric

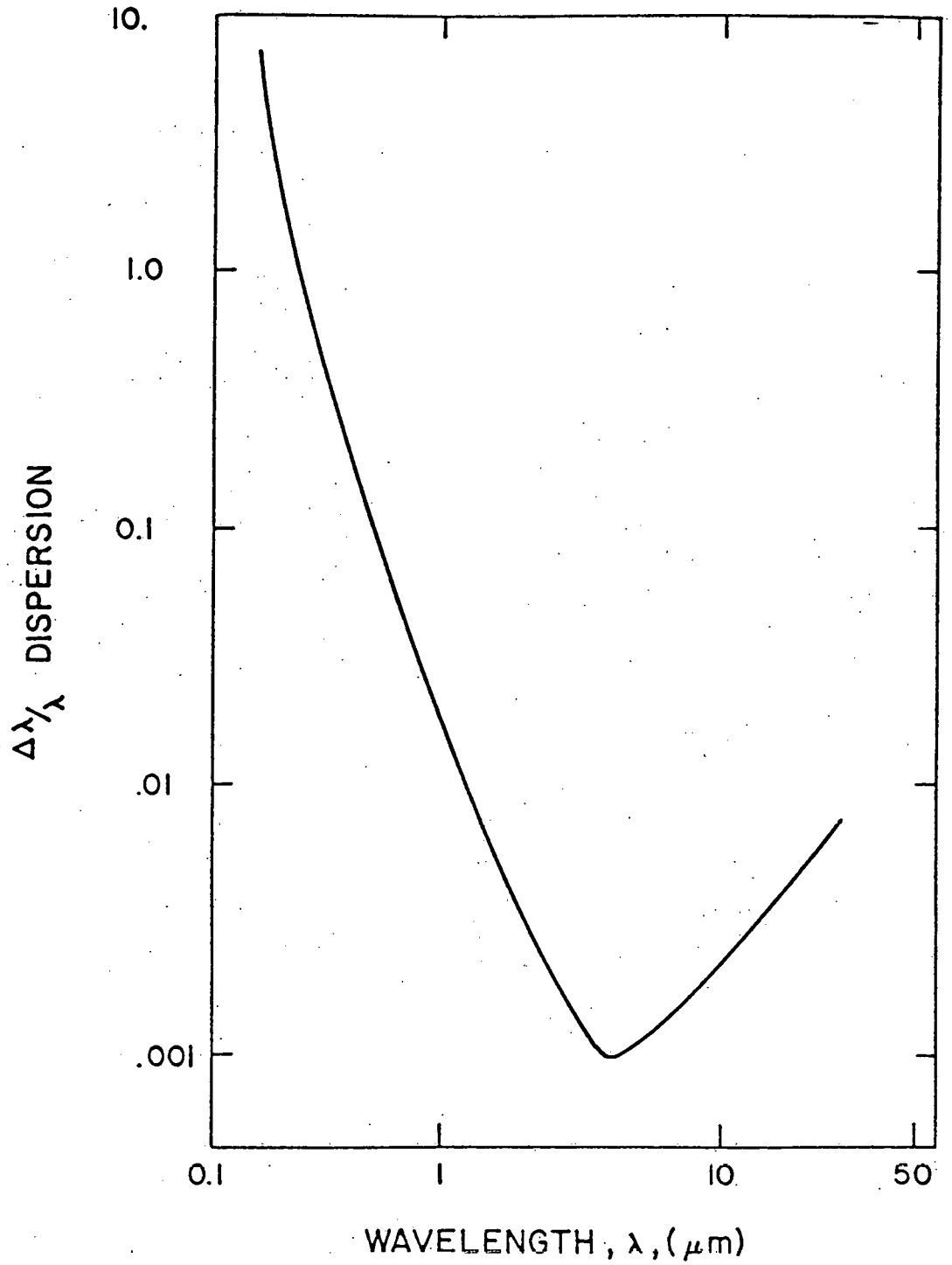

Figure 6.5. Dispersion of KBr.

absorption bands were more easily seen during narrow slit high resolution single beam spectra.

Additional calibration points, particularly at longer wavelengths, were obtained by using the dual beam photoacoustic spectrometer in a predispersive IR spectrophotometer mode. In this case, the sample photoacoustic cell was filled with carbon black with the result that the apparatus was transformed into a spectrophotometer. A thin sheet of polystyrene was then placed in one beam and the transmission spectrum recorded by monitoring the output of the ratiometer as a function of monochromator dial setting. This procedure was repeated for several slit widths, since the transmission spectrum of polystyrene, shown in Figure 6.6. contains several extremely sharp absorption peaks.

One of the sharpest and most often used polystyrene calibration absorption lines is the 6.234 μm band (σ = 1601.8 cm^{-1}). A comparison of this band obtained from the photoacoustic spectrometer and the same band measured in a Beckman 4250 commercial spectrophotometer is presented in Figure 6.7. Examination of the two curves reveals that the basic shapes are extremely similar. In both cases, the main absorption band and its side band are well resolved. The two scales are slightly different and as a result, the two bands do not exactly trace the identical curve. However, it is clear that the absorption bands are in good

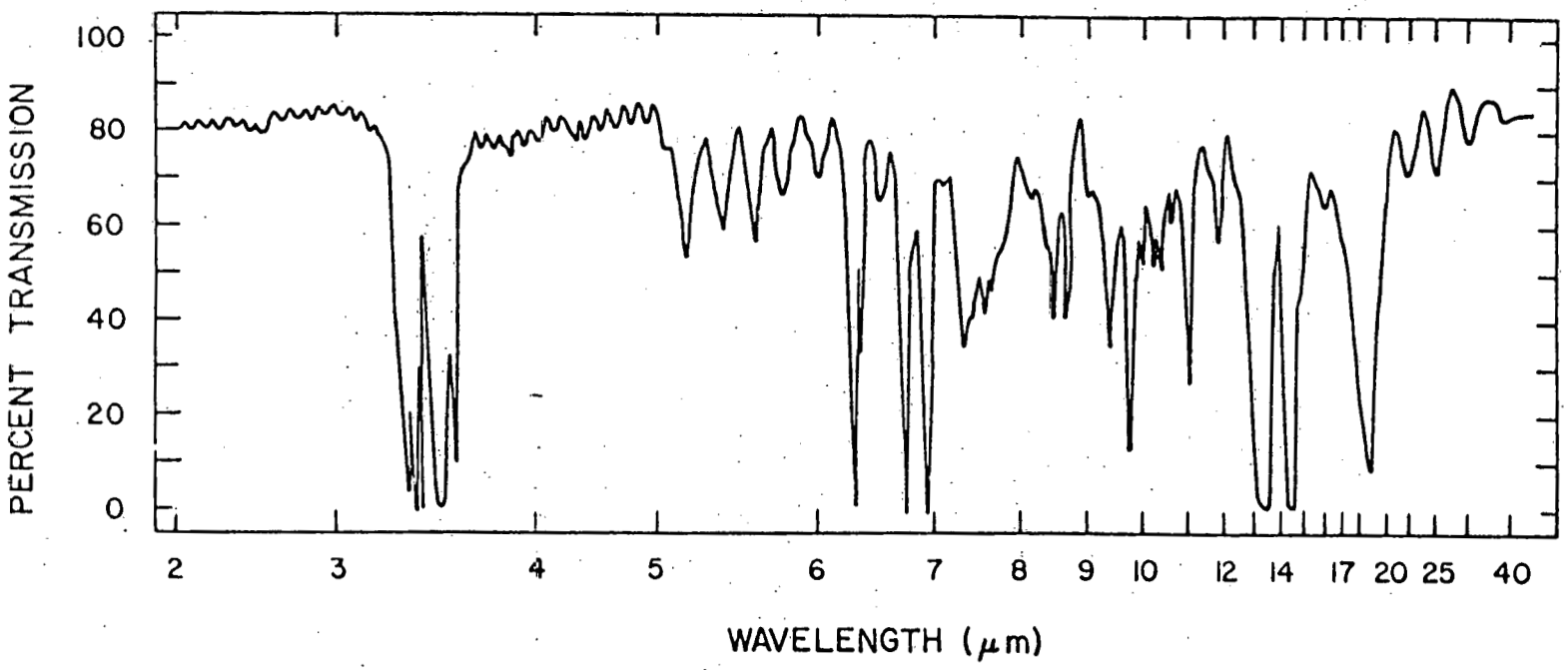

Figure 6.6. Infrared transmission spectrum of polystyrene.

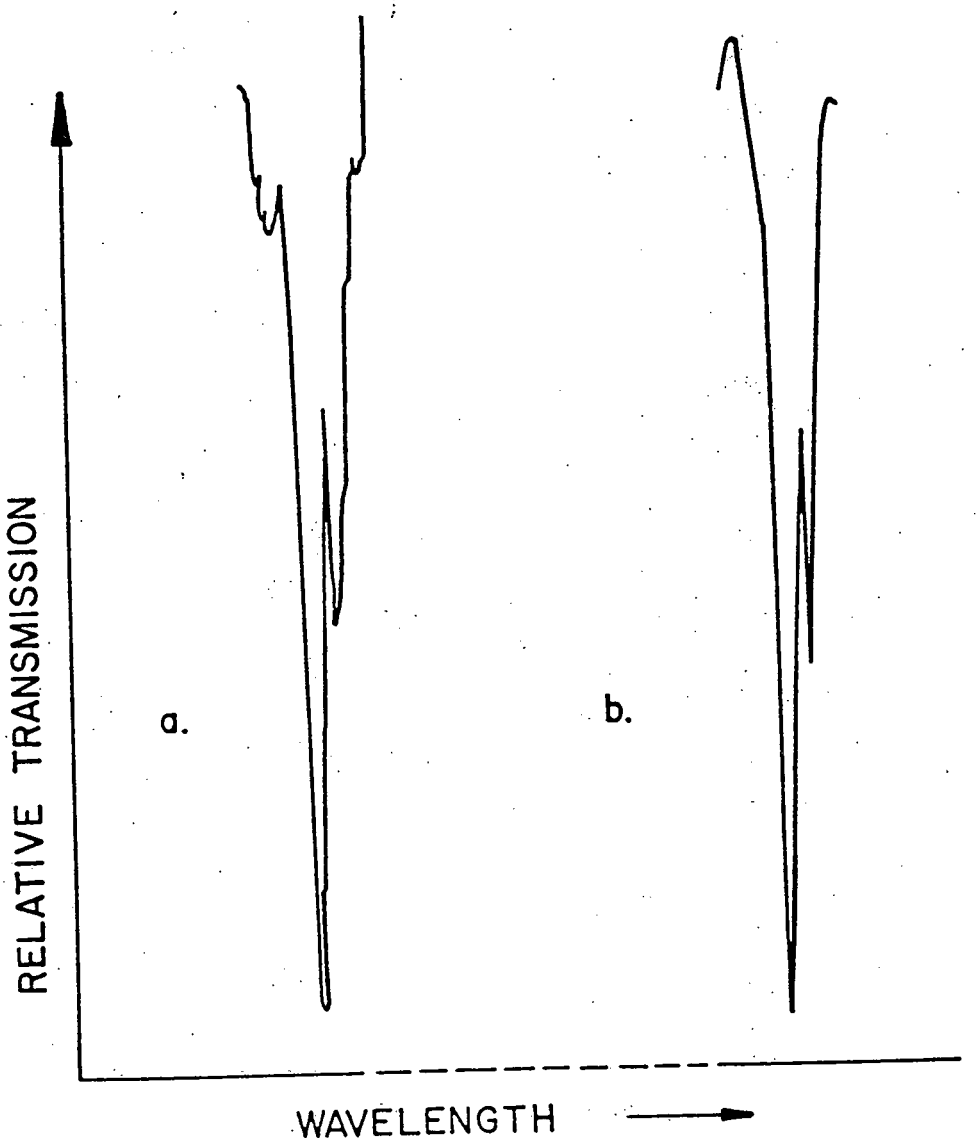

Figure 6.7. Comparison of the 6.243 μm polystyrene absorption bands obtained from the photoacoustic spectrometer (a) and from the Beckman spectrometer (b).

agreement, which indicates that the photoacoustic spectrometer is well aligned and operating in a known and predictable fashion.

Two additional calibration points were obtained by focusing the beams from a Nd:YAG (λ = 1.06 μm) and a CO_2 laser (λ= 10.6 μm) onto the entrance slits of the monochromator and detecting their presence at the exit slits. With extremely narrow slits, it was possible to locate the position of the wavelength dial to within $\pm$ 1/2 number.

Using these procedures, it was possible to obtain a monochromator calibration curve which related the wavelength at the exit slits to the dial number of the monochromator wavelength drive. The calibration graph is presented in Figure 6.8 and is seen to be a well behaved continuous function from 1 to 14 μm. At the two extremes of the curve, where λ is less than ~ 2 μm or λ is greater than ~ 10 μm, we note that the dispersion of the monochromator increases dramatically. For constant slit size, this implies that the resolution of the instrument is much greater in these regions than in the intermediate wavelength regime. Both of these observations are in agreement with the KBr dispersion drive presented in Figure 6.6. As a final note, we mention that it was possible to determine the dial locations to within $\pm$ 1.5 numbers. As such, the wavelength error will vary as a function of wavelength. For 5 μm, the uncertainty in the absolute value of the wavelength is $\pm$ .1 μm.

6.5. Photoacoustic spectra of germanium powder

Intrinsic grade germanium powder with an average particle size of 112 μm was placed in the sample photoacoustic cell. The photoacoustic cell was then placed in the spectrometer and the normalized photoacoustic spectrum recorded from 1 μm to 15 μm at a constant slit width. The resultant spectrum is shown in Figure 9-8 and may be compared to the absorption spectrum obtained from germanium flats which were presented earlier in Figure 5-1. In the noisier portions of the photoacoustic spectrum, a line has been drawn through the rms value in order to aid in the comparison. There are several features of interest.

6.5.1. Qualitative features

Qualitatively, we note that there is a good overall agreement between the general shape of both spectra. At short wavelengths, the photoacoustic spectrum easily detects and resolves the Urbach tail(98,99) of the .9 eV (λ = 1.37 μm) energy band gap in the germanium semiconductor powder. The tail is seen to extend from approximately 1.3 μm to approximately 3.1 μm, in general agreement with the data reported for the germanium flats. At longer wavelengths, a general overall increase in the photoacoustic signal is noted, particularly for wavelengths greater than 5 μm. This may be interpreted as the onset of free carrier(33,42,83) and multiphonon(100-102) absorption

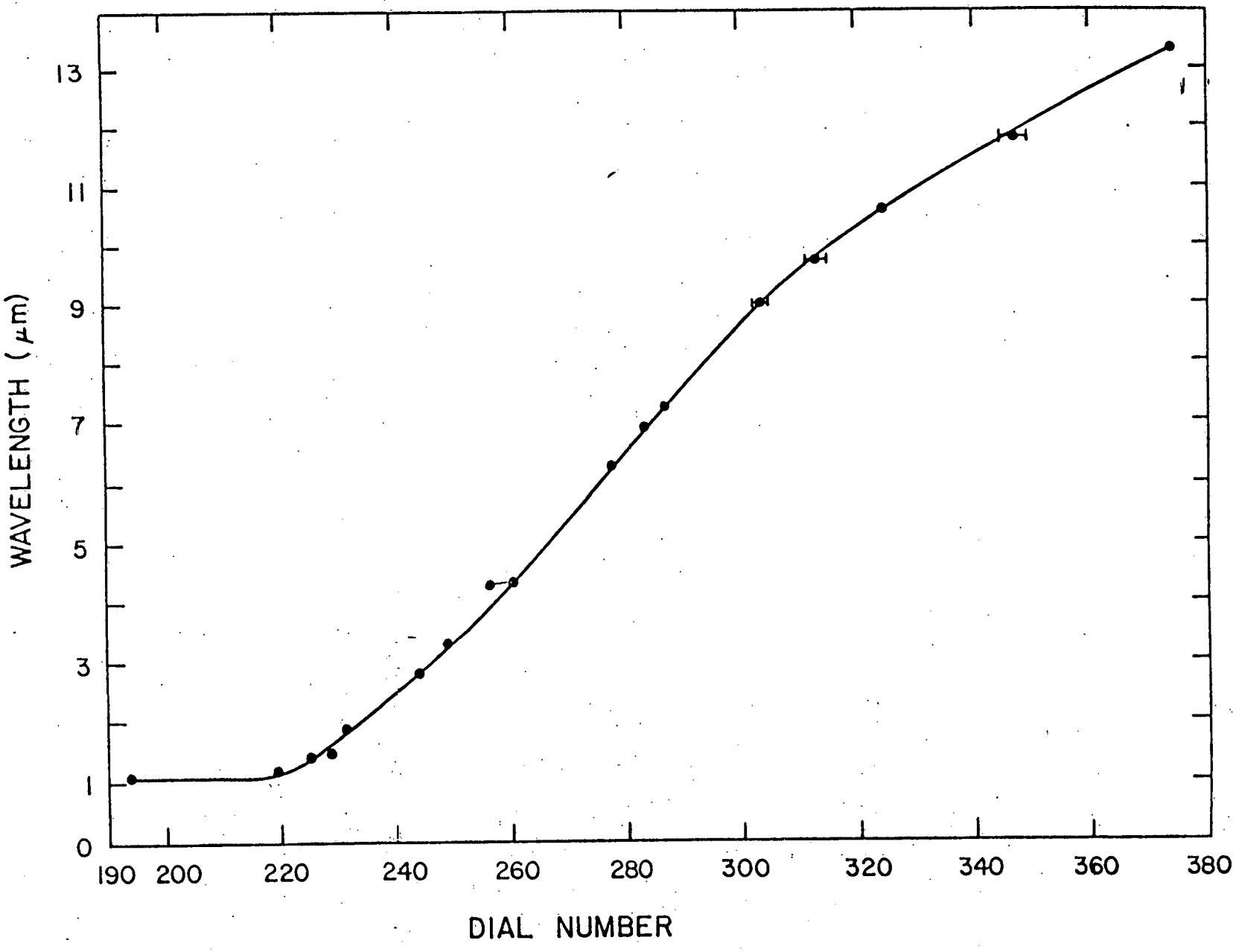

Figure 6.8. Calibration curve for the photoacoustic spectrometer.

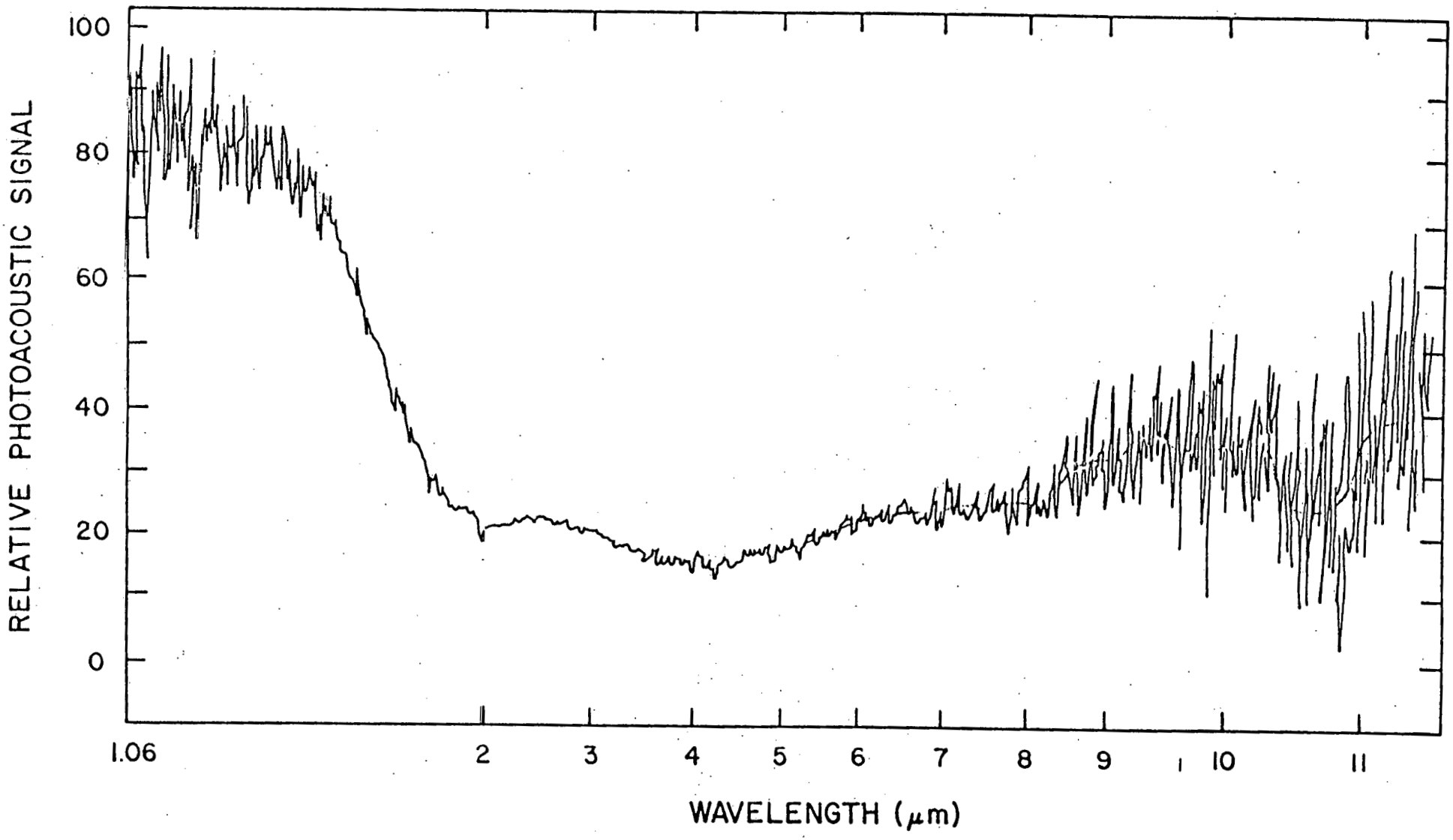

Figure 6.9. Photoacoustic spectrum of germanium powder.

and the general position and shape of the photoacoustic spectrum agrees well with the spectrum reported for the polished flats. Particular similarities should be noted in the increase in signal at 6 μm, the flattening out at 8.0 μm, the increase and plateau at 9 μm, the increase and plateau at 10 μm, and the dip and increase at 11 μm and 11.2 μm respectively.

The only main discrepancy between general features observed in the photoacoustic spectrum of the powder and the absorption spectrum of the polished flats is an apparent absorption peak in the former centered at 2.7 μm. However, as we shall see later, this is most likely attributed to the presence of a minute amount of residual water in the powder material, and is not of major consequence.

Some consideration should be given to the reproducibility and signal to noise ratio of the photoacoustic spectrum. In the 1.5 μm - 10.5 μm region, all of the photoacoustic spectra reported in this investigation were found to be reproducible to within $\pm$ 1.5% provided that the apparatus and/or lock-in was not seriously disturbed or nudged out of alignment. Due to the spectral output of the Nernst glower and monochromator, the signal to noise ratio was best in this region. For wavelengths less than ~ 1.5 μm or greater than ~ 11 μm, the reproducibility of the rms photoacoustic signal and the signal to noise ratio

were both reduced, although the seriousness of the degredation depended mainly upon the sample under investigation. This result is a direct consequence of the reduction in optical flux available at these extremes using the Nernst glower source and KBr monochromator. It should be noted, however, that both the reproducibility and signal to noise ratio could be improved by decreasing the bandwidth of the lock-in amplifier and/or increasing the monochromator slit width. Although the latter is only accomplished at the expense of spectral resolution, the large dispersion of the KBr prisms at the extrema wavelength regions often permitted the use of wide slits without serious degredation to the spectral resolution.

6.5.2. Quantitative results

In infrared spectroscopy, it is often sufficient to locate the relative size or position of spectral features in order to identify compounds or extract the information desired from the spectral analysis. However, in many cases, it is of extreme importance to obtain quantitative data, particularly regarding the absorption coefficient of the material under consideration. In photoacoustic spectroscopy, it may be possible to extract the average absorption coefficient of the powder particles through the application of a theoretical analysis. The analysis, shows that the photoacous-

tic signal and the quantity $\beta\delta$ were related by:

$$\Delta P = \beta\delta \quad (1 - j)\exp j(\omega t - \pi/4) \qquad 6.1$$

where β= attenuation coefficient, δ = grain diameter and where K is an unknown constant which contained information regarding the cell parameters and the thermal constants of the powder material[78]. It should be noted that K is independent of wavelength.

If we assume that the absorption coefficient of the powder particles is known at a given wavelength and that the near particle diameter is also known, then it should be possible to calculate K and establish an absolute calibration curve which relates the photoacoustic signal at any wavelength to the optical absorption coefficient of the powder grains. For germanium, the absorption coefficient of the powders was unknown. However, it may be anticipated that the absorption properties of the polished flats and the powders will be extremely close in spectral regions which are not dominated by impurities. Thus, selection of a calibration point should be made in a region of intrinsic absorption. Furthermore, the photoacoustic signal at that wavelength should also be well known. As a result of these considerations, the germanium powder calibration point was chosen for λ = 10.6 μm, where β is assumed to be the same value as it was in the large polished flats,

$\beta = .027\ cm^{-1}$. The calibration curve, which relates the magnitude of the photoacoustic signal relative to the 10.6 μm value and the quantity ($\beta\delta$) is presented in Figure 6.10.

Using the photoacoustic spectrum and the calibration curve, it is possible to obtain a plot of the absolute absorption coefficient of the powder particles as a function of wavelength for the germanium powders. This spectrum has been calculated and is compared with the absorption spectrum of bulk germanium in Figure 6.11.

Comparison of the two spectra shows remarkable agreement between 2 μm and 10 μm. In most cases, the absolute values for the absorption coefficient agree well within the experimental error of the photoacoustic data. Increased absorption is noted at 2.7 μm and 6 μm. These two peaks may be interpreted as water in the germanium powder, since the two most prominent water absorption bands match these locations. The water most likely entered the powder during a particle sizing procedure, and apparently did not completely evaporate during the heating period when the powder was placed in the photoacoustic cell. The small $.002\ cm^{-1}$ increase in absorption coefficient, however, indicates that the concentration of water is extremely low in the powder.

Although there is excellent agreement between the photoacoustically generated spectrum and the spectrum for

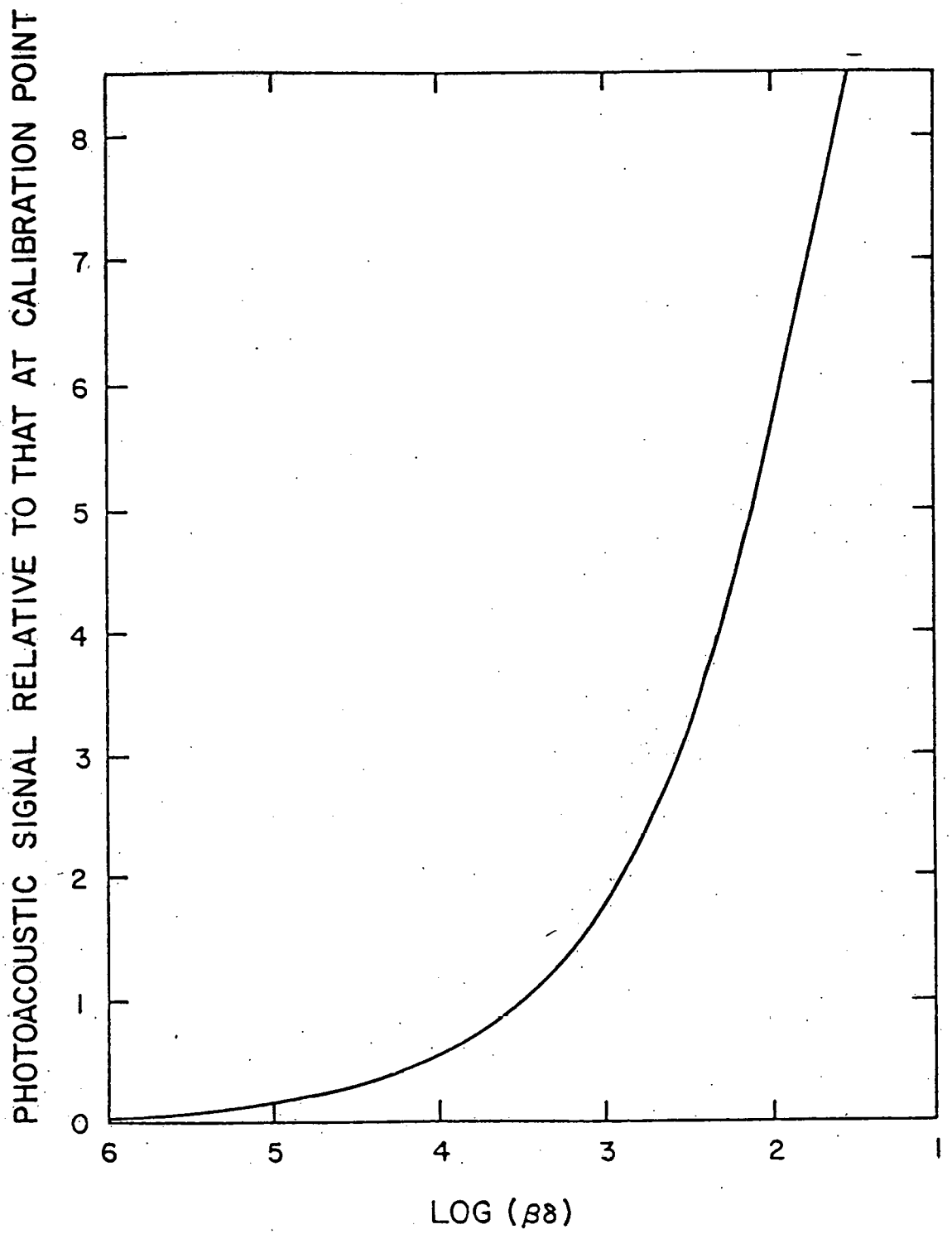

Figure 6.10. Calibration curve for the photoacoustic spectrum of germanium powder.

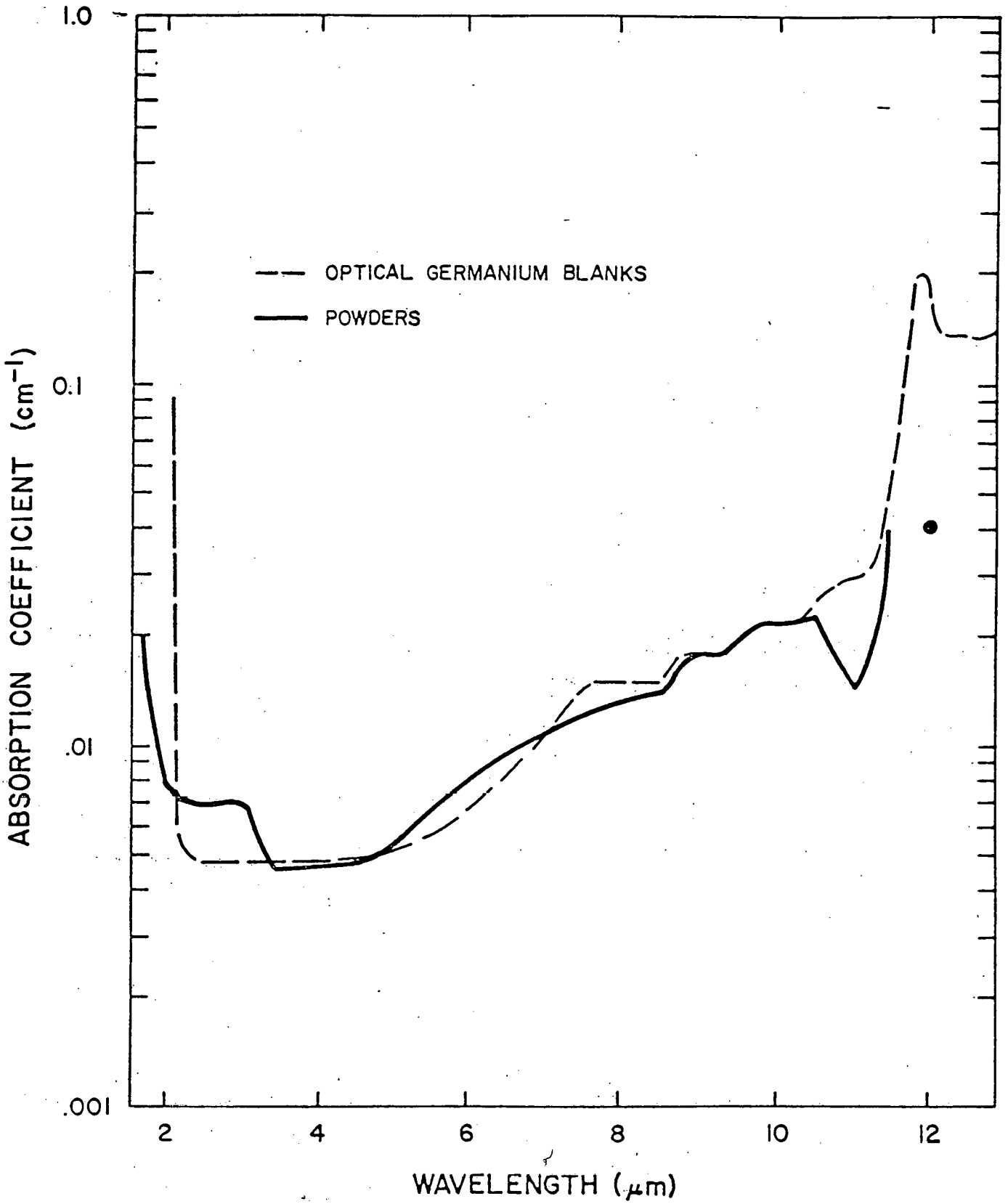

Figure 6.11. Quantitative photoacoustic spectrum of germanium powder.

the large optical blanks, major discrepancies appear for wavelengths less than 2 μm and greater than 10.6 μm. At both of these extrema, the photoacoustic values appear to be low by as much as an order of magnitude. These discrepancies do not appear to be related to the higher absorption coefficient itself, since absorption coefficients roughly of the same value agree well in other regions of the spectrum. For the same reason, the model should still be valid up to absorption coefficients on the order of 10 cm^{-1} due to the constraint that $\beta\delta << 1$.

The short wavelength and long wavelength problems may be explained by considering the effect of the ratiometer reading as both numerator and denominator go to zero. Due to the blackbody source and the high dispersion of the KBr in these regions, very little optical radiation is incident upon the photoacoustic samples. As a result, the photoacoustic signals in both the reference and sample beams tend rapidly toward zero in spite of the fact that the absorption coefficient of the sample increases dramatically at both short and long wavelengths. When the two weak signals are fed into the ratiometer, a slight offset in either the numerator or denominator can cause an extremely large error to be introduced into the quotient. For example, if the denominator has a slight positive zero offset, the quotient will tend toward zero as the two signals go to zero. Alternatively, if the denominator has a slight

negative zero offset, the quotient will tend toward infinity as the signals go to zero. Thus, the absolute value of the ratiometer is subject to considerable error in the regions of the spectrum where the total optical power is small. In the case under consideration, division of two small signals resulted in a quotient which tended toward zero at both long and short wavelengths. This result was confirmed by blocking the optical beam at the entrance slits of the monochromator and noting that the output of the ratiometer went to zero.

Interestingly enough, it should be noted that in spite of the zero effect problems, relative changes in the spectrum are still recorded. Thus, we see that while the large dip recorded in the photoacoustic spectrum at 11 μm is incorrect in its magnitude, the position of the change is maintained. Similar behavior was found to exist at longer wavelengths, and a good correlation was obtained between the location of changes in the photoacoustic signal and the location of features in the optical absorption coefficient spectrum.

The good agreement between the photoacoustically generated absorption spectrum and the optically obtained graph provides support for the theoretical model developed earlier. There were two assumptions implicit in the derivation of equation (6.1): 1) that the particles be optically transparent (i.e., $\beta\delta \ll 1$) and 2) that the grains be

thermally thin ($\delta/\mu_s << 1$). While the latter parameter is not a function of wavelength, consideration must be given to the optically transparent constraint since it may be violated in spectral regions of high absorption coefficients. A particular example is provided by the germanium spectrum, where $\beta\delta$ may be on the order of one or even larger for the extremely high (10^2 - 10^{-4} cm^{-1}) absorption coefficients encountered in the band gap region ($\lambda \sim$ 1.4 μm).

For regions where $\beta\delta \sim 1$, the analysis used to derive equation (8-1) breaks down. However, we note that for slightly less than 1, the grains approximate the photoacoustic case of being optically transparent and thermally thin. As we saw earlier, in this region, the photoacoustic signal should be proportional to β . When $\beta\delta >> 1$, the grains become photoacoustically opaque and the photoacoustic signal saturates at a value independent of . Thus, for extremely high values of β (10^3-10^4 cm^{-1}) the photoacoustic signal resulting from the powders should become independent of the absorption coefficient.

In the germanium photoacoustic spectrum, the onset of photoacoustic saturation may be seen to occur around 1.1 μm. Careful studies where the zero effect was well adjusted in this region confirmed the photoacoustic saturation.

6.6. Photoacoustic spectra of $CdCr_2Se_4$ powder

Several different samples of $CdCr_2Se_4$ were manufactured in our laboratory or obtained from Kodak Research Labs (104) and analysed in the photoacoustic spectrometer. The photoacoustic spectrum of $CdCr_2Se_4$ Batch 20, which was manufactured in our lab, is presented in Figure 6.12. and may be compared to the absorption spectrum which was obtained from single crystals using transmission techniques by Bongers and Zammarachi (36). The latter spectrum is given in Figure 3.3. Comparison of the two spectra reveals both similarities and differences in the general shape of the curves.

6.6.1. Qualitative features

$CdCr_2Se_4$ is a semiconductor with an energy gap of 1.36 eV (λ - .91 μm). The well-known Urbach tail of the band gap transition is clearly seen in both the photoacoustic spectrum and the single crystal data for wavelengths less than ~ 2 μm. The absorption coefficient also increases in both spectra at long wavelengths greater than ~ 10 μm. In the single crystal data, this absorption edge has been attributed (36) to multiphonon absorption and is a result of the fundamental lattice vibrations encoun-

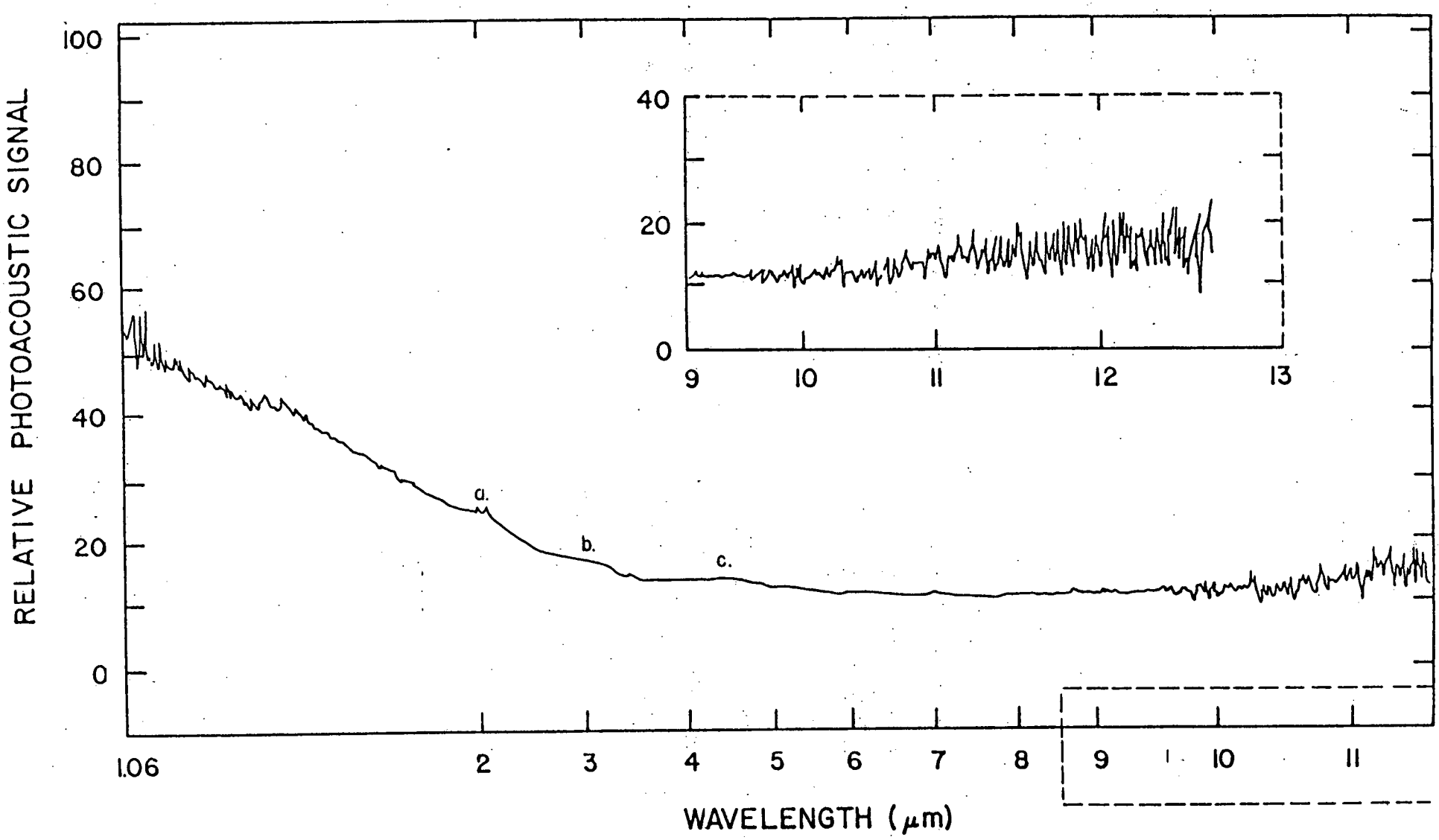

Figure 6.12. Photoacoustic spectrum of $CdCr_2Se_4$ Batch 20 powder (virgin).

tered in $CdCr_2Se_4$. It should be noted that, in the photoacoustic spectrum, the onset of this absorption occurs at ~ 10 μm, which is significantly earlier than the ~ 17 μm onset encountered in the single crystal mosaic spectrum. This observation will be discussed in further detail later. In the spectral regions between the band gap and the multiphonon edge, both spectra appear to be relatively flat and reach their minimum absorption values in the 7 μm - 10 μm region. Thus, the overall qualitative shape of the $CdCr_2Se_4$ Batch 20 photoacoustic spectrum is found to be in good agreement with the absorption features reported by others for pure single crystals.

Close inspection of the photoacoustic spectrum, however, reveals some very important differences between the powder and single crystal spectra. In particular, three broad absorption peaks centered at 2.0 μm, 3.0 μm, and 4.5 μm are observed in the powder spectra but not in the single crystal data. The first two features, labeled a and b, respectively, exhibit linewidths of approximately .2 μm. The third feature, labeled c, is extremely broad in nature and extends from ~3.8 μm to ~ 5.5 μm. Since these absorption features are obviously sample dependent, it seems likely that they may be related to impurities or non-stoichrometries. Miyatani (46) for example, has observed similar type features at 2.0 μm and 4-5 μm in indium doped and vacuum annealed $CdCr_2Se_4$. In his study, Miyatani

concluded that the broad absorption band at 4.5 μm could be attributed to selenium vacancies in the crystal lattice, while the 2.0 μm band appeared to be associated with the indium doping concentration.

The photoacoustic spectra obtained in this investigation provide evidence which suggests that the 2.0 μm, 3.0 μm, and 4.5 μm absorption bands and the premature onset of absorption at 10 μm may be attributed to an excess of selenium in the $CdCr_2Se_4$ powder. It has already been noted that the onset of the long wavelength absorption in the $CdCr_2Se_4$ Batch 20 powder occurred at a wavelength (10 μm) which was significantly shorter than the ~ 17 μm onset observed for the single crystal mosaic. This increase in absorption may be attributed to the existence of free carrier absorption in the powder material. Free carrier absorption results when energy is tranferred from incident photons to free electrons or holes in a lattice (note: conservation of energy and momentum forbids a complete tranfer of energy from the radiation to the perfectly free electrons or holes. However, any free electron or hole in a real lattice will interact with the vibrating structure, thus permitting the absorption of radiation). Free carrier absorption has been observed in most semiconductors(105)and is characterized by $a\lambda^n$ spectral dependence. For classical models, $n = 2$ (83). However, semiconductors have been observed to exhibit a wavelength de-

pendence which varies between n = 1.8 and n = 3.5 (105).

Close inspection of the photoacoustic spectrum for $CdCr_2Se_4$ Batch 20 for wavelengths greater than 10 μm reveals a monotonically increasing function whose shape is highly reminiscent of the classical λ^2 dependence of free carrier absorption observed in other infrared semiconductors. Indeed, this observation is supported by a least squares curve fit of this portion of the spectrum. Using the quantitative data presented later, we find a λ^n dependence where n= 2.2. Thus, it seems likely that the absorption in this region may be attributed mainly to free carrier absorption.

Additional evidence which supports this theory and clarifies the nature of the three absorption features at 2.0 μm, 3.0 μm, and 4.5 μm may be obtained by comparing the photoacoustic spectra of several different powder samples. The photoacoustic spectra of two other $CdCr_2Se_4$ powder samples is presented in Figure 6.13 and Figure 6.14.

In the first case, a portion of the Batch 20 powder discussed above was placed in an open ampule, heated to 500 °C and exposed to a continuous stream of hydrogen gas. In this manner, the concentration of selenium in the powders was reduced and carried away in the H_2Se gaseous from due to the reaction:

$$Se_{(s)} + H_{2\ (g)} \rightarrow H_2Se_{(g)} \qquad 6.2.$$

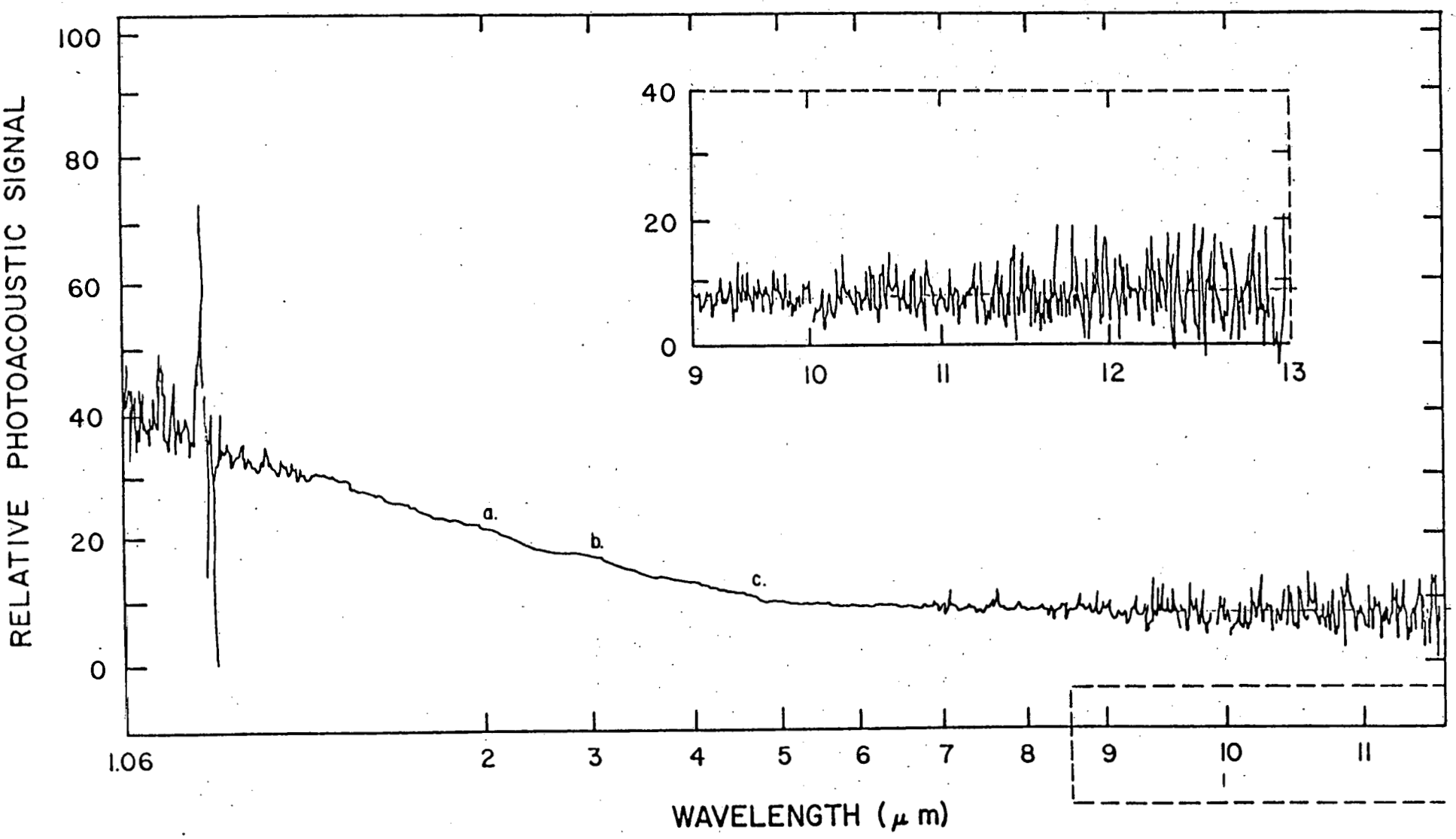

Figure 6.13. Photoacoustic spectrum of $CdCr_2Se_4$ Batch 20 powder (heat treated).

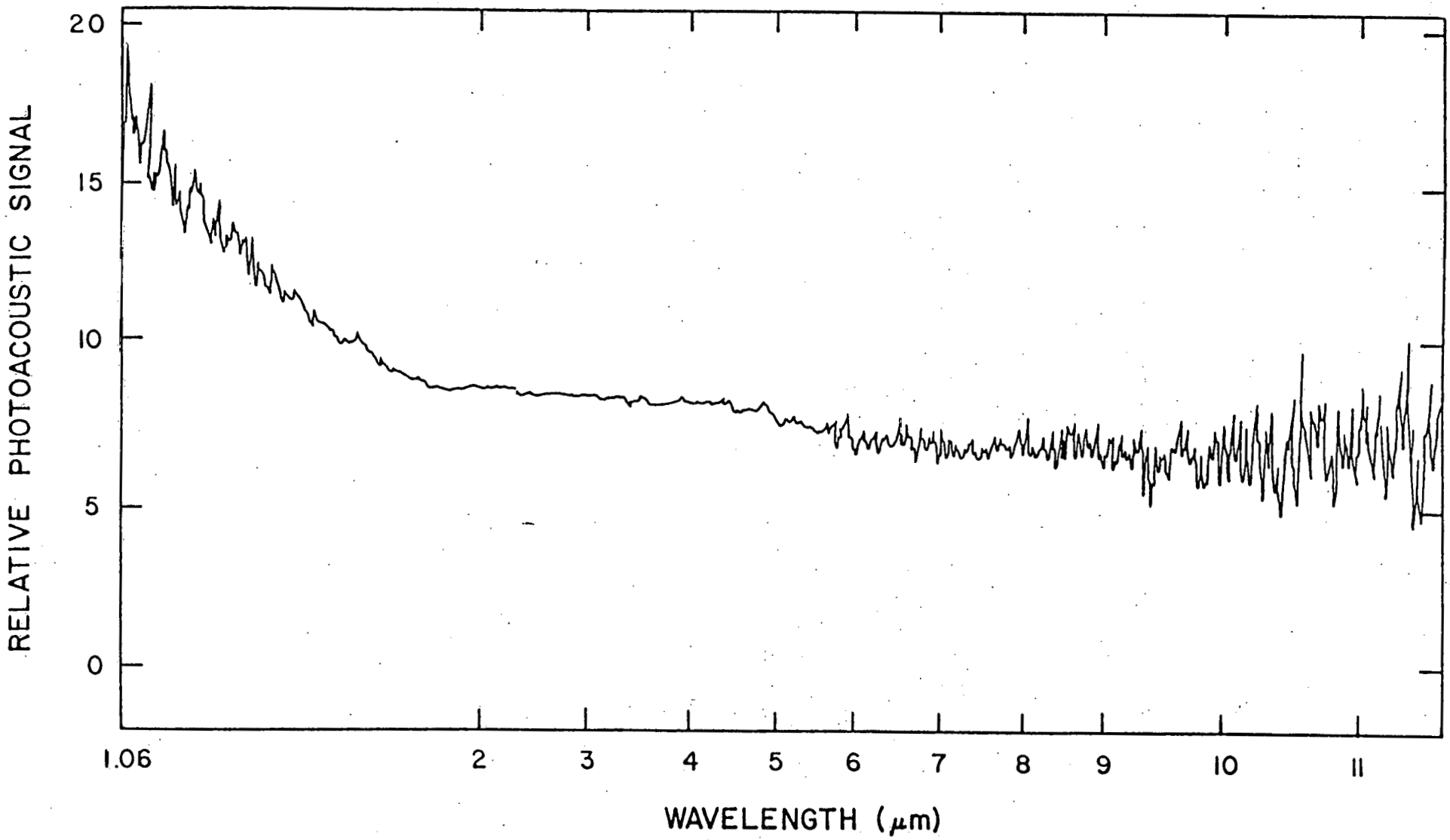

Figure 6.14 Photoacoustic spectrum of $CdCr_2Se_4$ (Kodak powder).

The heat treated powder was then allowed to cool and was placed in a photoacoustic cell and analysed. The photoacoustic spectrum of this sample is presented in Figure 6.13.

Comparison of this photoacoustic spectrum with that obtained from the virgin powder reveals that two important changes have taken place. First, we note that while all of the three absorption peaks at 2.0 μm, 3.0 μm, and 4.6 μm still remain, their strength has been reduced by more than a factor of two. Additionally, we observe that the relative strength of all three features has been reduced by the same amount. As such, it would appear that all three of these features are related to the concentration of selenium in the powder material. Second, we note that the free carrier absorption present in the virgin powder in the 10 m region has almost disappeared. Instead of increasing monotonically from 10 μm on, the absorption coefficient is actually observed to decrease. However, careful and repeated analysis of the entire spectrum reveals that the classic λ^2 signature of free carrier absorption is still present in the treated powder, but only for wavelengths greater than ~ 11.5 μm. A least squares curve fit on the quantitative data presented later for the powder reveals a $n = 2.1$ dependence in good agreement with the previous fit in the same spectral region.

The shift of the onset of the free carrier absorption is indicative of a reduced concentration of carriers. Since the only significant difference between the virgin and heat treated powders is a decrease in the selenium content in the latter, it thus seems likely that both the free carrier absorption and the three features observed at 2.0 μm, 3.0 μm, and 4.5 μm are intimately related to the selenium concentration in the powders. Furthermore, a decrease in the concentration was found to result in a decrease in the free carrier absorption. Since stoichrometric compounds may be expected to be more transparent than their non-stoichrometric counterparts, the virgin powder must therefore have contained a selenium excess. Finally, we note that an excess amount of selenium in $CdCr_2Se_4$ would result in the formation of acceptors and acceptor levels, the latter being located at energies less than the band gap of the semiconductor (90). Thus, it seems likely that the absorption features at 2.0 μm, 3.0 μm, and 4.5 μm represent acceptor levels and that the free carriers responsible for the free carrier absorption are holes.

Additional evidence which supports these conclusions is presented in Figure 6.14 where the photoacoustic spectrum of $CdCr_2Se_4$ powders (δ = 100 μm) obtained from Kodak Research Labs is presented. The spectrum has been expanded by a factor of five over the previous $CdCr_2Se_4$ spectra in an effort to illustrate the influence of the

three acceptor levels observed in $CdCr_2Se_4$ Batch 20 powders. Careful inspection of Figure 6.12 reveals that all evidence of the three discrete peaks has vanished. At the same time, we note that the long wavelength free carrier absorption has also disappeared. The photoacoustic spectrum, even under repeated and close scrutiny, was found to remain flat to ~ 13 μm. Thus, the relationship between the selenium acceptor levels and the free carrier absorption in $CdCr_2Se_4$ is confirmed.

It should be noted that the excess selenium and free carrier absorptions relationship may not necessarily be a one to one correspondence. We have found that the existence of the excess selenium in $CdCr_2Se_4$ gives rise to free carrier absorption. However, it is possible that free carrier absorption in $CdCr_2Se_4$ can also result from other non-stoichiometries or impurities. Thus, the absence of selenium acceptor levels does not necessarily guarantee the absence of free carrier absorption.

Finally, we note the observation of an extremely broad absorption peak in the Kodak $CdCr_2Se_4$ powder spectrum from ~ 2 μm to ~ 5 μm. The origin of this peak is not clear. However, the peak has been observed only in the Kodak powders, and may be attributed to an impurity, donor, or acceptor level which is related to the method or materials used to manufacture the powders

6.6.2. Quantitative data

It may be possible to obtain quantitative information regarding the absorption coefficients of the $CdCr_2Se_4$ powders by using the same technique employed for the germanium powders. Although the absolute absorption coefficient of the powder is unknown, a suitable calibration point may be selected from the single crystal data if care is taken to insure that the absorption at the wavelength is intrinsically limited. In this manner, the calibration point should be fairly independent of the composition or purity of the material, regardless of whether it is in the single crystal or powder form. For $CdCr_2Se_4$, the calibration point selected, $\beta = 50\ cm^{-1}$ at $\lambda = 1.19$ m, was located on the intrinsic Urbach tail of the band gap transition from the data obtained from the single crystal mosaic by Bongers and Zanmarchi (36).

The quantitative photoacoustic spectra of the virgin and heat treated $CdCr_2Se_4$ powders is presented in Figure 6.15. For the virgin powders, we note that the minimum absorption coefficient is $3.0\ cm^{-1} \pm .2\ cm^{-1}$ at a wavelength of $7.5\ \mu m$. For the heat treated powders, the minimum absorption coefficient is $1.9\ cm^{-1} \pm .2\ cm^{-1}$ at $10.6\ \mu m$. Thus, the removal of excess selenium is seen to improve the optical quality of the powders and decrease their infrared absorption coefficients. At $10.6\ \mu m$, the improvement is roughly a factor of two. The result agrees with

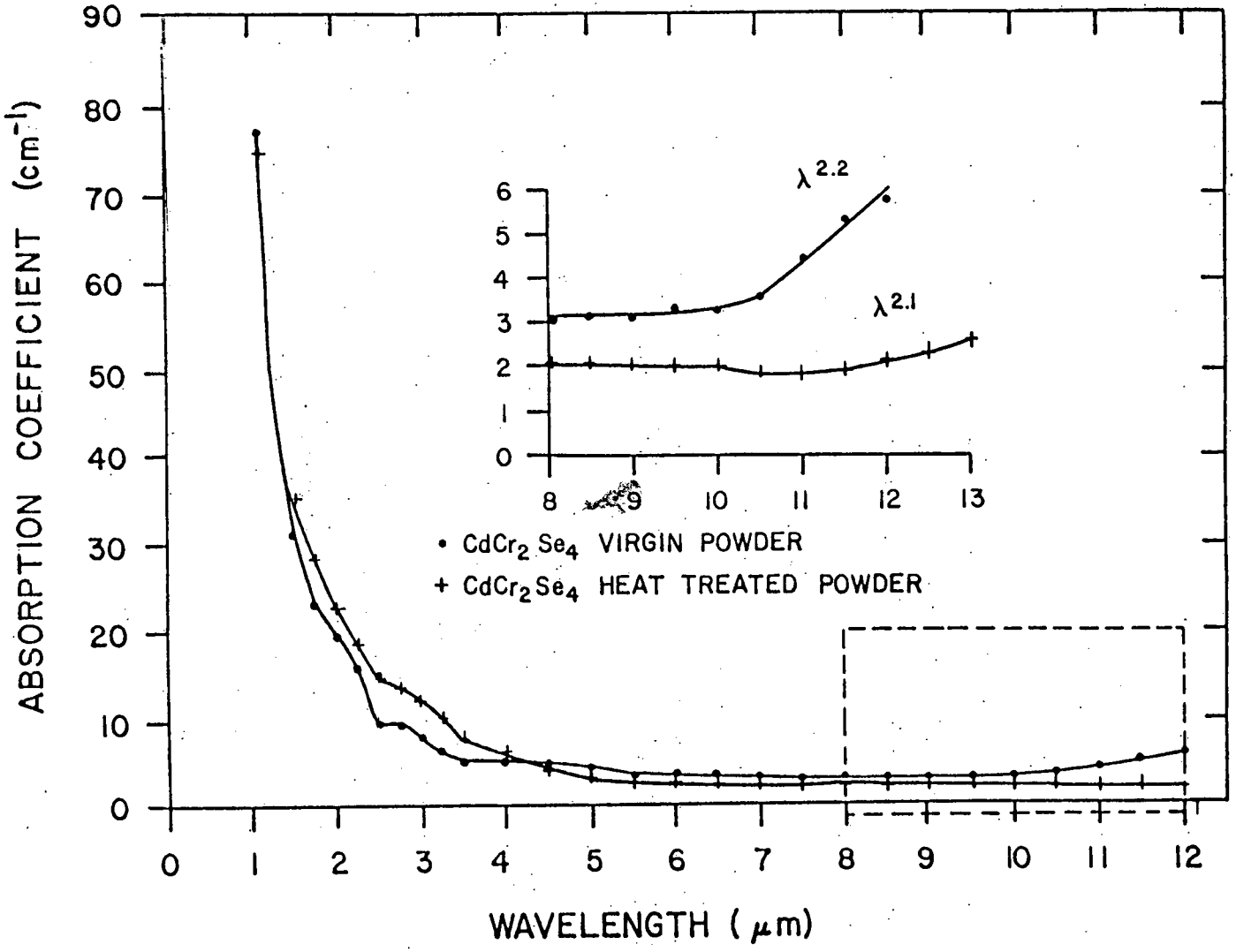

Figure 6. 15. Quantitative photcacoustic spectrum of $CdCr_2Se_4$ powder Batch 20 (virgin and treated).

physical intuition and our previous conclusion regarding the detrimental influence of excess selenium on the infrared optical absorption coefficient in $CdCr_2Se_4$. It also provides evidence to support the ability of the photoacoustic method to obtain quantitative data regarding the optical properties of powders.

It is interesting to compare the absorption coefficient data obtained from the heat treated powders with that of the single crystal mosaic. In the latter case, the lowest absorption coefficient is 13 cm^{-1} in the 8 - 16 μm region of the spectrum. This is a factor of ~7 higher than for our powders. However, Bongers and Zanmarchi[109] attribute this high value to reflection and/or scattering losses which they encountered in their transmission methods. Thus, the true absorption, as would be measured in the photoacoustic techniques, is probably lower. The lowest reported absorption coefficients for $CdCr_2Se_4$ single crystals is 4 cm^{-1} (37). Thus, our photoacoustic results on powder samples are in general agreement with those reported in the literature. However, it should be emphasized that the literature values were obtained using transmission techniques, and are therefore succeptible to considerable error due to the influence of scattering or reflection losses.

It is also useful to compare the absorption coefficient of the powders with the attenuation (includes

scattering) coefficients of the final hot-pressed elements. To date, the best hot-pressed attenuation coefficients at 10.6 μm and room temperature have been ~ 15 cm^{-1}, or a value which is an order of magnitude larger than the starting powder. X-ray analysis of the two samples reveals that second phase impurities are roughly the same in both cases. However, density measurements on the hot-pressed samples show that the latter is only ~99.5% of the theoretical value. Consequently, it appears that the attenuation coefficient of hot-pressed $CdCr_2Se_4$ at 10.6 μm is limited primarily by scattering and trapping mechanisms resulting from an incomplete densification during the hot-pressing process and not by absorption due to starting powder impurities or non-stoichrometries.

6.7. Photoacoustic spectra of $CdCr_2S_4$

The photoacoustic spectrum of $CdCr_2S_4$ powder obtained from Kodak Research Labs is presented in Figure 8-16. It may be compared to the generalized absorption spectrum obtained by Jacobs(1) in Figure 6.17. and the absorption spectrum obtained using transmission methods on one of the hot-pressed $CdCr_2S_4$ samples in Figure 6.18. Comparison of the three figures reveals that the features in the photoacoustic spectrum are similar to those observed in the other two spectra.

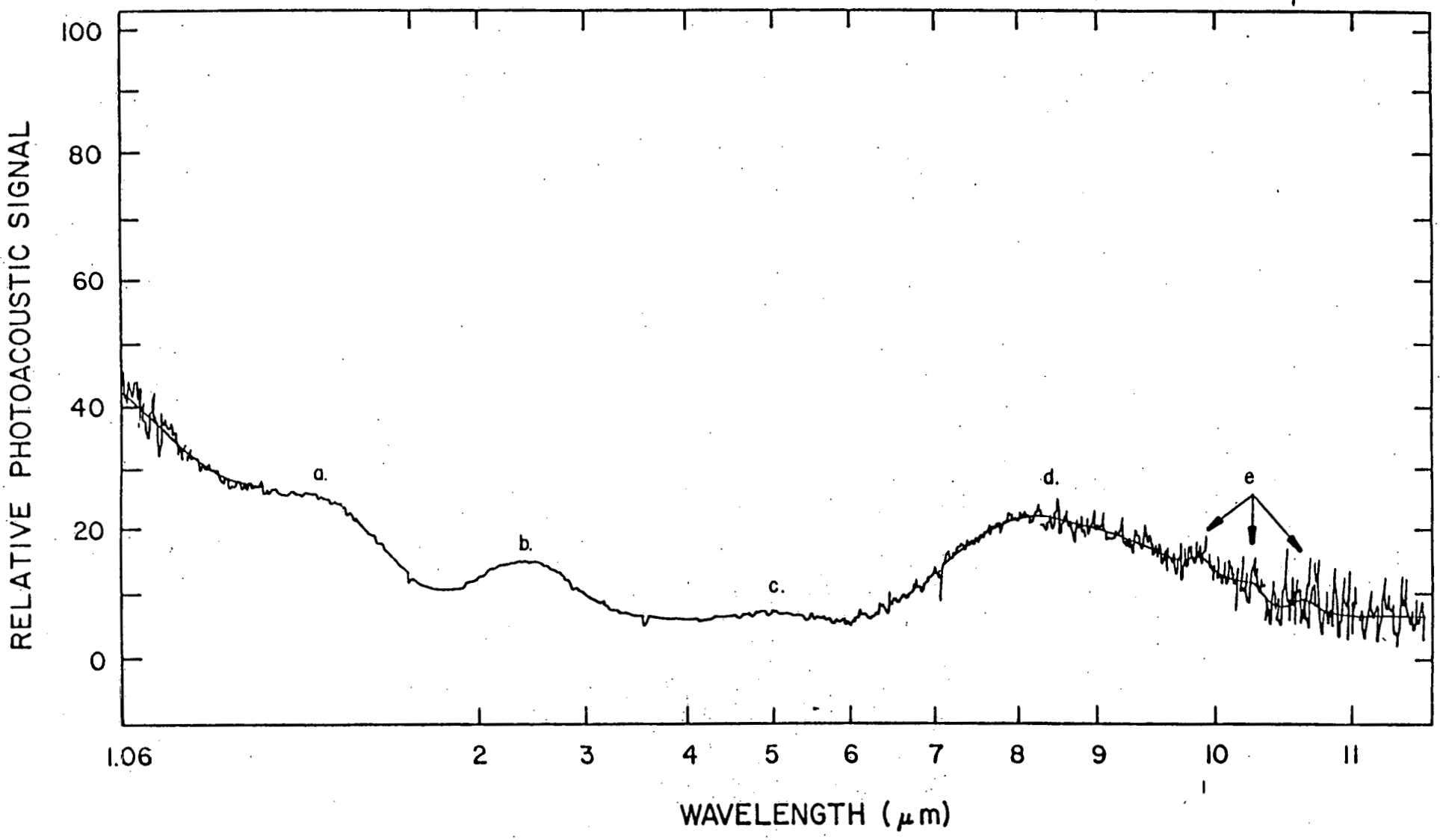

Figure 6.16. Photoacoustic spectrum of $CdCr_2S_4$ powder (Kodak).

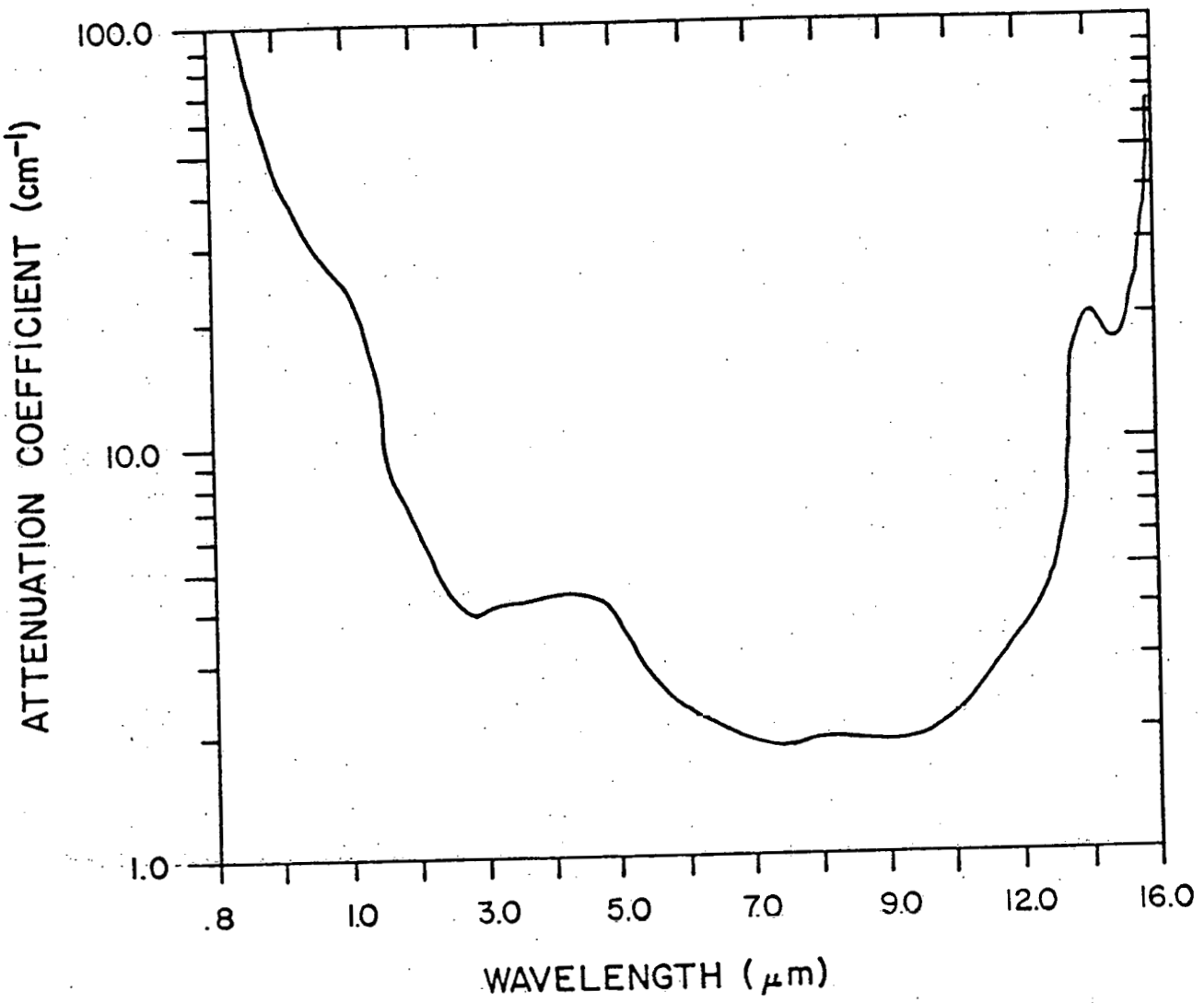

Figure 6.17. Generalized absorption spectrum of $CdCr_2S_4$ (adapted from ref. (1)).

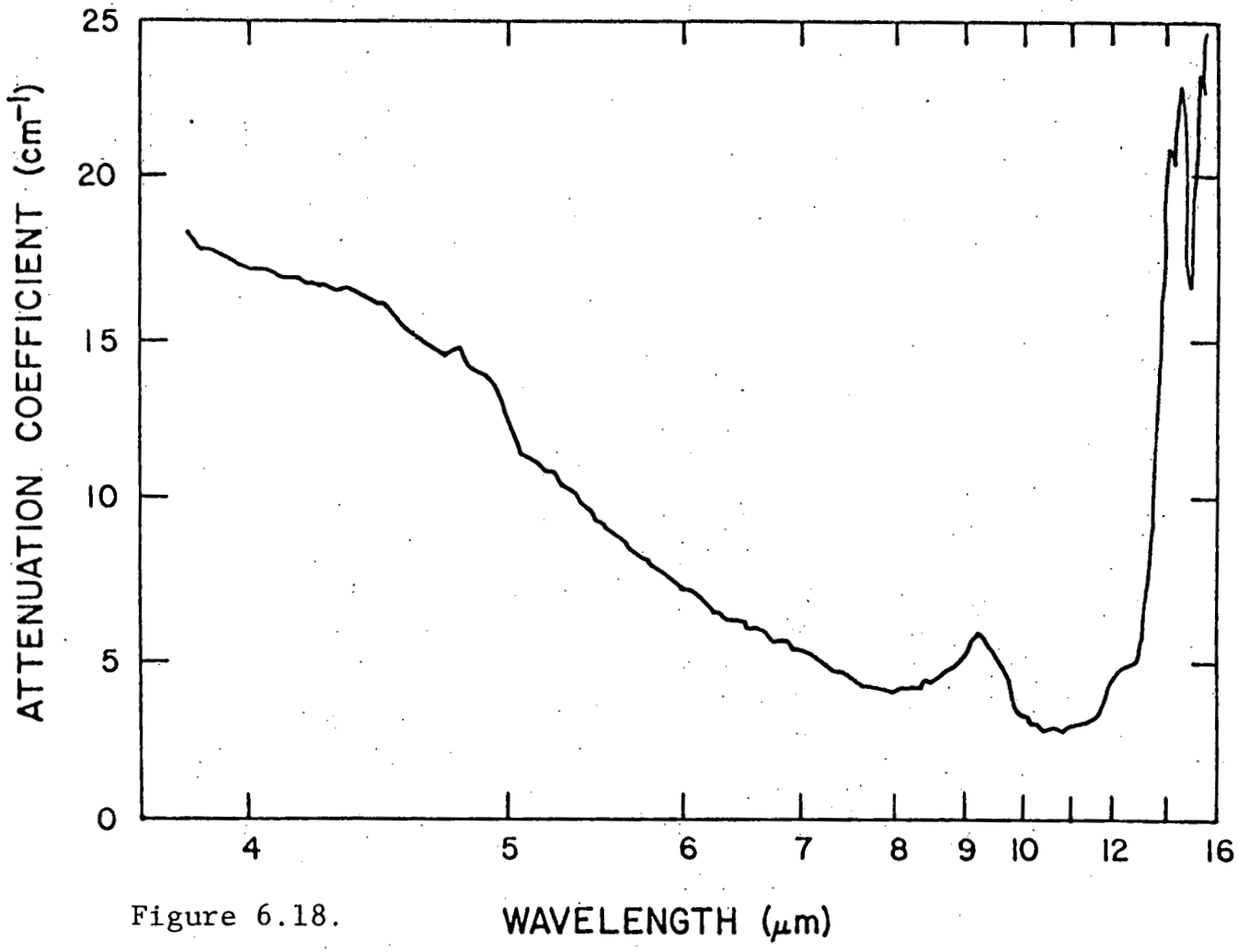
ATTENUATION COEFFICIENT (cm⁻¹)
25
20
15
10
5
0
4
5
6
7
8
9
10
12
16
WAVELENGTH (μm)

Figure 6.18.

6.7.1. Qualitative features

At short wavelengths (< 3 μm) we note the presence of a strong absorption in all three spectra. Considerable work has been conducted to show that this absorption is attributable to a 1.62 eV (λ = .76 μm) Cr^{3+} crystal field transition rather than the 2.5 eV (λ = .49 μm) energy band gap of $CdCr_2Se_4$(108-112). In the photoacoustic spectrum, the tail of the crystal field transition extends down to roughly 4.0 μm in good agreement with the previously published data.

In addition to the Cr^{3+} crystal field transition, several other absorption peaks are observed in the photoacoustic spectrum and they have been labeled a, b, c, d, and e in Figure 6.16. The feature labeled "a" is located at λ = 1.2 μm (.97 eV) and may be related to the stoichrometry of the powder. Miyatani(40), for example, has seen an absorption feature at the identical wavelength for a sample of sulfur-deficient $CdCr_2S_4$. Our experiments, which indicate that the strength of this peak varies as a function of powder sample, would support this hypothesis.

The origin of the "b" and "c" bands at 2.5 m and 4.5 μm, respectively, seem to be impurity related. Both features have been observed in the hot-pressed elements, and considerable variation in their strength has been noted from sample to sample. It is interesting to note the the location of the 4.5 μm peak is the same as that

observed for an anomaly in the Faraday rotation of $CdCr_2S_4$ (113). Wittekock and Bongers (113) and others (2) however, were unable to identify the absorbing specie and simply attributed the feature to an unknown impurity. Our observations would support this hypothesis. However, it should be mentioned that these authors did not see the 2.5 μm band in their investigations. Consequently, it seems likely that the two peaks, if they can indeed be attributed to impurities, are related to two separate impurities. Finally, we mention that x-ray analysis of the powders did not reveal any second phases present.

The extremely large absorption feature at 8.5 μm is similar to absorption bands seen in the hot-pressed samples. Interestingly enough, the absorption band was observed to be far stronger in the starting powder than in the hot-pressed elements. Indeed, the band was not even observed in many of the hot-pressed samples. Thus, it appears that the hot-pressing has actually improved the optical quality of the powder, a fact which may help to clarify not only the origin of the band, but also the details of the hot-pressing process.

In particular, we note that the class of so called oxy-sulfate impurities exhibit an absorption peak around 9.0 μm (113) in good agreement with the peak "d" observed in the photoacoustic powder spectrum. If we assume that a slight excess of sulfur is present in the initial starting powder, then it is possible that the sulfur-oxygen substitution could be completed during the high temperature phase of the hot-pressing process, thus resulting in a purer final hot-pressed element and a reduction in the 8.5 μm oxygen related absorption band. Since the experimental evidence confirms the latter prediction, it therefore seems likely that the origin of the 9.5 μm absorption feature lies in oxygen related impurities in the starting powder which exist possibly as a result of the incomplete formation of $CdCr_2S_4$ in the intital powder preparation procedure.

Several small peaks labeled "e" were also observed at wavelengths greater than 9.5 μm. These features are located at the same wavelengths as similar peaks in the hot-pressed elements and have been identified as the classic signature of multiphonon absorption also shown in Figure 5.25. The existence of absorption bands at sum and difference frequencies of fundamental lattice vibrations has been well established in several semiconductors, including ZnSe, ZnS, GaAs and others. Applying a similar analysis to $CdCr_2S_4$, we find an excellent agreement between

the positions of theoretical and observed two and three phonon absorption peaks, see Table 5.1. We also note that these peaks were observed in every $CdCr_2S_4$ sample investigated at the same strength. Thus, we conclude that they are intrinsic and the result of multiphonon absorption.

6.7.2. Quantitative data

It may be possible to obtain quantitative information about the absorption coefficient of the $CdCr_2S_4$ powder grains if an appropriate calibration point can be found. Although previous data is not available for $CdCr_2S_4$ powders, Jacobs(1) has reported a minimum absorption coefficient of 23 cm^{-1} at 1.06 μm for hot-pressed samples. Since this wavelength is located on the intrinsic Cr^{3+} crystal field transition, the absorption coefficient may be expected to be relatively independent of sample purity and thus appropriate for use as the photoacoustic spectrum calibration point. The resulting quantitative absorption spectrum of the $CdCr_2S_4$ powder is presented in Figure 6.19.

Inspection of this figure reveals that the minimum absorption coefficient is .25 cm^{-1} at 6.0 μm while the 10.6 μm value is .55 cm^{-1}. The latter value is in good agreement with the 1 cm^{-1} - 2 cm^{-1} room temperature attenuation coefficient reported(1) for the best hot-pressed elements at 10.6 μm. The residual difference between the powder and hot-pressed coefficients may be attributed to

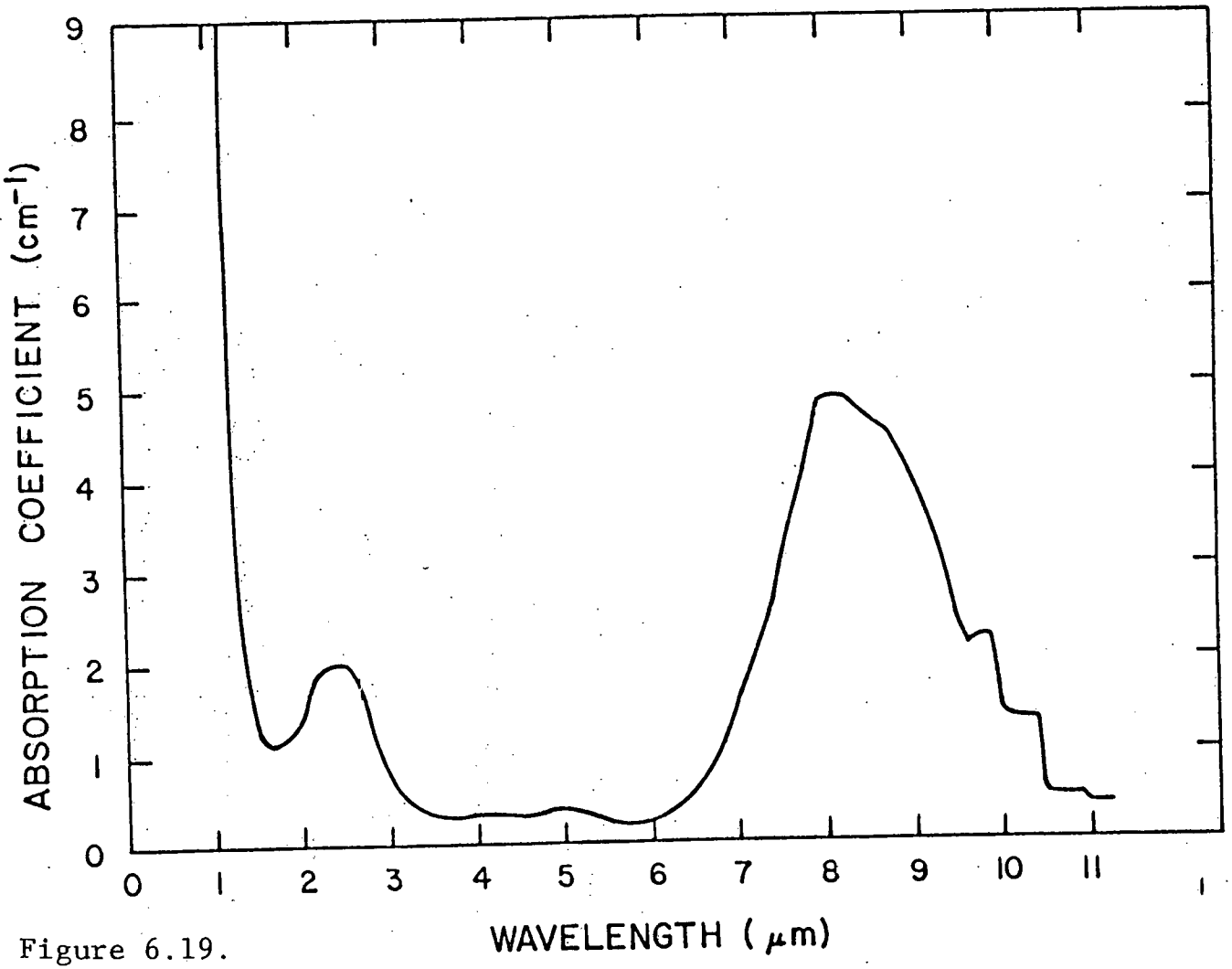
ABSORPTION COEFFICIENT (cm⁻¹)
0
1
2
3
4
5
6
7
8
9
0
1
2
3
4
5
6
7
8
9
10
11
WAVELENGTH (μm)

Figure 6.19.

the increased scattered and trapped radiation in the latter due to the incomplete densification of the $CdCr_2S_4$ during the hot-pressing process.

It is of interest to estimate the intrinsic absorption coefficient of $CdCr_2S_4$ at 10.6 μm due to multiphonon absorption. One experimental method of calculating this absorption coefficient is to assume that the extrinsic contribution to the absorption coefficient is the same at 10.6 μm and 6.0 μm. The intrinsic absorption coefficient is then simply found be subtracting the two values. For $CdCr_2S_4$, we find that the intrinsic absorption coefficient at 10.6 μm is 0.30 cm^{-1}, which is in excellent agreement with the estimate of 0.3 cm^{-1} obtained from a similar analysis using transmission techniques or hot-pressed samples(35).

6.8. Additional comments regarding the photoacoustic spectrometer

The monochromator used in this investigation was employed primarily as a result of its availability and because of economic considerations. The design of the photoacoustic spectrometer is therefore not optimal, and it is useful to consider two improvements in the system which could be easily implemented to improve either the speed, resolution, and/or signal to noise ratio.

In the measurement of infrared photoacoustic spectra,

primary consideration must be given to the maximization of the etendue of the optical system. In the present apparatus, the effective cone angle was only f/9. Conversion to f/4 optics could result in an increase in the total flux by a factor of 5.

An additional factor of two could also be achieved by simply using a front surface coated reflecting chopper blade to both modulate the radiation while supplying an a.c. reference beam. In the present apparatus, this would not only eliminate the wasteful beamsplitter, but would also eliminate the critical alignment associated with the device. It should be noted that this type of modulation was not used due to economic considerations.

Thus, we see that using a chopper beamsplitter in combination with a f/4 monochromator, it would be possible to gain a factor of 10 in the signal to noise ratio over the current system. In the infrared, where blackbody sources of radiation are notoriously poor, this increase would allow the examination of solids to proceed in addition to the current powder capability.

REFERENCES

1. S.D. JACOBS. Ferromagnetic isolation and modulation in the infrared using hot-pressed cadmium chromium sulfide and cobalt chromium sulfide, Ph.D. Thesis, University of Rochester, 1975.

2. T.J. COBURN, F. MOSER, R.K. AHRENKIEL, and K.J. TEEGARDEN, "Infrared absorption spectrum and Faraday rotation of hot-pressed $CdCr_2S_4$," IEEE Trans. on Magnetics, MAG-7, 392 (1971).

3. N. NOVROTSKY and O.J. KLEPPA. The thermodynamics of cation distrbutions in simple spinels, J. Inorg. Nucl. Chem. 29, 2701-2714, 1967.

4. D.S. McCLURE. The distribution of transition metal cations in spinels, J. Phys. Chem. Solids 3, 311-317, 1957.

5. A. MILLER. Distribution of cations in spinels, J. Appl. Phys. 30(4), 24S-25S, 1959.

6. R.W.G. WYEKOFF. Crystal structure, (New York: Interscience Publishers) 2nd Edition, v. 3, 1965.

7. F.D. BLOSS. Crystallography and Crystal Chemistry: an introduction, (New York: Holt, Rinehart and Winston, Inc.) p. 255, 1971.

8. H. von PHILIPSBORN. Growth of single crystals of cadmium chromium selenide by liquid transport with platinum catalyst, J. Appl. Phys. 38(3), 955-956, 1967.

9. H. von PHILIPSBORN. Crystal growth and characterization of chromium sulfo- and seleno-spinels, J. Crystal Growth 9, 296-304, 1971.

10. H. von PHILIPSBORN. Growth and properties of single crystals of the ferromagnetic semiconductors $CdCr_2Se_4$, Helv. Phys. Acta 40, 810-812, 1967.

11. L.K. SHICK, A.R. von NEIDA. Single-crystal growth of some chalcogenide spinels, J. Appl. Phys. 40(3), 1013-1015, 1969.

12. F.H. WEHMEIER. The growth of cadmium chromium selenide by chemical transport with cadmium chloride and the behavior of cadmium chromium selenide at elevated temperatures, J. Crystal Growth 5, 26-28, 1969.

13. D. KUSE. Influence of magnetic ordering on the Faraday effect in $CdCr_2Se_4$, IBM J. Res. Develop. 14(3), 315-317, 1970.

14. H.L. PINCH and L. EKSTROM. Vapor-phase growth of magnetic semiconducting spinels, RCA Rev. 31, 692-701, 1970.

15. K.G. BARRACLOUGH and A. MEYER. The CdSe-Cr_2Se_3 system and the formation of the ferromagnetic semiconducting spinel, $CdCr_2Se_4$, J. Crystal Growth 20, 212-216, 1973.

16. T. KIYOSAWA and K. MASUMOTO. P-T phase diagram for ferromagnetic semiconductor $CdCr_2Se_4$, J. Phys. Chem. Solids 38, 609-616, 1977.

17. D. PEARLMAN, E. CARNALL, JR. and T.W. MARTIN. The preparation of hot-pressed chalcogenide spinels, J. Solid State Chem. 7, 138-148, 1973.

18. P.J. WOJTOWICZ, P.K. BALTZER and M. ROBBINS, Magnetic and crystallographic properties of the system $(1-x)CdCr_2S_4 \cdot x\ CdCr_2Se_4$, J. Phys. Chem. Solids 28, 2423-2427, 1967.

19. J. PICKARDT, E. RIEDEL and B. REUTER. Herstellung von einKristallen im system $CdCr_2(S_{1-x}Se_x)_4$, Z. Anorg. Allg. Chemic. 373, 15, 1970.

20. I. BALBERT and A. MAMAN. Critical behavior of the optical absorption edge in $CdCr_2Se_4$, Phys. Rev. B, 16(10), 4535-4545, 1977.

21. D.M. EAGLES. Optical absorption due to transitions between bands and local levels in $CdCr_2Se_4$, J. Phys. Chem. Solids 39, 1243-1250, 1978.

22. S.G. STOYANOV, M.N. ILEIV and S.P. STOYANOVA. Spectral dependence of the photoconductance in $CdCr_2Se_4$: band and donor level splitting due to ferromagnetic ordering, Solid State Commun. 18, 1389-1392, 1976.

23. J.B. GOODENOUGH. Descriptions of outer d-electrons in thiospinels, J. Phys. Chem. Solids 30, 261-280, 1969.

24. M.D. COUTINHO-FILHO and I. BALBERG. New evidence for a narrow conduction band in $CdCr_2Se_4$, J. Appl. Phys. 50(3), 1920-1922, 1979.

25. A. AMITH and L. FRIEDMAN. Mixed-conduction model for charge transport in n-type $CdCr_2Se_4$, Phys. Rev. B. 2(2), 434-445, 1970.

26. L.R. FRIEDMAN and A. AMITH. Hole and electron bands in n-type $CdCr_2Se_4$, IBM J. Res. Develop. 14(3),

27. P.K. LARSEN and A.B. VOERMANS. Origin of the conductivity minimum and the negative magnetoresistance in n-type sulpho-spinels, J. Phys. Chem. Solids 34, 645-650, 1973.

28. T. ARAI, K. WAKAMURA and K.KUDO. Far infrared absorption and reflection on some semiconducting spinels, $CdCr_2Se_4$ and $CdCr_2S_4$, J. Phys. Soc. Japan 30, 1762, 1971.

29. H.D. LUTZ and M. FEHER. Gitterschwingungsspektren - IV. Mitterlung. Die absorptionsspektren von chalkogeno-spinellen ion langwelligen infrarot, Spectrochim Acta 27A, 357-365, 1971.

30. P. BRUESCH and F. D'AMBROGIO. Lattice dynamics and magnetic ordering the chalcogenide spinels $CdCr_2S_4$ and $CeCr_2Se_4$, Phys. Stat. Sol. (B), 513-526, 1972.

31. E.F. STEIGMEIER and G. HARBEKE. Phonons and magnetic order in ferromagnetic $CdCr_2Se_4$ and $CdCr_2S_4$, Phys. Kondens. Materic 12, 1-15, 1970.

32. M. BORN and M. BLACKMAN. Z. Physik 82, 421, 1933.

33. T.F. DEUTSCH. Absorption coefficient of infrared laser window materials, J. Phys. Chem. Solids 34, 2091-2104, 1973.

34. B. LAX and E. BURNSTEIN. Infrared lattice absorption in ionic and nonpolar crystals, Phys. Rev. 97, 39-52, 1955.

35. R.P. FREESE, K.J. TEEGARDEN. Hot-pressed $CdCr_2S_4$ for optical isolation at 10.6 μm, intrinsic absorption properties, Presented at the CLEOS Conference held in San Diego, CA, Feb. 7-9, 1978.

36. P.F. BONGERS and G. ZANMARCHI. Infrared absorption spectrum and Faraday rotation of ferromagnetic $CdCr_2Se_4$, Solid State Commun. 6, 291-294, 1968.

37. A.G. GUREVICH, YU M. YAKOVIEV, V.I. KARPOVICH, M.A. VINNIK and E.V. RUBALSKAYA. Ferromagnetic semiconductor, (review) Sov. Phys. Semicond. 9(1), 1-5, 1975.

38. T.H. LEE. Infrared Refectance of $CdCr_2S_4$ and $CdCr_2Se_4$, J. Appl. Phys. 42(4), 1441-1442, 1971.

39. V. WAGNER, H. MITLEHNER and R. GEICK. Infrared active phonons in $CdCr_2Se_4$, Optics Commun. 2(9), 429-430, 1971.

40. K. MIYATANI, F. OKAMOTO, P.K. BALTZER, S. OSAKA and T. OKA. Optical properties of impurity levels in $CdCr_2Se_4$ and $CdCr_2S_4$, AIP Conference on Mags. and Mag. Material 5, 285-289, 1971.

41. T. MOSS. Optical properties of semiconductors, (London: Butterworths Scientific Publications), 1959.

42. H.Y. FAN. Effects of free-carriers on the optical properties, Semiconductors and Semimetals, Vol. 3, R. K. Willardson and A.C. Beer, Editors, (New York: Academic Press), 1967.

43. J.G.J. PEELEN and R. METSELAAR. Light scattering by pores - in polycrystalline materials: transmission properties of alumina, J. Appl. Phys. 45(1), 216-220, 1974.

44. H.E. BENNETT. Scattering characteristics of optical materials, Opt. Engr. 17(5), 480-488, 1978.

45. M. KERRER. The Scattering of Light, (New York: Academic Press), 1969.

46. K. MIYATANI. The critical phenomena of the Heisenberg ferromagnet $CeCr_2Se_4$, J. Phys. Soc. Japan 28, 259-260, 1970.

47. N. MENYUK, K. DWIGHT and R.J. ARNOTT. Ferromagnetism in $CdCr_2Se_4$ and $CeCr_2S_4$, J. Appl. Phys. 37(3), 1387-1388, 1966.

48. P.K. BALTZER, P.J. WOJTOWICZ, M. ROBBINS and E. LOPATIN. Exchange interactions in ferrogmanetic chromium chalcogenide spinels, Phys. Rev. 151(2), 367-377, 1966.

49. J.M. ZIMAN, F.R.S. Principles of the Theory of Solids, (London: Cambridge University Press), 1972.

50. H.L. PINCH and S.B. BERGER. The effects on non-stoichiometry on the magnetic properties of cadmium chromium chalcogendie spinels, J. Phys. Chem. Solids 29, 2091-2099, 1968.

51. H.A. BROWN. Mixed magnetic systems: a model with applications to $(1-x)CdCr_2S_4 \cdot x\ CdCr_2Se_4$, J. Phys. Chem. Solids 30, 203-209, 1969.

52. H.A. BROWN. The classical-spin Bethe-Peierls-Weiss Method - I. Simple ferro- and antiferromagnetics, J. Phys. Chem. Solids 26, 1369-1378, 1965. The classical-spin Bethe-Peierls-Weiss Method - II. Ferrimagnetics and other extensions, J. Phys. Chem. Solids 26, 1379-1394, 1965.

53. B. LAX and K.J. BUTTON. Microwave ferrites and ferrimagnetics, (New York: McGraw-Hill Book Co., Inc.) 1962.

54. ALLAN H. MORRISH. The Physical Principles of Magnetism, (New York: John Wiley & Sons, Inc.), 594, 1966.

55. R.K. AHRENKIEL. Properties of $CoCr_2S_4$ applicable to Faraday rotators for CO_2 laser systems, IEEE-Trans. on Magnetics, 15, 1979.

56. R.C. GIFKINS. Transistions in creep behavior, J. Mater. Sci 5, 156-165, 1970.

57. E.D. CARNALL. Private Communication

58. M.R. NOTIS. Deformation mechanisms maps: a review with applications, Deformation of Ceramic Materials, R.C. Bradt and R.E. Tressler, Editors, (New York: Academic Press) 1010126, 1975.

59. E.J. FELTEN. Hot-pressing of alumina powders at low temperatures, J. Am. Ceram. Soc. 44, 38, 1961.

60. R.L. COBLE. A model for boundary diffusion controlled creep in polycrystalline materials, J. Appl. Phys. 34(6), 1679-1682, 1963.

61. R.L. COBLE. Diffusion models for hot-pressing with surface energy and pressure effects as driving forces, J. Appl. Phys. 41(12), 4789-4807, 1970.

62. P.A. URICK and M.R. NOTIS. Final-stage densification during pressure-sintering of CoO, J. Am. Ceram. Soc. 56(11), 570-574, 1973.

63. D.S. WILKINSON and M.F. ASHBY. The development of pressure sintering maps, Materials Science Research: Sintering and Catalysis, G.C. Kuczynsky, Editor, 473-492, 1975.

64. B. BRENNON and D.L. JOHNSON. Non-isothermal initial stage of sintering of silver, Materials Science Research: Sintering and Related Phenomena, G.C. Kuczunsky, Editor, 269-274, 1973.

65. F.R.N. NABARRO. Report of a conference on the strength of solids, Physical Society, London 75-90, (1948). Steady-State Diffusional Creep, Phil. Mag. 16, 231-237, 1967.

66. C. HERRING. Diffusional viscosity of a polycrystalline solid, J. Appl. Phys. 21, 437-445, 1950.

67. J. HARPER and J.E. DORN. Viscous creep of aluminum near its melting temperature, Acta Met. 5, 654, 1957.

68. B. BURTON and G.W. GREENWOOD. The limits of the linear relation between stress and strain rate in the creep of copper and copper-zinc alloys, Acta Met. 18, 1237, 1970.

69. P.C. DOKKO and J.A. PASK. Plastic deformation of ceramic materials, Mater. Sci. Eng. 25, 77-86, 1976.

70. B. WILSHIRE and B. WATKINS. Factors affecting the stress dependence for creep of polycrystalline magensia, J. Mater. Sci. 14, Letters, 1767-1769, 1979.

71. T.G. LANGDON. Grain boundary deformation processes, Deformation of Ceramic Materials, R.C. Bradt and R.E. Tressler, Editors, (New York: Academic Press), 101-126, 1975.

72. R.J. CHEN. Electrical properties of hot-pressed InSb and its application as an infrared detector, Ph.D. Thesis, University of Rochester, 1973.

73. W.P. STOLLAR and H.I. MOSS. Pressure sintering of gallium arsenide, J. Am. Ceram. Soc. 52(4), 204-210, 1969.

74. P. MURRAY, D.T. LIVELY and T. WILLIAMS. Ceramic fabrication processes p. 147-171, W.D. Kingery, Editor, (New York: Technology Press of Massachusetts Institute of Technology, and John Wiley & Sons, Inc.) 1958.

75. TUNG CHENG. The cadmium chromium selenide as an isolator for high power laser systems, M.S. Thesis, University of Rochester, 1976.

76. L. TREITINGER, H. PINK and H.GOBEL. Influence of Se-Deficiencies on the properties of In-doped $CdCr_2Se_4$ single crystals, J. Phys. Chem. Solids 39, 149-153, 1978.

77. L.J. VAN DER PAUW. A method of measuring specific resistivity and hall effects of discs of arbitrary shape, Philips Res. Repts. 13, 1-9, 1958.

78. R.B. FREESE. Photoacoustic investigation of infrared absorption, inhomogeneity, and laser damage in some highly transparent semiconductor thin films, substrates, and powders, Ph.D. Thesis, University of Rochester, 1980.

79. Annual Book of ASTM Standards. Standard method of test for density of glass by buoyancy. Designation C-693-74, 0.17, p. 688, 1975.

80. H.A. BOWMAN and R.M. SCHOONOVER. (M.W. JONES: Appendix), Procedure for high precision density determinations by hydrostatic weighing, J. Res. NBS 71C(3), 1967.

81. R.P. FREESE and K.J. TEEGARDEN. Applications of photo-acoustic spectroscopy in the infrared from 1 μm to 15 μm, presented at the Topical Meeting on Photoacoustic Spectroscopy held in Ames, Iowa, Aug. 1-3, 1979.

82. L.B. KREUZER. "The physics of signal generation and detection," in Optoacoustic Spectroscopy and Detection, edited by Y.H. Pao, Academic Press, N.Y. 1977.

83. P.W. KRUSE, L.D. McGLAUCHLIN and R.B. McQUISTAN. Elements of Infrared Technology, John Wiley & Sons, Inc. N.Y. 1962, p. 122.

84. Data supplied by B&K, Cleveland, Ohio, 1977.

85. L.B. KREUZER. "Ultralow gas concentration infrared absorption spectroscopy," J. Appl. Phys. 42, 2934, 1971.

86. N. FERNILIUS. "helmholz resonance effect in photoacoustic cells," Appl. Opt. 18, 1784, 1979.

87. A.L. ROUFF. Mass transfer problems in ionic crystals with charge neutrality, J. Appl. Phys. 36(9), 2903-2907, 1965.

88. B. BURTON. On the mechanism of the inhibition of diffusional creep by second phase particles, Mater. Sci. Eng. 11, 337-343, 1973.

89. T.J. COBURN, D. PEARLMAN, E. CARNALL, JR., F. MOSER, T.H. LEE, S.L. LYU and T.W. MARTIN. The preparation and magneto-optical properties of hot-pressings of the magnetic semiconductors $Cd_xCo_{1-x}Cr_2S_4$, AIP Conf. Proc. on Mag: and Mag: Materials (10(1), 740-744, 1971.

90. C. KITTEL. Introduction to Solid State Physics, (New York: John Wiley & Sons, Inc.) 5th Ed., 1976.

91. V. PROSSER, P. HLIDEK, P. HOSCHL, P. POLIVKA and M. ZVARA. Preparation and basic physical properties of single crystals of cadmium chromium selenide $CdCr_2Se_4$, Czech. J. Phys. B-24, 1168-1175, 1974.

92. G. LUCOVSKY, R.J. SLADEK and J.W. ALLEN. Infrared-active phonons in Cr_2O_3, Phys. Rev. B 16(10), 4716-4717, 1977.

93. R. MARSHALL, S.S. MITRA, P.J. GIELISSE, J.N. PLENDL and L.C. MANSUR. Infrared lattice spectra of α-Al_2O_3 and Cr_2O_3, J. Chem. Phys. 43(8), 2893-2894, 1965.

94. H.W. LEHMANN and M. ROBBINS. Electrical transport properties of the insulating ferromagnetic spinels $CdCr_2S_4$ and $CdCr_2Se_4$, J. Appl. Phys. 37(3), 1389-1390, 1966.

95. M.D. BANUS and M.C. LAVINE. Polymorphism in seleno-spinels - a high pressure phase of $CdCr_2Se_4$, J. Sol. State Chem. 7, 109-116, 1969.

96. See Chapter 5.2 of this report.

97. Staff, RCA Electro-Optics Handbook, RCA Corporation, Lancaster, PA (1974), pp. 83-84.

98. F. URBACH. "The long wavelength edge of photoacoustic sensitivity and of the electronic absorption of solids," Phys. Rev. 92, 1324, 1953.

99. D.L. DEXTER. "interpretation of Urbach's Rule," Phys. Rev. Lett. 19, 1383, 1967.

100. W.G. SPITZER. "Multiphonon lattice absorption," in Semiconductors and Semimetals, 3, Edited by R.K. Willardson and A.C. Beer, Academic Press, N.Y., 1967.

101. B. BENDOW, H.G. LIPSON and S.D. YUKON. "Residual lattice absorption in semiconducting crystals: frequency and temperature dependence," Appl. Opt. 16, 2909, 1977.

102. M. HASS and B. BENDOW. "Residual absorption in infrared materials," Appl. Opt. 16, 2882, 1977.

103. B.N. BROCKHOUSE and P.K. Iyengar. Phys. Rev. 111, 747, 1958.

104. D. PEARLMAN, E. CORNALL, JR., and T.W. MARTIN. "The preparation of hot-pressed chalcogenide spinels," J. Solid State Chem. 7, 138, 1973.

105. H.Y. FAN. "Effects of free carriers on the optical properties," in Semiconductors and Semimetals, 3, Edited by R.K. Willardson and A.C. Beer, Academic Press, N.Y., 1967.

106. D. PEARLMAN, E. CORNALL, JR., and T.W. MARTIN. "The preparation of hot-pressed chalcogenide spinels II stoichiometry and optical transmission in $CdCr_2S_4$ and $CdCr_2Se_4$," J. Solid State Chem. 9, 165, 1974.

107. L. COLOMBO. "Vacuum hot-pressing of $CdCr_2Se_4$ and $CdCr_2Se_{4-x}$ for infrared magneto-optical devices," Ph.D Thesis, University of Rochester, 1980.

108. S.B. SEYER and L. EKSTROM. "Optical properties of single crystal films of $CdCr_2S_4$," Phys. Rev. Lett. 23, 1499, 1969.

109. G. HARBEKE and H.W. LEHMANN. "Optical transitions and band structure model for cadmium chromium chalcogenides," Sol. State Comm. 8, 1281, 1970.

110. S. WITTEKOCK and G. RINZEMA. "The magneto-optic Ken effect and Faraday rotation of $CdCr_2S_4$ for radiation between 1.0 and 4.0 μm," Phys. State Sol. B 44, 849, 1971.

111. S. WITTEKOCK and P.F. BONGERS. "Observation of Cr^{+3} absorption bands in $CdCr_2S_4$ (Cr) and the consequences for the interpretation of the absorption edge in $CdCr_2S_4$," Sol. State. Comm. 7, 1719, 1969.

112. S. WITTEKOCK and P.F. BONGERS. "Magneto-optical investigation of the band edge of $CeCr_2S_4$ and related absorption measurement on Cr_2-doped $CdIm_2S_4$," IBM J. Res. Rev. 14, 312, 1970.

113. R.A. NYQUIST and R.O. KAGEL. Infrared Spectra of Inorganic Compounds, Academic Press, New York, 1971.